

# COHERENT SPIN DYNAMICS IN FERMIONIC QUANTUM GASES

FROM TWO-BODY TO MANY-BODY PHYSICS

Dissertation  
zur Erlangung des Doktorgrades  
des Fachbereichs Physik  
der Universität Hamburg

vorgelegt von  
Jasper Simon Krauser  
aus Berlin

Hamburg  
2014

Gutachter der Dissertation:	Prof. Dr. Klaus Sengstock Prof. Dr. Ludwig Mathey
Gutachter der Disputation:	Prof. Dr. Klaus Sengstock Prof. Dr. Henning Moritz
Datum der Disputation:	14. März 2014
Vorsitzender des Prüfungsausschusses:	Prof. Dr. Günter Sigl
Vorsitzender des Promotionsausschusses:	Prof. Dr. Daniela Pfannkuche
Dekan der Fakultät für Mathematik, Informatik und Naturwissenschaften:	Prof. Dr. Heinrich Graener

# Abstract

The spin plays a fundamental role for various many-body effects in nature, ranging from magnetism in solids to even more complex phenomena in high-spin systems such as the quark-gluon plasma. Quantum gases are ideally suited to study such systems in an exceptionally clean and controllable environment. For example, experiments with spinor Bose-Einstein condensates have revealed completely new high-spin phenomena in the last years. In this context, interaction-driven dynamics of the spin degree of freedom have been found. However, since the constituents of matter are fermions, there is a huge interest in current research activities to understand to which extent these effects also exist in fermionic systems.

This thesis is devoted to the investigation of fermionic spin dynamics. For the first time, spin-changing collisions could be observed in fermionic quantum gases. This novel effect has been explored in various regimes, ranging from the microscopic two-body process to the many-body regime.

For these investigations, new methods for the experimental preparation and control of fermionic high-spin systems have been developed. In a first approach, spin dynamics were investigated between two isolated fermions, realized in deep optical lattices. The results demonstrate novel coherent multi-flavor spin dynamics, involving up to ten different spin states. An excellent agreement with a two-particle scattering model allowed for the determination of fundamental scattering parameters and for the first demonstration of spin-changing collisions with high-collision quanta. Moreover, the experiments reveal a new instability of a band insulator in high-spin systems – in contrast to conventional solid-state systems – induced by spin-changing collisions.

Inspired by these fundamental findings, the impact of spin-changing collisions on a fermionic many-body system has been investigated. In a Fermi sea, consisting of several  $10^5$  particles with a spatial extension of several hundred micrometers, a fully unexpected phenomenon could be observed: the Fermi sea exhibits giant and long-lived spin oscillations induced by microscopic collisions despite its multi-mode structure. A detailed experimental study demonstrated that the whole system can be well captured in a mean-field approach using a single-mode approximation. This novel collective behavior is one of the few collective effects known in fermionic many-body systems such as superfluidity and constitutes a central result of this work.

In a further investigation, these collective spin dynamics have been employed to study relaxation effects, which are currently one of the most important topics of many-body physics. Doing so, studies demonstrated that collective spin dynamics are only stabilized due to Pauli blocking at ultralow temperatures. In addition, a new stabilization mechanism was discovered, which stabilizes magnetically excited spin mixtures governed by the interplay between different collision processes. In addition, spin-relaxation dynamics of fermionic atoms were observed for the first time, which lead to a thermalization of the fermionic many-body system on long time scales.

The results presented in this thesis provide an important contribution to a deeper understanding of fermionic many-body systems. They pave the way towards exciting studies of novel high-spin quantum phases, which so far have remained widely unexplored.



# Zusammenfassung

Für eine Fülle von Vielteilcheneffekten in der Natur spielt der Spin eine entscheidende Rolle, angefangen bei Magnetismus in Festkörpern bis hin zu noch komplexeren Effekten in Hochspin-Systemen wie dem Quark-Gluon Plasma. Anhand von Quantengasexperimenten können solche Systeme in einer beispiellos reinen und kontrollierbaren Umgebung untersucht werden. So haben Experimente mit Spinor Bose-Einstein Kondensaten in den letzten Jahren völlig neuartige Hochspin-Phänomene ans Licht gebracht. Ein Beispiel hierfür ist eine durch Stöße getriebene Spindynamik. Da die Grundbausteine der Materie aber Fermionen sind, ist es eine fundamentale Frage, inwieweit solche Hochspin-Phänomene auch in fermionischen Systemen zu finden sind.

Vor diesem Hintergrund widmet sich die vorliegende Arbeit der Untersuchung fermionischer Spindynamik. Zum ersten Mal konnten spinändernde Stöße in einem fermionischen Quantengas beobachtet werden. Dieser neuartige Effekt wurde von der mikroskopischen Zweiteilchenebene bis hin zum Vielteilchenregime intensiv erforscht.

Dafür wurden neue Methoden zur Präparation und zur experimentellen Kontrolle von fermionischen Hochspin-Systemen entwickelt. Zunächst wurde in tiefen optischen Gittern die Spindynamik zwischen zwei isolierten Fermionen untersucht. Die Ergebnisse zeigen eine neuartige multidimensionale Spindynamik, die bis zu zehn verschiedene Spinzustände kohärent einschließt. Die hervorragende Übereinstimmung mit einem Zweiteilchen-Stoßmodell erlaubte es, fundamentale Streuparameter zu bestimmen und zum ersten Mal Spinaustausch-Prozesse mit hohen Kollisionsquanten nachzuweisen. Erstmals wurde auch gezeigt, dass ein Bandisolator in Hochspin-Systemen – im Gegensatz zu Festkörpern – durch spinändernde Stöße instabil werden kann.

Inspiziert von diesen grundlegenden Erkenntnissen wurden spinändernde Stöße in fermionischen Vielteilchensystemen untersucht. In einem Fermisee, bestehend aus mehreren  $10^5$  Teilchen und mit einer Größe von einigen hundert Mikrometern, wurde ein völlig unerwartetes Phänomen entdeckt: Getrieben durch mikroskopische Stöße dreht der Fermisee kollektiv seinen Spin. Anhand einer detaillierten Studie konnte gezeigt werden, dass das gesamte Vielteilchensystem trotz seiner räumlichen Komplexität in einer Molekularfeldnäherung als eine einzige örtliche Mode beschrieben werden kann. Dieses neuartige kollektive Verhalten ergänzt die wenigen bisher bekannten kollektiven Effekte in Fermionen, wie z.B. Suprafluidität, und stellt ein zentrales Ergebnis der vorliegenden Arbeit dar.

In einer weiterführenden Untersuchung wurde die kollektive Spindynamik als Modellsystem zur Untersuchung von Relaxationseffekten eingesetzt, einem der zentralen Themen in der aktuellen Forschung der Vielteilchenphysik. In diesem Zusammenhang konnte nachgewiesen werden, dass das kollektive Verhalten nur durch eine Pauli-Blockade bei ultrakalten Temperaturen ermöglicht wird. Dabei wurde ein neuartiger Mechanismus entdeckt, der magnetisch angeregte Zustände durch Kollisionen intrinsisch stabilisiert. Des Weiteren konnte erstmals eine Relaxationsdynamik beobachtet werden, die das Hochspin-System auf einer langsamen Zeitskala thermalisieren lässt.

Die Ergebnisse dieser Arbeit tragen grundlegend zu einem besseren Verständnis der Physik fermionischer Vielteilchensysteme bei. Durch die erzielten Resultate eröffnet sich eine Fülle von vielversprechenden Perspektiven, z.B. die Untersuchung von neuartigen Quantenphasen in fermionischen Hochspinsystemen, die bislang weitgehend unerforscht sind.



## Publikationen

Im Rahmen der vorliegenden Arbeit sind die folgenden wissenschaftlichen Veröffentlichungen entstanden.

## Publications

The following research articles have been published in the course of this thesis.

- [1] J. S. Krauser, U. Ebling, N. Fläschner, J. Heinze, K. Sengstock, M. Lewenstein, A. Eckardt and C. Becker, *Giant Spin Oscillations in an Ultracold Fermi Sea*, *Science* **343**, 157 (2014)
- [2] U. Ebling, J. S. Krauser, N. Fläschner, K. Sengstock, C. Becker, M. Lewenstein and A. Eckardt, *Relaxation Dynamics of an Isolated Large-spin Fermi Gas Far from Equilibrium*, *Phys. Rev. X* **4**, 021010 (2014)
- [3] J. Heinze, J. S. Krauser, N. Fläschner, K. Sengstock, C. Becker, U. Ebling, A. Eckardt and M. Lewenstein, *Engineering Spin Waves in a High-Spin Ultracold Fermi Gas*, *Phys. Rev. Lett.* **110**, 250402 (2013)
- [4] J. Heinze, J. S. Krauser, N. Fläschner, B. Hundt, S. Götze, A. P. Itin, L. Mathey, K. Sengstock and C. Becker, *Intrinsic Photoconductivity of Ultracold Fermions in Optical Lattices*, *Phys. Rev. Lett.* **110**, 085302 (2013)
- [5] J. S. Krauser, J. Heinze, N. Fläschner, S. Götze, O. Jürgensen, D.-S. Lühmann, C. Becker and K. Sengstock, *Coherent multi-flavour spin dynamics in a fermionic quantum gas*, *Nat. Phys.* **8**, 813-818 (2012)
- [6] J. Heinze, S. Götze, J. S. Krauser, B. Hundt, N. Fläschner, D.-S. Lühmann, C. Becker and K. Sengstock, *Multiband Spectroscopy of Ultracold Fermions: Observation of Reduced Tunneling in Attractive Bose-Fermi Mixtures*, *Phys. Rev. Lett.* **107**, 135303 (2011)
- [7] U. Bissbort, S. Götze, Y. Li, J. Heinze, J. S. Krauser, M. Weinberg, C. Becker, K. Sengstock and W. Hofstetter, *Detecting the Amplitude Mode of Strongly Interacting Lattice Bosons by Bragg Scattering*, *Phys. Rev. Lett.* **106**, 205303 (2011)



# Contents

<b>1</b>	<b>Introduction</b>	<b>1</b>
<b>2</b>	<b><math>^{40}\text{K}</math> – an ideal candidate for fermionic spin dynamics</b>	<b>7</b>
2.1	The internal structure of $^{40}\text{K}$ . . . . .	7
2.2	Scattering properties of $^{40}\text{K}$ . . . . .	9
2.2.1	Interactions in high-spin systems . . . . .	9
2.2.2	Spin-changing collisions in $^{40}\text{K}$ . . . . .	12
<b>3</b>	<b>High-spin fermions in the laboratory</b>	<b>17</b>
3.1	The <i>Bose-Fermi Mixture</i> experiment . . . . .	17
3.1.1	The experimental setup . . . . .	18
3.1.2	The general procedure . . . . .	18
3.2	Preparing, cooling and probing high-spin fermions . . . . .	20
3.2.1	Producing a spin-polarized Fermi sea . . . . .	20
3.2.2	The spin-state preparation . . . . .	23
3.2.3	Realizing ultracold spin mixtures . . . . .	25
3.2.4	Probing high-spin fermions . . . . .	28
3.3	Magnetic field control . . . . .	30
3.3.1	Magnetic offset fields . . . . .	31
3.3.2	Magnetic gradients . . . . .	33
<b>4</b>	<b>Spin dynamics in optical lattices</b>	<b>39</b>
4.1	Characterizing fermions in optical lattices . . . . .	40
4.1.1	Calibration of the optical lattice . . . . .	40
4.1.2	Describing high-spin fermions in optical lattices . . . . .	43
4.2	Two-particle spin dynamics . . . . .	46
4.2.1	The experimental procedure . . . . .	46
4.2.2	A proof-of-principle experiment . . . . .	48
4.2.3	A fermionic spin resonance . . . . .	52
4.2.4	Coherent multi-flavor spin dynamics . . . . .	55
4.2.5	Crossover to depolarized multi-flavor spin dynamics . . . . .	58
4.2.6	Observation of high-collision quanta . . . . .	60
4.3	Spin dynamics at finite lattice depth . . . . .	62
4.3.1	Multi-site spin dynamics . . . . .	62
4.3.2	Observation of multi-site spin dynamics . . . . .	65
4.3.3	Studying the transition to the many-body regime . . . . .	66
4.4	Spin dynamics between different bands . . . . .	70

4.4.1	Multi-band spin dynamics . . . . .	70
4.4.2	Observation of interband spin transfer . . . . .	72
4.5	Conclusion and outlook . . . . .	74
<b>5</b>	<b>Collective spin dynamics in fermionic bulk systems</b>	<b>75</b>
5.1	A mean-field description for high-spin fermions . . . . .	76
5.1.1	The collisionless Boltzmann equation . . . . .	76
5.1.2	Requirements for spin dynamics . . . . .	79
5.2	Observation of giant and long-lived spin oscillations . . . . .	81
5.3	Studying the collective nature of spin oscillations . . . . .	82
5.3.1	The influence of the trapping potential . . . . .	83
5.3.2	Suppression of spatial structures . . . . .	84
5.3.3	Influence of magnetic gradients . . . . .	85
5.3.4	Implementation of a fermionic single-mode approximation . . . . .	87
5.4	Studying the spin-oscillation properties . . . . .	89
5.4.1	The influence of the magnetic field . . . . .	89
5.4.2	The influence of the density . . . . .	90
5.4.3	Engineering the mean-field background . . . . .	92
5.4.4	Spin dynamics between different spin mixtures . . . . .	94
5.4.5	Direct observation of high-collision quanta . . . . .	95
5.5	Conclusion and outlook . . . . .	97
<b>6</b>	<b>Relaxation in high-spin fermions</b>	<b>99</b>
6.1	Collision processes in a high-spin Fermi sea . . . . .	100
6.1.1	A microscopic approach . . . . .	100
6.1.2	The collision term . . . . .	102
6.2	Impact of temperature on collective spin dynamics . . . . .	104
6.2.1	Scattering processes at higher temperatures . . . . .	104
6.2.2	Observation of strong damping at higher temperatures . . . . .	106
6.3	Suppression of collective dynamics at intermediate interactions . . . . .	110
6.3.1	Observation of fermionic spin instabilities . . . . .	110
6.3.2	Suppression of instability dynamics at higher densities . . . . .	112
6.4	Spin-relaxation dynamics in high-spin fermions . . . . .	116
6.4.1	A single-mode approximation for the collision term . . . . .	116
6.4.2	Observation of spin-relaxation dynamics . . . . .	117
6.4.3	Studying the spin-relaxation properties . . . . .	118
6.5	Conclusion and outlook . . . . .	122
<b>A</b>	<b>Appendix: Non-interacting fermions</b>	<b>123</b>
<b>B</b>	<b>Appendix: Feshbach resonances in <math>^{40}\text{K}</math></b>	<b>127</b>
<b>C</b>	<b>Appendix: Details for fermionic spin dynamics</b>	<b>131</b>
	<b>List of Figures</b>	<b>141</b>
	<b>List of Tables</b>	<b>145</b>
	<b>Bibliography</b>	<b>147</b>

# Chapter 1

## Introduction

The advent of quantum mechanics in the early 20<sup>th</sup> century was driven by groundbreaking findings that required to discard the well-established classical understanding of physics. One of these striking discoveries was observed in the famous Stern-Gerlach experiment in 1922 [8], revealing that the magnetic moment of atoms is quantized. Only a few years later, new theories introduced the spin [9, 10], which plays a fundamental role in various many-body effects in nature. In electronic spin 1/2 systems, for example, the microscopic interplay between two spin states gives rise to fascinating phenomena with high relevance for modern research and technology, e.g. ferromagnetism, giant magnetoresistance or superconductivity. Beyond this, there are systems in nature with more than two spin components, such as the quark-gluon plasma or atomic ensembles. The resulting high-spin interactions lead to even more complex and counterintuitive many-body effects, which are the subject of this thesis.

With the experimental realization of ultracold atoms, such many-body effects can be addressed in an unprecedented way. At ultralow temperatures, the atomic systems are dominated by their quantum mechanical properties and called quantum degenerate. There are two fundamental groups of particles with different quantum statistics: bosons and fermions. Bosons have an integer spin and form a Bose-Einstein condensate, where all atoms macroscopically occupy the same single-particle state. In contrast, fermions have a half-integer spin and form a Fermi sea, where each available single-particle state can be occupied with only one particle. The experimental realization of Bose-Einstein condensation was achieved in 1995 for the first time [11–13] and was awarded with the Nobel Prize (2001). Only a few years later in 1999, the first quantum degenerate Fermi gas was realized [14–16]. These discoveries opened a new and rapidly growing field of research. Until today, a large number of experiments studying quantum degenerate atomic gases have been realized and several elements have been cooled to ultralow temperatures [11–30].

These systems of ultracold atoms allow for an excellent control of the crucial experimental parameters [31] such as the interaction strength, the spatial configuration, and the internal state of the atoms. Moreover, the application of optical lattices in quantum gas systems closely relates to solid-state systems [32]. These features have triggered tremendous experimental and theoretical studies in recent years, exploring, e.g., quantum phase transitions [33–44] and magnetic properties [45–47]. Recently, a lot of effort has been directed towards fermionic quantum gases. They are described by the same quantum statistics as the constituents of matter like quarks, leptons, or baryons

and resemble real many-body systems closer than their bosonic counterpart. A variety of experimental settings with spin 1/2 fermions were realized, including harmonically trapped systems, fermions in optical lattices or lower-dimensional systems. Ground-breaking studies of fundamental many-body effects have been performed, ranging from ground-state phase diagrams to non-equilibrium phenomena [38–40, 47–62].

Beyond this, quantum gases also allow to study systems with higher spin, involving more than two spin components. The additional spin degree of freedom has dramatic consequences: all participating spin states interact, constituting a completely new class of many-body systems.

In this respect, bosons with high spin have been widely explored, combining high-spin interactions with the superfluidity immanent to Bose-Einstein condensates [63–65]. Starting with the first realization in 1998 [66], experimental and theoretical studies have revealed a variety of phenomena (for review articles on this topic see [67, 68]). The phase diagrams of magnetic ground states [69], spin domains induced by spontaneous symmetry breaking [70], and pattern formation [71] are only a few prominent examples. Another research direction of this field focuses on spin squeezing and spin entanglement, prosperous for quantum information applications [72, 73]. Furthermore, spin-changing collisions are a unique high-spin feature, which induces an intriguing dynamics of the spin degree of freedom. Experiments have studied bosonic spin dynamics in different regimes. In deep optical lattices, the fundamental two-body collision process, apparent in coherent spin oscillations, has been investigated [74, 75]. In harmonically trapped Bose-Einstein condensates, collective spin dynamics have been observed, involving the whole many-body system. This includes coherent spin-mixing oscillations [76–80] and fluctuation-induced dynamical instabilities [81, 82]. Recently, high-spin bosons governed by dipolar interactions have been realized, leading to the discovery of spin dynamics mediated by anisotropic and long-range interactions [83, 84].

While many experimental studies have been performed with high-spin bosons, the research field of high-spin fermions emerged only recently and has been growing rapidly especially from the theoretical side [85]. A natural extension of the conventional fermionic spin 1/2 systems are three-component spin mixtures. This could be realized in experiments with fermionic lithium, allowing for a wide tunability of the high-spin interaction parameters [86, 87]. This system has raised tremendous interest, and several novel features have been proposed [88–96]: a fascinating example is an unconventional BCS pairing involving different pairs of spin states. For increasing interactions, a quantum phase transition from a color superfluid state to strongly bound trions is predicted, related to color superconductivity of quark matter in nuclear physics. A further extension of this system are fermionic alkaline-earth atoms with high spin, which allow to study many-body physics exploiting the unique feature of  $SU(N)$ -symmetry [97], where the s-wave scattering lengths are equal. In this context, exotic many-body phenomena are proposed [98–101], connected to the physics of heavy-fermion materials or strongly-correlated transition-metal oxides. Recently, also these systems have been experimentally realized, employing quantum degenerate gases of fermionic strontium [28] and ytterbium atoms [102]. Moreover, experiments were able to prove the effect of Pomeranchuk cooling in an  $SU(6)$ -symmetric Mott-insulator [103], which is due to the increased entropy associated with the large spin.

A completely different approach focuses on the dynamical properties of high-spin fermions [104, 105], which is inspired by the intriguing spin dynamics observed in

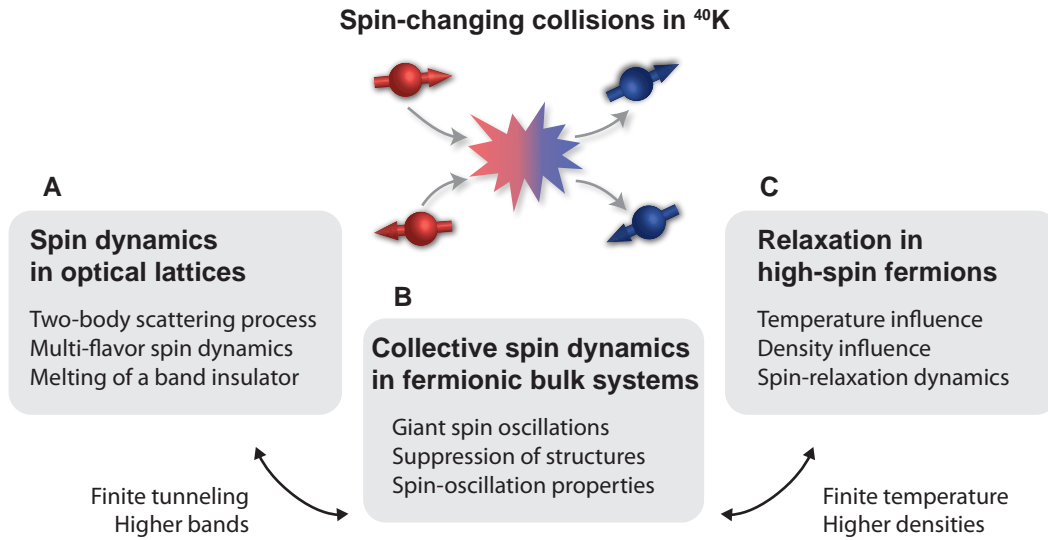


**Figure 1.1: The key results of this thesis.** A quantum gas of  $^{40}\text{K}$  with ten available spin states has been employed allowing for the first observation of fermionic spin-changing collisions (see illustration in the figure), which have been investigated in different regimes: **(A)** A study in deep optical lattices allowed to access the pure two-body scattering process (see chapter 4). **(B)** Spin dynamics have been studied in a large Fermi sea revealing giant and long-lived spin oscillations (see chapter 5). **(C)** Relaxation effects in a Fermi sea have been investigated, which lead to a suppression of collective behavior (see chapter 6).

bosonic systems. In particular the different quantum statistics raise fundamental questions, which so far have remained widely unanswered: Can fermions also perform spin-changing collisions, analogous to their bosonic counterpart? How does a fermionic many-body system evolve under such collisions? Which phenomena observed in Bose-Einstein condensates survive in an intrinsically multi-mode Fermi sea?

Motivated by these questions, this thesis is devoted to fermionic spin dynamics. For the experiments, an ultracold gas of fermionic  $^{40}\text{K}$  with ten available spin states was employed, allowing to address the above-mentioned questions. Spin-changing collisions could be observed in fermionic quantum gases for the first time. The experiments cover a broad range from local spin oscillations in the two-body limit to collective spin dynamics in the many-body regime. Figure 1.1 outlines the main results and their connections.

New experimental methods for the preparation and the control of high-spin fermions have been developed. The route pursued to study fermionic spin dynamics started with the investigation of the fundamental collision process: two fermions collide and change their spin configuration. These experiments, realized in deep optical lattices, revealed long-lived coherent spin dynamics with a unique multi-flavor character for the first time. The high control of this system allowed for deep insight into the spin-changing collision process on a microscopic level. Inspired by these results, the impact of the microscopic process on a fermionic many-body system has been investigated. Here, a completely unexpected macroscopic phenomenon could be observed: a Fermi sea exhibits collective and giant spin oscillations, despite its intrinsic multi-mode structure.

This intriguing collective behavior was found to be induced by the interplay between spin and spatial dynamics. It was demonstrated that this can last for several seconds, even in large samples with several  $10^5$  particles and a spatial extension of hundreds of micrometers. A detailed experimental study revealed that the dynamical properties are very well captured in a mean-field approach even in a single-mode approximation. These findings motivated further studies on relaxation effects in a high-spin Fermi sea and particularly on the role of different collision processes, which also occur on very different time scales. For the first time the experiments could show that Pauli blocking stabilizes the collective spin oscillations at ultralow temperatures. Increasing temperature and interaction strength, in contrast, leads to a suppression of the collective behavior. In this context, a novel spin-stabilization mechanism induced by the intrinsic collisional properties of the many-body system has been found, which can stabilize magnetically excited spin mixtures. Moreover, slow spin-relaxation dynamics, driving the system towards an equilibrium spin distribution, were observed for the first time.

The results presented in this thesis experimentally pioneer the new research field of fermionic spin dynamics. From the two-particle to the many-body regime, a high experimental control over this novel phenomenon could be demonstrated. The understanding of the microscopic interaction process provides an important step for further fermionic high-spin experiments. In addition, the results in the many-body regime allow for a deep insight into high-spin magnetic properties and pave the way towards the realization of completely new high-spin quantum phases. The question whether or not these systems exhibit even richer features has to be revealed in future experiments.

## Structure of this thesis

### Chapter 2: $^{40}\text{K}$ – an ideal candidate for fermionic spin dynamics

The isotope  $^{40}\text{K}$  combines two important features for the study of fermionic spin dynamics, which will be highlighted in this chapter: it has a large spin of  $f = 9/2$  in the lowest hyperfine manifold allowing for experiments with ten spin states. Moreover, its scattering properties are particularly well suited for spin-changing collisions.

### Chapter 3: High-spin fermions in the laboratory

The experimental realization of high-spin fermions faces several challenges. Versatile experimental tools, which were implemented throughout this work, will be described. This includes the preparation and probing of ultracold arbitrary spin mixtures. In addition, important methods developed for the magnetic field control will be presented.

### Chapter 4: Spin dynamics in optical lattices

In this chapter, a detailed investigation of spin dynamics in optical lattices and the first realization of fermionic spin-changing collisions will be presented. First, the pure two-body collision process will be studied, realized in deep optical lattices. Then the impact of finite tunneling, which leads to a novel melting process of a band insulator, will be presented. Finally, the system is further extended to higher bands and a band population transfer induced by spin-changing collisions will be reported. The results of this chapter have partly been published in [5].

---

**Chapter 5: Collective spin dynamics in fermionic bulk systems**

In this chapter, the impact of spin-changing collisions on a fermionic many-body system will be studied. As a key result of this research work, the first observation of giant and collective spin dynamics in a Fermi sea can be reported. To explain this unexpected behavior, the mechanism inducing the collective dynamics and a single-mode approximation in a mean-field approach are discussed. Subsequently, a detailed investigation of the spin-oscillation properties will be presented. The results of this chapter have partly been published in [1].

**Chapter 6: Relaxation in high-spin fermions**

Based on the observation of giant spin oscillations, relaxation effects in a fermionic quantum gas with high spin will be studied in this chapter. Different collision processes, described by a Boltzmann approach including a collision term, will be worked out. The impact of increasing temperature will be investigated, which demonstrates a continuous suppression of collective dynamics. Subsequently, the influence of intermediate interactions will be studied, where a new spin-stabilization mechanism can be presented. Finally, experiments investigating a new spin-relaxation dynamics will be discussed. The results of this chapter have partly been published in [1, 2].

Being involved in the research leading into this thesis, I have also participated in several further studies, which are not presented. This includes the detection of the amplitude mode in a strongly interacting Bose gas using Bragg spectroscopy [7], which will be in detail explained in the thesis of S. Götze [106]. In addition, multi-band spectroscopy of Bose-Fermi mixtures [6] and higher-band dynamics in optical lattices [4] have been studied. Moreover, a detailed investigation of tensorial spin waves has been performed in a fermionic bulk system [3]. These topics have been also discussed in the thesis of J. Heinze [107]. Furthermore, Feshbach resonances in  $^{40}\text{K}$  have been explored, which is described in the diploma theses of N. Fläschner [108] and M. Langbecker [109]. This is discussed in appendix B, where 20 new Feshbach resonances are identified. I have also participated in the implementation of a hexagonal lattice for future experiments at the *Bose-Fermi Mixture* setup in Hamburg.



## Chapter 2

# $^{40}\text{K}$ – an ideal candidate for fermionic spin dynamics

The study of fermionic spin-changing dynamics (also referred to as spin dynamics) demands a fermionic system with more than two spin states. At first glance it seems that there is a plethora of fermionic high-spin systems available due to the complex internal structure of atoms. However, the instability of most atomic and molecular states occurs on time scales much faster than observable effects. This limits quantum gas experiments typically to the ground-state hyperfine manifolds. Nevertheless, various fermionic isotopes with high spin have been cooled to quantum degeneracy. Besides the conventionally used potassium [14] and lithium [15, 16], recently also ultracold fermionic helium [26], ytterbium [27], strontium [28], dysprosium [29], and erbium [30] have been realized.

In addition, the scattering properties are crucial to study spin dynamics. In this context, two fundamentally different scenarios can be distinguished:  $\text{SU}(N)$ -symmetric systems (for example ytterbium) exhibit the same interaction energy for all combinations of spin mixtures [97]. Spin-changing dynamics, however, require a broken  $\text{SU}(N)$ -symmetry, which leads to different interaction energies for different spin mixtures. Moreover, dipolar interactions induced by the magnetic moment of the atoms can be present (for example in strontium, dysprosium and erbium), which have an anisotropic and long-range character [110]. In contrast to conventional s-wave scattering, this allows to study a variety of novel phenomena but also leads to a complex high-spin scattering behavior as recently demonstrated for bosonic chromium [83, 84].

$^{40}\text{K}$  combines a high spin of  $f = 9/2$  with suitable s-wave scattering properties. As worked out in this chapter, it is an ideal candidate for the exploration of fermionic spin-changing collisions. In section 2.1, the internal structure of  $^{40}\text{K}$  in the ground-state hyperfine manifolds will be reviewed. Subsequently, the general concept of high-spin scattering will be introduced, including the possibility of spin-changing collisions. I will apply this to the case of  $^{40}\text{K}$  (section 2.2), apparent in an intriguing structure of available spin systems and spin-dependent scattering properties.

### 2.1 The internal structure of $^{40}\text{K}$

$^{40}\text{K}$  belongs to the alkali group with one electron in the outer shell. Its hyperfine ground-state structure corresponds to different orientations of the total angular momentum

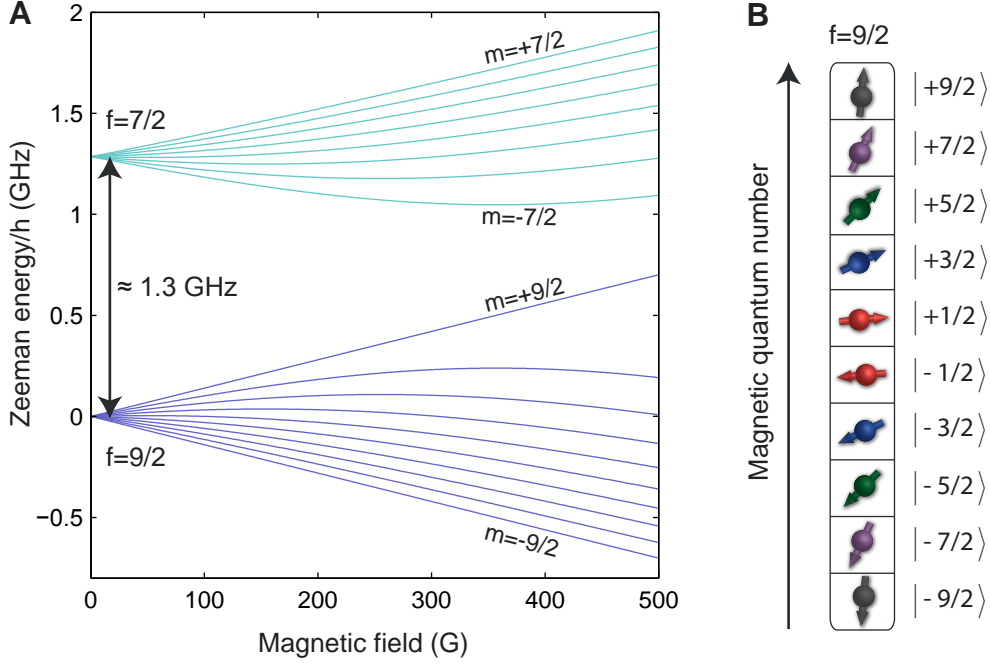


**Figure 2.1: Zeeman splitting of the ground-state hyperfine manifolds of  $^{40}\text{K}$ .** (A) The energy of the spin states in the ground-state manifolds  $f = 9/2$  and  $f = 7/2$  is depicted as a function of the magnetic field. The calculations are performed using the Breit-Rabi formula 2.1. The linear splitting in the Zeeman regime and the nonlinear splitting in the Paschen-Back regime are clearly visible. (B) Illustration of the ten spin states in the lowest hyperfine manifold of  $^{40}\text{K}$  ranging from  $m = +9/2, \dots, -9/2$ , which is widely used throughout this thesis.

$j = 1/2$  and the nuclear spin  $i = 4$ . Therefore, two ground-state hyperfine manifolds with total spin  $f = i \pm j = \{9/2, 7/2\}$  exist. The manifold with  $f = 9/2$  comprises ten different spin states with magnetic quantum numbers ranging from  $m = -9/2, \dots, +9/2$ . In the manifold with  $f = 7/2$  eight spin states with magnetic quantum numbers ranging from  $m = -7/2, \dots, +7/2$  are available. Both manifolds are separated by the hyperfine interaction, which has its origin in the interplay between electronic and nuclear spin, yielding an energy splitting of approximately 1.3 GHz. Note that  $^{40}\text{K}$  has an inverted hyperfine structure such that the  $f = 9/2$  manifold has the lowest energy.

If the atoms are exposed to a magnetic field, the degeneracy of the spin states in each manifold is lifted. Due to the Zeeman effect, different spin states exhibit different energy shifts [111]. For alkali atoms, the Zeeman energy can be calculated analytically yielding the Breit-Rabi formula [112]:

$$E_{\text{BR}}^{(m)}(B) = -\frac{\Delta E_{\text{hfs}}}{2(2i+1)} + g_i \mu_B B (m_i \pm 1/2) \pm \frac{\Delta E_{\text{hfs}}}{2} \sqrt{1 + \frac{4x(m_i \pm 1/2)}{2i+1} + x^2}. \quad (2.1)$$

Here,  $\Delta E_{\text{hfs}} = (i + 1/2) A_{\text{hfs}}$  is the hyperfine splitting and we have introduced the abbreviation  $x = (g_j - g_i) \mu_B B / \Delta E_{\text{hfs}}$  containing the Bohr magneton  $\mu_B$  and Landé factors  $g_j$  and  $g_i$ . The sign accounts for both possible alignments of the total angular momentum  $m_j = \pm 1/2$ .

The Zeeman splitting is depicted for the spin states of both hyperfine manifolds in Fig. 2.1 A. Two different regimes can be classified: at low magnetic fields, the hyperfine interaction dominates the system and  $f$  as well as  $m$  are good quantum numbers. This motivates the notation  $|f, m\rangle$ , which is widely used for the spin-state representation in the following. The notation  $|m\rangle$  is employed for simplicity implying that the total spin is  $f = 9/2$ . In the so-called Zeeman regime, the magnetic field dependence of the spin states is rather linear and corrections are well described in a quadratic expansion of equation 2.1. The experiments presented in this thesis have been carried out in this regime. At large magnetic fields, strong nonlinear contributions appear. In this so-called Paschen-Back regime, the magnetic quantum numbers of the electronic and the nuclear spin themselves are good quantum numbers. Large magnetic fields are important for  $^{40}\text{K}$  since experimentally relevant Feshbach resonances occur in this regime (see appendix B).

Both hyperfine manifolds of  $^{40}\text{K}$  comprise 18 spin states. However, due to lifetime limitations (see section 3.2.3), the experimental studies presented in this thesis are limited to the lowest hyperfine manifold with  $f = 9/2$ . The upper manifold is mainly employed for spin-selective detection schemes. Nevertheless, this fermionic high-spin system involves ten spin states (illustrated in Fig. 2.1 B) and is ideally suited to study fermionic spin dynamics.

## 2.2 Scattering properties of $^{40}\text{K}$

In this section, the general concept of high-spin interactions will be discussed, focusing on spin-changing collisions between fermionic atoms. Subsequently, these concepts will be applied to  $^{40}\text{K}$ . This will show that also the scattering properties of  $^{40}\text{K}$  are particularly well suited to study fermionic spin dynamics.

### 2.2.1 Interactions in high-spin systems

Scattering of atoms with high spin has been explored with Bose-Einstein condensates (several review articles on this issue are available [67, 68]). The concept can also be applied to fermionic atoms taking into account the particular symmetry of the system.

#### The high-spin scattering Hamiltonian

Consider two colliding fermions in the spin states  $|f_1, m_1\rangle$  and  $|f_2, m_2\rangle$ . To derive the corresponding scattering Hamiltonian, several approximations are commonly made in spinor physics [68]:

##### S-wave scattering

We assume that only the lowest order partial wave participates in the collision process. This assumption is valid at low temperatures, when the thermal de-Broglie length of the relative atomic motion is much larger than the effective range of the potential.

##### Rotational invariance

One assumes a rotationally symmetric interaction, which ensures the conservation of the total angular momentum  $\vec{F} = \vec{f}_1 + \vec{f}_2$  of the colliding atom pair. This

neglects the inner structure of the atoms as well as external sources such as inhomogeneous magnetic fields or trapping potentials [113, 114].

### Suppression of hyperfine-changing collisions

This approximation excludes collisions between different hyperfine manifolds. All experiments presented in the following are limited to the  $f = f_1 = f_2 = 9/2$  manifold.

### Identical particles

We consider collisions between atoms of the same isotope and species. Hence, the particles are indistinguishable, requiring a well-defined symmetry of the total wave function, e.g., a symmetric wave function for bosons and an antisymmetric wave function for fermions.

Using the pseudo-potential method [115], the following interaction Hamiltonian can be derived [63–65]:

$$\mathcal{H}_I = \frac{4\pi\hbar^2}{m} \delta(\vec{r}_1 - \vec{r}_2) \sum_{F=0,2,\dots}^{2f} a_F \sum_{M=-F}^F |F, M\rangle \langle F, M|. \quad (2.2)$$

Here,  $m$  is the atomic mass. The delta function accounts for the effective contact interaction and is only non-zero when both particles are at the same position ( $\vec{r}_1 = \vec{r}_2$ ). Due to the rotational symmetry of the system, the total-spin operator commutes with the interaction Hamiltonian ( $[F^2, \mathcal{H}_I] = 0$ ). Hence, the total spin  $\vec{F} = \vec{f}_1 + \vec{f}_2$  and the total magnetization  $M = m_1 + m_2$  are conserved and form a suitable basis  $\{|F, M\rangle\}$ . The collision process is characterized by the s-wave scattering lengths  $a_F$ , which depend on the total-spin collision channel  $F$ . Note that the sum in equation 2.2 includes only even values of the total spin, which is a direct consequence of the symmetry of the wave function and holds for fermions and bosons.

The total-spin basis described above exploits the rotational symmetry of the scattering problem and is hence well suited to describe the scattering process. In real experiments, the typical observation basis are the spin states  $|m\rangle$  of the individual atoms. Their occupation can be observed for example in a Stern-Gerlach experiment (see section 3.2.4). In this context, it is suitable to introduce the two-particle states

$$|m_1, m_2\rangle = \frac{1}{\sqrt{2}}(|m_1\rangle |m_2\rangle - |m_2\rangle |m_1\rangle), \quad (2.3)$$

which constitute a complete basis set for all different spin configurations. To reformulate the interaction Hamiltonian, the corresponding transformation from the total-spin basis  $\{|F, M\rangle\}$  to the observation basis  $\{|m_1, m_2\rangle\}$  yields

$$\mathcal{H}_I = \frac{4\pi\hbar^2}{m} \delta(\vec{r}_1 - \vec{r}_2) \sum_{m_1+m_2=m_3+m_4} a_{m_1 m_2 m_3 m_4} |m_3, m_4\rangle \langle m_1, m_2|. \quad (2.4)$$

The spatial part is not affected by this transformation. The spin part contains all scattering processes, which conserve the total magnetization  $M = m_1 + m_2 = m_3 + m_4$ . Each collision channel is characterized by spin-dependent scattering lengths  $a_{m_1 m_2 m_3 m_4}$ ,

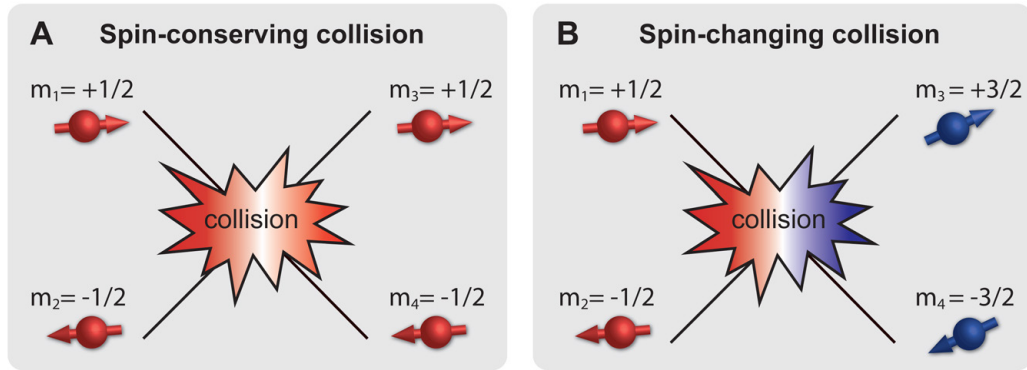


**Figure 2.2: Sketch of a high-spin scattering process.** In a simplified picture, two different contributions of the collision can be distinguished: **(A)** a conventional spin-conserving collision, where the initial and final spin configuration are equal ( $|m_1, m_2\rangle = |m_3, m_4\rangle$ ). **(B)** a spin-changing collision, where the spin configuration is changed ( $|m_1, m_2\rangle \neq |m_3, m_4\rangle$ ), conserving the total magnetization ( $M = m_1 + m_2 = m_3 + m_4$ ) and obeying the Pauli exclusion principle ( $m_1 \neq m_2$  and  $m_3 \neq m_4$ ).

which are directly related to the total-spin scattering lengths  $a_F$  by the Clebsch-Gordan coefficients:

$$a_{m_1 m_2 m_3 m_4} = \sum_{F=0}^{2f} a_F \sum_{M=-F}^F \langle m_1, m_2 | F, M \rangle \langle F, M | m_3, m_4 \rangle. \quad (2.5)$$

The four indices of the spin-dependent scattering lengths account for the initial and final spin configuration. If  $|m_1, m_2\rangle = |m_3, m_4\rangle$ , the collision is spin-conserving. In contrast, if  $|m_1, m_2\rangle \neq |m_3, m_4\rangle$ , then the scattering process corresponds to a spin-changing collision as described in the following.

### The concept of fermionic spin-changing collisions

Consider two particles in two different spin states  $m_1$  and  $m_2$  with a total magnetization  $M = m_1 + m_2$ . The corresponding two-particle state  $|m_1, m_2\rangle$  is typically not an eigenstate of the interaction Hamiltonian, but a superposition of different  $|F, M\rangle$ , where  $F \geq |M|$ . Each  $|F, M\rangle$  has an eigenenergy, which is proportional to the respective total-spin scattering length  $a_F$ .

In  $SU(N)$ -symmetric systems such as alkaline-earth or alkaline-earth-like atoms (for example strontium [28] or ytterbium [27]), the scattering lengths  $a_F$  are nearly equal due to the decoupling of nuclear and electronic spin [116]. Therefore, all  $|F, M\rangle$  acquire the same phase and also have the same interaction energy. However, in alkali atoms like  $^{40}\text{K}$ , the coupling of nuclear and electronic spin leads to different scattering lengths. For this reason, the  $|F, M\rangle$  acquire a different phase in each total-spin channel. In the observation basis, this results in a time-dependent coupling of different spin configurations apparent as spin-changing dynamics. Note that these so-called spin-changing collisions are a pure interaction effect, which occurs on top of conventional non-spin-changing collisions. This is sketched in Fig. 2.2, where a spin-conserving and a spin-changing collision are shown. There are two restrictions for this process:

### Conservation of the total magnetization $M$

The spin-changing collision process conserves the total magnetization, which implies  $M = m_1 + m_2 = m_3 + m_4$ . This is a direct result of the rotational symmetry of the interaction and reduces the amount of available collision channels. Note that this restriction holds for fermions as well as for bosons.

### Obeying the Pauli exclusion principle

A unique fermionic effect arises from the Pauli exclusion principle. Due to the symmetry of the wave function, both particles have to be in different spin states before and after the collision process ( $m_1 \neq m_2$  and  $m_3 \neq m_4$ ). This restriction also reduces the amount of available collision channels considerably.

## 2.2.2 Spin-changing collisions in <sup>40</sup>K

In this work, spin-changing collisions in <sup>40</sup>K have been studied in different regimes: starting from isolated atoms pairs (see chapter 4) to collective effects (see chapter 5) and relaxation properties (see chapter 6) in many-body systems. All obtained results rely on the same microscopic spin-changing process as introduced above. Here, the concept of spin-changing collisions is applied to the experimentally relevant case, namely two colliding particles in the  $f = 9/2$  hyperfine manifold of <sup>40</sup>K.

### Available spin systems

The ten spin states of the  $f = 9/2$  manifold give rise to a plethora of two-particle states  $|m_1, m_2\rangle$ . The corresponding collisions can in principle involve the total-spin channels  $|\vec{F}| = |f_1 + f_2| = 0, \dots, 9$ . However, due to the symmetry of the wave function, only the five even channels with  $F = 0, 2, 4, 6, 8$  contribute. Therefore, possible total magnetizations range from  $M = -8, \dots, +8$ , yielding 45 interacting two-particle states coupled by spin-changing collisions. In this context, the above-mentioned restrictions limit the possible couplings significantly. Moreover, the conservation of the total magnetization also allows to uniquely define the different spin subsystems according to their total magnetization  $M$ .

In Table 2.1, all possible spin systems of <sup>40</sup>K are summarized. Typically, spin systems with  $M = -8, -7$  are employed for experiments with spin 1/2 fermions, where only one spin configuration is involved. However, they are not suited for spin-changing dynamics. In general, a lower absolute total magnetization  $|M|$  involves more two-particle states. Spin-changing dynamics are possible in spin systems with  $M = -6, \dots, +6$ , where more than one two-particle state is available. Most suitable in this context is the system with  $M = 0$  including five two-particle states, which has been intensively studied in the presented experiments.

### Scattering lengths of <sup>40</sup>K

The exact values of the scattering lengths can be calculated from the molecular potentials, which are well known for <sup>40</sup>K [118]. In this context, nine spin-dependent scattering lengths  $a_{m_1 m_2 m_3 m_4}$  have been kindly provided by T. Hanna and coworkers [117], which were calculated using multi-channel quantum defect theory [119]. The error of this calculation is not precisely known but estimated to be below  $0.5 a_B$  [117], where  $a_B$  is the

Magnetization $M$	Involved two-particle states $ m_1, m_2\rangle$ coupled by spin-changing collisions	Number of levels
-8	$\{ -7/2, -9/2\rangle\}$	1
-7	$\{ -5/2, -9/2\rangle\}$	1
-6	$\{ -3/2, -9/2\rangle,  -5/2, -7/2\rangle\}$	2
-5	$\{ -1/2, -9/2\rangle,  -3/2, -7/2\rangle\}$	2
-4	$\{ +1/2, -9/2\rangle,  -1/2, -7/2\rangle,  -3/2, -5/2\rangle\}$	3
-3	$\{ +3/2, -9/2\rangle,  +1/2, -7/2\rangle,  -1/2, -5/2\rangle\}$	3
-2	$\{ +5/2, -9/2\rangle,  +3/2, -7/2\rangle,  +1/2, -5/2\rangle,  -1/2, -3/2\rangle\}$	4
-1	$\{ +7/2, -9/2\rangle,  +5/2, -7/2\rangle,  +3/2, -5/2\rangle,  +1/2, -3/2\rangle\}$	4
0	$\{ 9/2, -9/2\rangle,  7/2, -7/2\rangle,  5/2, -5/2\rangle,  3/2, -3/2\rangle,  1/2, -1/2\rangle\}$	5
+1	$\{ +9/2, -7/2\rangle,  +7/2, -5/2\rangle,  +5/2, -3/2\rangle,  +3/2, -1/2\rangle\}$	4
+2	$\{ +9/2, -5/2\rangle,  +7/2, -3/2\rangle,  +5/2, -1/2\rangle,  +3/2, +1/2\rangle\}$	4
+3	$\{ +9/2, -3/2\rangle,  +7/2, -1/2\rangle,  +5/2, +1/2\rangle\}$	3
+4	$\{ +9/2, -1/2\rangle,  +7/2, +1/2\rangle,  +5/2, +3/2\rangle\}$	3
+5	$\{ +9/2, +1/2\rangle,  +7/2, +3/2\rangle\}$	2
+6	$\{ +9/2, +3/2\rangle,  +7/2, +5/2\rangle\}$	2
+7	$\{ +9/2, +5/2\rangle\}$	1
+8	$\{ +9/2, +7/2\rangle\}$	1

**Table 2.1: Spin configurations in the lowest hyperfine manifold of  $^{40}\text{K}$ .** The different subspaces with the involved two-particle states  $|m_1, m_2\rangle$  are listed according to their total magnetization  $M = m_1 + m_2 = -8, \dots, +8$ . The number of involved spin configurations ranges between one and five. Most important for the described experiments are the  $M = 5$  and the  $M = 0$  spin systems, involving two and five two-particle states, respectively.

Bohr radius. These values have been used in the first place to identify Feshbach resonances (see appendix B). Beyond this, one can also recalculate the scattering lengths in terms of the total spin using the linear equation set 2.5. The results are depicted in Table 2.2.

This reveals a special feature of  $^{40}\text{K}$ : The difference between the total-spin scattering lengths  $a_F$  exceeds 40%. Especially the differences between the channels  $F = 0, 2, 4$  are pronounced, while the differences between the channels  $F = 4, 6, 8$  are comparably small. In general, these differences are large compared to other isotopes, which were used to study spin dynamics.  $^{23}\text{Na}$  exhibits a total-spin scattering length difference of 10% in the  $f = 1$  manifold [80]. For  $^{87}\text{Rb}$ , the difference is only 1% in the  $f = 1$  manifold and about 13% in the  $f = 2$  manifold [68, 75].  $^{52}\text{Cr}$  with a total spin of  $f = 3$  has a total-spin scattering length difference similar to  $^{40}\text{K}$  [120, 121]. However, it is governed by dipolar interactions, which induce demagnetization dynamics, and hence constitutes a completely different system.

The scattering lengths of  $^{40}\text{K}$  lead a rich variety of high-spin interaction effects. Spin systems with a large total magnetization  $M$  contain only scattering channels with a high total spin ( $F \geq |M|$ ), where the difference between the involved scattering lengths is rather small. Decreasing the magnetization, however, involves also scattering lengths with lower total spin. This increases the differences between the involved scattering lengths, which has important consequences: First, the spin-conserving interactions between different spin configurations vary considerably. For example, the two-particle

Total-spin channel $F$	Scattering length $a_F$ ( $a_B$ )	Magnetizations $ M  \leq F$ of the involved spin systems
0	119.92	0
2	147.83	$0, \pm 1, \pm 2$
4	161.11	$0, \pm 1, \pm 2, \pm 3, \pm 4$
6	166.00	$0, \pm 1, \pm 2, \pm 3, \pm 4, \pm 5, \pm 6$
8	168.53	$0, \pm 1, \pm 2, \pm 3, \pm 4, \pm 5, \pm 6, \pm 8$

**Table 2.2: Total scattering lengths for the lowest manifold of <sup>40</sup>K.** Given are the scattering lengths  $a_F$  for the total-spin channels  $F = 0, 2, \dots, 8$ . These values have been calculated using equation 2.5, inserting the spin-dependent scattering lengths kindly provided by T. Hanna and coworkers [117]. Note the pronounced differences between  $F = 0, 2, 4$ , which are relevant for spin systems with small total magnetizations as depicted in the third column. Spin systems with a large total magnetization involve only large total-spin scattering channels.

state  $|+9/2, -9/2\rangle$  has a spin-conserving scattering length  $a_{9/2, -9/2, 9/2, -9/2} = 145.77 a_B$ , while the spin configuration  $|+9/2, +7/2\rangle$  has  $a_{9/2, 7/2, 9/2, 7/2} = 168.53 a_B$ . Second, the spin-changing scattering lengths also vary significantly. For example, the scattering length describing the spin-changing collision between  $|+1/2, -1/2\rangle$  and  $|+3/2, -3/2\rangle$  has a value of  $a_{1/2, -1/2, 3/2, -3/2} = 13.42 a_B$ . At the same time, for the two-particle states  $|+9/2, +3/2\rangle$  and  $|+7/2, +5/2\rangle$  it is only  $a_{9/2, 3/2, 7/2, 5/2} = 1.16 a_B$  (see Table C.1).

Therefore, the choice of suitable spin mixtures can strongly enhance spin-changing collisions. This is widely exploited in the experiment presented in section 4.2, where multi-flavor spin dynamics are observed for the first time. As an additional feature, <sup>40</sup>K also allows to bridge the gap from nearly SU(N)-symmetric to broken SU(N)-symmetric systems. This can be achieved by simply choosing different spin mixtures.

### Influence of the Zeeman effect

As discussed above, a spin-changing collision transfers the atoms between different spin configurations. This also changes the Zeeman energy of the two-particle states, which can be well understood in a series expansion of the Breit-Rabi formula (equation 2.1). The first-order contribution to the Zeeman energy is the so-called linear Zeeman shift, proportional to the magnetization  $m$  and to the magnetic field  $B$ :

$$E_{\text{ize}}^{(m)}(B) = \frac{g_j \mu_B}{9} m \cdot B. \quad (2.6)$$

The second-order contribution is the quadratic Zeeman effect [122], quadratic in magnetization and magnetic field:

$$E_{\text{qze}}^{(m)}(B) = -qm^2 \cdot B^2. \quad (2.7)$$

Here, the parameter  $q = (2^3 \mu_B^2) / (9^3 A_{\text{hfs}})$  is introduced for simplicity.

In a spin-changing collision, the linear Zeeman energy remains constant due to the conservation of the total magnetization. Nonlinear contributions such as the quadratic Zeeman energy are typically not conserved [76].

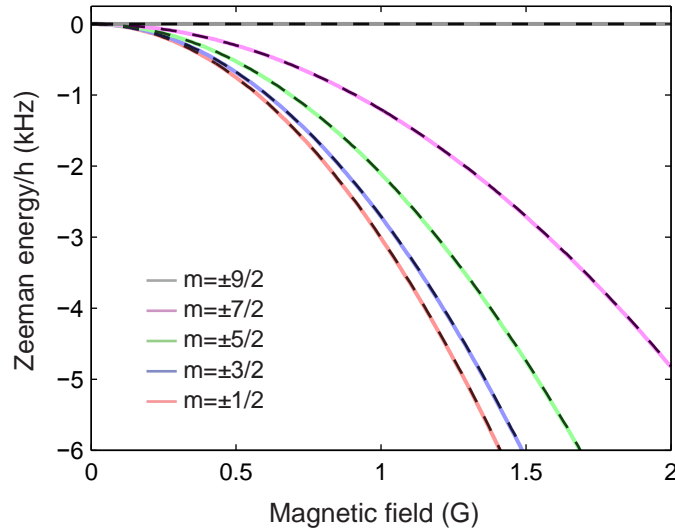


**Figure 2.3: Zeeman energy of the five spin configurations of the  $M=0$  spin system.** Dashed lines correspond to calculations using the Breit-Rabi formula 2.1. Solid lines are calculated from the quadratic expansion (equation 2.7). In the relevant magnetic field regime, there is no discernible difference. The lowest magnetic energy of this spin system has the two-particle state  $|+1/2, -1/2\rangle$ .

$$E_{\text{lze}}^{(m_1)}(B) + E_{\text{lze}}^{(m_2)}(B) = E_{\text{lze}}^{(m_3)}(B) + E_{\text{lze}}^{(m_4)}(B) \quad (2.8)$$

$$E_{\text{qze}}^{(m_1)}(B) + E_{\text{qze}}^{(m_2)}(B) \neq E_{\text{qze}}^{(m_3)}(B) + E_{\text{qze}}^{(m_4)}(B) \quad (2.9)$$

In particular in the regime of low magnetic fields, where spin-dynamics experiments are typically performed, the relevant contribution of the magnetic energy arises essentially from the quadratic Zeeman effect. To illustrate this, the Zeeman energies of all five two-particle states of the  $M=0$  spin system are exemplarily depicted in Fig. 2.3. Compared are calculations using the full Breit-Rabi formula (equation 2.1) and the quadratic Zeeman energy (equation 2.7). This demonstrates that in the experimentally relevant regime no discernible deviations can be found. In this thesis, the quadratic Zeeman energy is employed for analytical approaches, while numerical calculations are performed using the full Breit-Rabi formula.



## Chapter 3

# High-spin fermions in the laboratory

The experiments presented in this thesis have been performed at the *Bose-Fermi Mixture* setup in the group of Prof. Dr. Klaus Sengstock, located at the *Institut für Laserphysik* in Hamburg. This setup was originally designed for the investigation of ultracold Bose-Fermi mixtures. In the course of this research work, however, the focus was shifted towards pure fermionic samples ranging from spin-polarized to high-spin systems. High-spin fermions constitute a novel class of many-body systems with only a few experimental realizations worldwide [86, 87, 102, 103, 123] and provide several experimental challenges.

This chapter will address these challenges and provide an overview of experimental methods and procedures that were applied to study fermionic spin dynamics in the laboratory. After a brief review of the general experimental procedure (section 3.1), I will focus on two important aspects: First, important tricks for the experimental handling of high-spin fermions (section 3.2) will be worked out. Then new methods to control the magnetic field will be described (section 3.3).

### 3.1 The *Bose-Fermi Mixture* experiment

The *Bose-Fermi Mixture* experiment is designed to efficiently cool the bosonic isotope  $^{87}\text{Rb}$  and the fermionic isotope  $^{40}\text{K}$  to very low temperatures – over a temperature scale of about ten orders of magnitude starting from about 400 K to several 10 nK. This allows for exciting experiments with quantum degenerate atomic samples: pure Bose-Einstein condensates, Bose-Fermi mixtures or pure Fermi gases. The system was set up in 2004 and is described and characterized in detail in the theses of S. Ospelkaus [124] and C. Ospelkaus [125]. Several modifications have been implemented throughout this work. This includes the design and installation of a new optical lattice setup, a new dipole trap setup as well as a new detection scheme. In the following section, I will provide a sketch of the experimental setup with its most important tools and briefly describe the general experimental procedure, which was employed to study fermionic spin dynamics.

### 3.1.1 The experimental setup

The setup consists of two vacuum chambers, which are vertically aligned and connected with a differential pumping stage (see sketches for example in [106, 124, 125]). In the upper chamber, the atomic sources – commercial dispensers for  $^{87}\text{Rb}$  and for  $^{40}\text{K}$  – are located. They continuously generate a background vapor with typical pressures of  $2 \times 10^{-10}$  mbar, which loads two overlapping two-dimensional (2d) magneto-optical-traps (MOT), cooling both species in the radial direction. A bicolor pushing beam transfers the atoms into the lower vacuum chamber with typical pressures below  $1 \times 10^{-11}$  mbar and loads two overlapping 3d MOTs. In this so-called *science chamber* the actual experiments are performed. There the atoms can be trapped and cooled further to quantum degeneracy in a 4D-cloverleaf magnetic trap. Moreover, the samples can be transferred into an optical dipole trap, which is derived from a commercial Ti:sapphire laser (MBR110 by Coherent GmbH), pumped with a frequency-doubled Nd:YAG laser (Verdi V18 by Coherent GmbH) and operated at a wavelength of  $\lambda_{\text{dt}} = 812$  nm. Furthermore, the atoms can be loaded into a cubic optical lattice. The corresponding laser light is provided by a commercial Yb:YAG thin disk laser (VersaDisk by ELS Elektronik Laser System GmbH), operated at a wavelength of  $\lambda_{\text{lat}} = 1030$  nm. Antennas for radio-frequency and microwave radiation are attached close to the *science chamber* and allow for the spin manipulation of the atomic samples. Besides, a detection setup is available, which can image the atomic samples from two orthogonal directions, either on the quantization axis (Pixelfly by PCO) or orthogonal to the quantization axis (iKon by Andor technology).

### 3.1.2 The general procedure

The procedure, which is employed for the experiments presented in this thesis, has a cycle time of typically 60–80 s. It is sketched in Fig. 3.1 and can be divided into the following steps:

The experiment starts with the loading procedure of the  $^{40}\text{K}$ -MOT and  $^{87}\text{Rb}$ -MOT for typically 30 s (see section 3.2.1). Next, the magnetic field is switched off and the atoms are further cooled in a 10 ms optical-molasses phase to sub-Doppler temperatures. Subsequently, both isotopes are optically pumped into magnetically trappable hyperfine states (see section 3.2.1).

In a second step, the atoms are transferred into a magnetic trap, which is then compressed adiabatically within 1 s. The atoms are cooled further with a forced radio-frequency evaporation procedure for 30 s [126] where an exponential frequency sweep is applied. During this procedure, the radio-frequency radiation is only resonant for rubidium and expels the hottest atoms from the trap while the whole sample thermalizes. Thereby, the  $^{87}\text{Rb}$  atoms are cooled to quantum degeneracy. The fermionic  $^{40}\text{K}$  atoms cannot thermalize at low temperatures, which is a consequence of the suppression of s-wave scattering due to the Pauli exclusion principle [127]. Collisions between the potassium and rubidium atoms, however, allow for sympathetic cooling [128–130] (see section 3.2.1). After the evaporation, most of the rubidium atoms are lost from the magnetic trap, leaving a quantum degenerate Fermi gas of  $^{40}\text{K}$ . The atoms are spin-polarized and hence form a non-interacting Fermi sea [131].

Subsequently, the atoms are transferred into a spin-independent optical dipole trap [132]. For this purpose, a crossed circular-elliptical dipole trap setup has been imple-

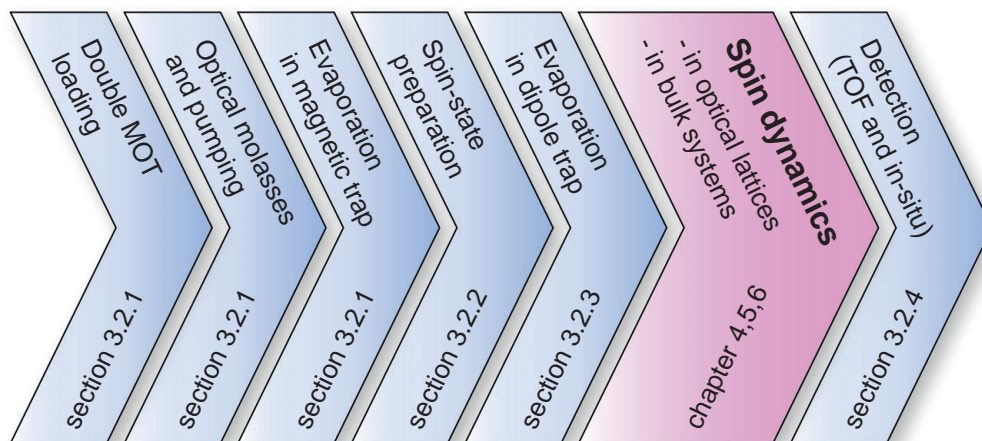


**Figure 3.1: The experimental procedure to study fermionic spin dynamics.** The procedure is depicted as flow chart. Blue charts indicate the general experimental steps, which are described in this chapter. Spin-dynamics experiments have been performed in optical lattices (chapter 4) and in bulk systems (chapter 5 and 6), indicated with the red chart.

mented, described in detail in the thesis of J. Heinze [107]. For the transfer of the atoms from the magnetic trap into the dipole trap, the respective laser power is switched rapidly to large values of approximately 300 mW. Subsequently, the magnetic trapping field is exponentially lowered within 500 ms. Only a homogeneous magnetic offset field of about 4.5 G is applied to avoid Majorana transitions [133]. With this procedure, about 95 % of the fermions can be transferred into the dipole trap with a temperature increase of approximately  $0.1 T_F$ , where  $T_F$  denotes the Fermi temperature (see appendix A).

In a next step, a spin-state preparation scheme is applied to generate arbitrary spin mixtures (see section 3.2.2). The resulting coherent superposition of spin states is initially still non-interacting but decoheres quickly in the presence of magnetic field gradients. This opens up the possibility for further evaporative cooling, which is performed by lowering the dipole trap power exponentially within 2 – 3 s (see section 3.2.3). Additionally, a cubic optical lattice can be superimposed onto the atoms, created by three retro-reflected orthogonal lattice beams. Depending on the laser power in the different branches, a simple cubic structure, two-dimensional pancakes, and one-dimensional tubes can be realized. New telescopes have been implemented in the course of this work, which are described in the diploma thesis of M. Weinberg [134].

After the experiments, the atomic sample is detected using absorption imaging (see section 3.2.4). A new diffraction-limited detection setup with high resolution has been implemented in the course of this work, which is described in the diploma thesis of B. Hundt [135]. The detection setup provides a magnification ranging from 1 to 5, allowing for in-situ imaging with high resolution and the simultaneous detection of all spin components in a time-of-flight (TOF) measurement.

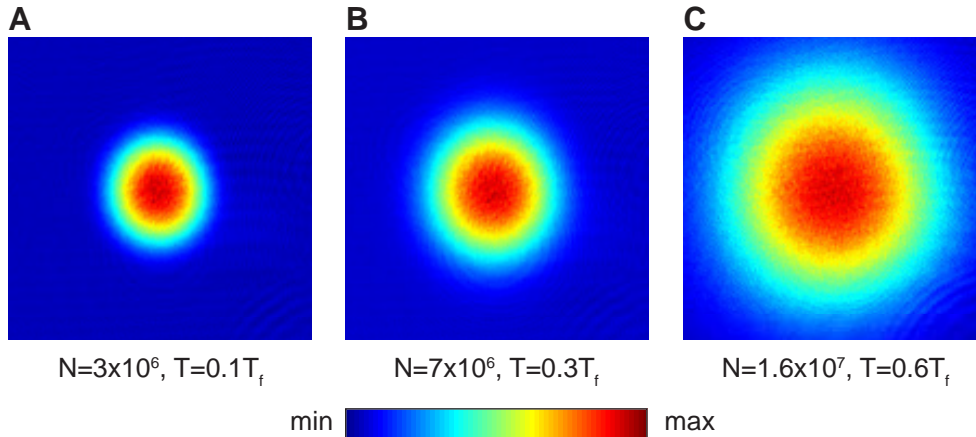


**Figure 3.2: Density distribution of an ultracold Fermi sea in the magnetic trap.** The atomic sample is spin-polarized in the state  $|f = 9/2, m = 9/2\rangle$  and hence non-interacting. (A)-(C) correspond to Fermi seas produced with different MOT loading and evaporation parameters. Typically  $1.5 \times 10^6 - 3 \times 10^6$  atoms at  $0.1 T_F$  are realized as a starting point for the experiments. The pictures are taken using absorption imaging after time-of-flight (see section 3.2.4).

## 3.2 Preparing, cooling and probing high-spin fermions

The experimental handling of high-spin fermions constitutes one key ingredient for spin-dynamics experiments. This includes the preparation, the cooling and the probing of arbitrary spin mixtures. In this section, important concepts and procedures addressing the corresponding challenges will be worked out with a particular focus on high-spin fermions. After the description of important optimization steps for the production of an ultracold Fermi sea, the spin-state preparation within the lowest hyperfine manifolds of  $^{40}\text{K}$  will be described. Furthermore, I will discuss the realization of quantum degenerate arbitrary spin mixtures as well as detection schemes for high-spin fermions.

### 3.2.1 Producing a spin-polarized Fermi sea

The preparation of an ultracold spin-polarized Fermi sea constitutes the starting point for the described experiments. Here, optimization steps that have provided essential improvements for the daily experimental operation are presented. This includes the optimization of the MOT loading procedure, the optical pumping and the double-species evaporation in the magnetic trap. Typically,  $1 \times 10^6 - 3 \times 10^6$  atoms at temperatures of  $50 \text{ nK}$  are realized, corresponding to  $T \approx 0.1 T_F$ . The realization of higher particle numbers is also possible, however, at the expense of an increase in temperature (see Fig. 3.2).

#### Double MOT loading procedure

To improve the efficiency of the  $^{40}\text{K}$ -MOT, a dark-spot configuration is implemented, which widely avoids light-assisted collisions between the potassium atoms [136]. This allows for a continuously growing accumulation of potassium atoms even for several minutes. However, collisions between rubidium and potassium atoms have to be consid-

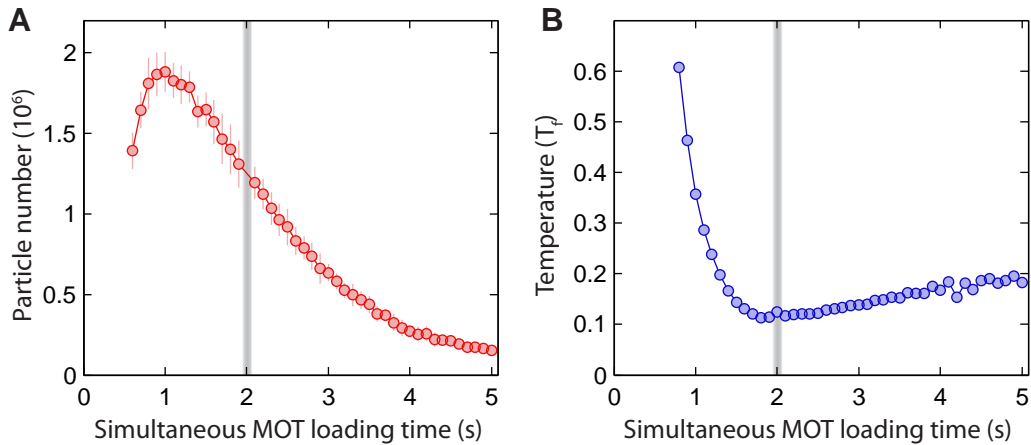


**Figure 3.3: Optimization of the MOT loading procedure.** The particle number (**A**) and temperature (**B**) of an atomic sample of  $^{40}\text{K}$  are depicted as a function of the MOT loading time of  $^{87}\text{Rb}$ . For  $^{40}\text{K}$ , the MOT loading time is always 30 s. The optimum  $^{87}\text{Rb}$ -MOT loading time is typically 2 s allowing to realize large Fermi seas as shown in Fig. 3.2. The grey shading indicates the parameters typically chosen in the experiments.

ered, which also induce considerable losses [19] and limit in particular the performance of the  $^{40}\text{K}$ -MOT. Therefore, a consecutive loading procedure is employed, starting with the exclusive loading of the  $^{40}\text{K}$ -MOT for 30 s followed by a short simultaneous loading of both MOTs for 1–3 s.

The exact ratio between  $^{40}\text{K}$  and  $^{87}\text{Rb}$  is optimized such that sympathetic cooling is still efficient and losses are avoided as good as possible. To illustrate this, the particle number and the temperature of the Fermi sea are depicted in Fig. 3.3 for different two-species MOT loading times with a fixed  $^{40}\text{K}$ -MOT duration. A maximum particle number is found for only 1 s (see Fig. 3.3 A). However, the corresponding temperature is still relatively high, indicating that the amount of  $^{87}\text{Rb}$  atoms is not sufficient for an efficient sympathetic cooling. Very cold fermionic samples require an approximately 2 s loading time (see Fig. 3.3 B). More rubidium atoms do not cool the sample any further but induce predominantly additional particle loss.

### Optical pumping

Before the transfer into the magnetic trap, the atoms are optically pumped into magnetically low-field seeking states. For this purpose, a pulse with circularly-polarized light is applied after the optical-molasses phase. This transfers the depolarized atoms into the maximally polarized low-field seeking states,  $|F = 2, m = 2\rangle$  for  $^{87}\text{Rb}$  and  $|F = 9/2, m = 9/2\rangle$  for  $^{40}\text{K}$ , respectively. The optical pumping enhances the particle number by a factor of up to five for  $^{87}\text{Rb}$  and up to ten for  $^{40}\text{K}$ , given by the amount of available spin states. This considerably shortens the MOT loading times and allows for a significantly better performance of the system.

In the experiment, the optical pumping is provided by a  $150\ \mu\text{s}$  bicolor pulse with a power of several  $10\ \mu\text{W}$ , detuned by a few MHz with respect to the corresponding  $D_2$ -lines. To optimize these parameters for the bosonic atoms, the BEC fraction is

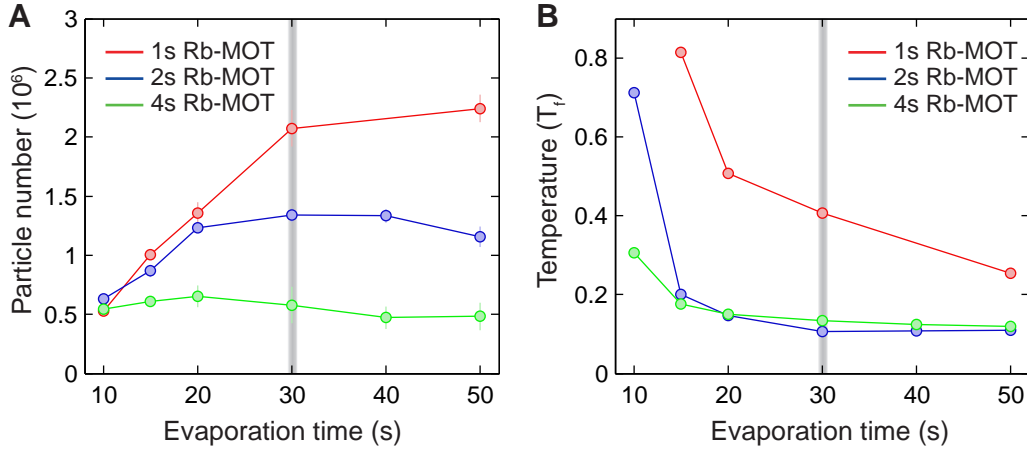


**Figure 3.4: Optimization of the evaporation in the magnetic trap.** The particle number (**A**) and temperature (**B**) of an atomic sample of  $^{40}\text{K}$  are depicted as a function of the evaporation time in the magnetic trap. For  $^{40}\text{K}$ , the MOT loading time is always 30 s and varies between 1–4 s for  $^{87}\text{Rb}$ , corresponding to the different colors in the graph. For the typical MOT loading time of 2 s, the optimum evaporation time is 30 s. The grey shading indicates the parameters typically chosen in the experiments.

maximized for short MOT loading times of about 300 ms. For potassium, the parameters are optimized by preparing a small Fermi sea with a short  $^{40}\text{K}$ -MOT loading time of only 2 s combined with a long  $^{87}\text{Rb}$ -MOT loading of 5 s. This provides a sufficient amount of rubidium atoms to cool all potassium atoms independent of the optical pumping efficiency.

### Evaporation in the magnetic trap

The evaporation in the magnetic trap constitutes the crucial cooling step to realize a quantum degenerate atomic sample. An exponentially decreasing radio-frequency sweep starting from 40 MHz to about 1 MHz is applied. During the evaporation, collisions between the potassium and rubidium atoms lead to sympathetic cooling [128–130], which crucially depends on the evaporation time. For long evaporation times significant losses are induced, while short evaporation times do not allow for efficient thermalization.

To illustrate this, the influence of the evaporation time on particle number and temperature of the Fermi sea is depicted in Fig. 3.4. As a result, the best compromise between losses and cooling efficiency yields an optimum evaporation time of 30 s for a  $^{40}\text{K}$ -MOT loading time of 30 s. Shorter evaporation times lead to higher temperatures, while a longer evaporation reduces the particle number and does not further cool the sample. Note that the final evaporation frequency is chosen such that most of the rubidium atoms are expelled from the magnetic trap, leaving a spin-polarized quantum degenerate Fermi sea. Remaining rubidium atoms are later kicked out by resonant light pulses.

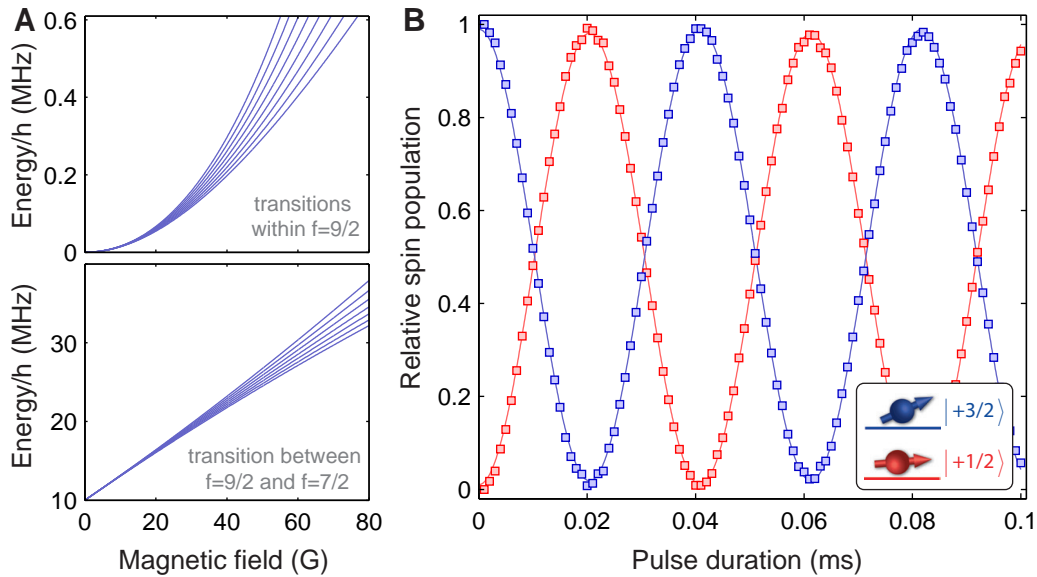


**Figure 3.5: Rabi-oscillations between two spin states within the  $f=9/2$  manifold of  $^{40}\text{K}$ .** (A) The transition energy differences within the  $f=9/2$  manifold are depicted as a function of the magnetic field (upper part). Non-linear contributions of the Zeeman effect are necessary to drive spin-selective transitions. Transitions between the manifolds  $f=9/2$  and  $f=7/2$  are also shown (lower part), but here the linear Zeeman splitting is large enough that all transitions can be addressed spin-selectively already at low magnetic field. (B) Typical Rabi-oscillations between the spin states  $|+3/2\rangle$  and  $|+1/2\rangle$  are depicted. The duration of the rf-pulse is varied at a constant frequency of 14.472 MHz, at constant power, and at a magnetic field of  $B=45$  G. Solid lines correspond to a sinusoidal fit.

### 3.2.2 The spin-state preparation

After the transfer of the atomic sample from the magnetic into the optical dipole trap, all fermions occupy the low-field seeking spin state  $|f=9/2, m=9/2\rangle$ . Reliable preparation schemes for arbitrary spin mixtures are required. Here, the most important spin-preparation techniques are described allowing to manipulate the spin configuration within the hyperfine ground-state manifolds of  $^{40}\text{K}$  (see also [137, 138]).

#### Radio-frequency preparation

For the spin-dynamics experiments, the spin-state preparation within the  $f=9/2$  manifold is performed by employing radio-frequency (rf) schemes, which couple different spin states with  $\Delta m = \pm 1$ . To realize a spin-selective coupling, the transition frequencies have to be sufficiently separated. This requires a large magnetic field with significant non-linear contributions from the Zeeman effect as depicted in Fig. 3.5 A. For the discussed experiments, the spin-state preparation is typically performed at 45 G, resulting in transition frequencies of about 14 MHz, separated by a quadratic energy splitting exceeding 200 kHz. In this regime, all transitions can be selectively addressed by simply tuning the radio frequency. Two techniques are employed:

First, rf-pulses are applied, which drive Rabi-oscillations between two spin states. When the frequency matches the energy difference between the involved states, a full

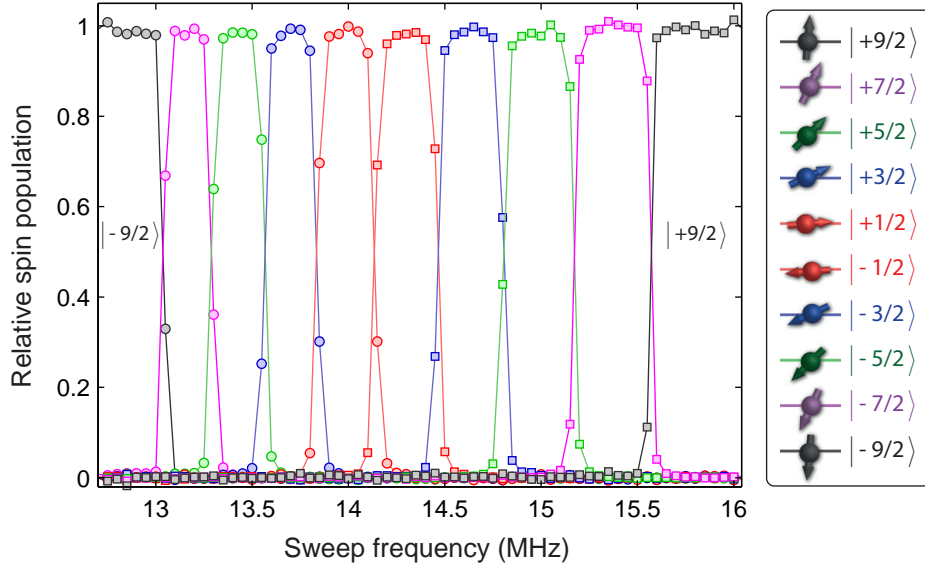


**Figure 3.6: Radio-frequency sweeps between the spin states of the  $f = 9/2$  hyperfine manifold of  $^{40}\text{K}$ .** A typical Landau-Zener sweep, starting from the energetically highest spin state  $|+9/2\rangle$  to all further spin states of the  $f = 9/2$  manifold, is shown. The starting frequency is 16.5 MHz, which is decreased to the final sweep frequency within 20 ms. The spin-state preparation is typically performed at 45 G.

transfer is achieved in a  $\pi$ -pulse. A pulse duration of only  $10 \mu\text{s}$  is employed, yielding a large Fourier broadening, which enhances the stability against magnetic field fluctuations but still clearly separates all transitions. With this technique, Rabi-oscillations are induced as exemplarily shown in Fig. 3.5 B. Depending on the applied rf-power and pulse duration, a well-controlled coherent superposition can be realized. The pulse technique is particularly well suited to realize spin mixtures either balanced or imbalanced. It can be optimized up to a transfer accuracy with a relative error of about one percent.

Coherent superpositions can be well realized with rf-pulses, but the error accumulates for a transfer between several spin states. In this case, it is favorable to apply Landau-Zener sweeps [139], where the frequency is ramped slowly across the transition. Thereby, the atoms are adiabatically transferred between the spin states. This technique is very robust against magnetic field fluctuations. In particular for a full spin transfer, it is significantly more reliable than rf-pulses, where this can only be achieved with a specific pulse power on the exact resonance frequency. We apply rf-sweeps with a typical duration of 10 ms, yielding an adiabatic transfer of the atoms between all possible spin states by simply adjusting the frequency sweep range. This is demonstrated in Fig. 3.6, where the atomic sample is transferred from the energetically highest spin state  $|f = 9/2, m = 9/2\rangle$  to all further spin states in the same manifold.

### Microwave-frequency preparation

Beyond the manipulation of the spin states within the  $f = 9/2$  manifold, a preparation scheme to transfer the atoms into the upper hyperfine manifold  $f = 7/2$  has been

employed, e.g., for spin-selective detection (see section 3.2.4). Both manifolds can be coupled by microwave (mw) radiation with  $\Delta m = 0, \pm 1$ , which requires frequencies of about 1.3 GHz. The basic preparation scheme follows the rf-preparation including microwave pulses and microwave sweeps. As a crucial difference, the transition frequencies are dominated by the linear Zeeman effect as depicted in Fig. 3.5 A. Hence, the spin states are well separated even at small magnetic fields. This constitutes an important experimental advantage since many of the presented experiments are performed at low magnetic fields. A simple hyperfine transfer without changing the magnetic field is possible.

### 3.2.3 Realizing ultracold spin mixtures

The spin-state preparation presented above manipulates the spin but not the spatial configuration of the atoms. Hence, the initially spin-polarized Fermi sea remains non-interacting. To explore interaction effects between different spin states, a second evaporation step is required. This can be achieved with an additional cooling in the dipole trap (see section 3.1.2), which also changes the spatial configuration. The necessity for this additional step constitutes a crucial difference to high-spin experiments with bosonic atoms. In the following, the preparation of ultracold spin mixtures is discussed and the problems arising from the realization of arbitrary spin configurations are addressed. This includes difficulties of the evaporation itself, but likewise the control of particle number and temperature as well as lifetime limitations. Note that the presented experiments start with an evaporated binary mixture, denoted as  $m = \{m_1, m_2\}$ . The discussed concepts can also be extended to spin mixtures with more than two spin components.

#### Evaporation of arbitrary spin mixtures

So far, experiments with  $^{40}\text{K}$  employed mainly two spin mixtures:  $m = \{-7/2, -9/2\}$  and  $m = \{-5/2, -9/2\}$ . Both can be directly evaporated and offer besides long lifetimes suitable Feshbach resonances to tune the interaction strength [140–142], rendering them ideal candidates for the study of spin 1/2 systems.

The preparation of arbitrary spin mixtures is experimentally challenging due to strong losses, which significantly limit the evaporation performance in the optical dipole trap. First of all, they stem from a zoo of Feshbach resonances at specific magnetic fields, which have been studied in the course of this research work. Calculations provided by T. Hanna and coworkers [117] allowed to identify 20 new Feshbach resonances listed in appendix B. These are often associated with strong losses occurring in a wide magnetic field range. To illustrate their problematic role for the preparation of arbitrary spin configurations, the evaporation efficiency of the spin mixture  $m = \{+1/2, -1/2\}$  is exemplarily depicted for different magnetic fields in Fig. 3.7. Strong losses occur at specific magnetic fields during the evaporation, inducing even a total loss of the sample. With the knowledge of these Feshbach resonances, this problem can be widely circumvented for several spin mixtures. For example, the evaporation of  $m = \{+1/2, -1/2\}$  was typically performed at 7 G or 45 G, where the losses are small. Second, losses induced by spin-changing collisions also limit the efficiency of the evaporation. This is a severe problem in particular for magnetically excited spin configurations and constitutes an important limitation. The direct evaporation of these spin mixtures is in

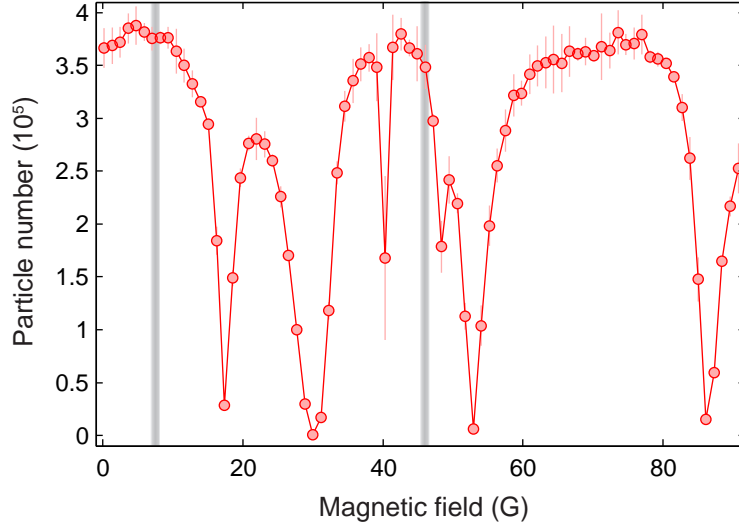


**Figure 3.7: Effect of Feshbach resonances on the evaporation efficiency.** The particle number of the spin mixture  $m = \{+1/2, -1/2\}$ , evaporated in the optical dipole trap at different magnetic fields, is plotted. Clearly visible is the strongly enhanced particle loss at specific magnetic fields, associated with a Feshbach resonance. In the experiments, the evaporation is typically performed at 7 G or 45 G indicated with the gray bar. Several Feshbach resonances observed in different spin mixtures are provided in appendix B (see Table B.2).

general inefficient and hence more sophisticated preparation schemes are required. Four particular cases, which play an important role in the following experiments, are briefly described:

**Spin mixture  $m = \{+1/2, -1/2\}$**

Starting with an rf-sweep from  $|+9/2\rangle$  to  $|+1/2\rangle$ , an rf-pulse creates a coherent superposition  $|+1/2\rangle + |-1/2\rangle$ , which can be directly evaporated. This spin mixture exhibits a long-term stability alongside very suitable Feshbach resonances (see appendix B) and constitutes the working horse for the described experiments.

**Spin mixture  $m = \{+7/2, +3/2\}$**

Starting with an rf-sweep from  $|+9/2\rangle$  to  $|+7/2\rangle$ , an rf-pulse creates a coherent superposition  $|+7/2\rangle + |+5/2\rangle$ , followed by an rf-sweep yielding  $|+7/2\rangle + |+3/2\rangle$ . This state can also be directly evaporated.

**Spin mixture  $m = \{+3/2, -3/2\}$**

Starting with an rf-sweep from  $|+9/2\rangle$  to  $|+1/2\rangle$ , an rf-pulse creates a coherent superposition of the states  $|+1/2\rangle + |-1/2\rangle$ , followed by an rf-sweep yielding  $|+1/2\rangle + |-3/2\rangle$ . This state can be evaporated and subsequently transferred with an rf-sweep to  $m = \{+3/2, -3/2\}$ . Note that a direct evaporation of the magnetically excited spin state  $|+3/2\rangle + |-3/2\rangle$  is associated with too strong losses.

**Spin mixture  $m = \{+9/2, -9/2\}$**

Starting with an rf-pulse a coherent superposition of the states  $|+9/2\rangle + |7/2\rangle$  is created, where  $|+7/2\rangle$  is then transferred with an rf-sweep to  $|+1/2\rangle$ . This state

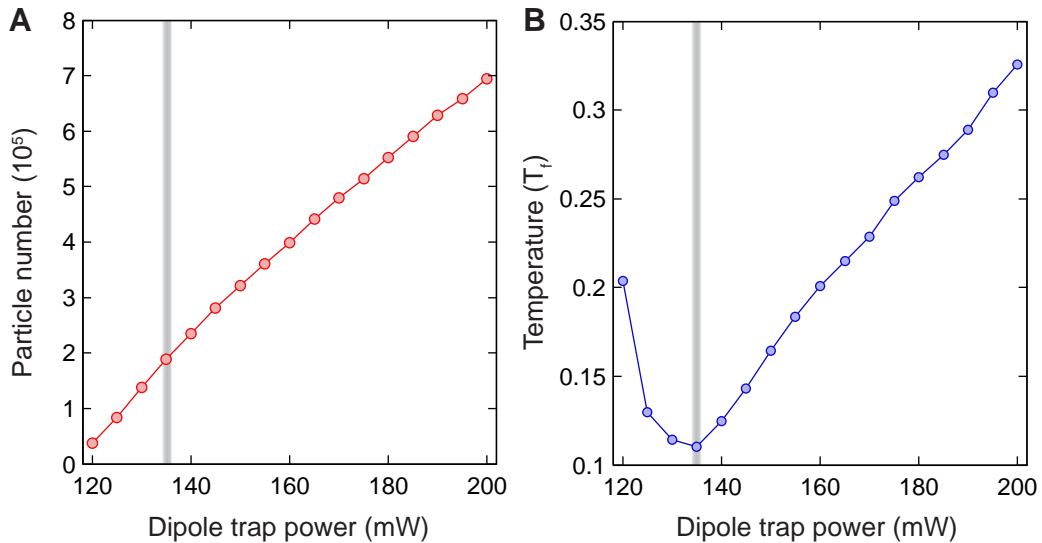


**Figure 3.8: Controlling temperature and particle number of a Fermi sea.** The particle number (A) and temperature (B) of the spin mixture  $m = \{+1/2, -1/2\}$ , evaporated in the optical dipole trap, are depicted. In this experiment, the dipole trap power is initially 200 mW in both branches, which is reduced to 30 mW in one direction while the second direction is varied. Particle number and temperature are lower for decreasing dipole trap depth. However, below 130 mW the evaporation becomes inefficient and the temperature increases again. The grey shading indicates the parameters typically chosen in the experiment.

can be evaporated and subsequently transferred with an additional rf-sweep to  $m = \{+9/2, -9/2\}$ . Note that a direct evaporation of this spin mixture is not feasible.

### Control of particle number and temperature

The independent control over particle number and temperature of the Fermi sea is important for the experiments presented in this thesis (see section 6.2.2). Two different approaches have been followed in this context:

First, the laser power of the dipole trap at the end of the evaporation ramp can be used as a tuning knob, which determines the relevant trap depth. Figure 3.8 reveals its impact on the particle number and the temperature of the Fermi sea. By lowering the dipole trap power, the amount of atoms remaining in the dipole trap is continuously reduced (see Fig. 3.8 A). At the same time, more hot atoms are expelled from the trap, resulting in lower temperatures of the thermalized sample (see Fig. 3.8 B). However, below a specific value of the trap depth, the temperature is not further reduced. In this temperature regime, the system cannot thermalize properly due to Pauli blocking [143] and the cooling becomes inefficient. At the same time, the expelled atoms lead to a temperature increase in units of the Fermi temperature  $T_F$ . In the experiments, ultracold fermionic samples with about  $2 \times 10^5 - 4 \times 10^5$  particles at a temperature of  $0.1 - 0.15 T_F$  can be typically realized using the spin mixture  $m = \{+1/2, -1/2\}$ . For other spin configurations, these values can be significantly different.

The dipole trap power leads to a particle number associated with a specific tem-

perature. Hence, an independent control of particle number and temperature requires an additional technique. For this purpose, the power of the dipole trap is increased again after the evaporation within 200 ms and a waiting time slot is included. During this time, the temperature increases due to photon scattering while the atom number remains approximately constant. Varying the waiting time between 0–10 s allows for an independent tunability of temperature and particle number.

### Lifetime limitations

An important aspect for spin-dynamics experiments is the lifetime of the prepared samples. After their preparation, binary spin mixtures can be regarded as closed systems, however, with important limitations. Unfavorable collisional properties constitute a crucial problem for atomic ensembles involving different spin states. Prominent examples are exothermic collisions in  $^{133}\text{Cs}$  [144] or negative scattering lengths in  $^{39}\text{K}$  [145], which are luckily both absent in  $^{40}\text{K}$ . In this case, spin mixtures consisting of different Zeeman states are mainly limited by the same processes, which also limit the efficiency of the evaporation: First, Feshbach resonances can induce significant particle loss [119]. However, most of the described experiments are performed at very low magnetic fields ( $B < 5$  G), where those resonances do not occur (see appendix B). Second, spin-changing collisions, which convert magnetic into kinetic energy, are associated with heating and losses from the trap. They reduce considerably the lifetime of magnetically excited spin mixtures.

In general, we find suitable lifetimes in the dipole trap for arbitrary spin mixtures involving only spin states of the  $f = 9/2$  manifold. The situation drastically changes, when spin states from the upper hyperfine manifold are involved. In this case, hyperfine relaxation collisions become possible [146]. These collisions change the total spin and release the hyperfine interaction energy, which is converted into kinetic energy. This energy release is much larger than any trapping potentials and leads to an immediate loss of both collision partners from the trap. While these collisions are rare for example in  $^{87}\text{Rb}$  [147], they considerably limit the lifetime in most other alkali atoms and also in  $^{40}\text{K}$ . In the latter case, a hyperfine relaxation collision involves at least one atom in the  $f = 7/2$  manifold and releases the hyperfine splitting energy of about 1.3 GHz. This leads to enhanced loss rates reducing the lifetime of the corresponding spin mixtures by several orders of magnitude [107]. Therefore, the presented experiments are restricted to the  $f = 9/2$  manifold. Note that the observed loss rates involving the  $f = 7/2$  manifold depend on the precise spin composition. In this context, a more detailed analysis might reveal reasonable stable mixtures for future experiments. Moreover, the tunability of such losses in different spin mixtures of  $^{40}\text{K}$  could allow to study exotic quantum states such as the quantum-Zeno insulator [107].

### 3.2.4 Probing high-spin fermions

For high-spin experiments, the relevant information is encoded in the spin and the spatial configuration of the atomic ensemble. First, the spin occupations have to be known, constituting the most important observable in the discussed experiments. Second, the spatial as well as the momentum distribution provide crucial information to identify for example spatial excitations such as spin waves [3, 58]. In addition, global properties such as the particle number and the temperature are important in particular for a quan-

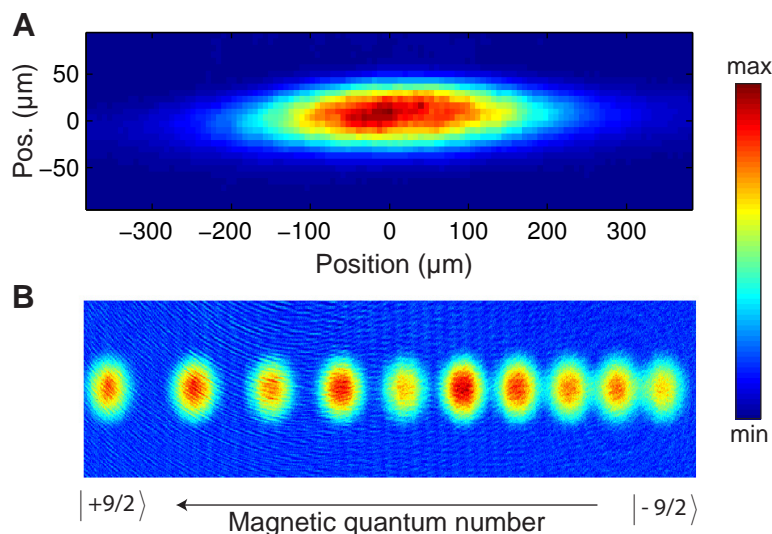


**Figure 3.9: Detection of high-spin fermions.** The density distribution for two spin-selective imaging techniques is shown: (A) In-situ image of one spin component of a multi-component Fermi sea. The visible density distribution belongs to the spin state  $|+1/2\rangle$ , while all further spin components  $m \neq 1/2$  are transferred to the  $f = 7/2$  manifold, which is transparent for the detection light. (B) Time-of-flight picture of a ten-component Fermi sea, where all spin components of the  $f = 9/2$  manifold are occupied. The asymmetric splitting of the spin states arises from non-linear contributions of the Zeeman effect during the Stern-Gerlach separation.

titative comparison with theoretical models. For these purposes, various methods are available in ultracold atomic systems [133]. In the *Bose-Fermi Mixture* setup, absorption imaging is employed [124, 125]. Here, in-situ and time-of-flight imaging techniques are discussed with a focus on adjustments for high-spin fermions.

### In-situ imaging

Imaging the atomic sample directly in the dipole trap is called in-situ imaging and allows to access the density distribution of the quantum gas [133]. This technique is typically limited by the resolution of the detection system, given by the pixel size of the CCD camera and the optical resolution of the objectives. Moreover, the attainable information can be limited by saturation effects. For fermions, however, the Pauli exclusion principle intrinsically limits the atomic density allowing for in-situ imaging in a wide parameter range.

In general, the applied absorption imaging is resonant for all spin states in the  $f = 9/2$  manifold. To image only one individual spin state, an additional procedure is employed. For this purpose, all spin states – except the one of interest – are transferred with microwave pulses into the  $f = 7/2$  hyperfine manifold. Here, the atoms are off-resonant for the detection light and hence not visible in the absorption pictures. To avoid any magnetically- or light-induced resonance shifts, a 1 ms waiting time is inserted before applying the microwave pulses with a typical duration of 50  $\mu\text{s}$ . This procedure remains short against most time scales of the experiment, allowing to address spin-dependent phenomena with spatial resolution in a broad range of parameters.

Note that the detection scheme is destructive and requires experimental runs for each spin component, which increases the experimental effort significantly. Nevertheless, this technique allows for intriguing insight into the spin and spatial configuration at the same time (see for example section 5.3.2). A typical example of an in-situ image taken in an elongated dipole trap is depicted in Fig. 3.9 A.

### Time-of-flight imaging

Imaging the atoms after a free expansion, when all trapping potentials have been switched off, is an additional technique referred to as time-of-flight imaging [133]. In the far-field limit of this expansion, the spatial distribution is converted into the momentum distribution. The expansion time, however, is limited by the vertical acceleration due to gravity. In our experiment, a time-of-flight of about 25 ms is possible, yielding a distribution close to the real momentum distribution. Furthermore, the lower density in the extended sample leads to a suppression of saturation effects. This allows for a reliable determination of the particle number, which is in more detail described in [106, 137]. To determine the temperature, an approach following [148] is employed by using a fugacity fit for the cloud shape, which is independent of further parameters such as the trapping frequencies or particle numbers (for more details see diploma thesis of N. Fläschner [108]).

The different spin states of a high-spin Fermi sea overlap in the time-of-flight pictures. Thereby, one can reliably measure the particle number, but the determination of the temperature is only possible in balanced spin mixtures. For imbalanced mixtures, more sophisticated schemes can be employed (see section 6.4.3). To separate different spin states, a Stern-Gerlach experiment can be performed, where an inhomogeneous magnetic field is applied during the expansion time. This induces a spin-dependent force due to the different magnetic moments of the spin states. Experimentally, the Stern-Gerlach field allows to separate all ten spin states of the  $f = 9/2$  manifold in one experimental run and constitutes the standard technique to measure spin occupations. Note that the different Fermi clouds require a large region on the CCD chip, which limits the expansion time to about 15 ms at a magnification of 1. A typical example of a ten-component Fermi sea using this technique is depicted in Fig. 3.9 B.

## 3.3 Magnetic field control

The control of the magnetic field constitutes a second key ingredient for spin-dynamics experiments. As discussed in section 2.2.2, the dynamical properties of high-spin systems are governed by the interplay between differential interaction and magnetic energy (see section 2.2.2). Even small deviations of the magnetic field are sufficient to induce perturbations, which macroscopically influence the system. This is a severe problem in particular for collective spin dynamics in bulk fermions (see chapter 5).

The magnetic field in the *Bose-Fermi Mixture* setup is provided by a number of coils, which are in detail described and characterized in [124, 125]: Large Helmholtz coils produce magnetic fields up to values of 600 G. They provide the magnetic field for the spin-state preparation and allow to address Feshbach resonances (see appendix B). Additionally, three pairs of small coils in each spatial direction, mounted on a cage system, surround the glass cell and provide a supplementary magnetic field of up to

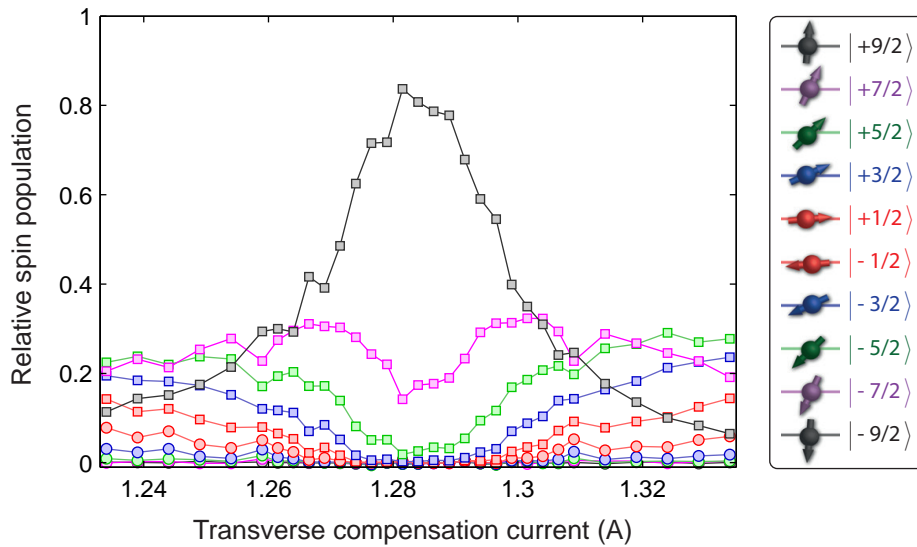


**Figure 3.10: Compensation of the magnetic offset field in the transverse direction.** The spin occupations are plotted as a function of the transverse magnetic field. The initial state is  $|+9/2\rangle$ . A current of  $I_{\text{tr}} = 1.282$  A reveals the best quantization, corresponding to the compensated magnetic field in this direction. The imperfect spin polarization is due to an additional magnetic field in the second transverse direction. For this experiment, a quantization field of 15 mG is applied.

3 G. The small coils are used to compensate stray fields and, moreover, to generate well-controlled homogeneous and gradient fields.

In the course of this research work, several methods have been developed allowing for a high control of the magnetic field. For this purpose, the atoms themselves are employed as a magnetic sensor. In the following, a description of calibration and compensation schemes for the magnetic offset and for the magnetic gradient field will be given.

### 3.3.1 Magnetic offset fields

A magnetic offset field is necessary to set the quantization axis for the atomic ensemble. The concept of the magnetic field compensation relies on the fact that at low magnetic field small perturbations significantly influence the accuracy of the quantization. This in turn changes the observed spin populations and allows to compensate magnetic stray fields with high precision. In this context, a similar method has been successfully applied to  $^{87}\text{Rb}$  in our group [138, 149], which has been extended to fermionic  $^{40}\text{K}$  throughout this work.

First, a spin-polarized Fermi sea in the spin state  $m = 9/2$  is prepared in the dipole trap. To compensate residual magnetic fields in the transverse direction (orthogonal to the quantization axis), a very low magnetic field is applied in the axial direction ( $\approx 10$  mG). At the same time, the current generating the transverse field  $I_{\text{tr}}$  is varied and the resulting spin occupations are measured after a time of 100 ms (see Fig. 3.10). One finds, that only for a specific current the initial spin polarization is maintained. This value corresponds to the compensated case, where the quantization axis is dominated by the axial field. However, if the magnetic field in the transverse direction significantly

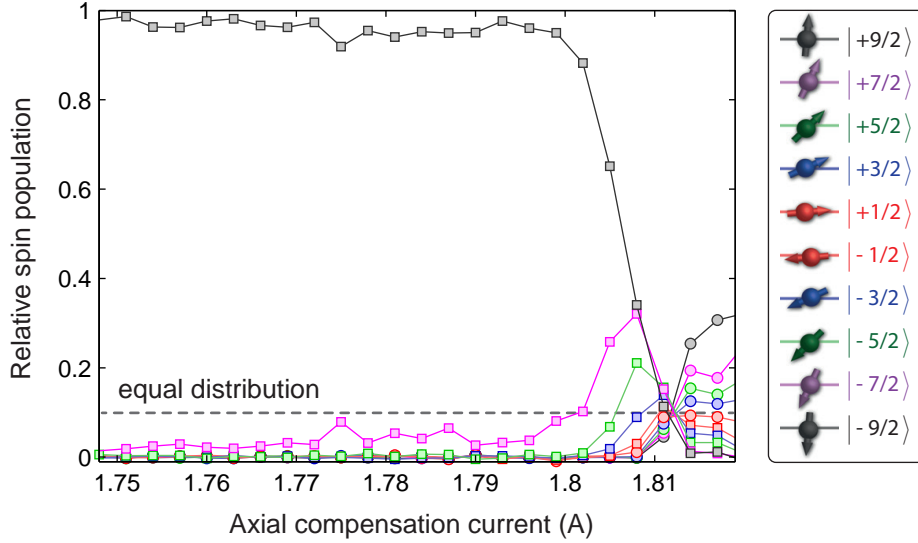


**Figure 3.11: Compensation of the magnetic offset field in the axial direction.** The spin occupations are depicted as a function of the axial magnetic field. The initial state is  $|+9/2\rangle$ . A current of  $I_{\text{ax}} = 1.811$  A reveals the best compensation, associated with an equal spin distribution (10% in each spin component), as indicated with the dashed line in the figure. The applied transverse magnetic field is 15 mG.

deviates, the quantization axis is effectively rotated. This becomes apparent in the occupation of new spin states visible in a Stern-Gerlach separation. Note that this procedure has to be performed for both transverse directions independently. A lower magnetic field in the axial direction leads to an even narrower signal as compared to the data depicted in Fig. 3.10. This allows for a compensation accuracy with an error well below 1 mG.

To cancel residual axial fields (parallel to the quantization axis), the magnetic field in the transverse direction is set to a low value ( $\approx 10$  mG) and the current generating the magnetic field in the axial direction  $I_{\text{ax}}$  is varied. The resulting spin populations for such an experiment are depicted in Fig. 3.11. For low currents, the atoms maintain polarized by the axial magnetic field. For higher currents, the axial field is lowered (due to the coil alignment) and spin components are continuously admixed until an equal distribution of all spin states is reached. This value corresponds to the compensated magnetic field in the axial direction. The compensation accuracy of the magnetic field in this direction is also estimated with an error below 1 mG.

After the compensation of the magnetic field in all spatial directions, additional small coils provide a well-controlled magnetic field in the axial direction [124, 125]. This field determines the Zeeman energy for the individual spin states during the spin-dynamics experiments and is calibrated using rf-spectroscopy (see [106]). For this purpose, the atoms are transferred between two spin states for different applied currents. From the transition frequency, one can recalculate the respective magnetic field using the Breit-Rabi formula (equation 2.1). Note that spin-polarized fermions are particularly well suited for this calibration technique due to the absence of interaction shifts.

It was checked that the same results for the magnetic field compensation are ob-

tained for bosonic and for fermionic atoms, which underlines the consistency of the presented method. The magnetic field uncertainty is estimated in total to be below 3 mG. A magnetic offset field of approximately 10 mG compensates sufficiently magnetic field perturbations and provides an adequate quantization field. The presented techniques provide a sufficient control over the magnetic offset fields for the experiments presented in the following. For a better performance, more enhanced magnetic field compensation techniques such as active shielding would be necessary (for example in [84]).

### 3.3.2 Magnetic gradients

In addition to residual magnetic offset fields, a magnetic gradient can also be present in the system. Typically, this gradient is small and arises from imperfections of the coils or surrounding technical devices. For high-spin experiments, this gradient must be well compensated and well controlled. In particular for harmonically trapped fermions, this compensation is highly important and turned out to be the key experimental issue for observing collective spin dynamics (see chapter 5).

#### Magnetic gradient compensation

To compensate magnetic gradients, a method has been developed based on spin waves, which are well-studied excitations occurring in bosonic and fermionic many-body systems [58, 61, 150]. Spin waves have been investigated in the course of this research work with a focus on high-spin fermions, published in [3]. As an important result of these investigations, it was found that even a very small magnetic gradient, which has no discernible influence on the energy levels of different spin states, strongly affects coherent spin superpositions. This can be used as a technical application for the gradient compensation.

The experimental starting point is a spin-polarized Fermi gas in the spin state  $|+9/2\rangle$ , prepared in an elongated dipole trap with trapping frequencies of  $\omega_{x,y,z} = 2\pi \times (70, 70, 10)$  Hz. The low confinement in the z-direction favors the formation of spin waves in this direction [3]. Using one coil pair in anti-Helmholtz configuration, a small current  $I_{\text{grad}}$  is applied, which induces a linear magnetic field gradient. Subsequently, a 10  $\mu\text{s}$  rf-pulse generates a coherent superposition of the spin states  $|+9/2\rangle$  and  $|+7/2\rangle$  with a homogeneous phase over the whole sample. If the current  $I_{\text{grad}}$  compensates for the unwanted magnetic field gradient in the experiment, then the system remains unaffected. The presence of a magnetic gradient, however, imprints a spatially-dependent phase on the coherent superposition. Combined with the harmonic confinement of the dipole trap, this induces counterflow dipole oscillations in both spin components, while the overall density of the Fermi sea remains constant [3]. These dipole oscillations can be detected in a Stern-Gerlach experiment, which is exemplarily depicted in Fig. 3.12 A. The complex excitation mechanism has been investigated in several works (see for example [151, 152]). In the following, the discussion is limited to the oscillation properties depending on the magnetic gradient strength.

For small gradients, the spin-wave frequency has a minimum value and increases for larger magnetic gradients up to the trapping frequency. The amplitude of the oscillations increases for intermediate magnetic gradients and decreases again for very large gradients [3]. Moreover, the phase of the induced spin oscillation is inverted by

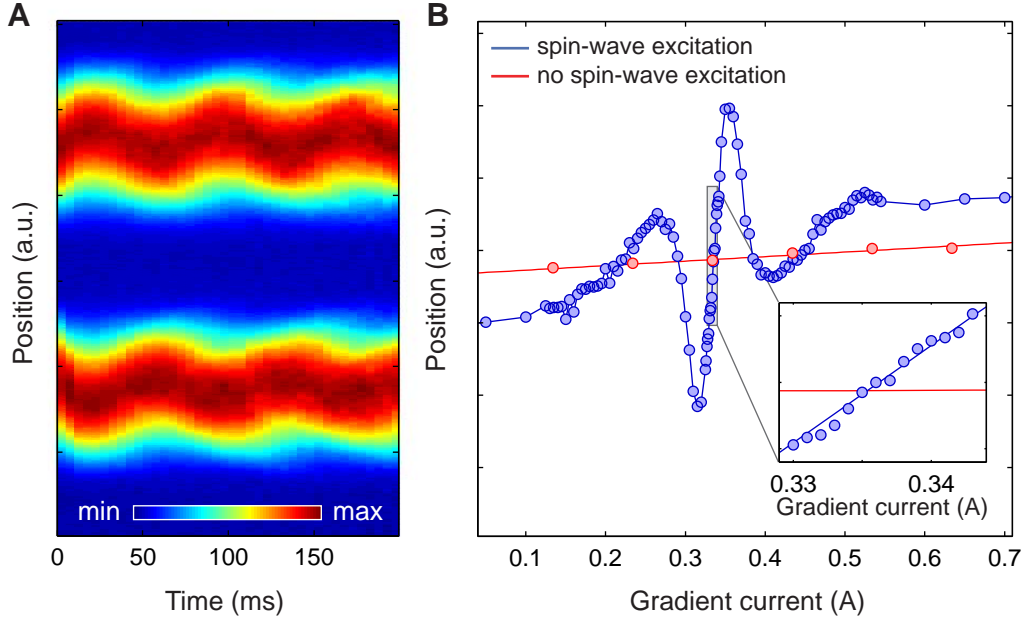


**Figure 3.12: Compensation of the magnetic gradient field.** (A) A spin-wave excitation in a two-component Fermi gas is depicted, which is excited with a magnetic gradient (see [109] for experimental details). Counterflow dipole oscillations of both spin components are clearly visible, while the overall density remains constant. (B) The position of the spin state  $m = 7/2$  after a time evolution of 100 ms is shown for different magnetic gradient fields. Blue dots result from a Fermi gas, initially prepared in a coherent superposition of the spin states  $|+9/2\rangle$  and  $|+7/2\rangle$ , showing a dispersive signal as a result of the spin-wave excitation. Red dots provide the reference measurement of a Fermi sea in the spin state  $|+7/2\rangle$ . The overall slope is due to the additional gradient potential. The inset shows a zoom into the zero-crossing, revealing a current of  $I_{\text{grad}} = 0.336$  A for the gradient compensation.

changing the gradient from positive to negative values, which is exploited to find the perfect compensation.

A typical compensation measurement is depicted in Fig. 3.12 B. The center-of-mass position of the spin state  $|+7/2\rangle$  is plotted after a time evolution of 100 ms as a function of the gradient current. This waiting time is optimized to observe the maximum deflection for small gradients. Two effects can be directly extracted from the data: First, the experiments reveal an overall linear shift of the atoms, which is a result of the additional gradient potential shifting the atoms in the shallow trap configuration. On top of this signal, a dispersive deflection of the atomic center-of-mass position around a gradient current of  $I_{\text{grad}} = 0.336$  A is observed, which arises from the spin-wave excitation. This signal can be used to determine the compensated gradient. As a reference, the center-of-mass motion of the pure spin state  $|+7/2\rangle$  has been monitored, where spin waves cannot be excited. Here, this dispersive feature is clearly absent, while the linear shift is also visible.

The zero-crossing of the dispersive signal coincides with the compensation of the magnetic gradient field. Deflections in both directions correspond to small positive and negative gradients. As demonstrated in the inset of Fig. 3.12 B, this allows for a precise magnetic gradient compensation with an error equivalent to  $40 \mu\text{G}/\text{cm}$ .

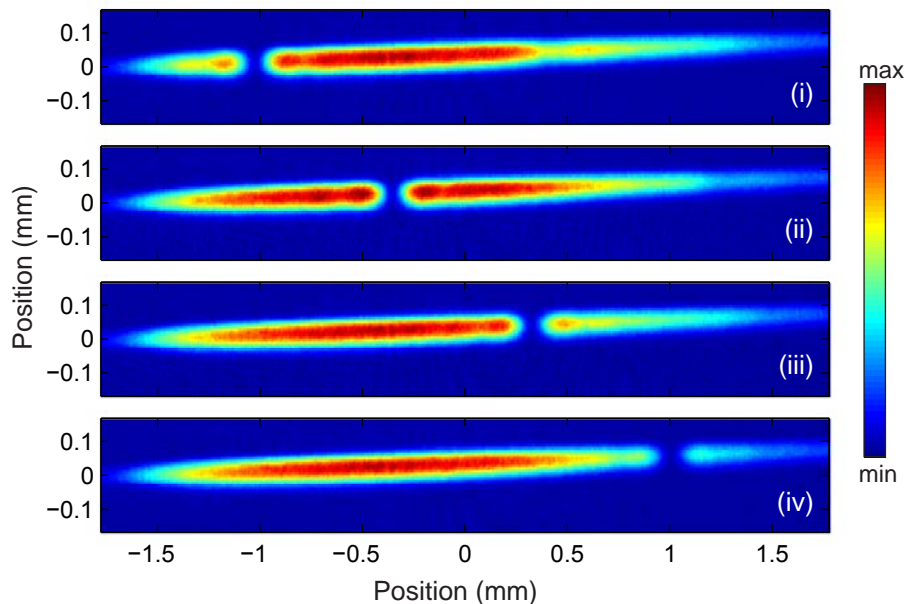


**Figure 3.13: Local microwave transfer in an elongated Fermi gas.** In-situ images of an elongated Fermi gas in the spin state  $|f = 9/2, m = 5/2\rangle$  with a spatial extension of about 2 mm in the elongated direction are shown. Using a 500  $\mu\text{s}$  mw-pulse with a frequency of 1284.634 MHz (i), 1284.616 MHz (ii), 1284.598 MHz (iii), and 1284.58 MHz (iv), the atoms are locally transferred to the state  $|f = 7/2, m = 5/2\rangle$ , which is transparent for the detection light. An additional magnetic field of  $B = 0.17$  G and a gradient current of  $I_{\text{grad}} = -5.0$  A are applied.

The presented gradient compensation technique is easy-to-implement and suitable for the daily experimental operation. Note that for a typical size of a Fermi sea of 100  $\mu\text{m}$  the remaining gradient is below 1  $\mu\text{G}$  over the extent of the sample. This precision also allowed for the observation that different applied magnetic fields require different gradient compensations. It demonstrates that a small contribution of the magnetic gradient arises from the small coils themselves, which is accounted for in the presented experiments. However, the large part of the gradient fields stems from environmental sources such as technical devices or magnetic items. This should motivate the experimentalist to displace any magnetic items in the laboratory only very carefully.

### Determination of the magnetic gradient field

The precise knowledge of the magnetic gradient is important for several applications such as the study of spin waves [3]. Its strength can be determined using microwave spectroscopy. Therefore, a spin-polarized Fermi gas in the spin state  $|f = 9/2, m = 5/2\rangle$  is prepared in a one-beam dipole trap with trapping frequencies  $\omega_{x,y,z} = 2\pi \times (80, 90, 3)$  Hz. After a 2 s expansion time in this configuration, the fermions have spatially redistributed in the shallow direction into a large extension of several millimeters. In the transverse directions, in contrast, the atoms are strongly confined to about 40  $\mu\text{m}$ . After this preparation step, a magnetic field gradient is applied in the axial direction, which can be resolved with microwave spectroscopy.

For this purpose, the atoms are transferred from the spin state  $|f = 9/2, m = 5/2\rangle$

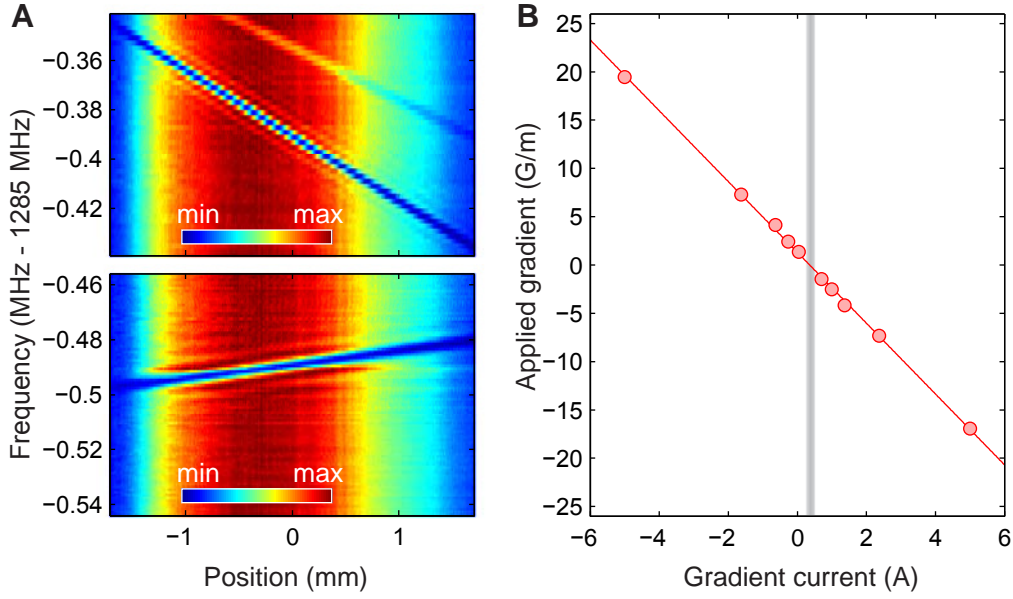


**Figure 3.14: Calibration of the magnetic field gradient.** (A) The column sums of measurements such as in Fig. 3.13 are shown as a function of the pulse frequency. The mw-pulse transfers the atoms locally from  $|f = 9/2, m = 5/2\rangle$  to  $|f = 7/2, m = 5/2\rangle$ . A gradient current of  $I_{\text{grad}} = -5.0$  A (upper part) and  $I_{\text{grad}} = +1.239$  A (lower part) is applied. The two stripes in the upper figure correspond to  $\pi$ -polarized and  $\sigma^+$ -polarized (to  $|f = 7/2, m = 7/2\rangle$ ) microwave transfers. (B) The magnetic gradient strength is shown for different gradient currents. It has been calculated for each magnetic gradient field from measurements such as in A using the Breit-Rabi formula 2.1. The solid line is a linear fit revealing a slope of  $\Delta B = -5.34$  G/(m · A). The compensated case corresponds to a current of  $I_{\text{grad}} = 0.336$  A.

to  $|f = 7/2, m = 5/2\rangle$  with a  $500 \mu\text{s}$  microwave pulse. Due to the rather long pulse duration, the microwave transfer is only resonant with a specific part of the atomic sample corresponding to the local value of the magnetic field. After the microwave manipulation, in-situ imaging is employed, where atoms in the  $f = 7/2$  manifold are not visible. This is exemplarily depicted for different microwave frequencies in Fig. 3.13, where the transferred fraction of atoms appears as dips in the density distribution. These holes show up at different positions of the Fermi sea, depending on the local magnetic field. In general, this demonstrates the capability to transfer atoms locally between both hyperfine manifolds. This feature is employed to determine precisely the magnetic gradient strength.

By varying the microwave frequency, holes are realized at different positions of the Fermi sea. In Fig. 3.14 A, the column sums in the radial direction are exemplarily depicted for a positive and a negative gradient. This measurement demonstrates that the position of the dips depends approximately linearly on the applied frequency. Since this transition is also dominated by the linear Zeeman splitting (see section 3.2.2), it validates in addition the linear form of the magnetic gradient over the region of interest. A linear fit of the dip position is employed, which allows to determine the magnetic gradient for a each current with the Breit-Rabi formula (equation 2.1).

The obtained magnetic gradient is depicted in Fig. 3.14 B as a function of the applied

gradient current. As the experiments demonstrate, the dependence turns out to be rather linear. This is expected for perfectly aligned coils in anti-Helmholtz configuration. Fitting these data with a linear function reveals a value of  $\Delta B = -5.34 \text{ G}/(\text{m} \cdot \text{A})$  for the gradient dependence on the applied current.

Combining this technique with the other above-mentioned methods, this constitutes an experimental toolbox, which is suitable for an adequate control of the magnetic field in the presented experiments.



## Chapter 4

# Spin dynamics in optical lattices

The experiments presented in this chapter constitute the first realization of fermionic spin dynamics. Due to the complex structure of fermionic many-body systems, the underlying fundamental interaction process was investigated first on a microscopic level. In this context, optical lattices provide an ideal experimental tool [31, 32].

Quantum gases in optical lattices have proven to provide ideal model systems for various phenomena in solid-state physics. Owing to technological progress, single-site resolution [153–156] and unconventional lattice structures [157] have been realized. A particular focus of the current research activities is directed towards lattice systems with spin 1/2 fermions, driven by microscopic interactions between two spin states. Ground-breaking experiments allowed to study fundamental electronic magnetic properties and quantum phases, e.g., the metal-to-Mott insulator transition [38–40] or short-range magnetic ordering [47].

Beyond these conventional spin 1/2 systems, high-spin fermions in optical lattices constitute completely new many-body systems. Only a few experimental realizations have been reported so far, such as the recent realization of Pomeranchuk cooling with fermionic ytterbium atoms in optical lattices [103, 158–160]. From the theoretical perspective, these systems have attracted a tremendously growing interest especially in the direction of ground-state properties. Various investigations have been performed, studying for example high-spin Mott insulators [95, 161–163] and SU(N)-magnetic properties [98–101]. Another important focus are magnetic ordering effects in high-spin systems, where the number of involved spin states is important for the character of the magnetic long-range correlations [96, 98, 164–166].

These exotic many-body phenomena are driven by microscopic interactions between the involved spin states, which are hence of general interest. Pioneering experiments have studied local high-spin interactions in bosonic quantum gases [74, 75, 84]. For fermions the high control over the experimental parameters combined with Pauli blocking allows to realize fermionic lattice systems in tailored spatial and spin configurations. This constitutes a perfect starting point to explore the fundamental collision process between two fermions with high spin [104].

In this spirit, this chapter will explore fermionic spin dynamics in optical lattices. First, I will briefly introduce important concepts of optical lattices (section 4.1). The investigation of spin dynamics starts in section 4.2, where I will present a detailed study of coherent spin dynamics on a two-particle level, established in deep optical lattices. Subsequently, the system will be extended to intermediate lattice depths (section 4.3)

and the crossover from the two-body to the many-body regime will be studied. Finally, experiments including also higher bands of the optical lattice will be presented (see section 4.4).

Parts of this chapter have been published in [5]. The experiments and the data analysis were performed with C. Becker, N. Fläschner, S. Götze, J. Heinze, and K. Sengstock.

## 4.1 Characterizing fermions in optical lattices

In the *Bose-Fermi Mixture* setup, a 3d cubic optical lattice is implemented, which can be superimposed on the atoms in the dipole trap [124, 125, 134]. The corresponding lattice potential leads to the formation of a band structure, consisting of energy bands  $n$  for quasimomenta  $q$  (see appendix A). A detailed discussion of quantum gases in optical lattices is available in the literature in various excellent articles (see for example [31, 32]).

In this section, I will focus on the characterization of fermions in optical lattices. First, a novel multi-band spectroscopy method for the lattice calibration will be presented. Subsequently, I will introduce the high-spin Hubbard model, which provides a suitable description for fermionic high-spin interactions.

### 4.1.1 Calibration of the optical lattice

Over the last years, several methods have been developed to probe the band structure of atoms in optical lattices. A prominent example is Bragg spectroscopy, which constitutes a perfect tool to probe these systems with momentum resolution [167–169], however, at the expense of significant experimental effort. Another widely employed method is lattice-amplitude modulation, which has become an inevitable tool for spectroscopy in optical lattices [170–172].

In the course of this research work, this method was combined with a band-mapping technique [173], providing an ideal tool for multi-band spectroscopy of fermions in optical lattices including momentum resolution. It is easy to implement, requires no further setup components and is hence well suited for the daily experimental operations. The high precision of this method allowed to observe an interaction-induced tunneling reduction in Bose-Fermi mixtures and to study for the first time fermionic higher-band dynamics, both performed throughout this work [4, 6]. A detailed discussion of the results is provided in the thesis of J. Heinze [107]. Here, I describe this versatile method as a calibration tool for the band structure in fermionic lattice systems.

The calibration starts with spin-polarized fermions, which are adiabatically loaded into an optical lattice, forming a band insulator. The system is excited by modulating the depth of the optical lattice for 1 ms with a variable frequency and a typical modulation amplitude of 20 %. Subsequently, a band-mapping procedure is applied, where the lattice depth is reduced within 200  $\mu$ s to zero. This is adiabatic with respect to the lattice potential and maps the quasimomenta onto real momenta as illustrated in Fig. 4.1 A. However, it is still much faster than trap-induced dynamics, which prevents the atoms from redistributing within each band. After a time-of-flight of typically 15 ms, the momentum distribution is measured via absorption imaging.

If the modulation frequency does not match any band transition, the atoms are not excited and remain in their initial momentum configuration (see Fig. 4.1 B). However, if

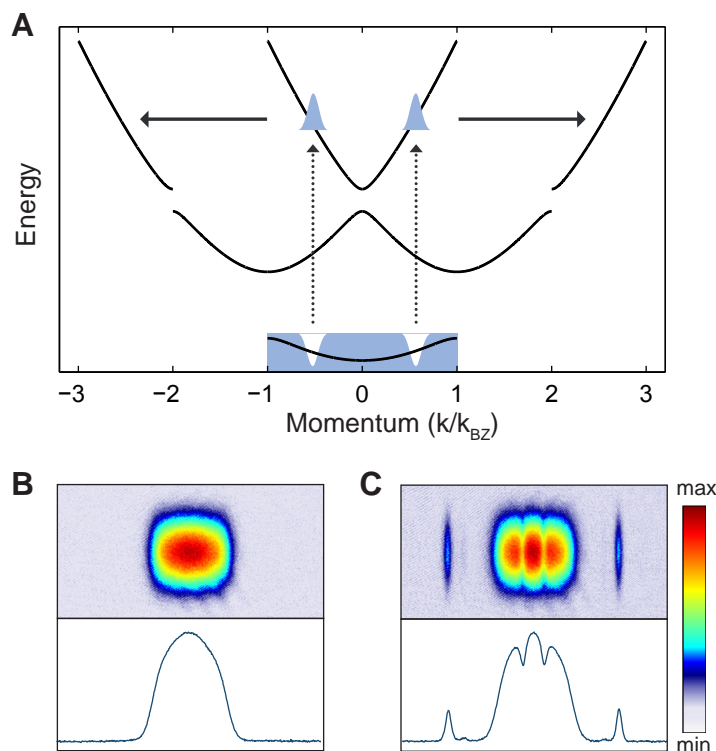


**Figure 4.1: Sketch of the multi-band spectroscopy technique.** (A) An illustration of this technique is provided, starting from a band insulator in an optical lattice. Arrows indicate the excitation by lattice-amplitude modulation (dashed lines) and the band-mapping procedure (solid lines). Typical time-of-flight pictures (upper row) show the momentum distribution for off-resonant (B) and resonant modulation (C). In the column densities (lower row), the corresponding unperturbed band insulator and the particle-hole excitation into the third band are visible. Experimental data have also been published in [6].

the modulation frequency is resonant, atoms are transferred into higher bands, leaving a hole in the lowest band. This corresponds to a particle-hole excitation [174]. An example for resonant modulation is depicted in Fig. 4.1 C, revealing that only a specific quasimomentum is excited. The experimental trick to obtain this momentum resolution is based on the different curvatures of the individual bands, providing that the resonance condition is fulfilled only for specific momenta. Note that due to the symmetry of the energy spectrum, atoms at positive and negative quasimomenta with equal absolute value are simultaneously excited.

By varying the modulation frequency, the full band structure can be obtained. This is depicted in Fig. 4.2, where the corresponding column densities are shown for different frequencies. The outcoupled particles correspond to the extended zone scheme of the band structure, while the holes reflect the reduced zone scheme [174]. Moreover, the opening of the band gap and the characteristic flattening of the individual bands at the edge of the Brillouin zones are clearly visible. The transfer at zero momentum is suppressed due to parity conservation and the influence of the harmonic potential (see also [6]).

Using the multi-band spectroscopy technique, one can extract the energy difference between the lowest band and the excited bands, allowing to determine the lattice depth

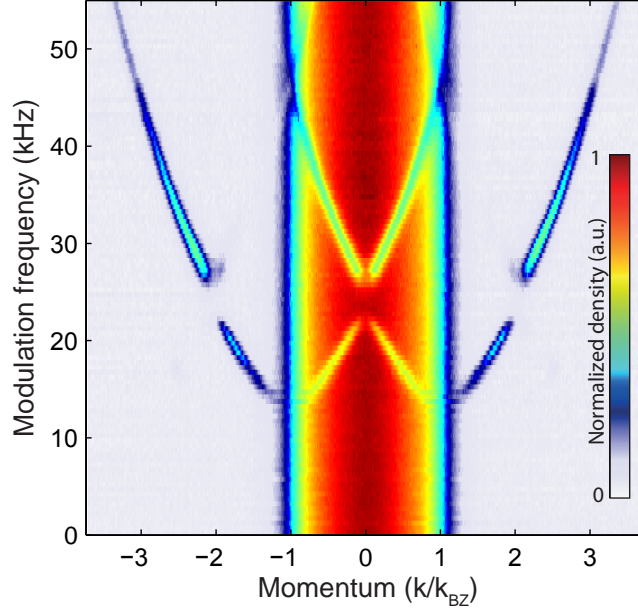


**Figure 4.2: Momentum-resolved band structure of fermions in optical lattices.** The energy spectrum for a lattice depth of  $V_L = 5 E_F$  is depicted. Shown are the column densities for different modulation frequencies at a modulation amplitude of 20%. The particle number is  $2 \times 10^5$  and temperature  $T = 0.2 T_F$ . The central plateau corresponds to atoms in the initial band insulator, which occupy the first Brillouin zone. Holes in the first Brillouin zone represent the reduced zone scheme. The peaks at higher momenta correspond to the excited particles, representing the extended zone scheme. Experimental data have also been published in [6].

$V_L$ . For this, the center-of-mass position of the outcoupled atoms is determined in the time-of-flight pictures. This technique works best for the third band, where a suitable overlap of the wave functions favors a clear excitation signal for all lattice depths. In Fig. 4.3, the extracted dispersion of the third band is shown and compared to single-particle calculations [32]. For intermediate momenta the experimental data agree very well with the calculated dispersion relation, while deviations appear at small and large momenta. The latter is a combined effect of the underlying harmonic confinement and the finite band-mapping time [6, 107].

Nevertheless, for intermediate momenta these distortion effects are small and can be well neglected. Therefore, the fitting of the data is restricted to a momentum range between  $0.55 - 0.85 k_{BZ}$ , which allows to determine the lattice depth with high precision. Note that interaction shifts are fully absent due to the spin polarization of the Fermi gas. The Gaussian shape of the lattice beams leads to a slightly inhomogeneous lattice potential resulting in a relative error of the lattice calibration accuracy of at least 2%.

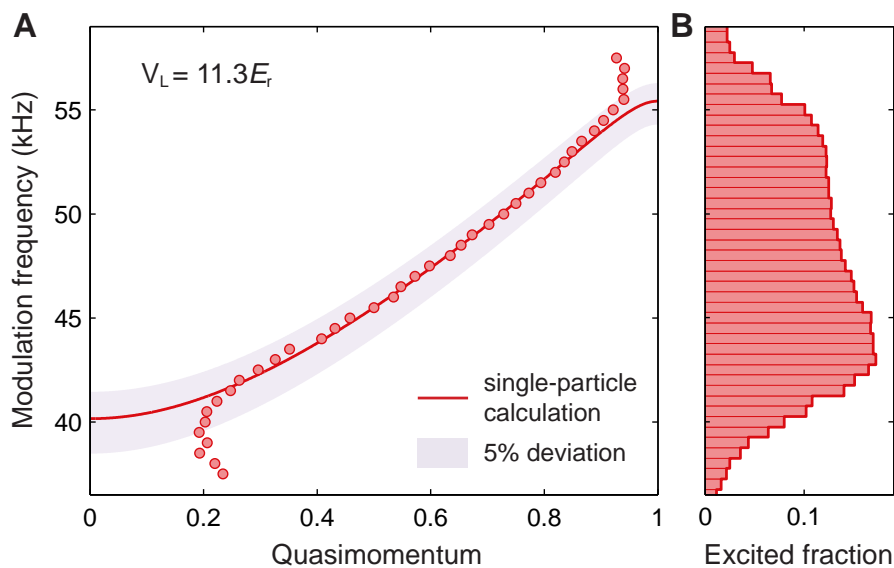


**Figure 4.3: Dispersion relation for the third band.** (A) The center-of-mass momenta, excited from the lowest into the third band, are depicted for different modulation frequencies. Solid line is a fit of the data to a single-particle band structure calculation for quasimomenta  $0.55 k_{\text{BZ}} < q < 0.85 k_{\text{BZ}}$  with the lattice depth as free parameter. The lattice depth is calibrated to  $V_L = 11.3 E_r$ . The shaded area depicts deviations of 5% from the fitted value. (B) A histogram showing the relative number of outcoupled atoms is depicted. Experimental data have also been published in [6].

### 4.1.2 Describing high-spin fermions in optical lattices

In a spin-polarized Fermi gas, interactions are suppressed at low temperatures due to Pauli blocking. However, the spin degree of freedom circumvents this restriction. Since two fermions in different spin states can occupy the same spatial single-particle state, they can also interact via s-wave scattering [14].

A suitable description of interacting lattice systems is the Hubbard model [175, 176], which is well-known from solid-state physics. It considers short-range interactions and describes bosonic and fermionic lattice systems typically restricted to the lowest band. The Hubbard model can be extended to particles with high spin [32], where the following contributions are important:

#### Tunneling energy

In the Hubbard model, tunneling processes are considered between adjacent lattice sites. In the tight-binding approximation [174], which is typically valid for lattice depths above  $5 E_r$ , tunneling is described by the Hamiltonian

$$\mathcal{H}_J = -J \sum_m \sum_{\langle i, j \rangle} f_{i,m}^\dagger f_{j,m}. \quad (4.1)$$

Here,  $J$  is the spin-independent tunneling matrix element. The summation includes all spin components  $m$ .  $\langle i, j \rangle$  denotes the sum over nearest-neighboring lattice sites.  $f_{i,m}^\dagger$  and  $f_{i,m}$  are the creation and annihilation operators for atoms in the spin state  $m$  at the lattice site  $i$ .

### Harmonic potential

Optical lattices are typically associated with an additional harmonic confinement. The corresponding Hamiltonian has the form of a single-particle operator

$$\mathcal{H}_{\text{conf}} = \sum_m \sum_i V_i f_{i,m}^\dagger f_{i,m}, \quad (4.2)$$

where  $V_i$  is spin-independent. This term adds an energy offset depending on the exact position in the harmonic trap.

### Magnetic energy

The Zeeman Hamiltonian accounts for the magnetic energy and is given by

$$\mathcal{H}_Z = E_{\text{BR}}^{(m)}(B) \sum_m \sum_i f_{i,m}^\dagger f_{i,m}, \quad (4.3)$$

yielding an individual energy offset for each spin state. For spin dynamics, it is suitable to introduce the two-particle Zeeman energy  $E_Z^{(m_1, m_2)} = E_{\text{BR}}^{(m_1)} + E_{\text{BR}}^{(m_2)}$ .

### High-spin interactions

Collisions between the atoms are considered as on-site interactions on the same lattice site. The high-spin interaction Hamiltonian is given by

$$\mathcal{H}_I = \sum_{m_1+m_2=m_3+m_4} U_{m_1 m_2 m_3 m_4} \sum_i f_{i,m_3}^\dagger f_{i,m_4}^\dagger f_{i,m_2} f_{i,m_1}. \quad (4.4)$$

Here,  $U_{m_1 m_2 m_3 m_4}$  is the spin-dependent on-site interaction, which varies for different spin configurations. It is given by

$$U_{m_1 m_2 m_3 m_4} = \frac{4\pi\hbar^2}{m} a_{m_1 m_2 m_3 m_4} \int d\mathbf{r} |w(\mathbf{r})|^4. \quad (4.5)$$

Thereby, the colliding particles occupy the same spatial wave function on the same lattice site, described by the Wannier function  $w(\mathbf{r})$  [177].

The full high-spin Hubbard Hamiltonian is the sum of all above-mentioned contributions:

$$\mathcal{H}_{\text{tot}} = \mathcal{H}_J + \mathcal{H}_{\text{conf}} + \mathcal{H}_I + \mathcal{H}_Z. \quad (4.6)$$

The additional spin degree of freedom extends the conventional Hubbard model considerably [32]. Its highly involved ground-state and non-equilibrium properties originate from the interplay between all contributions described above.

The experiments presented in this chapter focus on fermionic spin dynamics in three different regimes of the optical lattice, as outlined below:

### 1. Two-body limit

In deep optical lattices, tunneling is suppressed ( $\mathcal{H}_J = 0$ ) and the harmonic confinement  $\mathcal{H}_{\text{conf}}$  affects only the initial spatial distribution of the atoms in the optical lattice. This allows for the realization of a textbook-like two-particle experiment, which will be in detail explored in section 4.2. In this case, the full Hubbard Hamiltonian 4.6 is reduced to the two-body Hamiltonian

$$\mathcal{H}_{2\text{body}} = \mathcal{H}_I + \mathcal{H}_Z. \quad (4.7)$$

In this limit, the system is only governed by the interplay between high-spin interactions and magnetic energy, which strongly simplifies the resulting dynamics. Both atoms occupy the same spatial state described by the corresponding Wannier function. This requires a symmetric spatial part and hence an antisymmetric spinor part of the wave function (see section 2.2.1). The isolated atom pair is represented by the on-site two-particle state

$$|\Psi_{\text{on-site}}\rangle = \underbrace{w(\mathbf{r}_1)w(\mathbf{r}_2)}_{\text{spatial part}} \underbrace{|m_1, m_2\rangle}_{\text{spinor part}}. \quad (4.8)$$

In the two-body limit, the spatial part remains fixed and will be omitted in the following.

### 2. Multi-site spin dynamics

At intermediate lattice depths, the full Hubbard Hamiltonian 4.6 has to be considered. The dynamics are governed by the interplay between spin-changing collisions and spatial dynamics. It is particularly interesting, how this affects the conventional ground-state properties of the two-component Hubbard model [32]. It turns out that the metallic phase ( $\mathcal{H}_J \gg \mathcal{H}_I, E_F$ ) and the Mott-insulating phase ( $\mathcal{H}_I \gg \mathcal{H}_J, E_F$ ) are robust in the presence of spin-changing collisions. However, the situation changes for a band insulator ( $E_F \gg \mathcal{H}_I, \mathcal{H}_J$ ), which appears to be sensitive to spin dynamics. In this context, a novel interaction-induced instability of a band insulator has been observed, which will be discussed in section 4.3.

### 3. Multi-band spin dynamics

The Hubbard model is typically restricted to the lowest band. Spin dynamics have also been studied involving the orbital degrees of freedom. This requires an extension of the Hubbard Hamiltonian, which accounts for the full band structure [178–180]. Experiments demonstrating multi-band spin dynamics will be presented in section 4.4.

## 4.2 Two-particle spin dynamics

The tunability of optical lattices allows for the investigation of the most fundamental interaction process: two fermions with high spin collide (see section 2.2.1). This provides an ideal starting point for the investigation of spin dynamics in high-spin fermions.

To reduce the complexity of the lattice system described by the Hubbard Hamiltonian 4.6 to this case, a binary fermionic spin mixture is prepared in a very deep optical lattice, where tunneling is strongly suppressed. The harmonic confinement leads to an initial spatial distribution with a two-component band insulator in the core of the system surrounded by singly occupied sites. Note that triply occupied sites are not allowed due to the Pauli exclusion principle. Atoms on singly occupied sites do not have any collision partner, which prevents collisions as in the spin-polarized case. The doubly occupied sites, however, constitute the realization of a textbook-like two-particle experiment. Many of these two-particle experiments are independently realized and evolve fully simultaneously in time.

In this section, I will present a detailed study of fermionic spin dynamics in the two-body limit. After a description of the experimental procedure, I will report on the first observation of fermionic spin-changing collisions. This was observed in a pseudo-spin  $3/2$  system, where additionally a fermionic spin resonance could be found and fundamental scattering parameters could be extracted. Then I will present experiments exploiting the full spin  $9/2$  system and report on novel multi-flavor spin dynamics including high-collision quanta.

### 4.2.1 The experimental procedure

As a first step, a binary spin mixture is evaporated to quantum degeneracy. The best performance is achieved by choosing an exponentially decreasing magnetic field ramp during the evaporation, which is adjusted for each prepared spin mixture. This ramp suppresses uncontrolled spin-changing collisions, in particular in the beginning of the evaporative cooling. Furthermore, it allows for a fast switching to very low magnetic fields, where the experiments are performed. Typically a balanced spin mixture of  $4 \times 10^5$  particles at temperatures between  $0.15 - 0.25 T_F$  is realized. After the evaporation the dipole trap is compressed within 50 ms.

In a second step, the atoms are adiabatically loaded into a 3d optical lattice with a linear lattice ramp of 150 ms. This leads to the formation of a two-component band insulator in the core of the system as sketched in Fig. 4.4 A. A deep optical lattice has several advantages: First, the suppression of tunneling allows for a longer study of the two-body limit. Moreover, higher densities increase the local interaction, which leads to faster spin-changing dynamics. In addition, the relative number of doubly occupied sites increases due to the additional harmonic confinement originating from the lattice beams. Therefore, deep lattices with lattice depths between  $25 - 35 E_r$  are employed limited by the power of the lattice laser.

For quantitative insight into the resulting spatial distribution of the atoms in the optical lattice, calculations using Dynamical Mean-Field Theory (DMFT) [181] have been performed by A. Sotnikov and coworkers [182]. They reveal that at a lattice depth of  $35 E_r$  approximately 40% of the atoms occupy doubly occupied sites. As depicted in Fig. 4.4 B, the particles form a band insulator with two atoms per site in the core of the system, which extends over 40–50 lattice sites in each spatial direction. Besides,

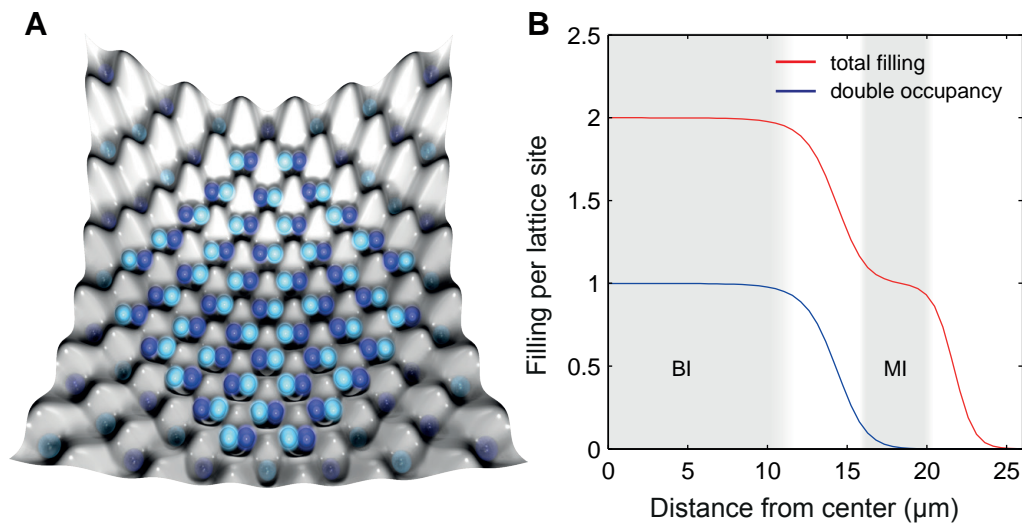


**Figure 4.4: Spatial distribution of the atoms in deep optical lattices.** (A) A sketch of the spatial distribution is shown. In the core of the system, a two-component band insulator with doubly occupied sites is formed, while singly occupied sites appear in the outer part. (B) Calculations of the spatial distribution in the optical lattice for the spin mixture  $|9/2, 1/2\rangle$  at  $35 E_r$  are depicted. The two-component band insulator (BI) in the core and a Mott-insulating shell (MI) are visible, surrounded by a metallic phase. The calculations are kindly provided by A. Sotnikov [182].

an occupation plateau with one atom per site is found, which corresponds to a Mott-insulating shell surrounded by metallic shells.

The spin dynamics are initialized by a quench of the magnetic field to a low value, typically between 0.1 – 1.6 G. After a certain time evolution the magnetic field is raised again to 14 G, which suppresses further spin-changing collisions. The magnetic field switching has been optimized independently using rf-spectroscopy, revealing switching times well below  $500 \mu\text{s}$ . This is much faster than the dynamics of the spin  $3/2$  system and reasonably faster than the dynamics of the spin  $9/2$  system. Optionally, a black-out-pulse procedure can be applied to record exclusively doubly occupied lattice sites (see section 4.2.2).

Subsequently, the optical lattice is ramped down within  $500 \mu\text{s}$ , which maps the atoms occupying the lowest band on the first Brillouin zone. This allows to ensure that higher-band excitations are suppressed. Moreover, all spin states can be well separated in a subsequent Stern-Gerlach experiment. The spin occupations are recorded after a time-of-flight of typically 18.5 ms.

Note that the inhomogeneity of the lattice potential and the magnetic field are estimated to be below 2% and 1 mG, respectively. Hence, it is justified to assume that all doubly occupied sites obey independently the same time evolution. Therefore, the global spin occupations are suitable observables for the microscopic spin dynamics.

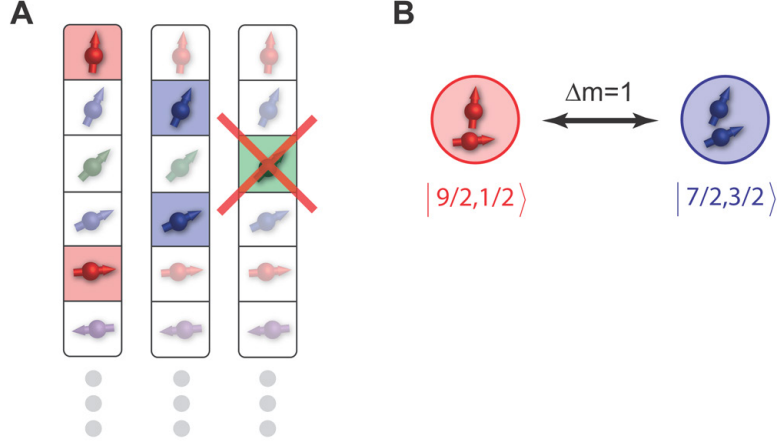


**Figure 4.5: Sketch of the pseudo-spin 3/2 system.** (A) The involved spin configurations are depicted. Colored boxes represent both two-particle states ( $|9/2, 1/2\rangle$  and  $|7/2, 3/2\rangle$ ). Note that the two-particle state  $|5/2, 5/2\rangle$  is forbidden due to the Pauli exclusion principle. (B) Sketch of the two-level system. Both spin configurations are coupled by spin-changing collisions with a spin transfer of  $\Delta m = 1$  for each particle.

#### 4.2.2 A proof-of-principle experiment

The experiments presented in the following provide the first experimental observation of fermionic spin dynamics. For this proof-of-principle experiment, the most fundamental system in spin space – the pseudo-spin 3/2 system – has been employed, corresponding to a two-level system.

##### Pseudo-spin 3/2 system

The two-particle states  $|7/2, 3/2\rangle$  and  $|9/2, 1/2\rangle$ , both with a total magnetization of  $M = m_1 + m_2 = 5$ , form a pseudo-spin 3/2 system. They are coupled by spin-changing collisions with a spin transfer of  $\Delta m = 1$  (see Fig. 4.5 A). Note that the two-particle state  $|5/2, 5/2\rangle$  is forbidden due to the Pauli exclusion principle. Further two-particle states are not allowed due to the conservation of the total magnetization with the result that an effective two-level system is realized (see Fig. 4.5 B).

Both two-particle states form a suitable basis

$$\mathcal{B}_{M=5} = \{|9/2, 1/2\rangle, |7/2, 3/2\rangle\}, \quad (4.9)$$

in which the interaction Hamiltonian reads

$$\mathcal{H}_I = \begin{pmatrix} U_{\frac{9}{2}, \frac{1}{2}, \frac{9}{2}, \frac{1}{2}} & U_{\frac{9}{2}, \frac{1}{2}, \frac{7}{2}, \frac{3}{2}} \\ U_{\frac{9}{2}, \frac{1}{2}, \frac{7}{2}, \frac{3}{2}} & U_{\frac{7}{2}, \frac{3}{2}, \frac{7}{2}, \frac{3}{2}} \end{pmatrix} = \frac{4\pi\hbar^2}{m} \int d\mathbf{r} |w(\mathbf{r})|^4 \begin{pmatrix} 167.01 & 1.24 \\ 1.24 & 167.52 \end{pmatrix} a_B. \quad (4.10)$$

Diagonal elements represent the interaction energies, while off-diagonal elements describe the coupling with spin-changing collisions. Due to the large total magnetization ( $M = 5$ ), only the scattering channels  $F = 6, 8$  contribute to the spin dynamics, which

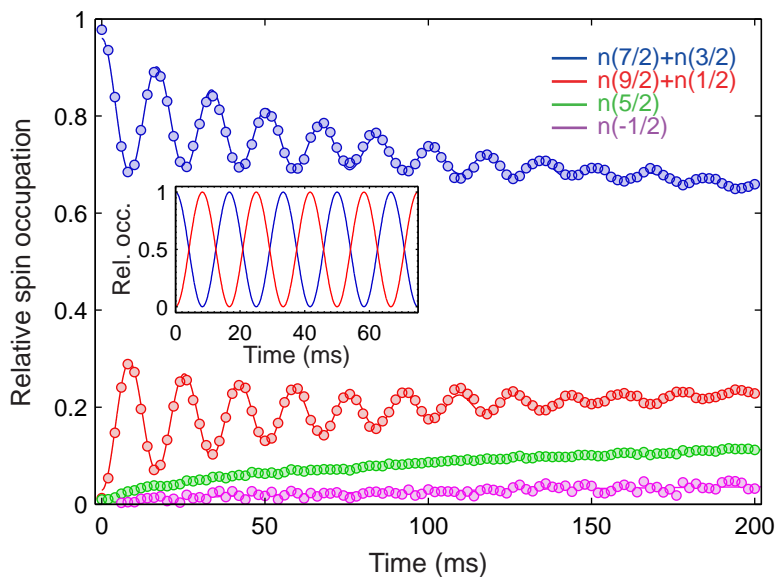


**Figure 4.6: Observation of spin-changing collisions in a pseudo-spin 3/2 system.** Relative occupations of the spin states  $n(m)$  are shown as a function of time. These data demonstrate for the first time fermionic spin dynamics, apparent in coherent oscillations between the involved two-particle states  $|7/2, 3/2\rangle$  and  $|9/2, 1/2\rangle$ . Solid lines are fits to the data using equation C.1. The magnetic field is  $B = 0.17$  G and the lattice depth is  $V_L = 30 E_r$ . In the inset, the time evolution calculated using equation 4.7 is depicted.

have similar absolute values (see section 2.2.1). This leads to small coupling elements below 1% of the interaction energies, which are also only slightly different for both two-particle states. Note that this system is inherently different from a real spin 3/2 system. In the latter the contributing scattering channels are  $F = 0, 2$ , which results in the same interaction energy for both two-particle states [158]. Therefore, the experimental system is referred to as a pseudo-spin 3/2 system.

The corresponding Zeeman Hamiltonian contains only diagonal elements and is given by

$$\mathcal{H}_Z = \begin{pmatrix} E_Z^{(9/2,1/2)} & 0 \\ 0 & E_Z^{(7/2,3/2)} \end{pmatrix}. \quad (4.11)$$

It accounts for the differential Zeeman energy of both two-particle states.

### Two-level dynamics

The investigation of spin dynamics in the pseudo-spin 3/2 system is performed in the two-body limit, established in a deep optical lattice of  $30 E_r$ . On each doubly occupied site the two-particle state  $|7/2, 3/2\rangle$  is realized. To study the time evolution at low magnetic field, the spin occupations of both involved two-particle states ( $|7/2, 3/2\rangle$  and  $|9/2, 1/2\rangle$ ) are recorded.

The result of this experiment, depicted in Fig. 4.6, constitutes the first observation of spin-changing collisions in fermionic quantum gases. As a key result, it provides the

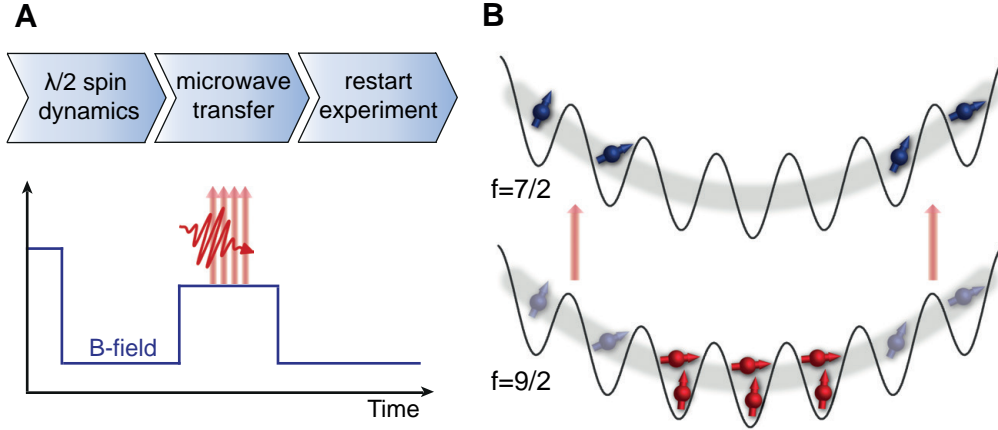


**Figure 4.7: Sketch of the black-out-pulse technique.** (A) A sketch of the experimental protocol is shown. After half a spin-oscillation period, the magnetic field is raised and microwave pulses transfer atoms on singly occupied sites into the  $f = 7/2$  manifold. The subsequent spin dynamics are only recorded from doubly occupied sites. (B) The spin distribution of the system is sketched after the black-out pulses. Only the core region with doubly occupied sites remains in the  $f = 9/2$  manifold.

basis for all further investigations presented in this thesis. The data reveal an intriguing oscillatory behavior, transferring the atoms between both two-particle states back and forth. This directly proves the coherent nature of the spin-changing collision process. Furthermore, the absence of coherent oscillations in the spin state  $m = 5/2$  underlines the fermionic character of the system since the corresponding two-particle state is Pauli blocked.

Comparing the data to calculations solving the two-particle Hamiltonian 4.7 (see inset in Fig. 4.6), a very good agreement of the spin-oscillation frequency is found. The oscillation amplitude, however, being approximately only 35% is significantly below the theoretically expected value. This deviation results from the global spin occupation measurement, where singly and doubly occupied sites contribute to the signal. As another observation, the oscillations are damped with a rate of approximately 15 Hz, and an incoherent increase of the spin states  $m = 5/2$  and  $m = -1/2$  is also visible. Finite tunneling explains these effects and relates the observed two-body dynamics to the many-body regime. This will be discussed in detail in section 4.3.

To record spin dynamics exclusively on the doubly occupied sites, the detection has to distinguish between the singly and the doubly occupied part of the system. Therefore, a so-called black-out-pulse technique was implemented. A similar approach has been employed in bosonic systems [74, 75], which was adapted to fermions in optical lattices. The corresponding procedure is sketched in Fig. 4.7 A. At first, the atoms prepared in the state  $|7/2, 3/2\rangle$  evolve at low magnetic field under spin-changing collisions for half a spin-oscillation period. The corresponding magnetic field is chosen such that a maximum spin-oscillation amplitude is achieved, which transfers the doubly occupied sites into the spin configuration  $|9/2, 1/2\rangle$  (see section 4.2.3). At the same time, the singly occupied sites remain in the initial spin states, either  $m = 7/2$  or  $m = 3/2$ .

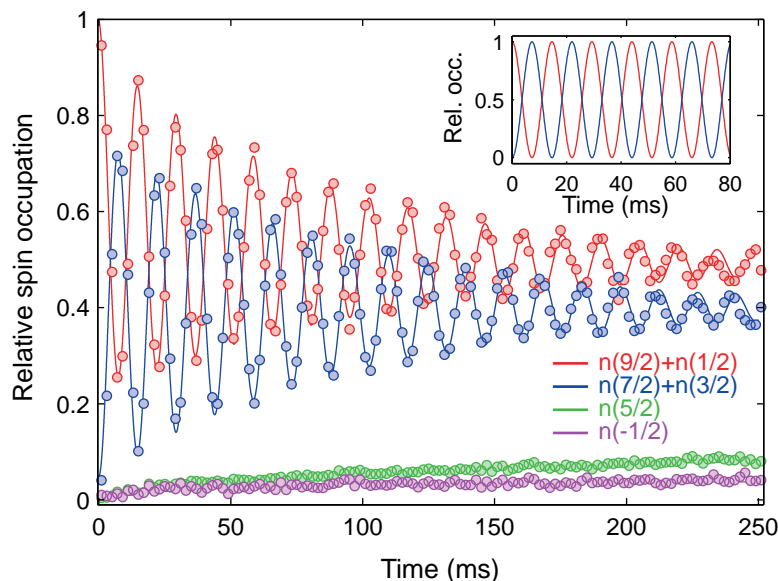


**Figure 4.8: Observation of high-contrast spin oscillations.** Relative occupations of the spin states  $n(m)$  are depicted as a function of time. Solid lines are fits to the data using equation C.1. The magnetic field is  $B = 0.19$  G and the lattice depth  $V_L = 35 E_r$ . Note the high contrast of about 70 %, revealing coherent oscillations for 250 ms. In the inset the time evolution calculated by solving Hamiltonian 4.7 is depicted. Experimental data have also been published in [5].

The outcome of this procedure is a locally occupation-dependent spin configuration. Subsequently, the dynamics are stopped by switching the magnetic field to  $B = 1.69$  G, where spin-changing collisions are suppressed. After a waiting time of 5 ms, linearly-polarized microwave pulses with a duration between  $35 - 50 \mu\text{s}$  transfer the atoms on singly occupied sites into the  $f = 7/2$  manifold. The pulses are resonant for the spin states  $m = 7/2, 5/2, 3/2, -1/2$  and account for first-order tunneling processes (see section 4.3). In the upper hyperfine manifold the atoms are not resonant with the detection light and hence not visible in the absorption images. Subsequently, the magnetic field is switched back to a low value. This again initializes spin dynamics, now from a very pure state, where all atoms contributing to the signal are exclusively on doubly occupied sites (see Fig. 4.7 B).

The time evolution of the spin occupations recorded from such an experiment is depicted in Fig. 4.8. The data show high-contrast spin oscillations with an amplitude of about 70 %, where coherent dynamics are observed for 250 ms. Note that the black-out-pulse technique leads to an initially reversed spin configuration, starting the dynamics from  $|9/2, 1/2\rangle$ . A very good agreement between the experimental data and two-body calculations is found, depicted in the inset of Fig. 4.8. The obtained amplitude exceeds the values observed in the experiments with bosons [74], but remains below the predicted full transfer. This can be mainly attributed to tunneling during the black-out-pulse procedure, which will be discussed in section 4.3. Moreover, spatial correlations inducing slightly different shapes of the on-site wave functions are a possible explanation for the decreased oscillation amplitude [180].

### 4.2.3 A fermionic spin resonance

Two-particle spin dynamics as demonstrated above are governed by the interplay between two energy scales: the differential interaction and the differential Zeeman energy. This has been studied with bosonic systems [74, 79, 80] and allowed for the determination of fundamental scattering parameters. It is a natural step to investigate this feature also for the fermionic system.

The interplay between both energy scales is illustrated in Fig. 4.9 A and can be understood in the following way: For increasing magnetic field, the interaction energy remains constant while the differential Zeeman energy increases quadratically. Therefore, the Zeeman energy dominates at large magnetic fields and the atoms are pinned to a fixed spin. In this so-called polarized regime, spin-changing collisions are off-resonant due to the large detuning between the two-particle states. In contrast, at low magnetic fields both energy scales are comparable. In this depolarized regime, large-amplitude spin oscillations can occur.

To demonstrate this general behavior, spin-dynamics experiments such as in Fig. 4.8 have been performed at different magnetic fields. The result is depicted in Fig. 4.9 B, clearly revealing the off-resonant behavior in the Zeeman regime.

For more insight into the crossover from the depolarized to the polarized regime, it is instructive to rewrite the on-site interaction in terms of the total-spin scattering lengths  $a_F$ . This yields the total-spin-dependent interaction  $U_F$ , given by

$$U_F = \frac{4\pi\hbar^2}{m} a_F \int d\mathbf{r} |w(\mathbf{r})|^4. \quad (4.12)$$

It is related to the spin-dependent interaction  $U_{m_1 m_2 m_3 m_4}$  by the Clebsh-Gordon coefficients. The resulting two-body Hamiltonian 4.7 then reads

$$\mathcal{H}_{2\text{body}} = \Delta U_{8,6} \begin{pmatrix} 0 & \sqrt{6}/5 \\ \sqrt{6}/5 & 1/5 \end{pmatrix} - qB^2 \begin{pmatrix} 0 & 0 \\ 0 & 6 \end{pmatrix}. \quad (4.13)$$

Here,  $\Delta U_{8,6} = U_8 - U_6$  is the differential interaction energy in terms of the total-spin scattering lengths. For this representation, the analytical expression for the quadratic Zeeman energy (equation 2.7) is employed and the offset energy  $U_{9/2,1/2,9/2,1/2} - 41/2qB^2$  is subtracted.

The Hamiltonian 4.13 has a Rabi-like form, where the magnetic field acts as detuning and the spin-changing collisions as coupling elements. In analogy to this, one can derive an analytical expression for the spin-oscillation frequency, given by

$$\nu(B) = \frac{1}{5 \cdot \hbar} \sqrt{(\Delta U_{8,6} - 30 \cdot q \cdot B^2)^2 + 24 \cdot \Delta U_{8,6}^2}, \quad (4.14)$$

and for the spin-oscillation amplitude, given by

$$A(B) = \frac{24 \cdot \Delta U_{8,6}^2}{(\Delta U_{8,6} - 30qB^2)^2 + 24 \cdot \Delta U_{8,6}^2}. \quad (4.15)$$

In this notation, the interplay between interaction and Zeeman energy is evident. At large magnetic fields, the frequency approaches the quadratically increasing differential Zeeman energy, while the amplitude vanishes. An interesting situation appears, when both energy scales are equal, which corresponds to  $30qB^2 = \Delta U_{8,6}$ . In this case, the

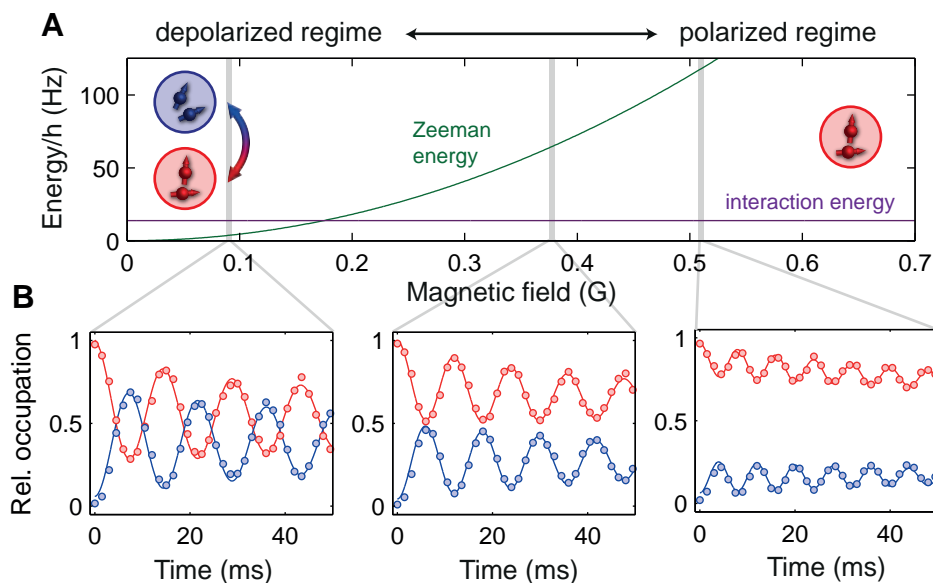


**Figure 4.9: Crossover from the depolarized to the polarized regime.** (A) Interaction and magnetic energy are plotted as a function of the magnetic field, illustrating the polarized and the depolarized regime. (B) Spin oscillations are shown for the same parameters as in Fig. 4.8 but for different magnetic fields as indicated in the figure. In the polarized regime, the spin oscillations are off-resonant, yielding high frequencies and small amplitudes. Only in the depolarized regime, large-amplitude spin oscillations occur.

system exhibits a Rabi-type spin resonance, reflected in resonant spin oscillations with a maximum amplitude and a minimum frequency. Note that a spin resonance at finite magnetic field only appears in a pseudo-spin 3/2 system, while in real spin 3/2 systems the resonance is located at zero magnetic field [158]. In this case, microwave dressing allows to artificially shift the resonance position, which has been demonstrated for bosonic systems [183].

To observe a fermionic spin resonance, the spin-oscillation measurements have been repeated for several magnetic fields, above and below the expected resonance position. The frequency and the amplitude of the spin oscillations are determined by fitting a multi-component damped oscillatory function to the data (see appendix C for details). Figure 4.10 depicts the outcome of this analysis. As an important result, a clear spin resonance feature is found for fermionic atoms, evident in the data zoom in the inset of Fig. 4.10. For higher magnetic fields, the system approaches the polarized regime and the spin oscillations vanish.

In a next step, these data have been compared with the formulas for frequency and amplitude from the two-particle model (equation 4.14 and 4.15). The amplitude is rescaled with a global factor of  $\alpha=0.69$  to account for the imperfect black-out-pulse procedure. With the differential interaction  $\Delta U_{8,6}$  as the only free parameter, the resonance position is determined at  $B=0.186$  G. As a key result, this demonstrates that the two-particle model captures the scattering behavior of the spin 3/2 system.

Moreover, the set of experiments presented above also allows to quantitatively extract fundamental scattering parameters [75]. Note that the spin resonance is uniquely

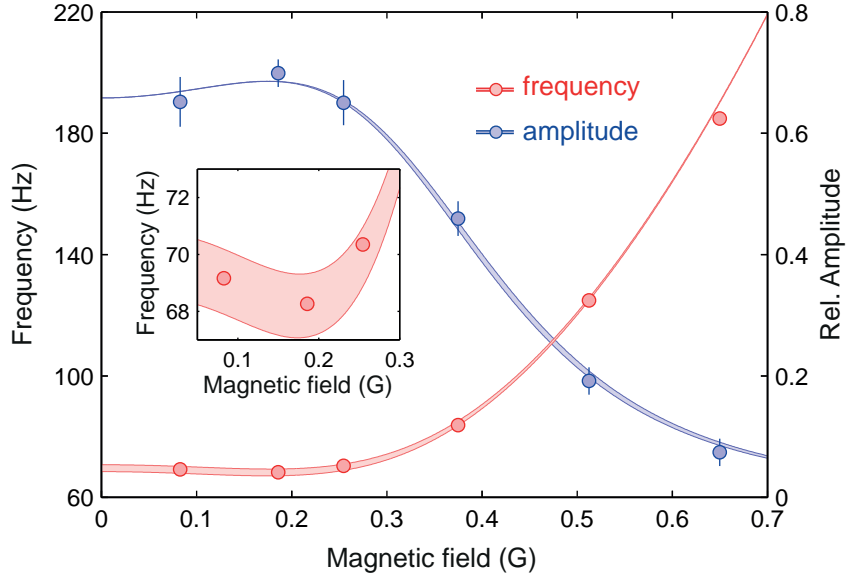


**Figure 4.10: A fermionic spin resonance.** Frequency (red) and amplitude (blue) are depicted as a function of the magnetic field. The same parameters as in Fig. 4.8 are used but for different magnetic fields. Data points are extracted from the spin oscillations by fitting equation C.1. Error bars correspond to fit errors and represent two standard deviations. Red and blue lines are calculations from the two-body model (equation 4.7). The width of the curves reflects the uncertainty of the lattice depth calibration. The inset shows a zoom into the spin-resonance regime. Experimental data have also been published in [5].

defined by the total-spin-dependent interaction  $\Delta U_{8,6}$ . In consequence, knowing the lattice depth and the magnetic field, the position and frequency of the spin resonance are directly connected to the differential total-spin-dependent scattering length  $\Delta a_{8,6} = a_8 - a_6$ . This provides a high-precision test for the calculations of the scattering lengths [117] (see section 2.2.2) and allows to directly compare the experimentally obtained with the calculated value:

**Experiment:**  $\Delta a_{8,6} = 2.26 \pm 0.07 a_B$

**Calculation:**  $\Delta a_{8,6} = 2.53 a_B$

This agreement is found without free parameters, which demonstrates the capability of spin-changing collisions to extract fundamental scattering parameters from a high-spin system [75]. The deviations between experiment and theory are about 10% and can be attributed to the following reasons: First, the theoretical error of the coupled-channel calculations is unknown [117], such that both results may be well consistent within the error bars. Deviations caused by systematic errors have been estimated, including the magnetic field uncertainty and the lattice depth. They lead to small corrections ( $\pm 0.01 a_B$  for the magnetic field and  $\pm 0.04 a_B$  for the lattice depth) and are unlikely to be the dominating errors in this measurement. Another error source could be the assumption of uncorrelated Wannier functions on each lattice site, which relate the interaction parameter  $U_F$  to the total-spin dependent scattering length  $a_F$ . Interaction-induced correlations, however, are predicted to affect the on-site wave function, which

in turn also effectively changes the on-site interaction [180]. The spatial deformation should decrease the on-site interaction, which would lead to an improved match between theory and experiment.

#### 4.2.4 Coherent multi-flavor spin dynamics

The pseudo-spin  $3/2$  system is well suited to demonstrate the feasibility of fermionic spin-changing collisions. The fermionic character is reflected in the blockade of specific collision channels due to the Pauli exclusion principle, which is beyond experiments with bosonic  $^{87}\text{Rb}$  atoms [74].

Another unique property of  $^{40}\text{K}$  is its large spin of  $f = 9/2$ . This allows for the realization of multi-flavor spin systems with up to five two-particle states involved. As a special feature, this system is governed by spin-changing collisions including high-collision quanta ( $\Delta m > 1$ ). So far, experiments with more than two involved levels have been performed with  $^{87}\text{Rb}$  ( $f = 2$ ) [74, 79] and  $^{52}\text{Cr}$  ( $f = 3$ ) [84]. However, high-collision quanta have not been observed in these systems. Here, I present experiments exploiting the full spin of  $^{40}\text{K}$ .

#### Spin 9/2 system

The largest spin system of  $^{40}\text{K}$  corresponds to a total magnetization of  $M = m_1 + m_2 = 0$ . It includes five two-particle states:  $|\pm 1/2\rangle$ ,  $|\pm 3/2\rangle$ ,  $|\pm 5/2\rangle$ ,  $|\pm 7/2\rangle$  and  $|\pm 9/2\rangle$ , where the notation  $|+m, -m\rangle = |\pm|m\rangle$  is used. A sketch of the five-level system is provided in Fig. 4.11 A.

Beyond the two-level system, the complex coupling structure involves ten different spin-changing collision channels (see Fig. 4.11 B), including high-collision quanta. The largest possible spin transfer with  $\Delta m = 4$  reflects collisions, which couple the two-particle states  $|\pm 1/2\rangle$  and  $|\pm 9/2\rangle$ . This complex multi-flavor spin system naturally raises the question whether the coherence of the collision process demonstrated in the two-level system is preserved.

As for the two-level system, it is suitable to choose a basis consisting of the involved two-particle states

$$\mathcal{B}_{M=0} = \{|\pm 9/2\rangle, |\pm 7/2\rangle, |\pm 5/2\rangle, |\pm 3/2\rangle, |\pm 1/2\rangle\}, \quad (4.16)$$

which form a five-dimensional subspace. In this basis, the interaction Hamiltonian is given by:

$$\mathcal{H}_I = \begin{pmatrix} U_{\pm 9/2, \pm 9/2} & U_{\pm 9/2, \pm 7/2} & U_{\pm 9/2, \pm 5/2} & U_{\pm 9/2, \pm 3/2} & U_{\pm 9/2, \pm 1/2} \\ U_{\pm 7/2, \pm 9/2} & U_{\pm 7/2, \pm 7/2} & U_{\pm 7/2, \pm 5/2} & U_{\pm 7/2, \pm 3/2} & U_{\pm 7/2, \pm 1/2} \\ U_{\pm 5/2, \pm 9/2} & U_{\pm 5/2, \pm 7/2} & U_{\pm 5/2, \pm 5/2} & U_{\pm 5/2, \pm 3/2} & U_{\pm 5/2, \pm 1/2} \\ U_{\pm 3/2, \pm 9/2} & U_{\pm 3/2, \pm 7/2} & U_{\pm 3/2, \pm 5/2} & U_{\pm 3/2, \pm 3/2} & U_{\pm 3/2, \pm 1/2} \\ U_{\pm 1/2, \pm 9/2} & U_{\pm 1/2, \pm 7/2} & U_{\pm 1/2, \pm 5/2} & U_{\pm 1/2, \pm 3/2} & U_{\pm 1/2, \pm 1/2} \end{pmatrix}. \quad (4.17)$$

It contains all collision processes, which are sketched in Fig. 4.11 B. These are represented by off-diagonal elements, while diagonal elements correspond to the spin-conserving interaction energies. The system provides four spin-changing collision channels with  $\Delta m = 1$ , three channels with  $\Delta m = 2$ , two channels with  $\Delta m = 3$  and one

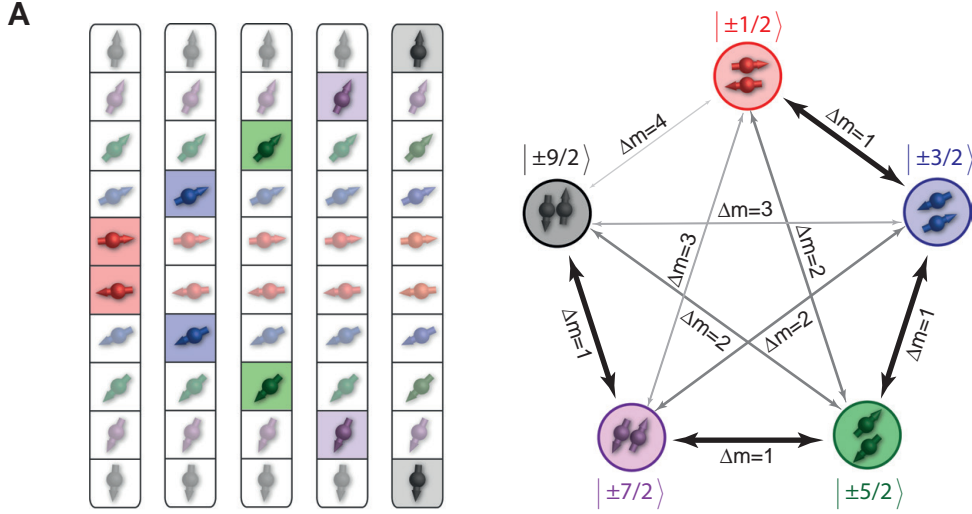


**Figure 4.11: The multi-flavor spin 9/2 system.** (A) The contributing two-particle states are sketched. Colored boxes represent the two-particle states, forming a five-level system. Magnetization conservation restricts the number of involved levels. (B) Possible multi-flavor spin couplings are shown. Circles represent the five involved two-particle states. They are coupled by ten different collision channels with  $\Delta m = 1, 2, 3, 4$ , indicated with arrows. The width of the arrows illustrates the coupling strength.

channel with  $\Delta m = 4$ . Inserting the numbers of the scattering lengths (see Table 2.2), the Hamiltonian yields

$$\mathcal{H}_I = \frac{4\pi\hbar^2}{m} \int d\mathbf{r} |w(\mathbf{r})|^4 \begin{pmatrix} 145.77 & 11.18 & -6.48 & 4.50 & -3.69 \\ 11.18 & 154.12 & 10.19 & -6.99 & 5.83 \\ -6.48 & 10.19 & 156.23 & 10.86 & -8.78 \\ 4.50 & -6.99 & 10.86 & 155.66 & 13.40 \\ -3.69 & 5.83 & -8.78 & 13.40 & 151.62 \end{pmatrix} a_B. \quad (4.18)$$

Again compared to the two-level system, the coupling (off-diagonal) elements are strong. This is the case in particular for spin-changing couplings with  $\Delta m = 1$ , which are approximately 8% of the interaction energy. The coupling for  $\Delta m = 2, 3, 4$  collisions continuously decreases, but even for  $\Delta m = 4$  it is about 2% of the interaction energy. The origin of this pronounced coupling strength arises from the contribution of all total-spin scattering lengths. Especially the pronounced differences in the collision channels  $F = 0, 2, 4$  (see section 2.2.2) favor the exceptional coupling and render the five-level system an ideal candidate to study complex multi-flavor spin dynamics.

The Zeeman Hamiltonian of the system is given by:

$$\mathcal{H}_Z = \begin{pmatrix} E_Z^{\pm 9/2}(B) & 0 & 0 & 0 & 0 \\ 0 & E_Z^{\pm 7/2}(B) & 0 & 0 & 0 \\ 0 & 0 & E_Z^{\pm 5/2}(B) & 0 & 0 \\ 0 & 0 & 0 & E_Z^{\pm 3/2}(B) & 0 \\ 0 & 0 & 0 & 0 & E_Z^{\pm 1/2}(B) \end{pmatrix}. \quad (4.19)$$

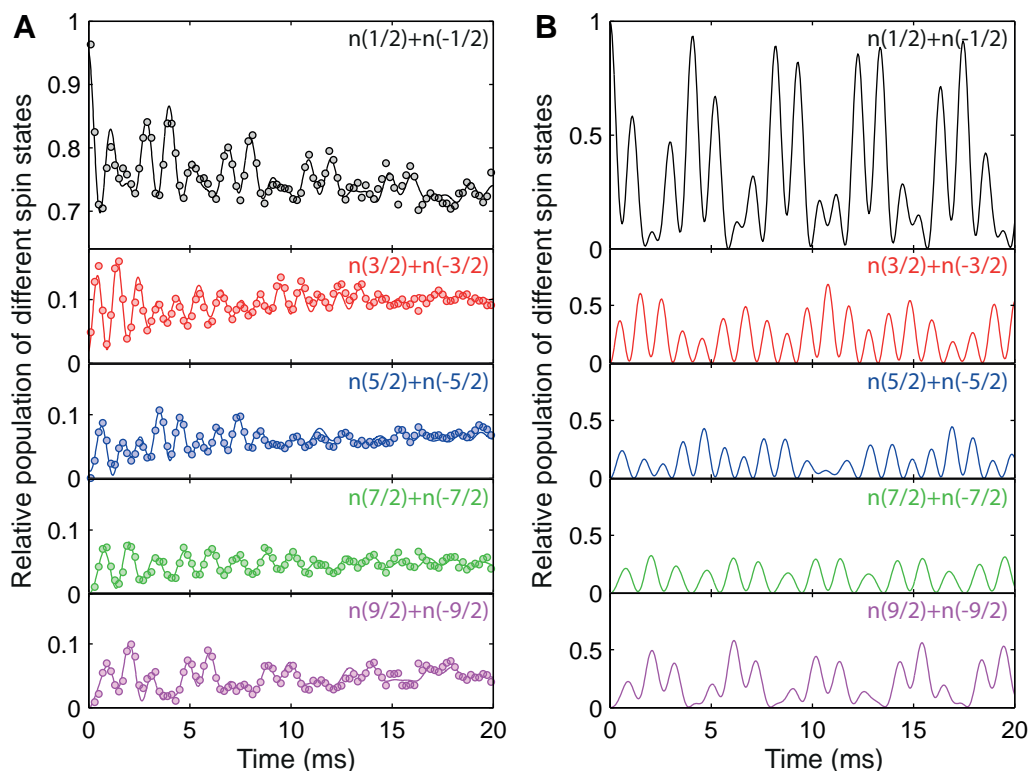


**Figure 4.12: Coherent multi-flavor spin dynamics in the spin 9/2 system.** (A) The relative populations  $n(m)$  of the two-particle states  $|\pm 1/2\rangle$ ,  $|\pm 3/2\rangle$ ,  $|\pm 5/2\rangle$ ,  $|\pm 7/2\rangle$ , and  $|\pm 9/2\rangle$  are plotted as a function of time. Solid lines are fits to the data using equation C.1. The lattice depth is  $V_L = 25 E_r$  and the magnetic field  $B = 0.372$  G. Experimental data have also been published in [5]. (B) The time evolution of the spin dynamics in A is calculated without free parameters by diagonalizing the two-body Hamiltonian 4.7.

In contrast to the two-level case, there is no analytical solution for the two-body Hamiltonian 4.7 of the five-level system. However, it can be numerically diagonalized.

### Five-level dynamics

To investigate the five-level system and its multi-flavor spin dynamics experimentally, the binary spin mixture  $m = \{\pm 1/2\}$  is loaded into a deep 3d optical lattice of  $V_L = 25 E_r$ . This spin mixture has the lowest magnetic energy and can be well evaporated (see section 3.2.3). The following procedure is the same as for the two-level system, which allows to monitor spin dynamics at low magnetic field.

Typical spin dynamics of the five-level system are depicted in Fig. 4.12 A. The data reveal a complex oscillatory behavior, involving all five two-particle states. As an important result, the coherent nature of the collision process is preserved in the multi-flavor system despite the large effective spin. The observed dynamics show pronounced beat notes, clearly visible in the oscillatory signal. This indicates that several frequencies and also several eigenstates are participating in the spin-changing dynamics. Note that in contrast to the two-level case, where two eigenstates contributed and a single frequency

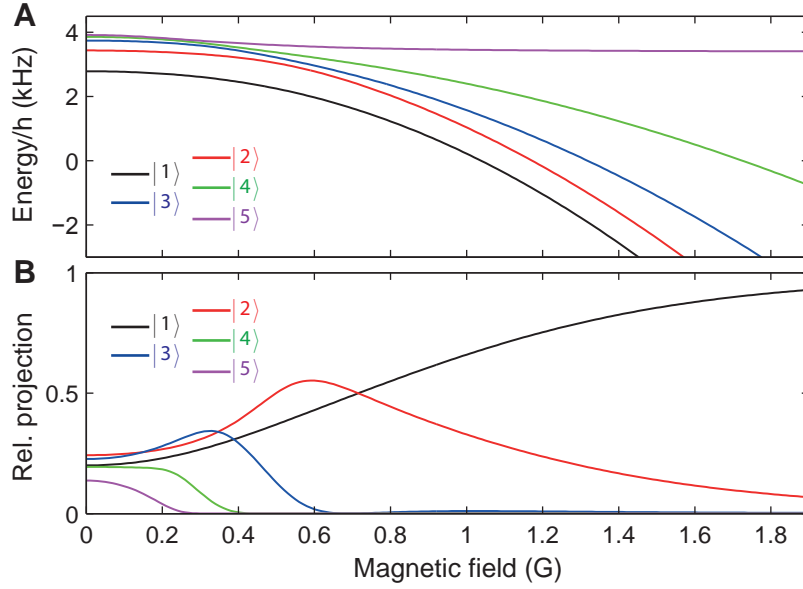


**Figure 4.13: High-spin interactions at the crossover to the depolarized multi-flavor regime.** (A) Calculated eigenenergies of the five eigenstates  $|n\rangle$  are depicted as a function of the magnetic field. (B) The overlap integral  $|\langle n|\pm 1/2\rangle|^2$  of the initial two-particle state  $|\pm 1/2\rangle$  with the eigenstates  $|n\rangle$  is shown versus the magnetic field. The calculations are performed solving the two-body Hamiltonian (equation 4.7).

was observed, five eigenstates and ten frequencies are available in the five-level system.

A comparison of the observed spin dynamics to calculations solving the two-body Hamiltonian 4.7 is provided in Fig. 4.12 B. Without free parameter, the numerical results show a good agreement. The observed amplitude, however, is significantly smaller compared to the calculations. This can be attributed to the number of atoms on doubly occupied sites, which is calculated to be approximately 30% [182]. Note that the black-out-pulse technique cannot be easily applied to this system since full-amplitude spin oscillations do not occur. Moreover, due to the high spin-oscillation frequencies ( $\approx$  kHz), the switching of the magnetic field ( $\approx 500 \mu\text{s}$ ) imprints small individual phases on the spin oscillations, which also leads to the deviations. However, this does not affect the contributing spin-oscillation frequencies. Therefore, this measure is ideally suited for a more detailed comparison with two-particle scattering model.

#### 4.2.5 Crossover to depolarized multi-flavor spin dynamics

Beyond the two-level system, the multi-flavor spin dynamics of the five-level system are governed by the interplay between several interaction and magnetic energies, originating from the couplings of the involved two-particle states. In general, this leads to complex dynamics even for an isolated atom pair (see Fig. 4.12 A). For a better understanding of this high-spin feature, the crossover from the interaction-dominated to the Zeeman-dominated regime has been studied.

First, some instructive calculations are presented. The energy spectrum, calculated from the two-body Hamiltonian 4.7, is depicted for different magnetic fields in

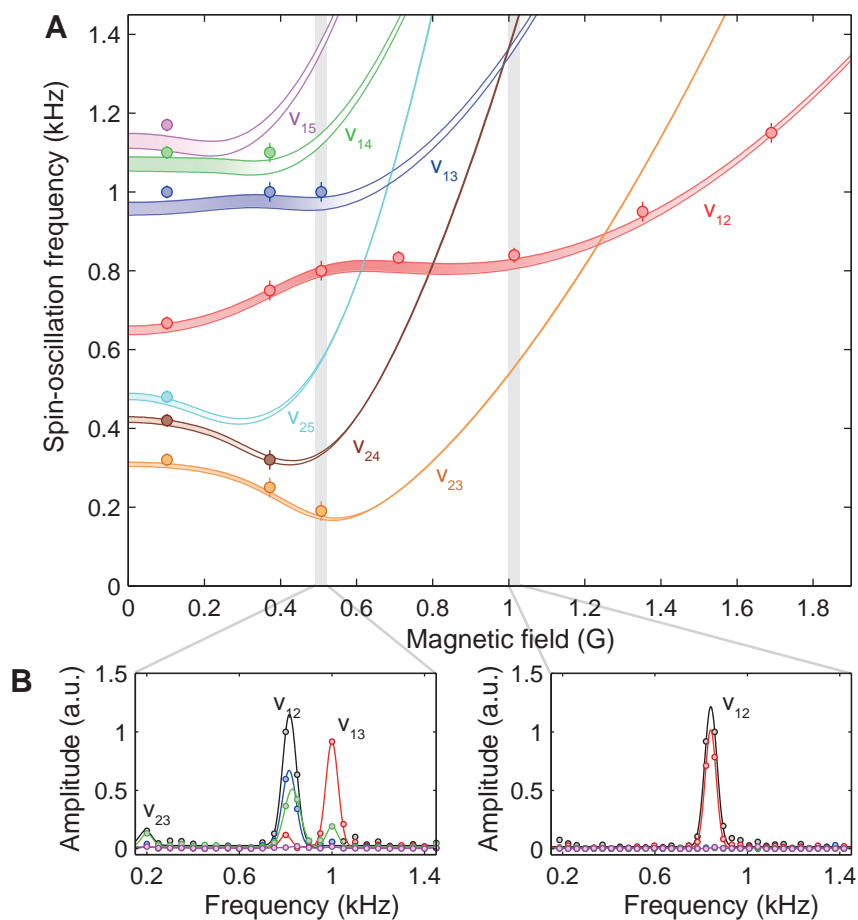


**Figure 4.14: Crossover to the depolarized multi-flavor regime.** (A) Spin-oscillation frequencies, obtained with a Fourier analysis, are depicted versus the magnetic field. The same parameters as in Fig. 4.12 are employed for different magnetic fields. Error bars result from finite Fourier sampling. Curves show numerical results from 4.7. The width is given by the uncertainty of the lattice calibration, and the shading is proportional to the transition strength, given by  $|\langle n|\pm 1/2\rangle|^2$ . (B) Typical Fourier spectra of spin populations at  $B = 0.372$  G and  $B = 1.014$  G are shown. Experimental data have partly been published in [5].

Fig. 4.13 A. In general, one expects up to ten spin-oscillation frequencies, which can be calculated from the eigenenergy differences. Moreover, the number of significantly contributing eigenstates is shown in Fig. 4.13 B for different magnetic fields. Depicted is the overlap integral  $|\langle n|\pm 1/2\rangle|^2$  of the initial two-particle state with all five eigenstates  $|n\rangle$ . At large magnetic fields, the initial state coincides with the eigenstate of the system to a large extent and spin dynamics is suppressed. Decreasing the magnetic field, more and more eigenstates are continuously admixed, which leads in turn to more contributing spin-oscillation frequencies.

To compare these considerations to the experiment, spin dynamics of the five-level system have been studied at different magnetic fields. The contributing oscillation frequencies have been extracted from experimental signals such as in Fig. 4.12 with a Fourier analysis. The result of this study is depicted in Fig. 4.14 A. As a central result, the amount of significantly contributing frequencies increases for decreasing magnetic

field. This is evident in the Fourier spectra of the spin dynamics, which are exemplarily depicted in Fig. 4.14B for two different magnetic fields.

The comparison with the theory shows that seven out of ten possible frequency branches can be precisely reproduced. Missing frequency branches have only small contributions, mainly below spin-oscillation frequencies of 200 Hz, and cannot be unambiguously resolved. This is due to experimental limitations such as finite observation time as well as sampling and damping of the spin oscillations.

In general, the experimental data are in very good agreement with the calculations as in the two-level case. This underlines that the multi-flavor spin system with its rich dynamics can also be well understood in terms of the two-particle scattering model. Note that the calculations are performed without free parameters, which validates in addition the values of the total-spin scattering lengths, provided by T. Hanna. The small deviations between theory and experiment can be attributed to numerical uncertainties of these values [117].

As a direct result from these experiments, the magnetic field provides an intriguing tuning knob for the effective spin of the system. At large magnetic fields, the binary mixture remains stable, corresponding to an effective spin of 1/2. Tuning the magnetic field to lower values continuously increases the number of contributing eigenstates. Hence, the spin dimensionality of the system continuously increases. This allows to tune the system from an effective spin 1/2 to an effective spin 9/2 system.

In contrast to the two-level system, where a clear spin resonance feature was observed (see section 4.2.3), the situation is more involved in the five-level case. All collision processes, associated with different magnetic and interaction energies, can individually exhibit a spin resonance, depending on the sign of interaction and Zeeman energy. The complex coupling mechanism does not allow to clearly identify a single resonance. It is more convenient to interpret this behavior as a multi-level spin-resonance feature, where parts of the Hamiltonian show resonant features leading to pronounced deformations of the spectrum.

#### 4.2.6 Observation of high-collision quanta

As worked out above, the high-spin system should involve collision processes with  $\Delta m = 1, 2, 3, 4$ . Collisions with  $\Delta m > 1$  have not been observed so far, neither in optical lattices nor in bulk systems [67, 68, 74, 79]. The experimental observation of seven spin-oscillation frequencies itself also does not prove that spin-changing processes with  $\Delta m = 2, 3, 4$  are contributing to the dynamics. This motivates a more detailed study of the two-body Hamiltonian 4.7 to address the role of high-collision quanta in the multi-flavor spin dynamics.

Therefore, calculations have been performed, where specific collision channels were excluded. The impact on the resulting energy spectrum has been studied. Numerically, this can be implemented by setting the corresponding matrix element  $U_{m_1, m_2, m_3, m_4}$  in the interaction Hamiltonian 4.18 to zero. In Fig. 4.15, the experimentally observed frequencies are compared to spectra, calculated for different situations: First, all spin-changing channels are considered, yielding a very good agreement with the experiments (see Fig. 4.15 A). However, the exclusion of collision channels induces strong deviations. In Fig. 4.15 B, channels with  $\Delta m = 4$  are excluded, which leads to a considerable distortion of the involved frequency branches. The deviations become even more pronounced, when more collision channels are excluded ( $\Delta m = 3, 4$  in Fig. 4.15 C and  $\Delta m = 2, 3, 4$

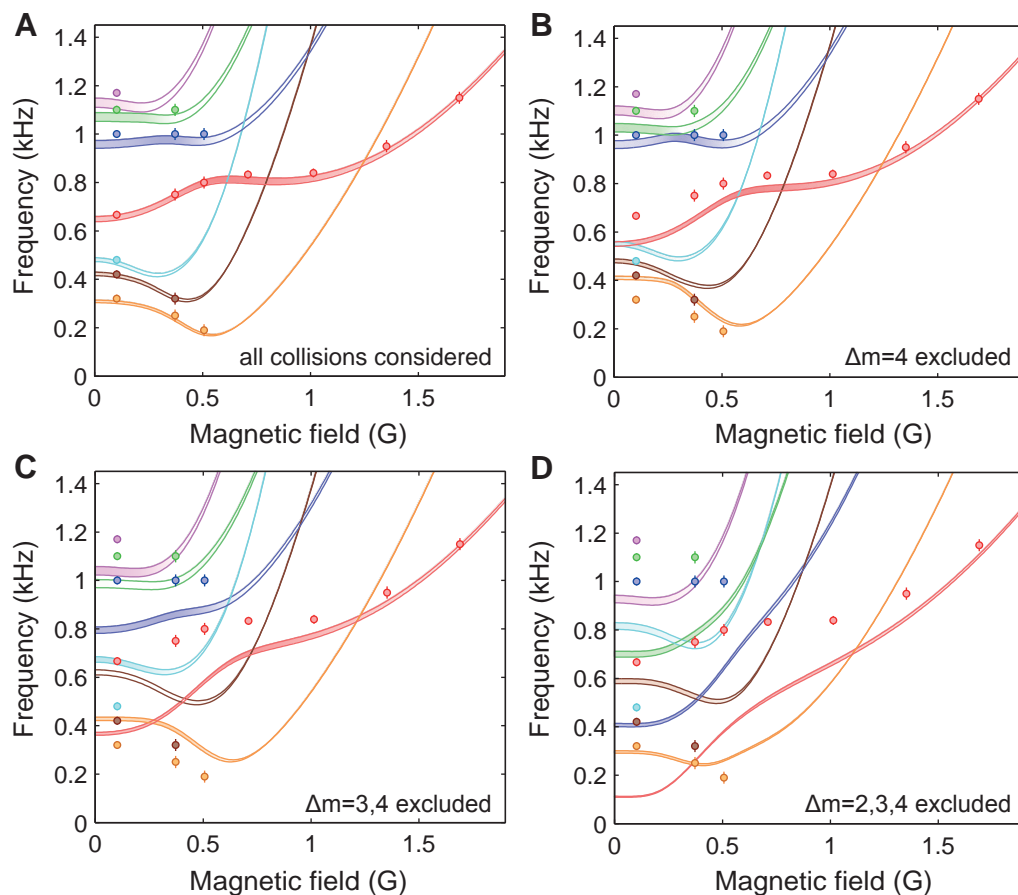


**Figure 4.15: Spectra for different spin-exchange processes.** Calculated energy spectra are depicted, compared to the experimental data from Fig. 4.14. The colors are also assigned in the same way. Specific collision channels are excluded: In (A), all ten coupling elements are considered. Significant deviations appear already when  $\Delta m = 4$  processes are neglected (B). When spin-changing collisions with  $\Delta m = 3, 4$  (C) and  $\Delta m = 2, 3, 4$  (D) are excluded, strong deviations are found.

in Fig. 4.15D).

As an important result, this demonstrates that collision processes with high-collision quanta provide a significant contribution to the high-spin dynamics. Obviously, only the full interaction Hamiltonian 4.18 describes the observed spin dynamics quantitatively, and each neglected collision process alters the result considerably. Only in the limit of large magnetic fields, where the dynamics is strongly dominated by  $\Delta m = 1$  collisions, high-collision quanta play a minor role.

This constitutes the first observation of coherent high-magnetization exchange in ultracold quantum gases, mediated by high-spin interactions. Note that the collision properties in this case are still dominated by  $\Delta m = 1$  collisions. A similar situation will be presented for spin-changing lateral collisions in the many-body regime (see section 6.4.3). Beyond this, an experiment with harmonically trapped fermions will be shown in section 5.4.5, where the dominating collision channel could be tuned to  $\Delta m = 2$ .

### 4.3 Spin dynamics at finite lattice depth

Spin dynamics in deep optical lattices are ideal candidates to gain deep insight into the local high-spin interaction process [5, 74, 75]. The multi-flavor spin dynamics, demonstrated in the last section, can be well understood in terms of a two-body scattering model. In this approach, the colliding atom pair is assumed to be perfectly isolated on its lattice site.

Finite tunneling, however, induces an intriguing interplay between spin and spatial degrees of freedom. Most important in this context are the corresponding time scales. In the two-body limit, established in deep optical lattices, spin-changing collisions occur at a higher rate than tunneling events. However, in shallow optical lattices, the tunneling time can become comparable and even exceed the time scale of spin dynamics. In this many-body regime, the fermionic character has a pronounced influence on the global dynamics of the system. While Pauli blocking excludes only specific spin-collision channels in the two-body limit, it is in particular important for the interplay between spin and spatial dynamics in the many-body limit. This naturally raises the question, to which extent the global properties of fermionic lattice systems are affected by microscopic spin-changing collisions.

In this section, I will present a study of spin dynamics in optical lattices in the presence of tunneling. The dominating tunneling processes and their impact on the dynamics will be discussed. In a first approach, tunneling will be investigated as a small perturbation on the two-particle dynamics, which can be qualitatively understood within a first-order tunneling model. As a key result, I will study the crossover from the two-body to the many-body regime, where a novel instability of the band insulator has been observed.

#### 4.3.1 Multi-site spin dynamics

Multi-site spin dynamics, including spin-changing collisions and tunneling, are described by the full high-spin Hubbard Hamiltonian 4.6. Sophisticated methods such as Density Matrix Renormalization Group (DMRG) [184] and Dynamical Mean-Field Theory (DMFT) [181] allow for a theoretical treatment for example of ground-state properties.

However, several effects can be already understood in terms of small-scale systems. As a starting point, a two-well model is employed in the following, where two wells are coupled by the tunneling matrix element  $J$ . Based on the experiments in the pseudo-spin 3/2 system, we consider six possible spin states ( $m = -1/2, \dots, 9/2$ ), which were significantly occupied in the corresponding experiments (see section 4.2.2). It is suitable to employ a two-well basis, which can be written as

$$\left| n_L^{-1/2}, n_L^{1/2}, n_L^{3/2}, n_L^{5/2}, n_L^{7/2}, n_L^{9/2} \right\rangle_L \otimes \left| n_R^{-1/2}, n_R^{1/2}, n_R^{3/2}, n_R^{5/2}, n_R^{7/2}, n_R^{9/2} \right\rangle_R. \quad (4.20)$$

Here, the indices L and R account for the left and right well, respectively.

In this two-well model, it turns out that the combination of spin dynamics and tunneling has two important consequences: First, it leads to local spin fluctuations ( $M_L \neq M_R$ ), while only the global magnetization  $M_{\text{tot}} = M_L + M_R$  is conserved. Moreover, density fluctuations can be induced, e.g., when triply occupied sites are formed out of three different spin states. Starting from these considerations, several tunneling processes can be distinguished:

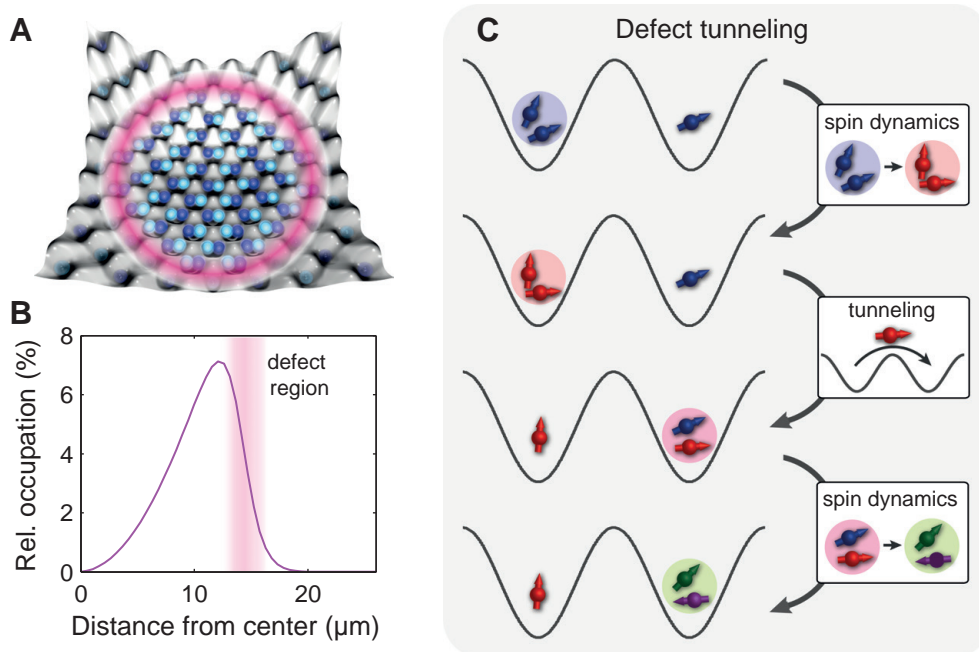


**Figure 4.16: Sketch of tunneling at defects.** (A) The spatial distribution of the system is sketched. The outer part of the band insulator is highlighted, comprising most of the defects. (B) The relative occupation of the 3d system is shown, where the shaded area indicates the defect-dominated region. (C) A typical defect tunneling process is sketched. Starting from a doubly occupied site adjacent to a singly occupied site, the interplay between spin-changing collisions and tunneling leads to the formation of new spin states. The spin states are illustrated as in Fig. 4.5.

### Tunneling at defects

First of all, defects (singly occupied sites) in the two-component band insulator allow for tunneling. Note that the underlying harmonic confinement and finite temperatures inevitably lead to defects in the experimental system. These are mainly located at the outer region of the band insulator as illustrated in Fig. 4.16 A. Calculations of the spatial distribution reveal, that this region extends over a shell of approximately 4–5 lattice sites [182]. Due to the geometry of the system, this shell contains about 20–30% of the atoms (see Fig. 4.16 B), which underlines the importance of defect tunneling.

This process can be modeled using a spatial configuration with one doubly occupied site adjacent to one singly occupied site. An example for defect tunneling is sketched in Fig. 4.16 C. As a starting point, two particles in  $|7/2, 3/2\rangle$  occupy the left well adjacent to a defect in the spin state  $m = 3/2$ . When a spin-changing collision occurs on the doubly occupied site, all atoms are in different spin states and Pauli blocking does not prevent tunneling. A subsequent tunneling process leads to a new two-particle state on the initially singly occupied site. This two-particle state has a different total magnetization and the resulting spin dynamics involve new spin states, which were initially Pauli blocked.

Since there is a large number of possible processes, defect tunneling leads in gen-

eral to a complicated spin redistribution among several spin states and to a contrast reduction of the spin oscillation. Thereby, this process is directly linked to the amount of defects in the system and increases with the tunneling matrix element  $J$ .

### Tunneling in the core

Tunneling processes in the core of the system are not evident, since a fundamental property of a band insulator is its insulating character. All single-particle states are occupied, which typically suppresses tunneling due to the Pauli exclusion principle.

As a unique high-spin effect, it turns out that tunneling can also occur in an initial band insulator under spin-changing collisions. To understand this intriguing feature, consider two wells, which are occupied with the same two-particle state  $|7/2, 3/2\rangle$  as sketched in Fig. 4.17. This situation is described by the state

$$|0, 0, 1, 0, 1, 0\rangle_{\text{L}} \otimes |0, 0, 1, 0, 1, 0\rangle_{\text{R}} . \quad (4.21)$$

In the presence of spin-changing collisions, on-site spin dynamics couple the initial two-particle state  $|7/2, 3/2\rangle$  in each well to  $|9/2, 1/2\rangle$ . Hence, in the absence of tunneling, this is described by

$$|\psi(t)\rangle = \left( c_1(t) |0, 1, 0, 0, 0, 1\rangle_{\text{L}} + c_2(t) |0, 0, 1, 0, 1, 0\rangle_{\text{L}} \right) \otimes \left( c_1(t) |0, 1, 0, 0, 0, 1\rangle_{\text{R}} + c_2(t) |0, 0, 1, 0, 1, 0\rangle_{\text{R}} \right) , \quad (4.22)$$

where the time-dependent coefficients  $c_i(t)$  are equal for both wells. Applying the tunneling Hamiltonian to this state (here exemplarily shown for the spin state  $m = 1/2$ ) gives

$$H_{J_{1/2}} |\psi(t)\rangle = J c_1(t) c_2(t) \left( |0, 0, 0, 0, 0, 1\rangle_{\text{L}} \otimes |0, 1, 0, 1, 1, 0\rangle_{\text{R}} + |0, 1, 1, 0, 1, 0\rangle_{\text{L}} \otimes |0, 0, 0, 0, 0, 1\rangle_{\text{R}} \right) . \quad (4.23)$$

This reveals a time-dependent tunneling probability in the presence of spin-changing collisions. Only when the system is either in the spin configuration  $|7/2, 3/2\rangle$  or  $|9/2, 1/2\rangle$ , it remains insulating and tunneling is suppressed. In contrast, when the system is in a coherent superposition of both two-particle states, tunneling becomes possible. Note that this is a genuine two-body effect, since the collision process involves two particles. A single-particle spin rotation (see in 3.2.2) does not affect the band insulator.

Figure 4.17 illustrates tunneling processes, which can occur if a band insulator is exposed to spin-changing collisions. In the initial configuration, tunneling is forbidden due to Pauli blocking. As described above, tunneling becomes possible in the presence of spin-changing collisions. The following dynamics crucially depend on the interplay between the interaction energy and tunneling, leading to two different processes: First-order tunneling as illustrated in Fig. 4.17 A induces triple occupations at an energy cost of  $U$ . This process is only possible at low interactions and induces spin and density fluctuations. At large interactions, however, the system is an effectively Mott-insulating regime and only super-exchange tunneling [185] at a rate of  $J^2/U$  is possible. This process is depicted in Fig. 4.17 B and induces spin fluctuations without density fluctuations. Both tunneling processes reduce the contrast of the spin oscillations [186].

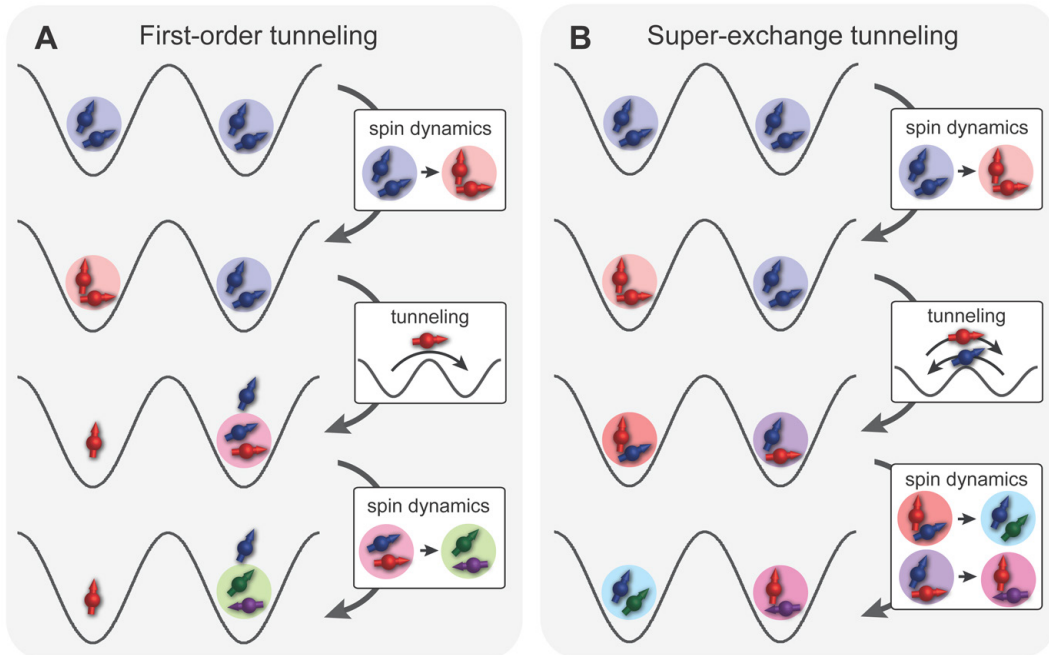


**Figure 4.17: Sketch of tunneling in the core.** Spin-changing collisions allow for finite tunneling also in the initially band-insulating system (see text). **(A)** First-order tunneling processes occur at low interactions inducing spin and density fluctuations. **(B)** Super-exchange tunneling is possible in deep optical lattices and induces only spin fluctuations. The spin states are illustrated as in Fig. 4.5.

### 4.3.2 Observation of multi-site spin dynamics

Multi-site spin dynamics can be addressed in a first approach by starting from a two-particle system with tunneling as a small perturbation. This was the case for all experiments in deep optical lattices presented in the last section. Here, a more detailed analysis of the results in the pseudo-spin 3/2 system is presented.

For these experiments the tunneling energy ( $\approx 2$  Hz) is small compared to the spin-changing energy ( $\approx 60$  Hz) and to the spin-conserving energy ( $\approx 4.5$  kHz). Therefore, tunneling in the core is suppressed: first-order tunneling by strong spin-conserving interactions and super-exchange tunneling by its very long time scale. However, defect tunneling can occur in this system.

In Fig. 4.18 A, the same experimental data as in Fig. 4.6 is depicted in the single-particle spin basis. Beyond the two-particle spin dynamics and its damping, there are two key observations: First, new spin states appear. Moreover, the damping of the spin oscillations comes alongside an asymmetric drift of the spin populations apart from each other.

These effects can be estimated in a first-order tunneling approximation. Consider the initially doubly occupied site in the two-particle state  $|7/2, 3/2\rangle$ , which is coupled to the two-particle state  $|9/2, 1/2\rangle$  by spin-changing collisions. This site is adjacent to a defect, either in the spin state  $m = 3/2$  or  $m = 7/2$ . After one tunneling process the initial spin system with the total magnetization  $M = 5$  evolves into spin systems with different total magnetizations. The spin redistribution has been calculated from

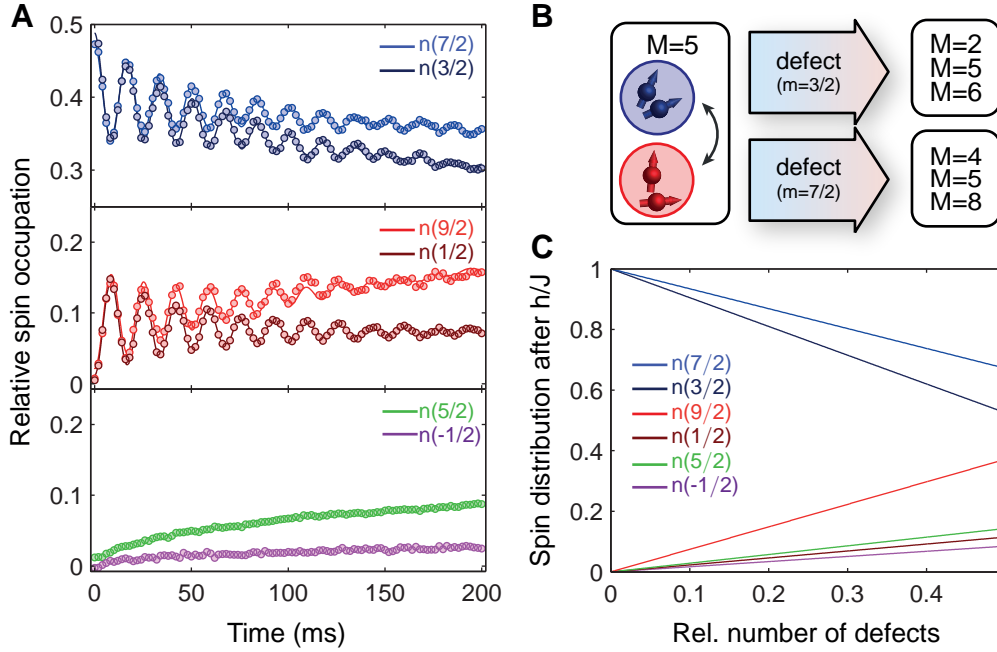


**Figure 4.18: Impact of small tunneling on the two-particle spin dynamics.** (A) Spin-oscillation data (from Fig. 4.6) are depicted in the spin-state basis. In the upper (middle) part, the spin states of the initial (second) two-particle state are shown. Lower part depicts the Pauli-blocked spin components. (B) A sketch of the involved spin systems, resulting from defect tunneling, is depicted, indicated with their total magnetization  $M$ . (C) Calculations of the spin-changing rates, employing a first-order tunneling model, are plotted versus the relative amount of defects.

all combinations, which result from one tunneling process accounting for Pauli blocking. For the defects  $m = 3/2$  and  $m = 7/2$  possible magnetizations are  $M = 2, 5, 6$  and  $M = 4, 5, 8$ , respectively (see Fig. 4.18 B). Averaging the resulting two-body dynamics allows to determine the corresponding spin-changing rates. To estimate the global spin redistribution, all possible processes have been averaged, yielding spin-changing rates for each spin component. Note that this approach is only valid for short times.

The result of this analysis is depicted in Fig. 4.18 C as a function of the amount of defects. In this context, a linear dependence is assumed, while the exact relation should depend on the specific geometry of the system. These results demonstrate that different spin states exhibit a different spin redistribution. The calculations qualitatively agree with the experimental findings. For example, the increasing amount of the spin states  $m = 9/2$  and  $m = 5/2$  is consistent with the experiments. Moreover, the decrease of the spin states  $m = 7/2$  and  $m = 3/2$  is also reproduced.

### 4.3.3 Studying the transition to the many-body regime

The experiments presented above reveal the intriguing influence of tunneling on the two-particle dynamics. This motivates a study of spin-changing dynamics also in the many-body regime, where these effects should be more pronounced. For this purpose, the depth of the optical lattice can be tuned to lower values. This allows to access a

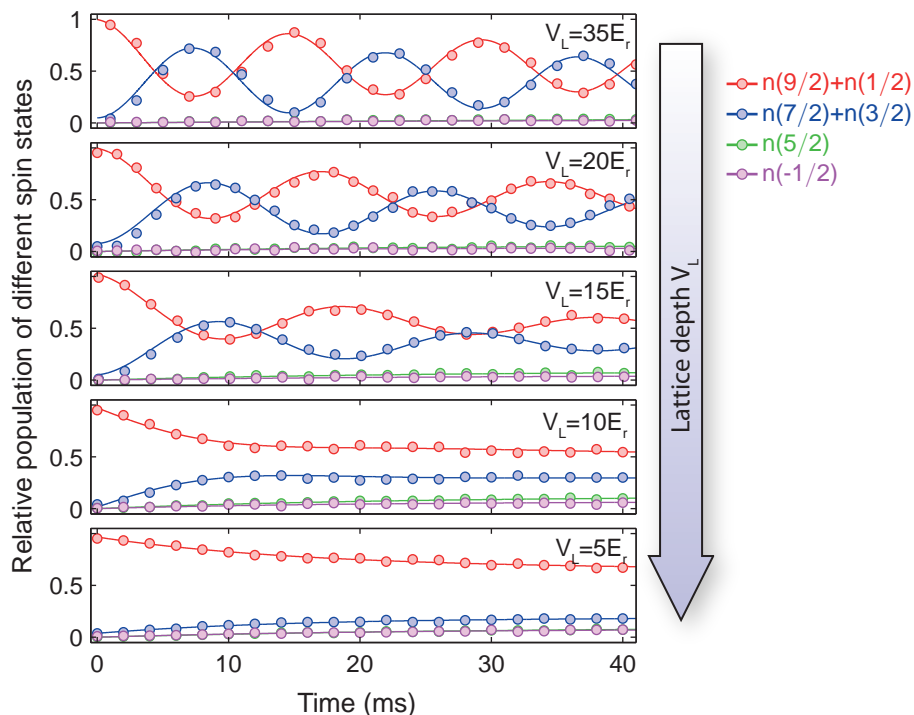


**Figure 4.19: Transition from the two-body to the many-body regime.** The time evolution of the spin occupations  $n(m)$  is depicted for different lattice depths  $V_L$ . Along the radial direction, the lattice depth is always  $V_L = 35 E_r$  and reduced in the axial direction as indicated in the figure. Experimental parameters are chosen as in Fig. 4.8. Solid lines are fits to the data using equation C.1. Data have also been published in [5].

regime, where tunneling and spin-changing dynamics occur on similar time scales.

To investigate this experimentally, the same procedure has been used, which was employed for high-contrast spin oscillations (see section 4.2.2). The atoms are adiabatically loaded into a 3d optical lattice, yielding the same initial spatial distribution as for the two-particle experiments. Subsequently, one lattice axis is quenched to a low value, which results in the formation of 1d tubes with an increased tunneling along one spatial direction. The tunneling time in the radial direction is approximately 1 Hz and varies in the lateral direction between 1 – 300 Hz, depending on the applied lattice depth between  $35 - 5 E_r$ . Therefore, the above-mentioned tunneling processes should occur on faster time scales. Note that due to the black-out-pulse technique, the singly occupied lattice sites are transferred to the  $f = 7/2$  manifold. Therefore, tunneling at defects will create to first order doubly occupied sites with mixed hyperfine spin. This leads to a strongly reduced lifetime due to hyperfine relaxation collisions (see section 3.2.3), which was checked independently [107]. Hence, the occupation of new spin states can only occur in second order with defect tunneling.

The result of this experiment is depicted in Fig. 4.19, where the influence of the decreasing lattice depth is clearly visible. The data allow for three main observations: First, the spin-oscillation frequency and amplitude slightly decrease, which can be understood in the two-particle picture. The lower local density in shallower lattices de-

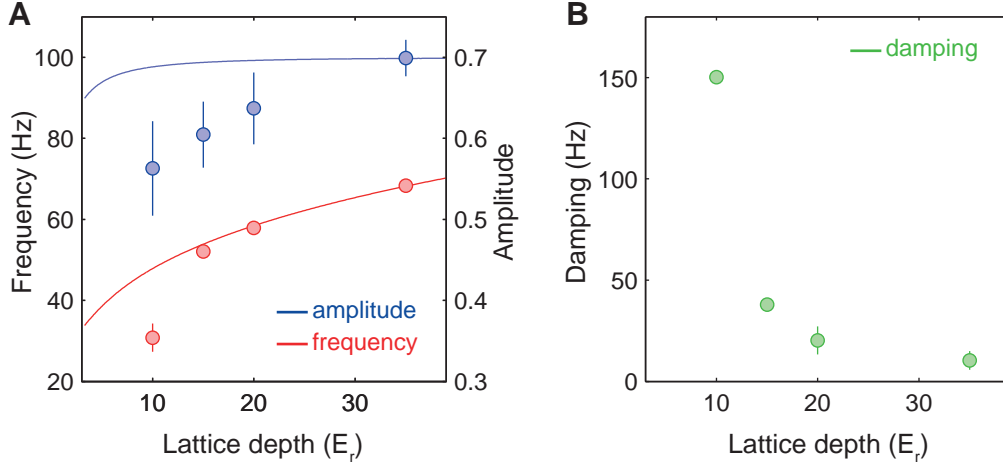


**Figure 4.20: Spin-oscillation properties from the two-body to the many-body regime.** (A) Frequency and amplitude of the spin-oscillation data in Fig. 4.19 are depicted. Solid lines are calculations of the two-particle Hamiltonian (equation 4.7). The amplitude is globally rescaled as in the two-body case. (B) Damping rates from Fig. 4.19 are shown. Error bars represent two standard deviations.

increases the on-site interactions, which leads to lower spin-oscillation frequencies and amplitudes (see Fig. 4.20 A). Consistent with these considerations, this can also be reproduced with calculations using the two-body Hamiltonian (equation 4.7). Moreover, the damping of the spin oscillations strongly increases in shallower lattices (see Fig. 4.20 B), resulting in a complete disappearance of any spin oscillations below  $V_L = 10 E_T$ . Beyond this, new spin components are populated, both in the spin states  $m = 5/2$  and  $m = -1/2$ , which is enhanced at lower lattice depth. Note that the latter two effects are not captured within the two-body model and result from tunneling events.

The dominating tunneling processes cannot be directly identified from these experimental observations. All of them lead to a damping of the spin oscillations as well as the population of new spin states. For more insight, numerical simulations have been performed by O. Jürgensen [186]. In this context, spin dynamics was simulated on a small 1d lattice chain with up to four lattice sites using periodic boundary conditions. A detailed description will be given in [187], while the following discussion is limited to the interpretation resulting from the comparison with the experimental data.

First, the time evolution was calculated for deep lattices, starting from a band insulator and in the presence of defects. In Fig. 4.21 A, the corresponding results are shown. For a pure band insulator, undamped spin oscillations are found in the simulations, implying that the system evolves without perturbations between a band and a Mott insulator. However, taking into account possible defects, i.e. singly occupied sites, the numerical simulations reproduce the experimentally observed damping as well as the appearance of new spin states. This is consistent with the experimental findings and demonstrates that defect tunneling dominates in the regime of deep optical lattices.

In contrast, calculations in shallow lattices reveal a fully different behavior (see Fig. 4.21 B). Tunneling in a perfect band insulator already leads to strong damping of the spin oscillations. Additional defects only have a small influence in this case. This

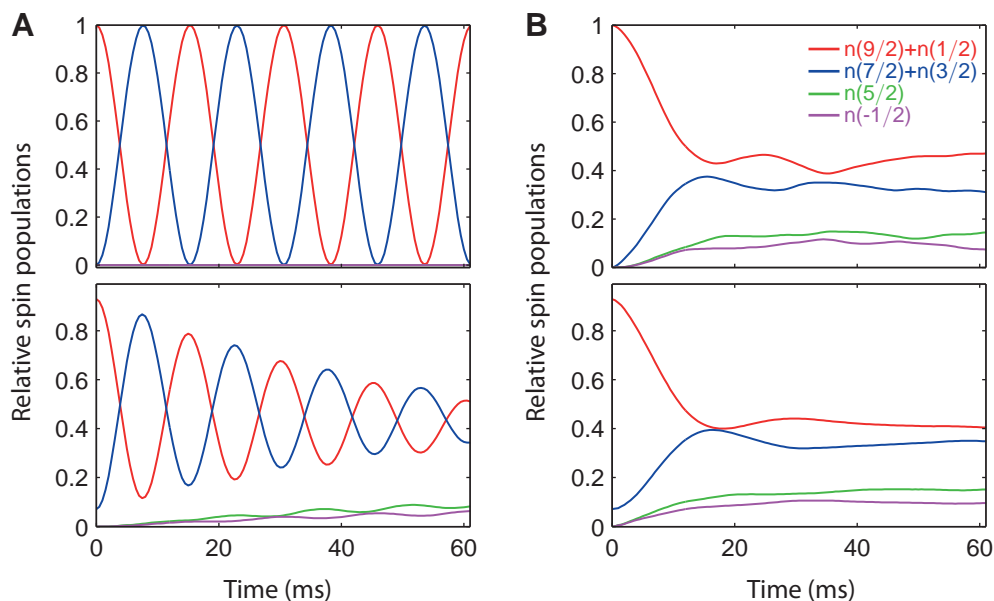


**Figure 4.21: Numerical simulation of spin oscillations in a four-well system.** Calculated spin oscillations – in a deep optical lattice of  $V_L = 20 E_r$  (**A**) and in a shallow optical lattice of  $V_L = 5 E_r$  (**B**) – are depicted. Upper parts show results for a perfect initial band insulator. Lower parts depict simulations for a band insulator with defects, which are included as one singly occupied site averaged for all possible spin states. The parameters are chosen as in Fig. 4.19. Calculations are performed using exact diagonalization and are kindly provided by O. Jürgensen [186].

behavior is found to be robust in a wide parameter regime, and even more defects do not significantly change the spin dynamics [186]. In general, the damping is very strong and leads to a complete disappearance of the spin oscillations consistent with the experiments.

The small size of the system does not allow for quantitative predictions. Naively, one would expect that the damping of the spin oscillations is even more pronounced in larger systems. A clear distinction between super-exchange and first-order tunneling remains a question to be solved, which requires further studies. In this direction, a profound theoretical analysis has recently shown that first-order tunneling is strongly suppressed in small-scale systems due to an energy gap. The authors propose the high-spin fermionic lattice system for the realization of large-amplitude super-exchange [188].

In conclusion, the experiments combined with the numerical analysis show that tunneling processes occur in the band-insulating core of the system and significantly contribute to the observed damping and the appearance of new spin states. As an important result, this implies a novel instability of the initially band-insulating state induced by spin-changing dynamics. It constitutes a unique fermionic high-spin feature, which is absent in conventional spin 1/2 systems.

## 4.4 Spin dynamics between different bands

The experiments presented in the last sections are restricted to the lowest band of the optical lattice: Initially, the atoms are prepared in the lowest band and the involved energy scales of the spin dynamics are too small to overcome the band gap. This constitutes a significant simplification of the multi-band lattice system, neglecting the orbital degrees of freedom.

In general, higher orbitals are believed to play a crucial role for various phenomena in solid-state physics, e.g. metal-insulator transitions or superconductivity. The study of higher bands in optical lattice systems has attracted a tremendously growing interest in recent years, both from the experimental side [168, 189–193] and the theoretical side [194–196]. As an example, spatial dynamics of fermions in higher lattice orbitals have been investigated in the course of this research work. In analogy to photoconductivity, the experiments reveal an intriguing spatial dynamics of particle-hole pairs, driven by the harmonic confinement. This is in detail discussed in the thesis of J. Heinze [107]. The results are published in [4].

In this direction, another approach to involve higher bands is the extension of spin dynamics to a multi-band system. This allows to combine the spin with the orbital degrees of freedom. Note that this is fundamentally different from the approach above, since the intrinsic interactions of the lattice system lead to the occupation of higher bands.

This approach will be discussed in the following section, providing in addition a possible outlook for future experiments. The experimental concept of this spin-orbital coupling induced by spin-changing collisions will be briefly introduced. Moreover, I will present a first experimental study, where enhanced spin-changing rates associated with interband spin transfer have been observed.

### 4.4.1 Multi-band spin dynamics

The population of higher bands of an optical lattice typically requires additional external manipulation, for example lattice-amplitude modulation [4, 191, 193]. Spin-orbital coupling, mediated by spin-changing collisions, constitutes a different approach, where spin-changing collisions lead to higher-band occupations.

This requires that the collision process releases enough energy for the band transfer. However, the spin-changing interaction energy ( $\approx$  kHz) remains well below the energy associated with a band transfer ( $\approx$  10 kHz). Instead, the Zeeman energy can be used in this context. To gain Zeeman energy in a spin-changing collision, the atoms have to be prepared in the lowest band in a magnetically excited spin configuration. The released Zeeman energy is converted into kinetic energy allowing to overcome the band gap [104]. Note that this is in contrast to the experiments presented so far, where the atoms were initially prepared in the magnetic ground states of the corresponding spin systems.

In a first approximation, the two-particle model (equation 4.7) can be extended to this case with an additional diagonal term accounting for the energy of the involved orbitals. For this purpose, it is also suitable to introduce a multi-band two-particle state  $|m_1^{(n_1)}, m_2^{(n_2)}\rangle$ , where  $m_i$  is the magnetic quantum number and  $n_i$  the band of the particle  $i$ . The influence of higher bands is equivalent to a detuning in addition to the Zeeman energy.

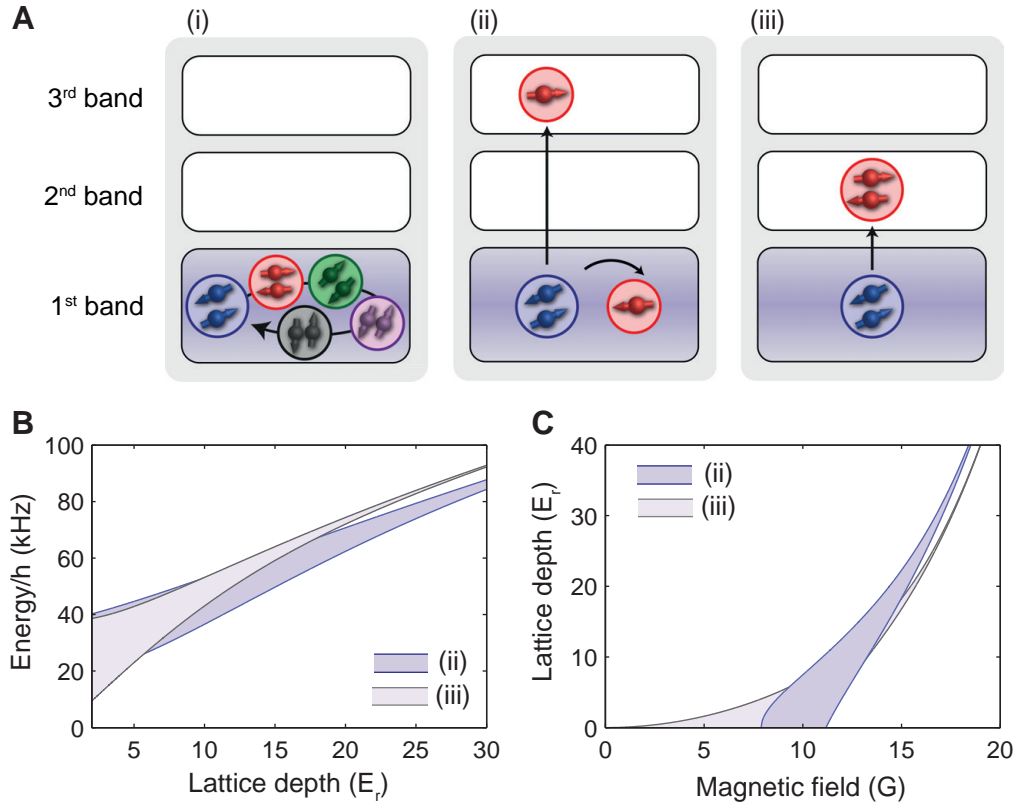


**Figure 4.22: Principle of multi-band spin dynamics.** (A) A sketch of three exemplary spin-changing collision processes in the multi-band system is provided: conventional intraband spin dynamics (i), single interband spin transfer (ii), and double interband spin transfer (iii), as described in the main text. The initial state (blue) is always  $|+3/2^{(1)}, -3/2^{(1)}\rangle$ , which is magnetically excited. The band transition energy as a function of the lattice depth (B) and the corresponding magnetic field dependence (C) for a magnetic resonance are depicted for processes (ii) and (iii).

As an example, consider one atom pair in the lowest band, which is prepared in the magnetically excited spin configuration  $\pm 3/2$  (see section 2.2.2). Magnetic energy is released in a spin-changing collision into the spin configuration  $\pm 1/2$ . Further two-particle states have even higher magnetic energies (see section 2.2.2) and hence only these two spin configurations are involved in the band transfer. Out of the myriad of possible scenarios in the multi-band system, three processes are exemplary sketched in Fig. 4.22 A:

#### Process (i): Intraband dynamics

This collision process corresponds to conventional spin dynamics in the lowest band. It involves the five two-particle states of the spin  $9/2$  system.

#### Process (ii): Single interband spin transfer

In this case, one particle is transferred into the third band, while the second particle remains in the lowest band. This collision couples the states  $|+3/2^{(1)}, -3/2^{(1)}\rangle$  and  $|+1/2^{(3)}, -1/2^{(1)}\rangle$ .

### Process (iii): Double interband spin transfer

In this process, both particles are transferred into the second band. This collision couples the states  $|+3/2^{(1)}, -3/2^{(1)}\rangle$  and  $|+1/2^{(2)}, -1/2^{(2)}\rangle$ .

The coupling between different bands crucially depends on the lattice depth. This dependence is depicted in Fig. 4.22 B, where the band energy difference is calculated for the single and the double interband spin transfer. It reflects that in deeper lattices the band gap increases, which has to match the released magnetic energy. The corresponding magnetic field is depicted in Fig. 4.22 C as a function of the lattice depth. In general, magnetic fields of  $B > 10$  G are necessary at intermediate lattice depths, which exceeds by far the magnetic field, where spin dynamics in the lowest band occur.

Note that the resonance feature described here is different from the spin resonance worked out in section 4.2.3. For spin transfer into higher bands, the involved energy scales are the magnetic energy and the band energy. This feature is therefore referred to as a magnetic resonance [104]. The interaction energy provides the coupling between the involved states and only leads to small corrections of the magnetic resonance position.

#### 4.4.2 Observation of interband spin transfer

For several reasons, one cannot expect coherent spin dynamics involving different bands in the available parameter regime: First, losses induced by Feshbach resonances limit the available magnetic field range to  $B < 14$  G (see appendix B), which in turn sets the available lattice depth to  $V_L < 12 E_r$ . In this shallow lattice configuration, the coherent oscillations are already damped in the lowest band (see section 4.3.2). Moreover, the lifetime of the atoms in higher bands is limited ( $\approx 30$  ms), which was checked independently [107, 109].

Nevertheless, the spin-changing rates can be investigated for different magnetic fields. In this direction, only a few measurements have been performed during this work, which constitute a proof-of-principle experiment and provide an outlook for future studies.

For this purpose, the atoms are adiabatically loaded into a 3d optical lattice at a lattice depth of  $V_L = 25 E_r$ . The spin mixture  $m = \{\pm 3/2\}$  is employed, which is magnetically excited and cannot be directly loaded into the lattice. This issue is circumvented by using the spin mixture  $m = \{+3/2, -1/2\}$  during the lattice ramp. A subsequent rf-sweep yields the initial two-particle state  $|+3/2^{(1)}, -3/2^{(1)}\rangle$ . The resulting spatial distribution is similar to the two-particle experiments with approximately 30% doubly occupied sites in the core of the system [182]. After this preparation, the lattice is quenched to a 1d configuration by reducing one lattice direction to  $11 E_r$ . The spin occupations are recorded after a time evolution of  $t = 50$  ms for different magnetic fields. Note that due to heating of the system, the different bands cannot be unambiguously resolved in the absorption images and therefore the spin occupations are analyzed.

The result of this experiment is depicted in Fig. 4.23, revealing several intriguing features: At lower magnetic fields, a pronounced spin redistribution is observed, which involves all two-particle states of the five-level system ( $|\pm 1/2\rangle$ ,  $|\pm 3/2\rangle$ ,  $|\pm 5/2\rangle$ ,  $|\pm 7/2\rangle$ , and  $|\pm 9/2\rangle$ ). This can be identified as conventional intraband spin dynamics, corresponding to process (i). Beyond this, a clearly enhanced spin-changing collision rate is found at a magnetic field of  $B = 11 - 13$  G. The width as well as the position of this resonance is in reasonable agreement with the calculated values of the interband dy-

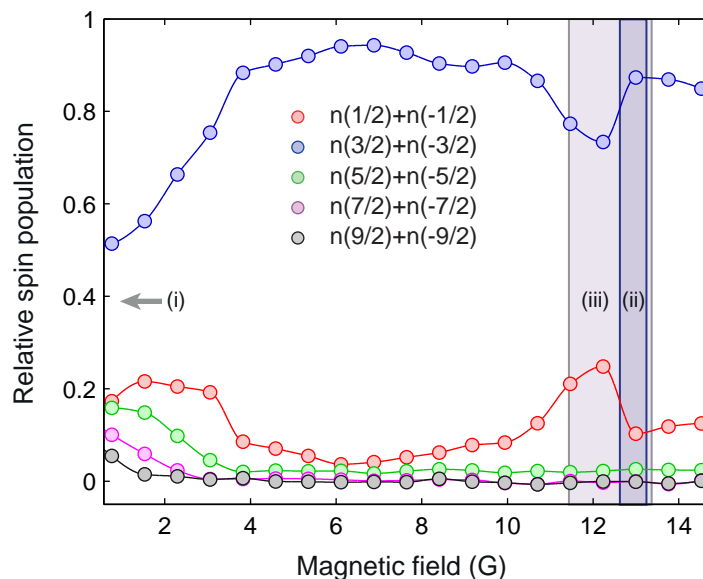


**Figure 4.23: Observation of spin-population transfer into higher bands due to spin-changing collisions.** The relative spin populations  $n(m)$  after  $t = 50$  ms are depicted as a function of the magnetic field. The initial state is  $|+3/2^{(1)}, -3/2^{(1)}\rangle$ , while the lattice depth is initially  $V_L = 25 E_r$  and quenched along one dimension to  $11 E_r$ . Shaded area indicated with numbers show the calculated resonance position for the corresponding processes shown in Fig. 4.22 A.

namics described by process (ii) and process (iii). This allows for the conclusion, that a fermionic magnetic resonance has been observed. It is highlighted by the fact that only the spin configuration  $\pm 1/2$  is populated at the corresponding magnetic field, which is the only one to obey the resonance condition.

However, the data also reveal several puzzling observations, which require further investigations: Interestingly, the intraband spin dynamics corresponding to process (i) are found in a broad magnetic field range ( $B = 0 - 4$  G), which clearly exceeds the calculated width of the first band ( $B < 1$  G). In addition, independent of the magnetic field, a small occupation of the spin configuration  $\pm 1/2$  is found. Both observations do not fulfill the resonance conditions neither for intraband spin dynamics nor for magnetic resonances. These effects are probably a consequence of collective spin dynamics. In this context, possible explanations are interaction-driven spin instabilities or spin-changing relaxation collisions. This has been studied in detail with harmonically trapped high-spin fermions and will be discussed in chapter 6.

## 4.5 Conclusion and outlook

In conclusion, the experiments presented in this chapter constitute the first realization of fermionic spin dynamics. This novel effect has been studied in various regimes of the optical lattice, governed by the interplay between high-spin interactions, Zeeman energy, tunneling and higher bands. In the two-body limit, established in deep optical lattices, the coherent nature of fermionic spin-changing collisions and multi-flavor spin dynamics were demonstrated. Within a two-particle model the dynamical properties could be very well described. This allowed to extract fundamental scattering parameters and provided the first proof of high-collision quanta. In the presence of tunneling, at intermediate lattice strength, a new instability of a large-scale band insulator was found, induced by microscopic spin-changing collisions. Finally, multi-band spin dynamics were observed, apparent in an interband spin transfer, driven by spin-changing collisions.

The investigated interaction process is fundamental for many-body systems with high spin and paves the way towards the exploration of various phenomena predicted in these systems: novel high-spin ground-state properties of optical lattices such as Néel and Haldane phases have been proposed [163]. This could be addressed in future experiments by adiabatically lowering the magnetic field in an initially band-insulating system. Combining the fermionic high-spin lattice system with Feshbach resonances – widely available in  $^{40}\text{K}$  (see appendix B) – opens another exciting field. Experiments are now possible to study the crossover from nearly  $\text{SU}(N)$ -symmetric systems to broken  $\text{SU}(N)$ -symmetry, where recent studies predict the existence of colorful Mott shells, driven by high-spin magnetic correlations [182]. Moreover, the transition from a Mott insulator to a quantum-Zeno insulator has been proposed [107], constituting another approach for the strongly-correlated regime. In another direction, a more detailed analysis of the tunneling mechanism presented in this chapter has revealed that large super-exchange dynamics could be directly observed in fermionic small-scale high-spin systems [188]. Furthermore, enhanced experimental schemes could allow to observe magnetically tunable multicolor spin resonances, which are proposed for small-scale systems [104] and head towards the realization of spin-orbital entanglement.

The approach in this chapter addressed high-spin interactions from the microscopic perspective. This was related to the many-body regime by corrections originating from tunneling or higher-band occupations. Naturally, this picture has to break down, when a system with a large spatial extension and many particles is considered – for example harmonically trapped high-spin fermions. The behavior of such a many-body system exposed to high-spin interactions will be the subject of the following chapter.

## Chapter 5

# Collective spin dynamics in fermionic bulk systems

A crucial question in many-body physics is how macroscopic collective effects such as superfluidity arise from microscopic processes. Quantum gases provide powerful model systems to explore such phenomena. In this context, the quantum statistics of the involved atoms play an important role. They favor collective behavior for Bose-Einstein condensates, in which all particles occupy the lowest spatial mode of the system. For fermions, on the other hand, each single-particle state can be occupied with only one particle and many spatial states are involved. Therefore, collective behavior is rare in fermionic many-body systems and has attracted particular interest in recent years. Important examples are studies of the BEC-BCS crossover [48–51], spin transport [57] and collective excitations such as spin waves [58, 61, 197] or solitons [60].

In high-spin systems the additional spin degree of freedom can lead to novel collective effects. Various phenomena have been proposed in this context, including a QCD-like color superfluidity or unconventional BCS superfluids [88–96]. In first experiments in this direction, performed during this research work, tensorial spin waves, which constitute novel collective spin-spatial excitations in high-spin fermions have been studied [3, 107].

These phenomena rely on the microscopic high-spin interactions, which have been investigated in the last chapter. This motivates to explore the impact of spin-changing collisions on a fermionic many-body system. Experiments with ultracold bosons have already revealed fascinating collective effects: spinor Bose-Einstein condensates can exhibit collective spin dynamics [76–82], apparent in long-lived oscillations of the spin degree of freedom. However, in a Bose-Einstein condensate the superfluid character suppresses spin structures on the scale of the spin healing length [67, 68, 71, 82]. For fermions, this raises a fundamental question (see sketch in Fig. 5.1): Can a whole Fermi sea also exhibit collective dynamics of its spin degree of freedom?

In this chapter, I will present experiments, which clearly prove that the answer is *yes*. Starting from a basic mean-field approach (section 5.1), I will show a proof-of-principle experiment, demonstrating giant and long-lived spin oscillations in a Fermi sea (section 5.2). This unexpected collective behavior, justifying a single-mode approximation, will be investigated in section 5.3. Finally, I will present a detailed study of the spin-oscillation properties including the dependence on the magnetic field, the density and the spin configuration (section 5.4).

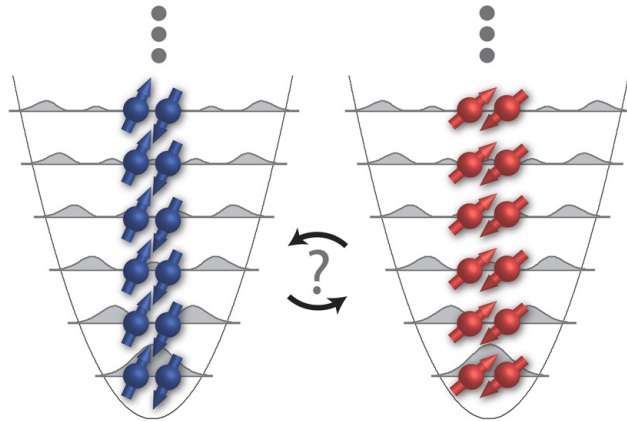


**Figure 5.1: Can a Fermi sea perform collective dynamics of its spin degree of freedom?** Collective spin-changing dynamics in a Fermi sea are sketched. Note the intrinsic multi-mode structure indicated by the different trap levels.

---

Parts of this chapter have been published in [1]. The experiments and the data analysis were performed with C. Becker, N. Fläschner, J. Heinze, and K. Sengstock.

## 5.1 A mean-field description for high-spin fermions

An interacting fermionic many-body system with high spin involves collisions, which can change the spin and the spatial configuration. In general, this leads to complex many-body dynamics, which is challenging to describe theoretically. The presented experiments employ high-spin fermions confined in a harmonic trap, where typical interaction strengths are rather low due to the diluteness of the sample. In this regime, a mean-field approximation has proven to provide a suitable description, which is used throughout this chapter. Further contributions become important in particular at higher temperatures and intermediate interaction strengths. These effects will be studied in chapter 6.

In this section, the collisionless Boltzmann equation, derived from a mean-field approach, will be introduced for a fermionic high-spin system (following [152]). Important requirements to realize collective spin dynamics and their experimental realization will be discussed.

### 5.1.1 The collisionless Boltzmann equation

The description of a fermionic many-body system with a Boltzmann equation has been successfully applied to various collective phenomena in spin 1/2 fermions [151, 152, 198–200]. This theory can be extended to high-spin systems [201, 202], yielding a high-spin Boltzmann equation.

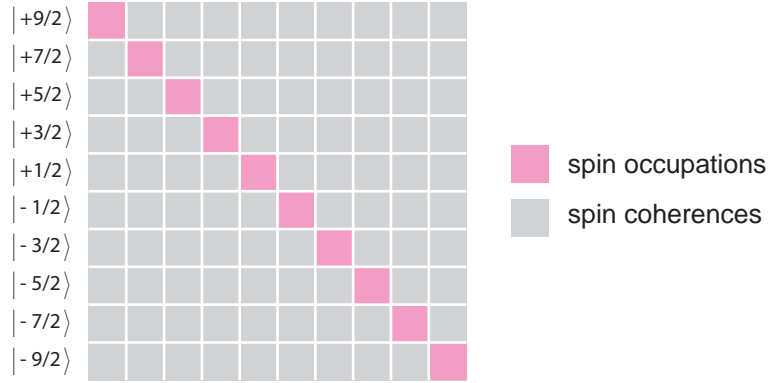


**Figure 5.2: Single-particle density matrix for the lowest hyperfine manifold of  $^{40}\text{K}$ .** The total spin ( $f=9/2$ ) gives rise to ten spin states, and the corresponding single-particle density matrix is described by a  $10 \times 10$  matrix. The basis is chosen as  $\{+9/2, \dots, -9/2\}$ . Diagonal elements account for spin occupations (magenta), while off-diagonal elements describe single-particle spin coherences (gray).

The Hamiltonian describing the full fermionic many-body system is given by [203]:

$$\mathcal{H} = \underbrace{\int d\mathbf{r} \sum_{ij} \hat{\psi}_i^\dagger(\mathbf{r}) \left( -\frac{\hbar^2}{2m} \nabla^2 \delta_{ij} + V_{\text{trap}}(\mathbf{r}) \right) \hat{\psi}_j}_{\mathcal{H}_{\text{kin}}} + \underbrace{\int d\mathbf{r} \sum_{ij} \hat{\psi}_i^\dagger(\mathbf{r}) q(S_z^2)_{ij} \hat{\psi}_j(\mathbf{r})}_{\mathcal{H}_{\text{qze}}} + \underbrace{\int d\mathbf{r} \sum_{ijkl} U_{ijkl} \hat{\psi}_i^\dagger(\mathbf{r}) \hat{\psi}_k^\dagger(\mathbf{r}) \hat{\psi}_j(\mathbf{r}) \hat{\psi}_l(\mathbf{r})}_{\mathcal{H}_{\text{int}}}. \quad (5.1)$$

Each single-particle state is described by the high-spin field operator  $\hat{\psi}_i(\mathbf{r})$ , following the anticommutation relations  $\{\hat{\psi}_i^\dagger(\mathbf{r}_1), \hat{\psi}_j(\mathbf{r}_2)\} = \delta_{ij} \delta(\mathbf{r}_1 - \mathbf{r}_2)$ , where  $i$  denotes the spin state. The first part of the Hamiltonian  $\mathcal{H}_{\text{kin}}$  accounts for the kinetic motion in the harmonic trap. The second part is the Zeeman energy  $\mathcal{H}_{\text{qze}}$ , where quadratic contributions are the most relevant ones in our case (for a definition of  $S_z^2$  see appendix C). The third part  $\mathcal{H}_{\text{int}}$  describes the high-spin interactions between the particles and is given by a sum over all possible scattering processes, weighted by the coupling constants  $U_{ijkl} = 4\pi\hbar^2 a_{ijkl}/m$ .

The derivation of the collisionless Boltzmann equation follows the route for conventional spin 1/2 systems [152] and includes several simplifications:

### Single-particle density matrix

The system is described by a single-particle density matrix  $\rho_{ij}$  as depicted for  $^{40}\text{K}$  in Fig. 5.2. This reduces the description of the many-body system to an effective single-particle picture. Diagonal elements of this matrix account for spin occupations, while off-diagonal elements are single-particle spin coherences. The latter describe how the spin states are coherently connected. For simplicity, the

single-particle density matrix and the single-particle spin coherences are referred to as density matrix and coherences in the following.

The time evolution of  $\rho_{ij}$  is given by the von-Neumann equation yielding [152]

$$i\hbar \frac{d}{dt} \rho_{ij}(t) = \left\langle \left[ \hat{\psi}_i^\dagger(\mathbf{r}_1) \hat{\psi}_j(\mathbf{r}_2), \mathcal{H} \right] \right\rangle. \quad (5.2)$$

### Hartree-Fock approximation

The evaluation of equation 5.2 reveals quartic interaction terms, which can be approximated in a Hartree-Fock treatment [152] as

$$\left\langle \hat{\psi}_i^\dagger \hat{\psi}_j^\dagger \hat{\psi}_k \hat{\psi}_l \right\rangle \approx \left\langle \hat{\psi}_i^\dagger \hat{\psi}_l \right\rangle \left\langle \hat{\psi}_j^\dagger \hat{\psi}_k \right\rangle - \left\langle \hat{\psi}_i^\dagger \hat{\psi}_k \right\rangle \left\langle \hat{\psi}_j^\dagger \hat{\psi}_l \right\rangle. \quad (5.3)$$

This reflects that two-body correlations formed in a binary collision are neglected, which is a valid approximation at low interaction strengths and high particle numbers. The Hartree-Fock approximation assumes that subsequent collisions between the same collision partners can be neglected [152].

### Wigner transformation

It is suitable to describe the time evolution of the density matrix in a phase-space representation, which motivates to introduce the Wigner function [152, 204]

$$w_{ij}(\mathbf{r}, \mathbf{p}) = \frac{1}{(2\pi\hbar)^3} \int d\mathbf{r}_2 e^{i\mathbf{p}\cdot\mathbf{r}_2/\hbar} \rho_{ij} \left( \frac{\mathbf{r} + \mathbf{r}_2}{2}, \frac{\mathbf{r} - \mathbf{r}_2}{2} \right). \quad (5.4)$$

It transforms the position-dependent variables  $\{\mathbf{r}_1, \mathbf{r}_2\}$  to position and momentum  $\{\mathbf{r}, \mathbf{p}\}$ . Note that each entry of the density matrix is described by its individual Wigner function.

### Semiclassical approximation

In the Wigner representation, equation 5.2 leads to an involved expression including a series expansion of gradient terms [152]. It is truncated to lowest order, which corresponds to a semiclassical approximation of the motional degrees of freedom. This is justified as long as the mean-field potential varies slowly compared to each Wigner function.

With these approximations, one obtains a collisionless Boltzmann equation of the form [152]

$$\begin{aligned} \partial_t w(\mathbf{r}, \mathbf{p}) = & \underbrace{\left( -\frac{\mathbf{p} \cdot \nabla_{\mathbf{r}}}{m} + m \sum_{\alpha} \omega_{\alpha}^2 (\mathbf{r} \cdot \nabla_{\mathbf{p}})_{\alpha} \right)}_{\text{kinetic motion}} w(\mathbf{r}, \mathbf{p}) + \\ & \underbrace{\frac{1}{i\hbar} [V(\mathbf{r}, \mathbf{p}), w(\mathbf{r}, \mathbf{p})]}_{\text{interaction}} + \underbrace{\frac{1}{i\hbar} [qS_z^2, w(\mathbf{r}, \mathbf{p})]}_{\text{Zeeman effect}}. \end{aligned} \quad (5.5)$$

This equation is used for the description of the experiments in this chapter. Its first term reflects the kinetic motion of the particles in the harmonic trap, while the two commutators account for the high-spin interactions and the magnetic energy, respectively. In equation 5.5, the mean-field potential

$$V_{ij}(\mathbf{r}) = \sum_{kl} \int d\mathbf{p} (U_{jikl} - U_{jlki}) w_{kl}(\mathbf{r}, \mathbf{p}) \quad (5.6)$$

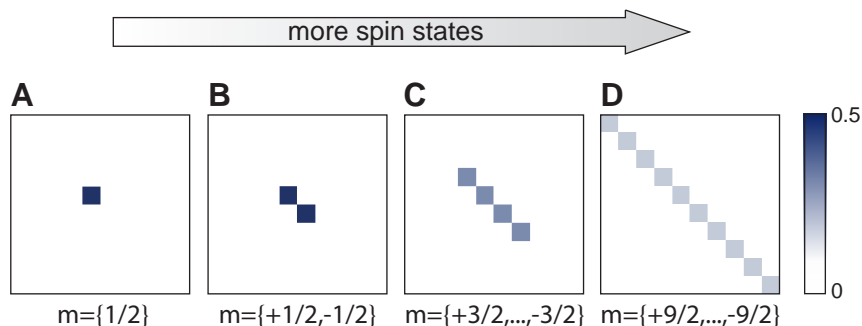


**Figure 5.3: Density matrix for different incoherent states.** The Fermi sea is assumed to be incoherent after the evaporation (only diagonal elements). A spin-polarized Fermi sea has only one diagonal entry (A). Increasing the number of spin components increases the number of diagonal elements (B-D). The corresponding spin mixtures are indicated below. The color bar is used in the following for the illustration of density matrices.

is introduced, which is proportional to the spatial density  $n(\mathbf{r}) = \int d\mathbf{p} w(\mathbf{r}, \mathbf{p})$ . This term drives mean-field dynamics, including spin-changing collisions or spin waves. Higher gradient orders provide non-local mean-field corrections to the harmonic trapping potential, which are small and thus neglected in the following [152].

### 5.1.2 Requirements for spin dynamics

A spin-polarized Fermi sea, which is non-interacting, intrinsically suppresses s-wave collisions. It corresponds to a density matrix with only one diagonal entry (see Fig. 5.3 A). An interacting Fermi sea involves several spin states and can be realized by evaporating the sample in the dipole trap. After the evaporation this corresponds to an incoherent state, represented by a density matrix with the corresponding diagonal entries (see examples in Fig. 5.3 B – D). However, also for incoherent states the Boltzmann equation 5.5 reveals a trivial time evolution. The commutator including the mean-field potential is only non-vanishing, when spin coherences (off-diagonal elements in the density matrix) are present.

The experiments start with an evaporated binary spin mixture  $m = \{\pm 1/2\}$ , corresponding to a density matrix with two diagonal entries (see Fig. 5.3 B). To create a state with significant coherences, a preparation scheme employing rf-radiation has been implemented for fermionic atoms for the first time, which was so far applied in experiments with bosonic atoms (see for example [77, 79]). By this, the incoherent spin mixture is exposed to a typically  $10 \mu\text{s}$  rf-pulse at low magnetic field. In this regime, the linear Zeeman effect dominates, resulting in approximately the same energy splitting for all spin states. Hence, the rf-pulse couples the ten spin states of the  $f = 9/2$  manifold simultaneously. This can be understood as a rotation of the two-component spin mixture on a generalized Bloch sphere [138]. Note that this preparation scheme is different from the preparation at large magnetic fields (see section 3.2.2), where individual spin states are selectively coupled.

The resulting density matrix can be calculated using the generators of rotation ( $S_x$

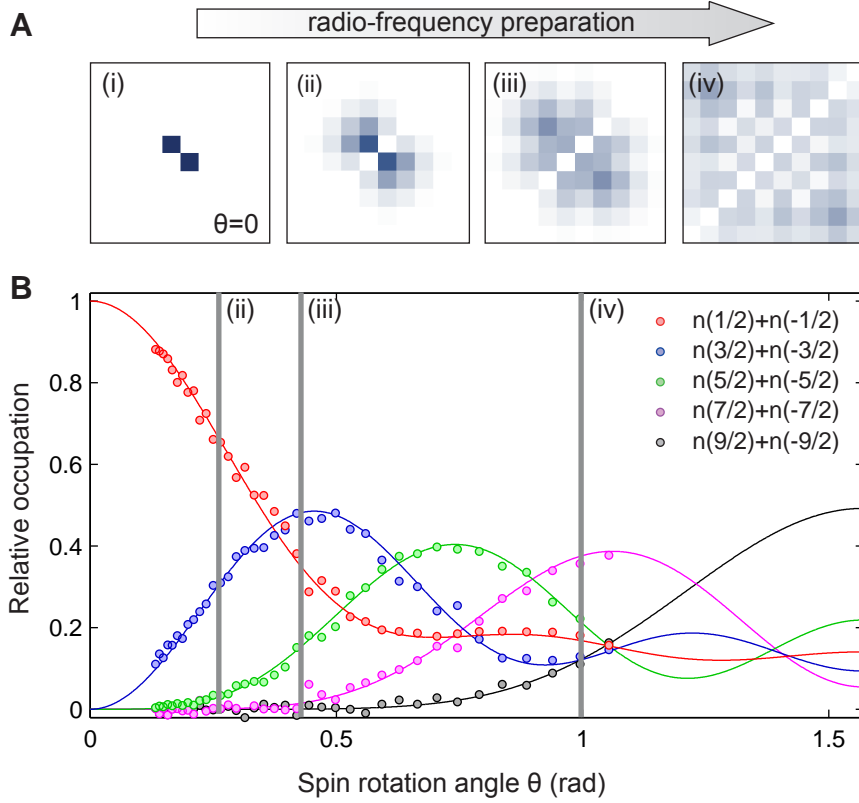


**Figure 5.4: Preparation of single-particle coherences in a Fermi sea.** (A) Density matrices are shown for different rotation angles  $\theta$  as indicated below. Plotted are the absolute values of the density matrix. The initial state is the spin mixture  $m = \{\pm 1/2\}$  (i), while the state widely used in the experiments is (iii). (B) Measured spin occupations starting from spin mixture  $m = \{\pm 1/2\}$  are depicted as a function of the rotation angle  $\theta$ . The latter corresponds to different rf-powers of the rf-pulse at a frequency of 159 kHz. The magnetic field is  $B = 0.5$  G. Solid lines are calculations using equation 5.7, with the Rabi-frequency as only free parameter. Experimental data have also been published in [1].

or  $S_y$ ) and is given by (for details see appendix C) :

$$\rho(\theta) = \exp\left(-\frac{iS_{x,y}\theta}{2}\right) \cdot \rho_0 \cdot \exp\left(\frac{iS_{x,y}\theta}{2}\right). \quad (5.7)$$

Here,  $\rho_0$  is the initial density matrix, and  $\theta$  is the spin rotation angle. Note that due to the rotational symmetry, a spin rotation with  $S_x$  and  $S_y$  yields density matrices, which exhibit the same dynamics.

To illustrate this preparation, the density matrix  $\rho$  is shown in Fig. 5.4 A for different spin rotations of the spin mixture  $m = \{\pm 1/2\}$ . This leads to the occupation of further spin components alongside the formation of coherences. In particular at large rotation angles, checkerboard-like structures are induced, which are a consequence of the combination of the incoherent initial state and the adjoined coherences.

Experimentally, the spin occupations can be easily measured for example in a Stern-Gerlach separation (see 3.2.4). Figure 5.4 B shows an experiment, where different rf-intensities, corresponding to different spin rotation angles, have been applied to the

spin mixture  $m = \{\pm 1/2\}$ . The data reveal the admixture of new spin components with increasing pulse intensity. Comparing this to equation 5.7 reveals a very good agreement with the Rabi-frequency as only free parameter.

This demonstrates that well-controlled initial states with significant coherences can be realized in the experiment. The state widely used in the following experiments corresponds to a spin rotation of  $\theta = 0.44$  of the spin mixture  $m = \{\pm 1/2\}$ . Its density matrix is depicted in Fig. 5.4 A(iii). It turns out that this spin configuration is advantageous, because it yields a nearly equal occupation of the spin states  $\pm 1/2$  and  $\pm 3/2$  connected with significant coherences. Moreover, the procedure described above can be applied to further spin mixtures (see more examples in appendix C). It provides a versatile tool to prepare various initial states allowing to explore spin-changing dynamics in a wide parameter range, which will be demonstrated in section 5.4.

## 5.2 Observation of giant and long-lived spin oscillations

Now I address the question, whether a Fermi sea can perform collective dynamics of its spin degree of freedom. I present the experimental procedure to study collective spin dynamics and then a proof-of-principle experiment.

To investigate spin-changing collisions in a high-spin Fermi sea experimentally, the following procedure has been employed: The starting point is the evaporation of an ultracold binary mixture by lowering the power of the dipole trap. After the evaporation, the trap is recompressed again, and the corresponding trapping frequencies are  $\omega_{x,y,z} = 2\pi \times (33, 33, 137)$  Hz. Subsequently, the magnetic field is switched to a low value, ranging from 15 mG to several G. Note that for these experiments a careful compensation of magnetic gradients is required (see section 5.3.1). To initialize spin dynamics, a radio-frequency pulse is applied. This generates an initial state, which is interacting and exhibits spin coherences at the same time as discussed above. After a certain time evolution the magnetic field is raised again preventing further spin-changing collisions. The atoms are released from the trap and the spin occupations are counted after a time-of-flight of typically 15 ms in a Stern-Gerlach field.

For a proof-of-principle experiment, the spin mixture  $m = \{\pm 1/2\}$  is initially evaporated to a temperature  $0.13 T_F$ . The resulting spatial configuration is an ultracold harmonically trapped Fermi gas with a spatial extension of approximately  $80 \mu\text{m}$  involving about  $1.3 \times 10^5$  particles. To initialize spin dynamics, a rf-pulse corresponding to a spin rotation of  $\theta = 0.44$  is applied to the spin mixture.

As a key result, the Fermi sea exhibits collective spin dynamics, which is depicted in Fig. 5.5. The data show giant spin oscillations, which constitute the first observation of collective spin dynamics in a Fermi sea. Note the very long lifetime of the coherent behavior, which is found for up to 1 s. The collective dynamics occur mainly between the initially occupied spin states, namely the spin configurations  $\pm 1/2$  and  $\pm 3/2$ . Further spin components do not significantly contribute. The spin oscillations appear with a frequency of 5.5 Hz and an amplitude of about 30%. This demonstrates that a significant fraction of the Fermi sea is involved in the dynamics.

This proof-of-principle experiment reveals a novel collective effect in a fermionic many-body system, namely giant spin oscillations. This phenomenon will be in detail investigated in the following. Thereby, I will focus on the mechanism, which leads to this unexpected collective behavior. Then I will present a detailed study of the spin-

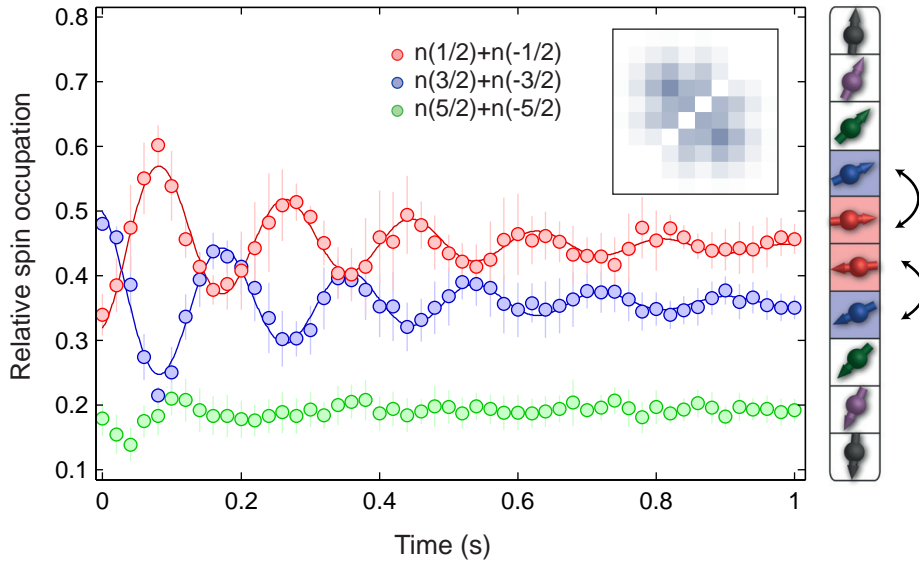


**Figure 5.5: Giant and long-lived spin oscillations in an ultracold Fermi sea.** Plotted are the occupations  $n(m)$  as a function of time. The dynamics are initialized by an rf-pulse, corresponding to a spin rotation of  $\theta = 0.44$  of the spin mixture  $m = \{\pm 1/2\}$  (depicted in the inset). The magnetic field is  $B = 0.12$  G, the peak density  $n_p = 5.9 \times 10^{12} \text{ cm}^{-3}$  (see appendix A) and the temperature  $T = 0.13 T_F$ . Solid lines are oscillatory fits to the data (equation C.1). The spin ladder (right) illustrates the involved spin components. Experimental data have also been published in [1].

oscillation properties for a wide range of parameters. Damping effects arising from finite temperature and higher densities will be the subject of chapter 6.

### 5.3 Studying the collective nature of spin oscillations

Due to the multi-mode spatial structure of fermionic many-body systems collective behavior is in general rare. The observed giant spin oscillations constitute a novel and surprising collective effect. Since the mean-field potential (equation 5.6) is proportional to the density, one would naively expect that the atoms are exposed to a spatially-dependent potential according to their position in the trap. This should be accompanied with a fast dephasing of the spin dynamics. The experimental result, however, clearly highlights the collective character of the spin oscillations for long time scales.

In this section, I will study the origin and the limits of this effect. It will turn out that the collective behavior can be attributed to the spatial dynamics of the underlying harmonic trap. This observation motivates to incorporate a fermionic single-mode approximation as was done for bosonic systems [65, 79, 205], where all spatial degrees of freedom of the many-body system are integrated out. In the presence of magnetic gradients, spin waves [3, 58, 150] can be excited limiting the collective dynamics.

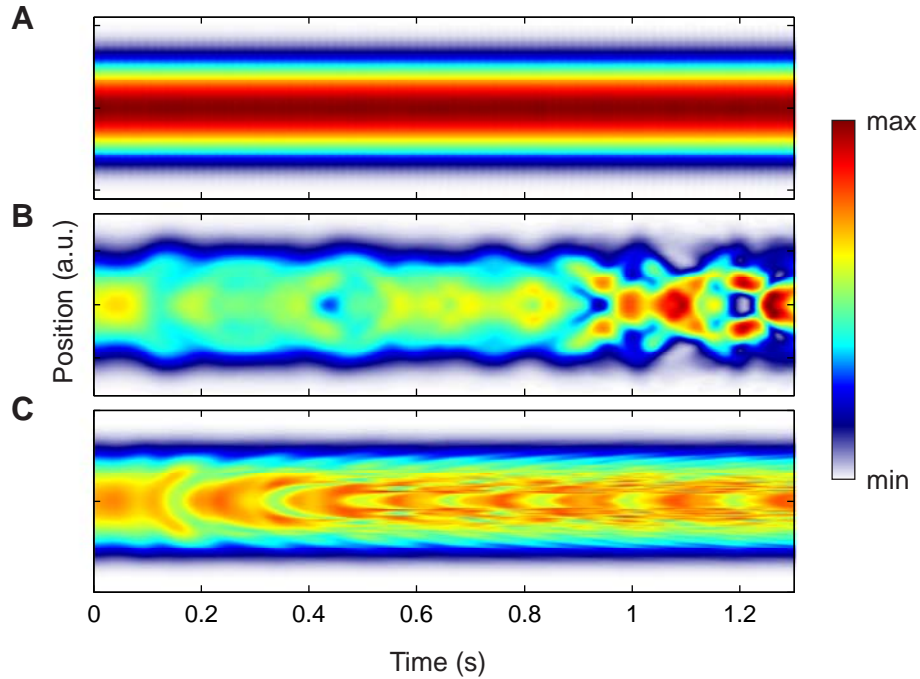


**Figure 5.6: Structure formation in a Fermi sea due to spin-changing collisions.** Simulations of the spatial distribution are shown as a function of time. This is depicted for one spin component ( $m = -1/2$ ), normalized to the same occupation at each time step. The same parameters are chosen as in Fig. 5.5. **(A)** Trap-dominated regime: Trap frequencies are large ( $\omega = 2\pi \times (32, 43, 137)$  Hz) such that  $E_t > E_{sc}$ , which suppresses structures. **(B)** Intermediate regime: One trap frequency is low ( $\omega = 2\pi \times (5, 200, 200)$  Hz) such that  $E_t \approx E_{sc}$  and significant structures appear. **(C)** Interaction-dominated regime: The particles are fixed in the trap and only exposed to the local mean-field potential, leading to strong structures. The calculations in **A** and **B** are kindly provided by U. Ebling [203], while **C** was performed in an extended single-mode approximation (see section 5.3.4).

### 5.3.1 The influence of the trapping potential

The experiments are performed with fermions in an optical dipole trap. This trapping potential induces spatial dynamics in addition to the observed spin oscillations.

In a simplified picture one can understand the influence of the trap in the following way: Consider one particle, which moves, driven by the harmonic confinement, through the mean-field background, provided by all other particles. The particle passes through different regions of the trap with different local potentials and performs spin-changing collisions. It is crucial, on which time scale the corresponding processes occur. If the trap dynamics are considerably faster than the spin-changing collision rate, the particle moves several times through the trap before a spin-changing collision occurs. This averages the local interaction and yields effectively a constant potential for all particles.

This effect can be understood as the formation of an effective long-range potential due to the influence of the harmonic trap. It can be more rigorously derived by using a transformation to a rotating frame and integrating out the trap dynamics, which has been demonstrated for 1d and connected to this work also for 3d systems [1, 200]. It

can be directly related to the ratio of two energy scales: First, there is the trap energy  $E_t = \hbar\omega_{x,y,z}$ , which accounts for the spatial dynamics. This is compared to the spin-changing mean-field energy  $E_{sc} = V_{ij}|_{i \neq j}$ , which reflects spin-changing collisions. Note that the spatial direction with the lowest trap frequency and the maximum value of the spin-changing collision channel are important for the following considerations.

In the regime accessible in the experiments, the trap energy is in general significantly higher than the spin-changing mean-field energy ( $E_t > E_{sc}$ ). The corresponding values for a 3d bulk system are  $E_t/h > 30$  Hz and  $E_{sc}/h < 7$  Hz and for a quasi 1d configuration  $E_t/h > 10$  Hz and  $E_{sc}/h < 3$  Hz. This makes it challenging to validate the considerations above experimentally. Therefore, a numerical study together with U. Ebling [203] has been performed to investigate the different regimes. In Fig. 5.6, the simulated time evolution of the spatial distribution is plotted, where three different scenarios can be distinguished:

**Trap-dominated regime** ( $E_t > E_{sc}$ )

The kinetic motion of the atoms, induced by the harmonic trap, is faster than the spin-changing dynamics. One clearly finds a suppression of any spatial deformations as shown in Fig. 5.6 A. This regime is realized in the experiments and justifies a single-mode approximation.

**Intermediate regime** ( $E_t \approx E_{sc}$ )

The kinetic motion and the spin-changing dynamics occur on comparable time scales. The formation of spatial structures is found in the simulations, which become even more pronounced for longer times (see Fig. 5.6 B). The single-mode approximation cannot be applied.

**Interaction-dominated regime** ( $E_t < E_{sc}$ )

The trap dynamics are slow and the local mean-field interaction drives local spin-changing dynamics. This induces the formation of strong spatial structures, where different parts of the system perform fully different spin dynamics. The limit of fixed particles in the trap is depicted in Fig. 5.6 C.

To conclude, the trap dynamics are found to induce the collective spin-changing behavior in the trap-dominated regime, which is an important result of this thesis. Note that only a few cycles in the harmonic trap are sufficient to average the mean-field potential considerably.

### 5.3.2 Suppression of spatial structures

The above-mentioned considerations motivate an experimental investigation of the spatial distribution arising from spin-changing dynamics. In the time-of-flight pictures no spatial structures could be found. However, the finite expansion time limits the significance of this observation.

Therefore, an in-situ experiment has been performed, directly revealing the spatial distribution of the atoms in the dipole trap. The fermions are loaded into a quasi 1d configuration with a large spatial extension of more than 300  $\mu\text{m}$  in the elongated direction. To resolve the time evolution of the spatial distribution experimentally, the spin-selective in-situ detection has been applied as described in section 3.2.4. In this case,

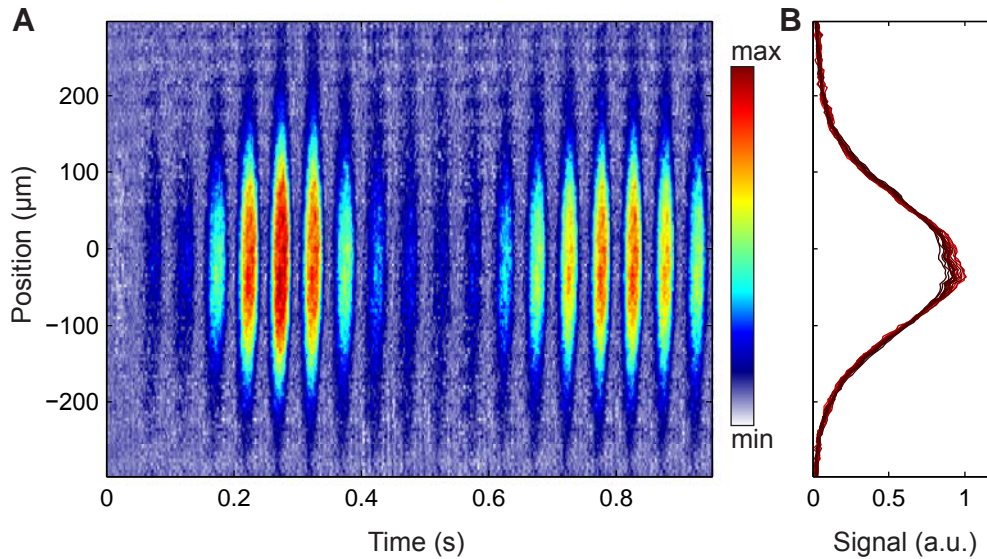


**Figure 5.7: Observed spatial distribution of a Fermi sea exposed to spin-changing collisions.** (A) In-situ images of the spatial distribution in the trap are depicted as a function of time. Shown is the difference to the initial spin distribution. Imaged is only the spin component  $m = -1/2$ , while the other spin components  $m \neq -1/2$  are transferred to the  $f = 7/2$  manifold prior to the detection. (B) Column sums of the pictures in A are depicted, normalized to the same occupation at each time step. The experiments are performed in a quasi 1d configuration with trapping frequencies of  $\omega = 2\pi \times (70, 70, 12)$  Hz. For a better experimental implementation, a spin instability (see section 6.3) is studied, similar to collective spin oscillations. The initial state is the spin mixture  $m = \{\pm 3/2\}$  at a magnetic field of  $B = 0.09$  G.

only one spin component ( $m = -1/2$ ) is imaged. Further spin components ( $m \neq -1/2$ ) are transferred to the  $f = 7/2$  manifold, which is transparent for the detection light.

Figure 5.7 A depicts the change of the spatial distribution as a function of time. As an important result, the observed distribution evolves accordingly to the density distribution in the trap. It reveals no discernible spatial structures within the experimental resolution. This is also illustrated in Fig. 5.7 B, where the spatial distribution normalized to the spin occupation is depicted. Note again the time scale of this effect, which extends up to 1 s. This experiment demonstrates that the observed collective spin dynamics can involve atomic ensembles with a large extension of several hundred micrometers, while spatial structures are widely suppressed. In general, it highlights the collective character of the spin dynamics despite the intrinsic multi-mode structure of the Fermi sea.

### 5.3.3 Influence of magnetic gradients

Spatial excitations constitute a limitation for the collective spin dynamics. In this context, the influence of a magnetic gradient is particularly important. It breaks the rotational symmetry of the system, which induces a spin-wave excitation (see section 3.3.2). This has been studied in detail in the course of this work, where spin waves in high-spin fermions were investigated [3]. The magnetic gradient induces a phase spiral, which

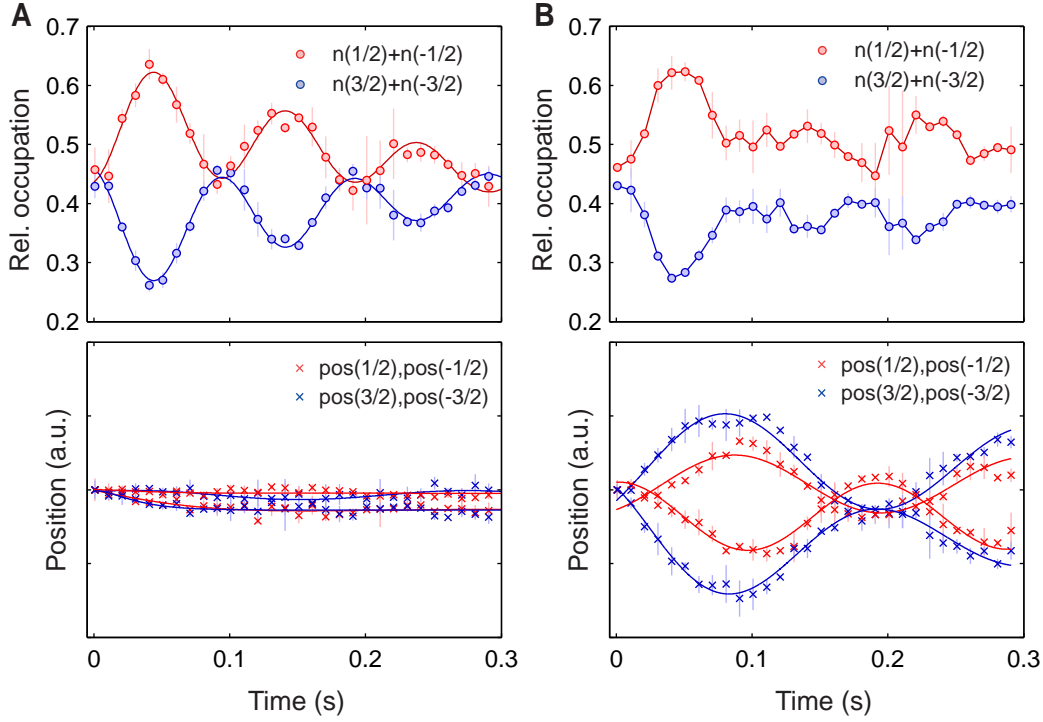


**Figure 5.8: Combination of spin waves and spin-changing collisions.** The time evolution of the relative spin populations  $n(m)$  (upper parts) and the corresponding center-of-mass positions after time-of-flight (lower parts) are depicted. **(A)** The magnetic gradient is compensated as good as possible. **(B)** A magnetic gradient of 1.2 mG/cm is applied during the experiment. The magnetic field is  $B = 0.17$  G and the trapping frequencies are  $\omega = 2\pi \times (70, 70, 12)$  Hz. The initial state preparation is chosen as in Fig. 5.5. Solid lines serve as guide-to-the-eyes.

leads combined with the harmonic confinement to counterflow dipole oscillations of the individual spin components, while the overall density remains constant (for details see thesis of J. Heinze [107]).

For the investigation of spin waves, spin-changing dynamics can be easily fully suppressed at large magnetic fields. However, spin waves are excited in the presence of very small magnetic gradients. Hence, they constitute a significant challenge to study spin-changing dynamics experimentally.

To investigate the impact of spin waves on spin-changing dynamics, the fermions are prepared in a quasi 1d configuration at low magnetic field. This favors spin-wave excitations and allows at the same time for spin-changing dynamics. First, the magnetic gradient is well compensated, revealing collective spin dynamics as depicted in Fig. 5.8 A. Depicted are the spin-occupation dynamics and the center-of-mass motion of the atoms. This experiment demonstrates that spin-changing oscillations are induced, while spatial oscillations are widely suppressed. In a second experiment, an additional small magnetic gradient of 1.2 mG/cm is applied, leading simultaneously to spin-changing dynamics and a spin-wave excitation. This is shown in Fig. 5.8 B, reflected in the spatial oscillations of the individual spin components.

As the data clearly show, the collective character of the spin-changing dynamics

is strongly affected by the spin-wave excitation. The occurrence of spatial dynamics leads to a complex behavior involving spin and spatial degrees of freedom. In this case, a single-mode approximation cannot be applied. To reproduce these results, full calculations with spatial resolution are necessary, which will be described in the thesis of U. Ebling [206]. The experimental data also suggest that after a full spatial oscillation period the spin-changing dynamics restart again, which underlines the coherence of the many-body system.

For the experiments described in the following, the magnetic gradient is compensated as good as possible to exclude spin-wave excitations. This can be achieved by carefully employing the compensation techniques described in section 3.3.2 prior to the experiments.

### 5.3.4 Implementation of a fermionic single-mode approximation

A single-mode approximation has been successfully employed to describe spin dynamics in spinor Bose-Einstein condensates [65, 79, 205]. This approach is a rather intuitive one for ultracold bosons, which occupy the same single-particle state and hence intrinsically share the same spatial distribution. Moreover, the superfluid phase of spinor bosons suppresses spin structures on the scale of the spin healing length [67, 68]. In contrast, a single-mode approximation is counterintuitive for fermions, which intrinsically have a multi-mode spatial structure. Nevertheless, the observed collective behavior alongside the trap-induced suppression of spatial structures motivates the implementation of a fermionic single-mode approximation.

In this approach the Wigner function  $w_{ij}(\mathbf{r}, \mathbf{p}, t)$  is assumed to separate into a product of a spatial part and a spin part. The spatial part can be approximated with the initial equilibrium distribution in a harmonic trap, given by the Thomas-Fermi distribution  $f(\mathbf{r}, \mathbf{p})$  (see appendix A). One assumes that the spatial part remains constant during the time evolution. Then the system can be approximated with

$$w_{ij}(\mathbf{r}, \mathbf{p}, t) = \underbrace{\rho_{ij}(t)}_{\text{spin part}} \cdot \underbrace{f(\mathbf{r}, \mathbf{p})}_{\text{spatial part}} . \quad (5.8)$$

Inserting this separation ansatz into the Boltzmann equation 5.5, all spatial and momentum degrees of freedom can be integrated out. This effectively replaces the Fermi sea with a fixed object, which is reflected in a vanishing spatial dependence. It yields the Boltzmann equation in single-mode approximation, given by

$$\partial_t \rho(t) = \underbrace{\frac{1}{i\hbar} \left[ \bar{V} \sum_{kl} (U_{klij} - U_{kjil}) \rho_{kl}(t), \rho(t) \right]}_{\text{averaged interaction}} + \underbrace{\frac{1}{i\hbar N} [qS_z^2, \rho(t)]}_{\text{Zeeman energy}} \quad (5.9)$$

with the interaction integral  $\bar{V}$ , which reads

$$\bar{V} = \int d\mathbf{r} n^2(\mathbf{r})/N . \quad (5.10)$$

Here,  $n(\mathbf{r}) = \int d\mathbf{p} f(\mathbf{r}, \mathbf{p})$  is the spatial density. The averaged interaction energy is characterized by a prefactor  $\bar{V}$ , which corresponds to the mean density of the system. Equation 5.9 forms a system of 100 differential equations, coupled by quadratic terms of the form  $(\rho_{ij} \cdot \rho_{kl})$ .

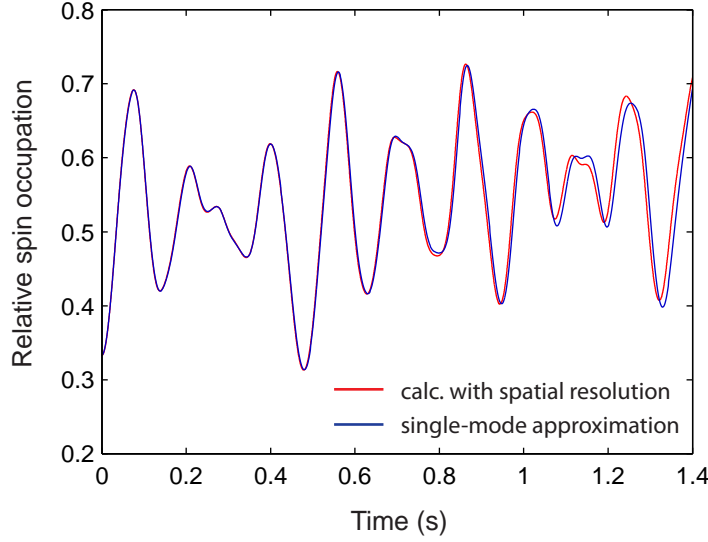


**Figure 5.9: Validity of the single-mode approximation.** The simulated time evolution of the relative occupation  $n(m = -1/2)$  is shown as a function of time. A calculation with spatial resolution in 1d (red line) reveals an excellent agreement with a single-mode approximation calculation (blue line). Simulations are performed in the trap-dominated regime with the same parameters as in Fig. 5.6. Calculations with spatial resolution are kindly provided by U. Ebling.

Figure 5.9 compares a single-mode approximation calculation (equation 5.10) to a simulation with spatial resolution in one dimension (equation 5.5). The parameters are chosen as in the actual experiments, where the spatial motion in the trap is much faster than the spin dynamics ( $E_t > E_{sc}$ ). As a key result, an excellent agreement between both approaches can be found. This highlights the justification of the single-mode approximation in the trap-dominated regime.

The fermionic single-mode approximation was worked out and implemented throughout this research work. In the following section, a detailed comparison between numerical simulations of this approximation and experimentally obtained spin-oscillation data will be presented.

## 5.4 Studying the spin-oscillation properties

The observation of giant spin oscillations in a fermionic many-body system constitutes a novel collective phenomenon. It is of general interest to study this in more detail, which also serves to investigate the validity of the mean-field approach introduced in section 5.1. In this context, the single-mode approximation provides a significant simplification. It allows to describe the many-body system only by global parameters, similar to spin dynamics in the two-body limit (see section 4.2).

In this section I will present a detailed study of the spin-oscillation properties. This will include the dependence on the magnetic field and the density. Moreover, the considerable control of the rf-preparation allows for a wide tunability of the initial spin configuration (see section 5.1.2), which will be investigated. Note that these experiments explore fermionic spin dynamics at low temperatures of about  $0.1 - 0.2 T_F$  in a 3d bulk system. It will turn out that this regime is dominated by mean-field interactions. The impact of higher temperatures and intermediate interaction strengths will be studied in chapter 6.

To extract the frequency and the amplitude from the spin-oscillation data, a damped oscillatory fit is employed as in the two-particle case (see appendix C). The experimental data are compared to single-mode approximation calculations solving the equation system 5.9. This requires only a small numerical effort and hence provides an ideal testing ground to study this simplified approach in depth. From the calculated spin dynamics, the frequencies are extracted with a Fourier analysis of the involved spin components. The oscillation amplitudes are taken as the differences between maximum and minimum of the spin oscillations. A phenomenological exponential damping with a rate of  $\Gamma = 2$  Hz is inserted in equation 5.9, which reduces the coherences exponentially (see appendix C). This accounts for the experimentally observed damping, while the spin-oscillation properties remain unaffected.

### 5.4.1 The influence of the magnetic field

The Zeeman energy is equally important for spin dynamics in the many-body system as in the two-body case. For the experimental study of this parameter, the initial state as in the proof-of-principle experiment has been employed, corresponding to a spin rotation of  $\theta = 0.44$  of the spin mixture  $m = \{\pm 1/2\}$ . Since the resulting spin oscillations occur mainly between the spin states  $\pm 1/2$  and  $\pm 3/2$ , the study is restricted to these spin configurations.

Figure 5.10 shows the obtained spin-oscillation properties for different magnetic fields. The data reveal that oscillation frequency and amplitude are strongly affected. This effect can be understood in the following way: With the magnetic field the system is tuned between two regimes. At large magnetic field, the Zeeman energy dominates and both spin configurations are strongly detuned from each other, yielding small-amplitude spin oscillations with high frequencies, which precisely follow the quadratic Zeeman effect. At low magnetic field, in contrast, interaction and Zeeman energy are about equal and giant spin oscillations with low frequencies are observed. In this regime, the oscillation frequencies are shifted to values larger than the Zeeman energy. The data of these experiments are compared to calculations using the single-mode approximation approach without free parameters. Over the whole magnetic field range, a very good agreement is demonstrated.

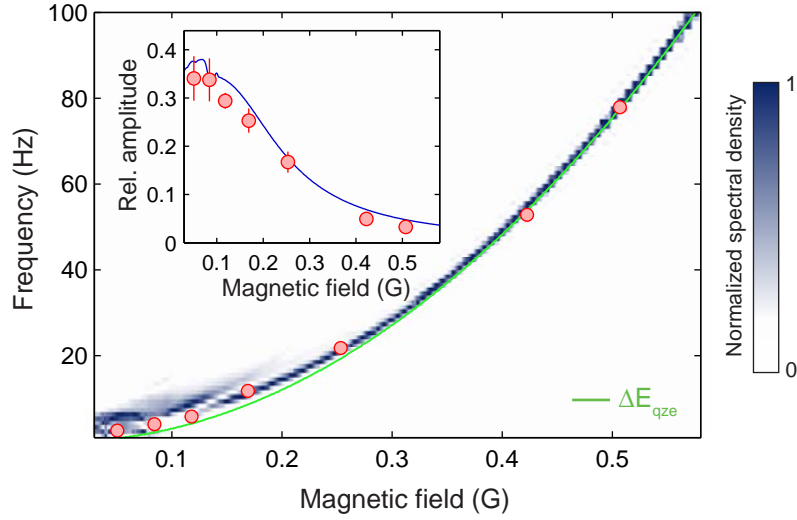


**Figure 5.10: Spin-oscillation properties for different magnetic fields.** Frequency (main graph) and amplitude (inset) of the collective spin dynamics are depicted as a function of the magnetic field. The initial state corresponds to the spin mixture  $m = \{\pm 1/2\}$  with a spin rotation of  $\theta = 0.44$ . The experimental parameters are  $n_p = 1.0 \times 10^{13} \text{ cm}^{-3}$  and  $T = 0.22 \text{ T}_F$ . Data points are deduced from fits and error bars correspond to two standard deviations. Amplitudes and frequencies are calculated in a single-mode approximation without free parameters (equation 5.9). They are depicted in false color in the main graph and as solid lines in the inset. The green line shows the differential Zeeman energy. Experimental data have also been published in [1].

While the general spin-oscillation behavior resembles the two-particle dynamics, a spin resonance as observed in the two-particle case (see section 4.2.3) cannot be clearly identified. In bosonic many-body systems with  $^{87}\text{Rb}$  in the  $f = 2$  hyperfine manifold [79], however, a spin resonance could be observed in our group, characterized by a maximum oscillation amplitude at vanishing oscillation frequency. In the fermionic experiment, in contrast, strong instability-driven dynamics are found at  $B < 0.1 \text{ G}$ , which will be discussed in chapter 6. These excitations emerge if the spin-changing mean-field energy and the differential magnetic energy are about equal. In this case, a strong spin redistribution sets in, which affects the spin-oscillation properties and also changes the resonance condition. This constitutes a general problem to observe a spin resonance in the fermionic many-body system.

#### 5.4.2 The influence of the density

The interaction strength of the system is characterized by the interaction integral  $\bar{V}$  (see equation 5.10), which is directly connected to the average density of the system. Combined with the involved scattering lengths, this value determines the mean-field energy.

The interaction integral depends on the temperature and the particle number of the system, which can be widely controlled (see section 3.2.3). In principle, it is also possible to tune this parameter by adjusting the underlying harmonic confinement. For a better general comparison with the single-mode approximation approach, however, this route

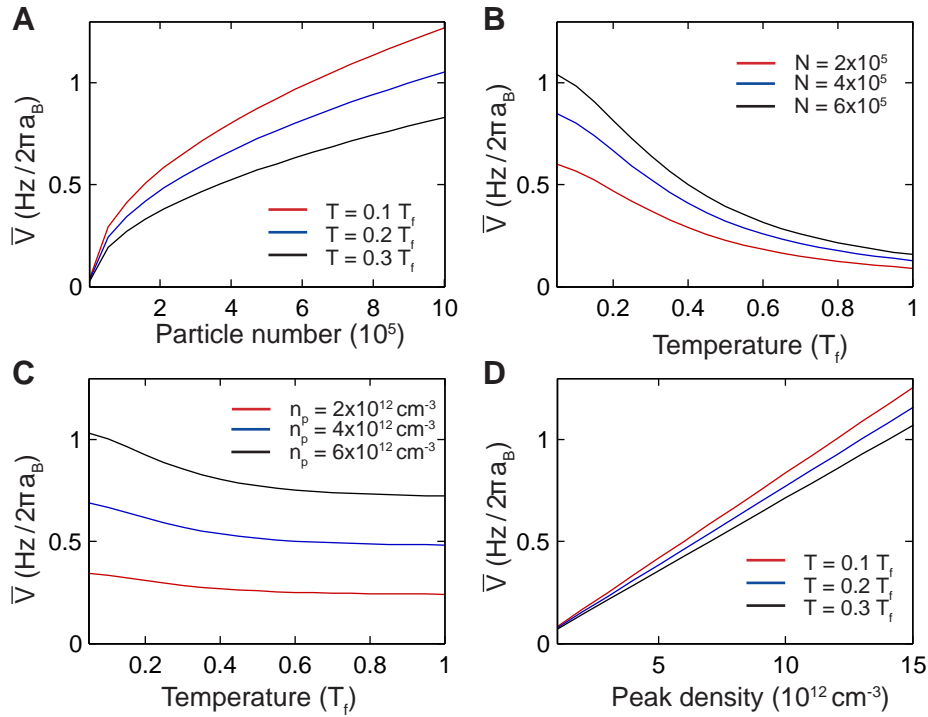


**Figure 5.11: The interaction integral  $\bar{V}$ .** Calculations of the interaction integral  $\bar{V}$  by solving equation 5.10 are shown. The values are calculated for different particle numbers  $N$ , temperatures  $T$ , and peak densities  $n_p$  in the 3d bulk system. **(A)**  $\bar{V}$  increases with  $N$  at constant  $T$ . **(B)**  $\bar{V}$  decreases at constant  $N$  for higher  $T$ . **(C)**  $\bar{V}$  decreases with  $T$  at constant  $n_p$ , which is only relevant in the quantum-degenerate regime. **(D)**  $\bar{V}$  increases linearly with  $n_p$  at constant  $T$ . Typically, the experimental parameters yields spin-changing mean-field interaction energies of several Hz.

has not been followed. Several important dependencies of  $\bar{V}$  are depicted in Fig. 5.11. The interaction integral is proportional to the density of the system. Moreover, it increases for higher particle number and decreases for higher temperatures. For the set of experiments described in the following, the density is tuned by adjusting the particle number. This provides a better comparison with the mean-field approach, while higher temperatures induce an enhanced damping of the spin oscillations (see chapter 6).

For the experimental study of the density dependence, again the initial state as in the proof-of-principle experiment has been employed, corresponding to a spin rotation of  $\theta = 0.44$  of the spin mixture  $m = \{\pm 1/2\}$ . Figure 5.12 depicts the spin-oscillation properties for different densities. Only a slightly increasing oscillation frequency is observed, which remains close to the quadratic Zeeman energy over the investigated density range. The mechanism behind this depends on the initially prepared spin configuration, which is in more detail discussed in section 5.4.3. As an important result, the oscillation amplitude is very small at low densities and significantly increases for higher densities. This effect can be intuitively understood in the following way: A higher average density increases the global collision rate alongside an enhanced spin-changing collision rate. Hence, with the density the system can be tuned continuously from suppressed spin

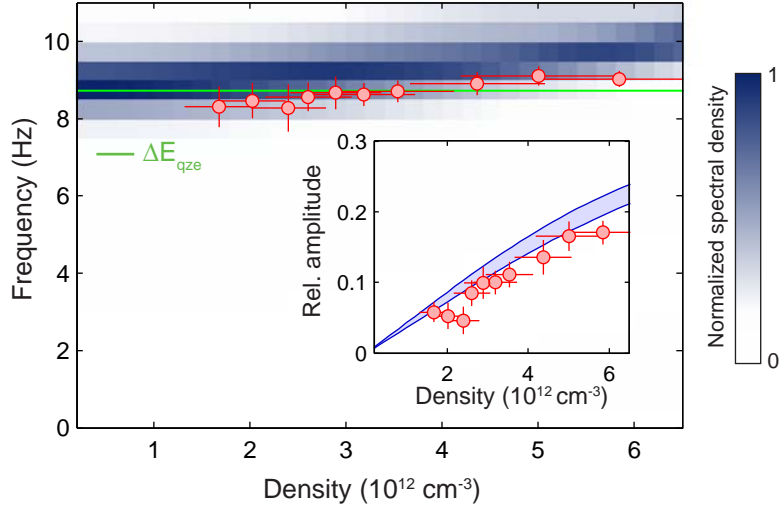


**Figure 5.12: Spin-oscillation properties for different densities.** Frequency (main graph) and amplitude (inset) of the spin oscillations are depicted as a function of the peak density. The initial state is the spin mixture  $m = \{\pm 1/2\}$  with a spin rotation of  $\theta = 0.44$ . The magnetic field is  $B = 0.17$  G and the density is varied by keeping  $T = 0.2 \pm 0.04 T_F$  constant. Data points are deduced from fits and error bars correspond to two standard deviations. Calculated amplitude and frequencies are derived from a single-mode calculation without free parameters (equation 5.9). Uncertainties in particle number and temperature are reflected in the shaded area in the inset. The green line shows the differential Zeeman energy. Experimental data have also been published in [1].

oscillations to the regime of giant spin oscillations.

The experimentally obtained data are compared to calculations employing the single-mode approximation. As for the magnetic field dependence, the whole density range yields a good agreement with the single-mode approximation approach without free parameters.

### 5.4.3 Engineering the mean-field background

Besides magnetic field and density, the initial spin configuration also strongly affects the spin oscillations. This parameter is ideally suited for a more intuitive understanding of the collisional properties in the mean-field regime. In experiments with Bose-Einstein condensates spin dynamics have been studied employing only a few specific spin rotation angles [77, 79, 80]. This restriction, however, is not necessary. The experimental control over the initial state allows to study spin dynamics initialized by arbitrary spin rotations (see section 5.1.2), which has been investigated.

For this purpose, the initial spin mixture  $m = \{\pm 1/2\}$  is prepared at low magnetic fields. In a second step, different rf-pulses are applied, which induce occupations as well as coherences presumable in the spin states  $\pm 1/2$  and  $\pm 3/2$ . The obtained spin-oscillation properties are depicted in Fig. 5.13, revealing a strong dependence on the initial pulse. First, the amplitude of the spin oscillations increases, which reflects the increasing initial spin occupations and coherences. Second, the frequency of the spin oscillations decreases and reaches nearly the quadratic Zeeman energy at large spin

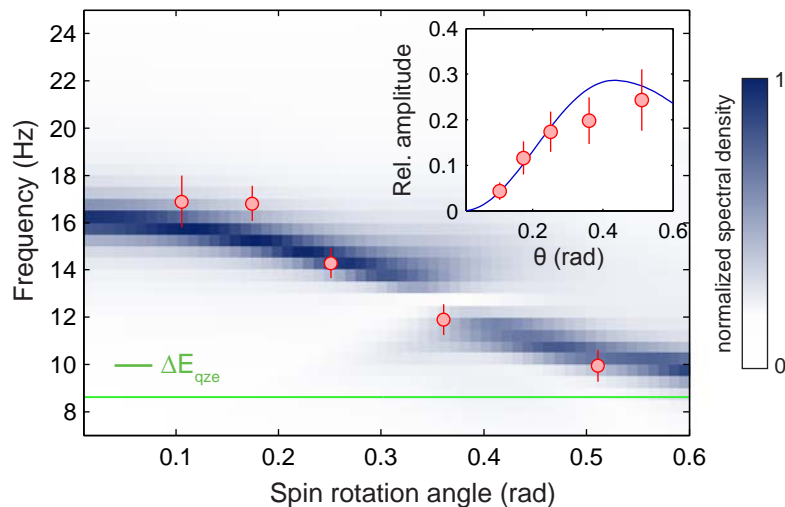


**Figure 5.13: Spin-oscillation properties for different spin rotations.** Frequency (main graph) and amplitude (inset) of the spin oscillations are shown as a function of the spin rotation angle  $\theta$ , applied to the spin mixture  $m = \{\pm 1/2\}$ . The experimental parameters are  $B = 0.17$  G,  $n_p = 1 \times 10^{13}$  cm $^{-3}$  and  $T = 0.22$  T $_F$ . Data points are deduced from fits and error bars correspond to two standard deviations. The calculations are performed using the single-mode approximation without free parameters (equation 5.9). The green line corresponds to the differential Zeeman energy.

rotations of  $\theta \approx 0.5$ . These experiments are also compared to simulations employing a single-mode approximation. Covering the investigated parameter regime, a good agreement is found without free parameters.

In particular the effect of the initial spin state on the spin-oscillation frequency is unexpected. This intriguing observation motivates a more detailed view on spin-changing collisions in the many-body regime and can be intuitively understood in the following way: Consider one atom pair, which performs spin-changing dynamics in the mean-field background provided by all other particles. Spin-changing collisions change the magnetic energy of the atoms in analogy to the two-particle case. In contrast, the situation is different for the interaction energy, which depends on the initial spin rotation in the many-body case. For small  $\theta$ , the mean-field background remains widely unaffected and is provided by the initial spin mixture. After a spin-changing collision, the atom pair is transferred into a new spin configuration and hence exposed to another mean-field interaction energy given by the different coupling constants  $U_{ijkl}$ . The resulting spin-oscillation frequency is therefore determined by the Zeeman energy with an additional mean-field shift. However, if the spin rotation is chosen, such that a balanced mean-field background is realized, the atom pair is exposed to the same mean-field interaction before and after the spin-changing collision. In this case, the spin-oscillation frequency is only given by the Zeeman energy.

These considerations are not only consistent with the experimental results depicted in Fig. 5.13, but also explain the frequencies observed for different magnetic fields (see Fig. 5.10) and different densities (see Fig. 5.12). In both cases, the spin-oscillation frequencies are similar to the Zeeman energy, which can be attributed to the rather

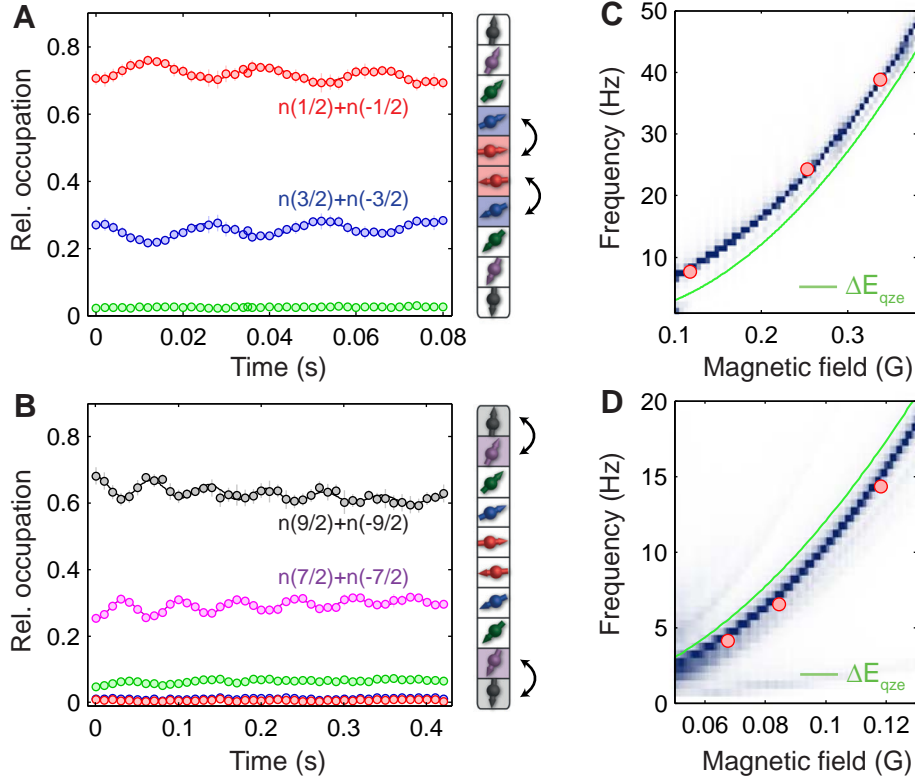


**Figure 5.14: Spin oscillations in different spin mixtures.** The time evolution of the spin occupations for the spin mixture  $m = \{\pm 1/2\}$  at  $B = 0.34$  G (A) and  $m = \{\pm 9/2\}$  at  $B = 0.12$  G (B) is depicted, both exposed to a spin rotation of  $\theta = 0.22$ . The spin-oscillation frequencies are plotted for  $m = \{\pm 1/2\}$  (C) and for  $m = \{\pm 9/2\}$  (D) as a function of the magnetic field. Data points are deduced from fits. The calculations are performed using the single-mode approximation without free parameters (equation 5.9). Green lines show the corresponding differential Zeeman energy.

strong rotation angle of  $\theta = 0.44$ . This preparation yields a nearly balanced mean-field background, which strongly reduces the mean-field shift and results in spin oscillations close to the Zeeman energy.

#### 5.4.4 Spin dynamics between different spin mixtures

As worked out above, the spin-oscillation properties depend significantly on the initial spin configuration. The data presented so far show that spin dynamics occur between occupied states connected with coherences, which sets the route for an experimental investigation. Beyond the tuning of the initial spin rotation, it is therefore interesting to evaluate spin dynamics for completely different spin mixtures. Due to the high spin of  $^{40}\text{K}$  combined with a versatile spin preparation tool (see section 5.1.2), the experimental system provides an ideal testing ground in this direction.

To realize this experimentally, two different spin mixtures are compared, namely  $m = \{\pm 1/2\}$  and  $m = \{\pm 9/2\}$ . In both cases, an initial spin rotation angle of  $\theta = 0.22$  is applied. It is chosen rather small to enhance the influence of the mean-field background

and to induce a significant interaction shift (see section 5.4.3).

As depicted in Fig. 5.14 A, the spin mixture  $m = \{\pm 1/2\}$  with prepared coherences exhibits spin oscillations between the spin states  $\pm 1/2$  and  $\pm 3/2$ . Due to the small spin rotation, the corresponding amplitude is below 10%. Moreover, the spin mixture  $m = \{\pm 9/2\}$  with prepared coherences (for details see appendix C) also shows spin oscillations. In this case, however, the involved spin states are  $\pm 9/2$  and  $\pm 7/2$  as depicted in Fig. 5.14 B. This is a direct consequence of the preparation scheme, which leads, starting from  $m = \{\pm 9/2\}$ , to spin occupations and coherences between these spin configurations. This experiment demonstrates that spin dynamics can be realized in different spin mixtures.

In this context, it is particularly interesting to study the interplay between interaction and quadratic Zeeman effect and its influence on the oscillation properties. Therefore, the experiments have been repeated at different magnetic fields. The resulting spin-oscillation frequencies for  $m = \{\pm 1/2\}$  are depicted in Fig. 5.14 C and clearly show an interaction shift. In this case, the mean-field interaction increases the spin-oscillation frequency compared to the corresponding Zeeman energy difference. This is consistent with the considerations as described in section 5.4.3. The spin mixture  $m = \{\pm 9/2\}$  also exhibits an interaction shift, however, the direction is inverted. It decreases the spin-oscillation frequency compared to the corresponding Zeeman energy difference as depicted in Fig. 5.14 D. This can be attributed to an effective change in sign of the interaction differences compared to the Zeeman energy difference and directly results from the initial preparation. For both cases, the data are compared to single-mode approximation calculations. The frequency shift can be well reproduced in the simulations without free parameter.

### 5.4.5 Direct observation of high-collision quanta

The presented spin-oscillation experiments are dominated by collisions, which change the spin configuration of each particle by  $\Delta m = 1$ . It is a fundamental question, whether collective spin dynamics can also involve higher collision quanta ( $\Delta m > 1$ ), which has not been reported so far. The observation of high-collision quanta in the two-body limit (see section 4.2.6) motivates an experimental study in this direction. As a final study of the spin-oscillation properties, I demonstrate the experimental realization of a Fermi sea performing spin oscillations with a collision quantum of  $\Delta m = 2$ .

So far, for most of the presented experiments the mixture  $m = \{\pm 1/2\}$  was rotated leading to occupations of the spin states  $\pm 1/2$  and  $\pm 3/2$  connected with coherences. In general, collective spin dynamics drive oscillations between occupied spin configurations, which are connected by coherences. Hence, the realization of high-collision quanta requires significant occupations and coherences between spin configurations coupled by  $\Delta m > 1$ . For this, one can perform a spin rotation of the spin mixture  $m = \{\pm 3/2\}$  (see appendix C). Figure 5.15 A depicts the corresponding initial density matrix and the impact of a spin rotation of  $\theta = 0.42$ . As a particular feature, this rotation yields occupations predominantly in the spin states  $\pm 1/2$  and  $\pm 5/2$  connected by significant coherences. Therefore, this state constitutes a promising candidate to study spin dynamics with high-collision quanta.

Monitoring the time evolution of such a state demonstrates that spin oscillations are induced, which are exemplarily depicted in Fig. 5.15 B. As a key result, the spin dynamics occur between the spin configurations  $\pm 1/2$  and  $\pm 5/2$ . This constitutes the

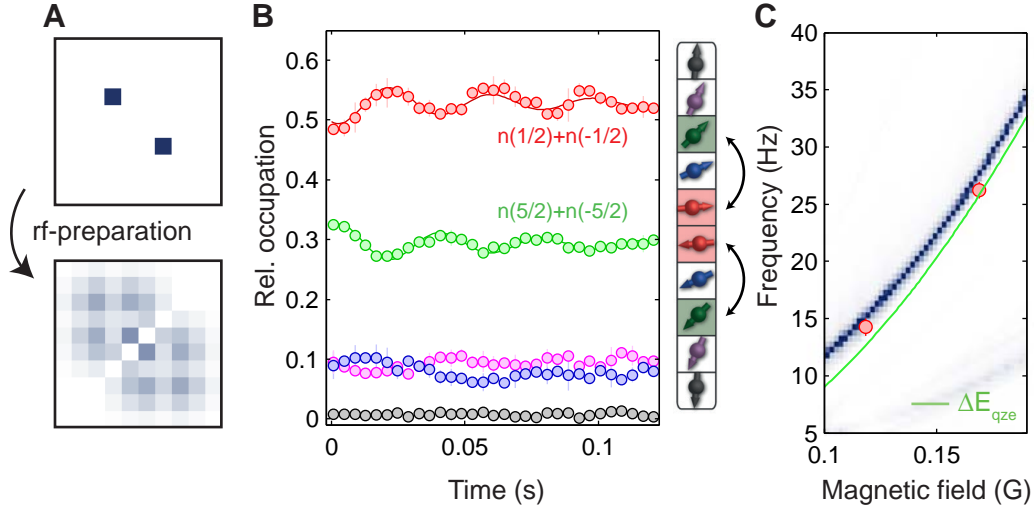


**Figure 5.15: Direct observation of spin oscillations with  $\Delta m = 2$ .** (A) Density matrices of the spin mixture  $m = \{\pm 3/2\}$  without spin rotation (upper part) and with  $\theta = 0.42$  (lower part) are shown. The spin states  $\pm 1/2$  and  $\pm 5/2$  are mainly occupied and connected by coherences. (B) Spin oscillations of an initial state as depicted in the lower part of A, revealing spin-changing collisions with  $\Delta m = 2$ . The magnetic field is  $B = 0.17$  G. (C) The spin-oscillation frequencies for the same initial state are plotted as a function of the magnetic field. Data points are deduced from fits. Experimental parameters are  $T = 0.25 T_F$  and  $n_p = 8 \times 10^{12} \text{ cm}^{-3}$ . The calculations are performed using the single-mode approximation (equation 5.9). The green line shows the differential Zeeman energy.

first observation of high-collision quanta in a many-body system. All further spin states have only minor occupations and do not considerably contribute to the spin dynamics. To underline that the collisions directly transfer atom pairs with a collision quantum of  $\Delta m = 2$ , the spin-oscillation frequencies have been measured for different magnetic fields. The data are compared to calculations in single-mode approximation as depicted in Fig. 5.15 C without free parameters. The resulting frequency is in good agreement with the simulations and shows a small positive shift from the Zeeman energy. The amplitude is only about 7%, which is due to the reduced coupling elements. These obtained results complement the study of the spin-oscillation properties and underline  $^{40}\text{K}$  as a perfect candidate to investigate many-body spin dynamics in high-spin fermions.

## 5.5 Conclusion and outlook

In this chapter, a detailed investigation of an ultracold Fermi sea exposed to microscopic spin-changing collisions was presented. As a key result, giant and long-lived spin oscillations have been observed, despite the intrinsic multi-mode structure of the fermionic many-body system. This constitutes a completely new collective effect for fermions. It could be attributed to the spatial dynamics of the harmonic trap: If these dynamics are faster than the spin dynamics, the Fermi sea acts as one object in spin space – even for large samples with a spatial extension of several hundred micrometers and several  $10^5$  particles. A detailed study of the spin-oscillation properties has validated a simplified description in a single-mode approximation. Moreover, the experiments demonstrate the tunability and the high experimental control over spin dynamics in the mean-field regime.

It turns out that the collective behavior of the Fermi sea is similar to spin-mixing dynamics in Bose-Einstein condensates [67, 68]. However, the spin oscillations are driven by a completely different mechanism in the fermionic many-body system. This intriguing mechanism induced by the harmonic trap is a general feature of trapped many-body systems and crucial for collective phenomena [1, 200]. For example, it also explains the recent observation of long-lived collective spin dynamics in a thermal Bose gas [207]. In addition, it should play a supportive role for further many-body effects of harmonically trapped high-spin fermions. In this respect, a variety of new many-body phenomena come experimentally into reach: Topological structures in superfluid high-spin fermions or high-spin pairing [88–96, 105, 158, 208] still remain widely unexplored. However, pairing requires attractively interacting Fermi gases, which cannot be directly realized with  $^{40}\text{K}$ . Alongside current studies with  $^6\text{Li}$ , where this is possible, another approach are attractively interacting spin mixtures in optical lattices at negative temperatures, which was recently demonstrated for bosons [209, 210]. Beyond this, the spin-changing dynamics combined with spin-spatial excitations such as spin waves [3, 58, 150] provide an ideal testing ground for the study of coherences properties. Furthermore, there is still a lack of understanding compared to high-spin bosons [67, 68]. Here further theoretical studies with analytical approaches are required [211].

The excellent agreement between the spin-oscillation properties and the single-mode mean-field approach has validated this single-particle description. However, damping effects and the incoherent rise of new spin states already suggest contributions beyond the mean-field approximation [212–215]. Indeed, the fermionic many-body system is driven by a complex interplay between several collision processes involving spatial and spin degrees of freedom [152]. This will be the subject of the following chapter.



## Chapter 6

# Relaxation in high-spin fermions

Relaxation is among the most puzzling phenomena in many-body physics [212–215]. Quantum gases provide an exceptional experimental platform to address these effects: They are well-isolated from their environment and constitute a nearly perfect realization of closed quantum systems. Moreover, the exceptional parameter control provides the unique possibility to simulate various Hamiltonians with tailored initial states [31]. A further advantage are the time scales of the relaxation processes, which are in general slow compared to solid-state or molecular systems. In recent years, this topic has gained a lot of attention: Experiments could address prethermalization, where the equilibration dynamics is driven by processes considerably faster than the thermal equilibration time [216–218]. Furthermore, the suppression of relaxation in strongly interacting lattice systems [219–221] has been studied.

Quantum gas systems with high spin allow for relaxation also among the spin degree of freedom. Experiments with spinor Bose-Einstein condensates have investigated for example the formation of spin domains [69, 70], and an intriguing interplay between condensate and thermal fraction has been observed [222]. High-spin fermions are especially interesting for the study of relaxation since they combine the spin degree of freedom with an intrinsic multi-mode structure. They are governed by collision processes, which involve spin and spatial degrees of freedom. Due to the fermionic quantum statistics, the interplay between these processes depends on global properties such as temperature or interaction strength. Here the observation of collective spin dynamics – which was presented in chapter 5 – constitutes an ideal starting point for a further experimental study. While the spin oscillations are well captured in a mean-field theory, the damping and the incoherent rise of new spin states allow to directly investigate relaxation properties.

In this chapter, I will present an investigation of the collisional properties of a weakly interacting fermionic many-body system. It will start from a microscopic approach, in which possible collision processes will be presented and which can be treated theoretically with a Boltzmann equation including a collision term (section 6.1). Then I will study the influence of finite temperature on the collective spin dynamics (section 6.2). Furthermore, the impact of higher densities will be investigated in section 6.3. Eventually, I will present experiments, which explore novel spin-relaxation dynamics in a high-spin Fermi sea (section 6.4).

Parts of this chapter have been published in [1, 2]. The experiments and the data analysis were performed with C. Becker, N. Fläschner, J. Heinze, and K. Sengstock.

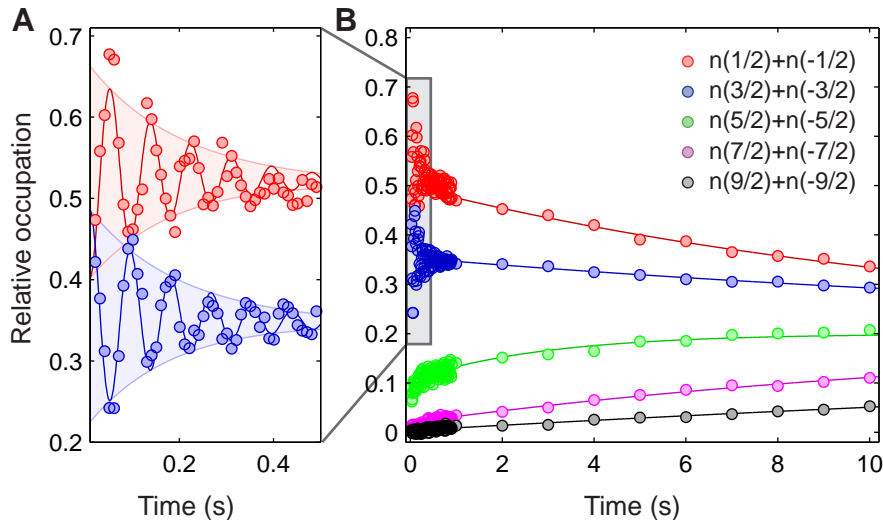


**Figure 6.1: Long-term spin dynamics.** Damped spin oscillations (**A**) and the subsequent spin relaxation of the system towards an equilibrium spin distribution (**B**) are depicted. As initial state, the spin mixture  $m = \{\pm 1/2\}$  with a spin rotation of  $\theta = 0.44$  is used. Solid lines are guide-to-the-eyes. The magnetic field is  $B = 0.17$  G, the particle number  $N = 4.9 \times 10^5$  and the temperature  $T = 0.22 T_F$ . Note the very different time scales of the spin dynamics. Experimental data have also been published in [2].

## 6.1 Collision processes in a high-spin Fermi sea

The giant spin oscillations studied in chapter 5 show an excellent agreement with simulations of the collisionless Boltzmann equation. This demonstrates that the observed collective behavior is well captured in a mean-field approximation.

However, this approach cannot describe the full dynamical behavior of the fermionic many-body system [152]. The observed damping and the incoherent rise of new spin components, which appear alongside the collective spin oscillations, suggest that further processes occur. These are identified as lateral collisions, which constitute a beyond-mean-field effect inducing relaxation of the many-body system.

In this section, different collision processes in a fermionic many-body system will be worked out on a microscopic level. They govern the macroscopic behavior of the Fermi sea and occur on very different time scales. For a theoretical description, a Boltzmann equation including a collision term will be introduced.

### 6.1.1 A microscopic approach

To identify different collision processes, a long-term spin-dynamics experiment has been performed, depicted in Fig. 6.1. The time evolution of an initial state prepared with coherences is monitored for ten seconds. In this long-term measurement, three effects occurring on very different time scales can be clearly distinguished:

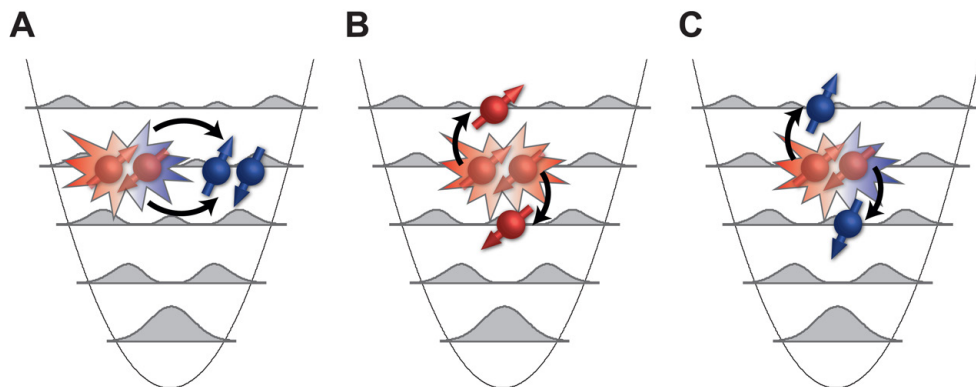


**Figure 6.2: Collision processes in a high-spin Fermi sea.** Three processes are sketched, driving the dynamics of the many-body system: (A) A spin-changing forward collision, preserving the momentum configuration. (B) A spin-conserving lateral collision, which changes the momentum configuration (illustrated as change of the trap level), but preserves the spin configuration. (C) A spin-changing lateral collision, changing the momentum and the spin configuration.

---

#### Observation (i): Mean-field spin oscillations

The system exhibits collective spin dynamics for about 500 ms (see data zoom in Fig. 6.1 A). The giant spin oscillations occur with a frequency on the order of several Hz.

#### Observation (ii): Damping of the collective dynamics

In addition, the spin oscillations are damped, which occurs on a time scale of a few Hz (see Fig. 6.1 A). Since the experiment is performed in the trap-dominated regime, mean-field driven spatial dephasing is widely suppressed [1, 200] and does not serve as an explanation.

#### Observation (iii): Spin-relaxation dynamics

After the spin oscillations are damped out, a slow spin redistribution is observed (see Fig. 6.1 B). This process occurs on a much longer time scale of several seconds and drives the system towards an equal spin distribution.

While the collective spin oscillations are well captured in a mean-field approach, the observed damping and the spin-relaxation dynamics constitute beyond-mean-field effects. In this context, a more detailed view of the collision process on a microscopic level is instructive.

For this purpose, the high-spin scattering process between two particles (introduced in section 2.2) can be extended to the spatial degrees of freedom, which are available in the many-body system. Consider two particles, each in the state  $|m_i^{(k_i)}\rangle$ , where  $m_i$  is the magnetic quantum number and  $k_i$  the momentum of the particle  $i$ . The corresponding two-particle state can be represented by  $|m_1^{(k_1)}, m_2^{(k_2)}\rangle$ . A collision can change the spin as well as the momentum configuration of the involved particles:

$$|m_1^{(k_1)}, m_2^{(k_2)}\rangle \rightarrow |m_3^{(k_3)}, m_4^{(k_4)}\rangle. \quad (6.1)$$

For this scattering process, the total magnetization ( $m_1 + m_2 = m_3 + m_4$ ) as well as the total momentum ( $k_1 + k_2 = k_3 + k_4$ ) have to be conserved. Moreover, the Pauli exclusion principle must be obeyed, implying that

$$\left| m_1^{(k_1)} \right\rangle \neq \left| m_2^{(k_2)} \right\rangle \text{ and } \left| m_3^{(k_3)} \right\rangle \neq \left| m_4^{(k_4)} \right\rangle . \quad (6.2)$$

Three different processes can be distinguished, which are sketched in Fig. 6.2:

**Process (i): Spin-changing forward collisions**

These collision processes change the spin configuration ( $\{m_1, m_2\} \neq \{m_3, m_4\}$ ), while the momentum remains unaffected ( $\{k_1, k_2\} = \{k_3, k_4\}$ ) (see Fig. 6.2 A). They drive the collective spin oscillations [152]. Note that there are also spin-conserving forward collisions, which can affect the system for example in the case of an applied gradient.

**Process (ii): Spin-conserving lateral collisions**

These collisions change the momentum configuration of the atoms ( $\{k_1, k_2\} \neq \{k_3, k_4\}$ ), but not the spin configuration ( $\{m_1, m_2\} = \{m_3, m_4\}$ ) (see Fig. 6.2 B). In general, this induces a damping of the collective spin dynamics [152]. These processes are crucial for the experiments presented in sections 6.2 and 6.3.

**Process (iii): Spin-changing lateral collisions**

These processes change both, the momentum ( $\{k_1, k_2\} \neq \{k_3, k_4\}$ ) as well as the spin configuration ( $\{m_1, m_2\} \neq \{m_3, m_4\}$ ) (see Fig. 6.2 C). Beyond a damping of the spin oscillations, they induce spin-relaxation dynamics towards an equal distribution among all available spin states. This is studied in section 6.4.

### 6.1.2 The collision term

Forward scattering is described within a mean-field approach by the collisionless Boltzmann equation, leading to undamped spin oscillations. The damping of the mean-field dynamics and the slow spin redistribution are driven by lateral collisions, which are not captured within this approximation. For this, a more sophisticated theoretical description is required.

In connection with the performed experiments, a description of lateral collisions in the framework of the Boltzmann equation has been derived by U. Ebling and coworkers, starting from the microscopic collision process [2]. The resulting Boltzmann equation reads

$$\partial_t w(\mathbf{r}, \mathbf{p}) = \underbrace{\partial_0 w(\mathbf{r}, \mathbf{p}) + \frac{1}{\hbar} [V(\mathbf{r}, \mathbf{p}) + qS_z^2, w(\mathbf{r}, \mathbf{p})]}_{\text{collisionless approach}} + \underbrace{I_{\text{coll}}(w(\mathbf{r}, \mathbf{p}))}_{\text{collision term}} . \quad (6.3)$$

Here,  $\partial_0$  accounts for the trap (see section 5.1.1) and  $I_{\text{coll}}$  is called the collision term or the collisional integral. The detailed derivation of the collision term for 1d and 3d systems can be found in [2].

In the following, I provide a sketch of the general concept. The collision term was derived using a method developed by Lhuillier and Laloë [152, 223, 224], which was extended to a high-spin system. In general, it can be applied to weakly-interacting and harmonically-trapped gases. Various effects have been successfully described within

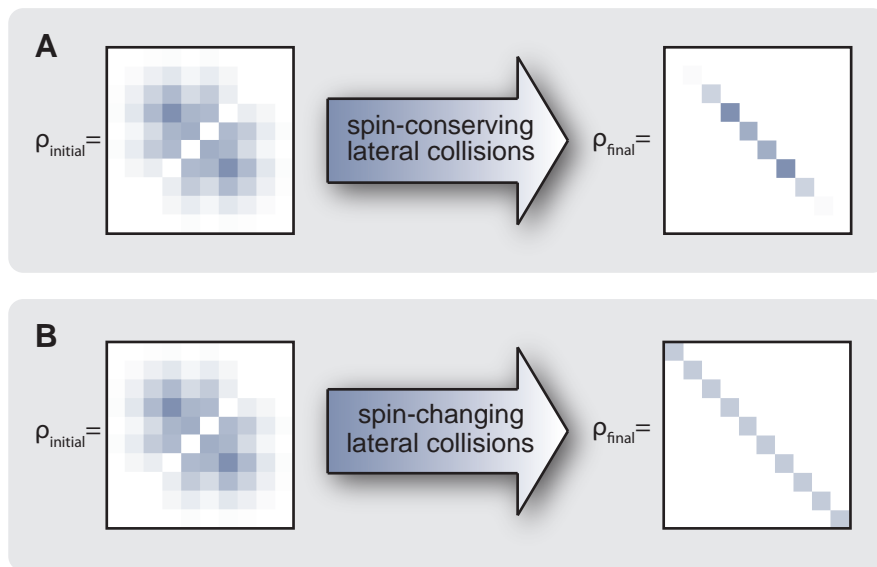


**Figure 6.3: Impact of lateral collisions on the density matrix.** Depicted is the initial density matrix with coherences  $\rho_{\text{initial}} = \rho(t=0)$  (used for the experiment in Fig. 5.5) as well as the final density matrix  $\rho_{\text{final}} = \rho(t \rightarrow \infty)$  for two processes: **(A)** Spin-conserving lateral collisions reduce the coherences, which drive the collective spin oscillations. **(B)** Spin-conserving lateral collisions reduce the coherences and lead in addition to a spin redistribution among all spin states.

this approach, including spin dynamics in liquid Hydrogen and Helium [223–229] and spin 1/2 fermions [152, 198]. In contrast to the mean-field treatment, where a single particle is considered (see 5.1), this ansatz considers two particles described by a two-body density matrix  $\rho(1, 2)$ . Binary collisions are described by the Heisenberg  $S$ -matrix, which accounts for the collisions on a quantum level. However, the particles are assumed to be uncorrelated before and after the collision ( $\rho(1, 2) = \rho(1) \otimes \rho(2)$ ), which is justified for a large and dilute system. Finally, the two-particle density matrix is reduced to the single-particle level by tracing out the second particle. In terms of the single-particle density matrix, one can regard the second particle as the thermal bath, which provides the collisional decoherence for the first particle [230, 231].

This ansatz accounts for lateral collisions: spin-conserving as well as spin-changing ones. They have a quadratic dependence in terms of the scattering length (see equation 6.9). This reflects their higher-order character in contrast to the mean-field contributions, which appear only linear in the scattering lengths (see equation 5.5). Moreover, this quadratic dependence is important for the ratio of spin-conserving and spin-changing lateral collisions, where the latter are quadratically suppressed, since they depend on the scattering length difference. The impact of lateral collisions on the density matrix is sketched in Fig. 6.3. In general, lateral collisions reduce the coherences of the system, which drive the collective spin oscillations [152] (see Fig. 6.3 A). This leads to a damping of the mean-field dynamics and can be interpreted as a redistribution of single-particle coherences into higher-order coherences. Beyond this, spin-changing lateral collisions lead in addition to a redistribution of the occupations among all spin states (see Fig. 6.3 B).

To compare the experiments to the theory described above, several routes have been followed: The full Boltzmann equation can be numerically solved for 1d systems (see section 6.4). However, most experiments are performed in 3d bulk systems, where the numerical simulations are too demanding. In this case, a phenomenological relaxation approximation is used, which is often employed in complex many-body systems [202, 232]. For this, the collision term is approximated with  $I_{\text{coll}}(w) = (w_{\text{eq}} - w) \cdot \Gamma$ , where  $w_{\text{eq}}$  is the equilibrium state and  $\Gamma$  the relaxation rate. The latter can be calculated from a linearized version of the collision term. The equilibrium state is phenomenologically assumed to be incoherent ( $w_{i,j}^{\text{eq}}|_{i \neq j} = 0$ ). This approach is used to calculate the damping of the spin oscillations for different temperatures and densities (see sections 6.2, 6.3) [1]. The 1d simulations as well as the calculations for the damping rates are kindly provided by U. Ebling. Beyond this, a single-mode approximation has been implemented for the collision term, which is presented in section 6.4.

## 6.2 Impact of temperature on collective spin dynamics

The quantum statistics dominates the collision processes in a fermionic many-body system. This has important consequences for various phenomena, for example for conduction and coherence properties in solid-state systems [174, 233]. Due to the Pauli exclusion principle, collision channels can be strongly suppressed at low temperatures, when only a few free states are available in the Fermi sea. At higher temperatures, the Fermi distribution is smoothed out and the influence of Pauli blocking is reduced.

Recently, experiments have demonstrated that also in thermal gases coherence and collective behavior can be preserved for long time scales [207, 234]. In these systems, however, the spatial degrees of freedom were energetically frozen out. Beyond this, it is fundamental to investigate the interplay between different scattering processes in the context of Pauli blocking and temperature. For this purpose, collective spin oscillations are ideally suited, since spin dynamics are intrinsically driven by collisions of the system.

In this section, I will study fermionic spin dynamics at different temperatures. In contrast to recent experiments investigating spin oscillations in thermal Bose gases [207], the experimental configuration allows for forward and lateral collisions due to the relatively shallow trap. First, the impact of higher temperatures for the different collision processes will be described. Then I will present experiments revealing a strong damping of collective spin dynamics for increasing temperature.

### 6.2.1 Scattering processes at higher temperatures

The collision processes introduced in section 6.1 depend on temperature in a different way. This can be intuitively understood in a general fashion as a direct result of the fermionic quantum statistics  $f_{\text{FD}}(E_k, T)$  (see appendix A).

Forward collisions, which drive the mean-field spin oscillations, conserve the momentum configuration ( $\{k_1, k_2\} = \{k_3, k_4\}$ ). Hence, these mean-field processes are intrinsically independent of the Fermi distribution. The temperature only affects mean-field interactions in a trivial way, which is related to the average density of the system (see section 5.4.2).

Lateral collisions, in contrast, are characterized by a momentum exchange ( $\{k_1, k_2\} \neq \{k_3, k_4\}$ ) and can strongly depend on temperature. These processes resemble particle-hole excitations in solid-state systems [174]. In a simplified picture, the corresponding

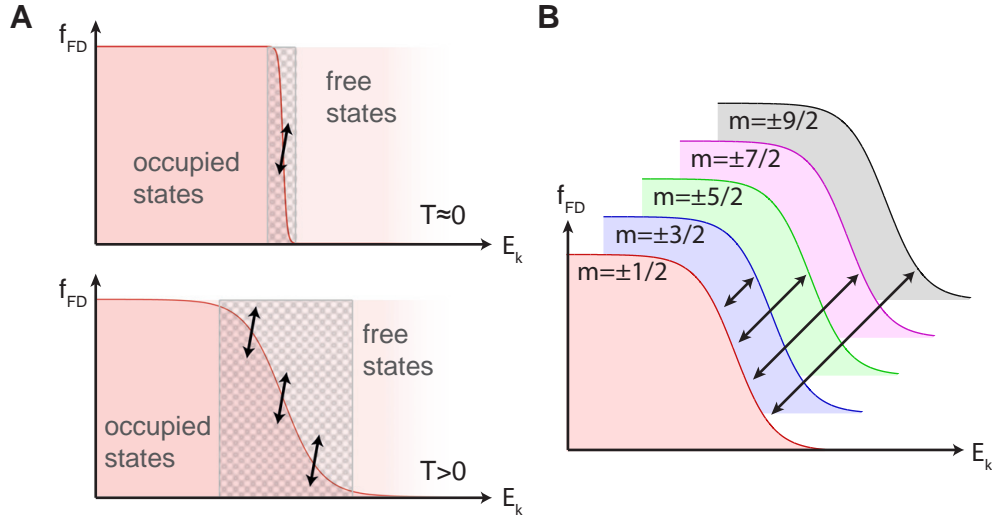


**Figure 6.4: Sketch of lateral collisions at finite temperature.** (A) Spin-conserving lateral collisions are illustrated, which are temperature-dependent due to the Pauli exclusion principle. Low temperatures (upper part) and higher temperatures (lower part) yield different collision rates indicated with the hatched region. (B) Spin-changing lateral collisions are sketched. The scattering process transfers the atoms between different spin configurations, whereby the corresponding rate is approximately temperature-independent. Arrows indicate lateral collisions.

collision rate can be approximated as the probability to find a particle (initial state) and a hole (final state). In this context, one has to distinguish between spin-conserving and spin-changing lateral collisions. They depend on temperature in a different way, as sketched in Fig. 6.4.

Spin-conserving lateral collisions change only the momentum and not the spin configuration ( $\{m_1, m_2\} = \{m_3, m_4\}$ ). Hence, they require free momentum states in the Fermi sea. The corresponding collision rate can be approximated as

$$\Gamma_{\text{lat}}^{\text{nc}} \propto \underbrace{f_{\text{FD}}(E_k, T)}_{\text{particles}} \cdot \underbrace{(1 - f_{\text{FD}}(E_k, T))}_{\text{holes}}. \quad (6.4)$$

Here, the second term reflects the probability to find a free momentum state. At ultralow temperatures, the Fermi sea is completely filled and the Fermi statistics do not provide free spatial states due to Pauli blocking. In this case, spin-conserving lateral collisions are fully suppressed [235]. However, for increasing temperature, free momentum states become available allowing for lateral spin-conserving collisions (see Fig. 6.4 A). Therefore, the corresponding collision rate  $\Gamma_{\text{lat}}^{\text{nc}}$  is temperature-dependent [232].

Spin-changing lateral collisions, in contrast, change the momentum and the spin configuration ( $\{m_1, m_2\} \neq \{m_3, m_4\}$ ). The corresponding collision rate can be approximated as

$$\Gamma_{\text{lat}}^{\text{sc}} \propto \underbrace{f_{\text{FD}}(E_k, T)}_{\text{particles}} \cdot \underbrace{1}_{\text{holes}}. \quad (6.5)$$

This directly reflects the reduced role of the Pauli exclusion principle for this collision process. Since the final state is available (see Fig. 6.4 B), spin-changing lateral colli-

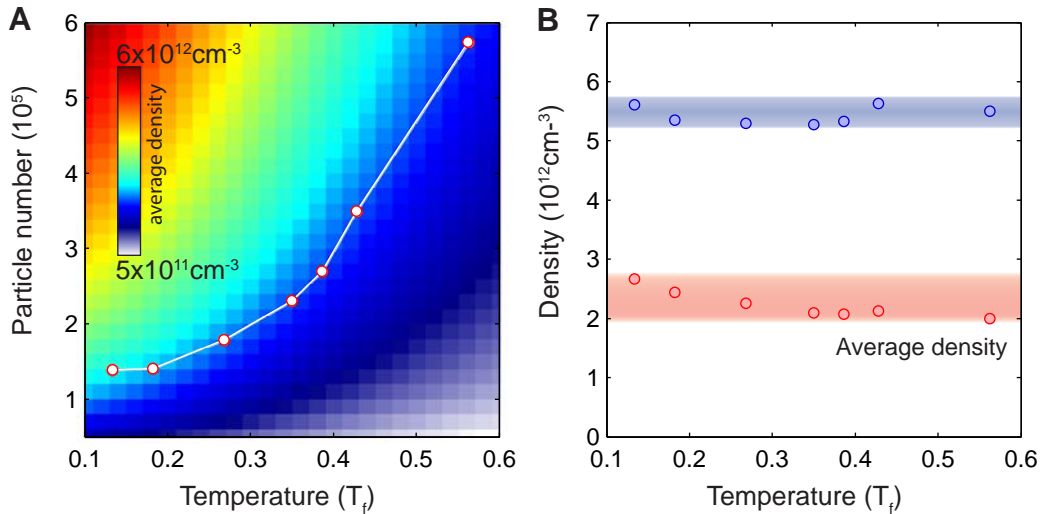


**Figure 6.5: Realizing the same mean-field interaction at higher temperatures.** The particle number (A) and the average/peak density (B) are depicted for the different temperatures realized in the experiment. The false color in A shows the average density, calculated from the Thomas-Fermi distribution (see appendix A). In separate experiments prior to the spin-changing dynamics, these values have been calibrated. Note that the mean-field interaction energy is proportional to the average density, which remains widely constant.

sions also occur at very low temperatures and the corresponding rate  $\Gamma_{\text{lat}}^{\text{sc}}$  is rather temperature-independent.

### 6.2.2 Observation of strong damping at higher temperatures

Giant spin oscillations constitute ideal candidates to study the temperature-dependent interplay between mean-field dynamics driven by forward collisions and relaxation induced by lateral collisions. Due to the long-range mean-field potential (see section 5.3), the Fermi sea acts as a fixed object in spin space, allowing to identify temperature effects directly in the spin dynamics.

To investigate the temperature influence experimentally, it is crucial to study spin dynamics with all relevant mean-field parameters kept constant. This includes the initial spin configuration, the magnetic field and the mean-field interaction. For the latter, the same average density has to be realized at each temperature. This can be experimentally controlled by adjusting the minimum dipole trap depth during the evaporation or by including an additional waiting time (see section 3.2.3).

The presented set of experiments studies spin dynamics at seven different temperatures. For this purpose, a temperature range between  $0.1 - 0.6 T_F$  with particle numbers between  $1 \times 10^5 - 6 \times 10^5$  has been realized, depicted in Fig. 6.5. These values have been calibrated in a separate measurement prior to each spin-dynamics experiment. To avoid systematic errors arising from spatial deformations no Stern-Gerlach field has been applied. The extracted values for particle number and temperature correspond to the initial experimental parameters. While the temperature slightly increases during the spin dynamics, the particle number remains widely constant. Note that for higher temperatures also the spatial extension of the system increases due to the higher particle

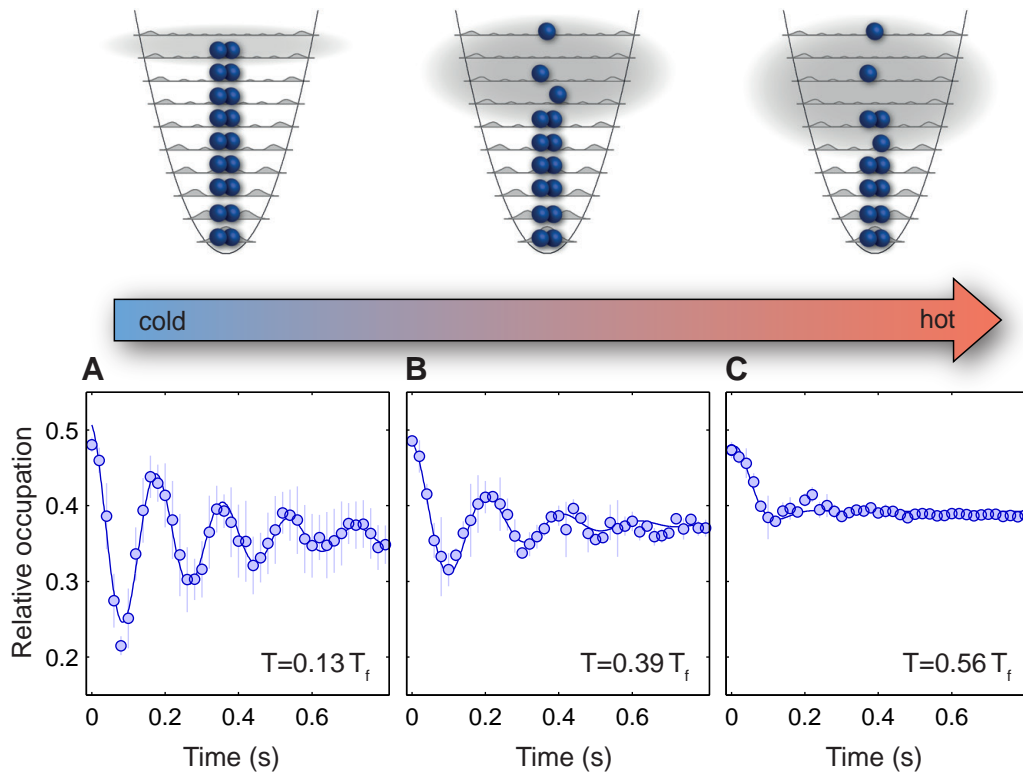


**Figure 6.6: Spin dynamics in a Fermi sea for increasing temperature.** The time evolution of the spin occupations  $n(\pm 3/2)$  is exemplarily depicted for three different temperatures as indicated in the figure. In the upper part, the Fermi sea and the resulting formation of holes is sketched. As initial state, the spin mixture  $m = \{\pm 1/2\}$  with a spin rotation of  $\theta = 0.44$  is employed. The experimental parameters are  $B = 0.12$  G and  $n_p = 5.2 \times 10^{12}$  cm $^{-3}$ . Solid lines are fits to the data and the error bars indicate one standard deviation. Experimental data have also been published in [1].

number. This requires a careful gradient compensation in order to avoid spin-wave excitations. The resulting average density for all experiments has a relative error of about 10%. Therefore, one can assume that forward scattering occurs at a similar rate for all experiments, while the rate for spin-conserving lateral collision  $\Gamma_{\text{lat}}^{\text{nsc}}$  is expected to increase for higher temperatures.

The experiments reveal a dramatic temperature impact on the collective spin dynamics. Spin-oscillation measurements monitored at three different temperatures are exemplarily depicted in Fig. 6.6. As a key result, a strongly enhanced damping of the spin oscillations is observed for increasing temperature. At  $T = 0.1 T_F$  (Fig. 6.6 A), the Fermi sea exhibits long-lived and large-amplitude spin oscillations. A damping rate of 3 Hz is found, similar to the experiments presented in chapter 5. For higher temperatures, however, the damping continuously increases, yielding a nearly full suppression of any collective behavior at  $T = 0.6 T_F$  (Figs. 6.6 B,C). This demonstrates that long-lived collective spin dynamics can be realized only at ultralow temperatures.

To analyze this effect in more detail, the oscillation frequency and amplitude have been extracted and compared to a mean-field calculation using the single-mode approximation (equation 5.9). This comparison is depicted in Fig. 6.7 and reveals a good

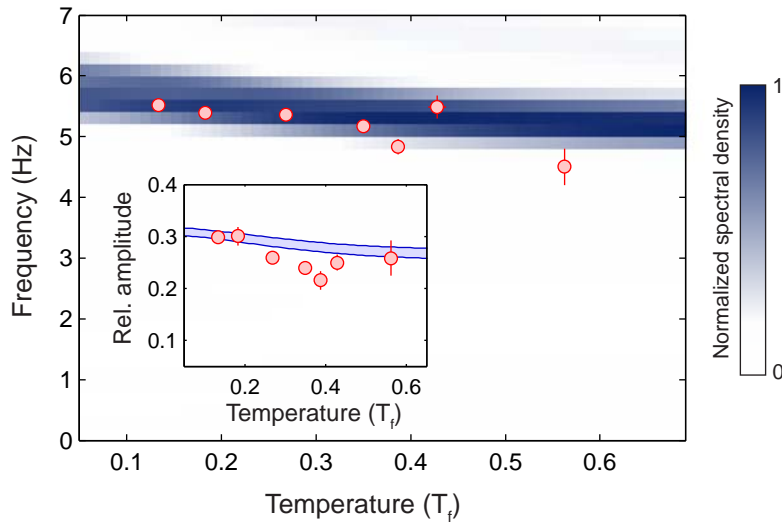


**Figure 6.7: Mean-field oscillation properties for increasing temperature.** The frequency (main graph) and amplitude (inset) of the spin oscillations are depicted for different temperatures. As initial state, the spin mixture  $m = \{\pm 1/2\}$  with a spin rotation of  $\theta = 0.44$  is employed. The experimental parameters are  $B = 0.12$  G and  $n_p = 5.2 \times 10^{12}$  cm $^{-3}$ . The calculations are performed within a single-mode approximation (equation 5.9). The shaded areas reflect the uncertainties in particle number and temperature. Error bars indicate two standard deviations. Experimental data have also been published in [1].

agreement for the whole temperature range without free parameters. It demonstrates that forward collisions, which drive the mean-field dynamics, are not significantly affected by the temperature increase, consistent with the considerations above.

Moreover, the data clearly show that the spin-oscillation damping increases for higher temperatures. The extracted damping rate is depicted in Fig. 6.8, showing a rather small increase for low temperatures, which is strongly intensified surpassing  $T = 0.4 T_F$ .

In general, this behavior can be attributed to spin-conserving lateral collisions. Following the considerations above, these collisions are suppressed at very low temperatures due to Pauli blocking [235]. This allows for long-lived spin oscillations driven by forward scattering. The observed stronger damping is associated with the formation of holes in the Fermi sea, leading to an enhanced rate of lateral collisions. Note that the small damping rate of 3 Hz at very low temperatures might be a consequence of spin-changing lateral collisions. Experimental imperfections such as magnetic gradients or photon scattering also serve as possible explanations.

For a comparison of the observed damping with the theoretical approach introduced in section 6.1.2, the corresponding damping rate was calculated by U. Ebling and coworkers without free parameters. In this context, a linearized version of the collision term has been employed (for details see [1, 206]). The result of this calculation is compared to the experimental data in Fig. 6.8. At low temperatures between  $0.1 - 0.3 T_F$ , a fair agreement is found. However, this simplified model does not capture the full many-body behavior at higher temperatures [203]. Since the collision term only constitutes a leading-order correction to the Hartree-Fock mean-field potential and is treated in a linearized fashion, a quantitative agreement cannot be expected to a large

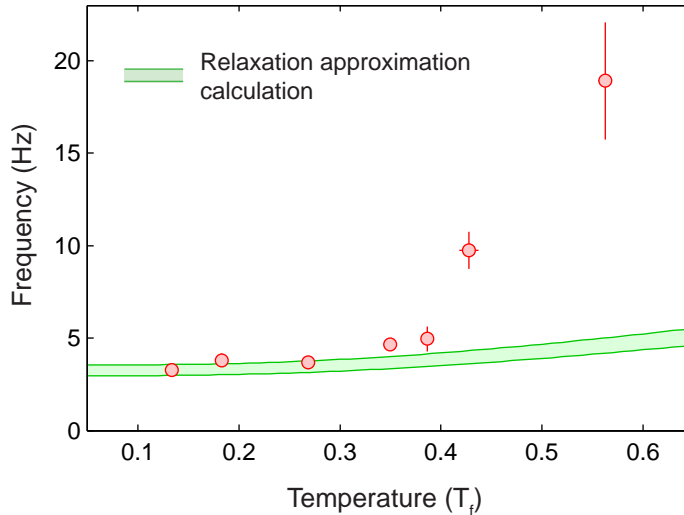


**Figure 6.8: Damping of the spin oscillations for increasing temperature.** The damping rate, extracted from spin-oscillation measurements as in Fig. 6.6, is depicted as a function of temperature. As initial state, the spin mixture  $m = \{\pm 1/2\}$  with a spin rotation of  $\theta = 0.44$  is employed. Experimental parameters are  $B = 0.12$  G and  $n_p = 5.2 \times 10^{12} \text{ cm}^{-3}$ . Data are compared to calculations using a linearized version of the collision term, kindly provided by U. Ebling [203]. The results are depicted as green shaded area, accounting for uncertainties in the average density. Error bars indicate two standard deviations. Experimental data have also been published in [1].

extent. In this direction, the use of a quantum Boltzmann equation or further more sophisticated approaches could provide a better agreement [152, 236, 237].

In conclusion, the presented experiments reveal for the first time that the fermionic spin dynamics are stabilized by Pauli blocking. Therefore, ultralow temperatures are essential for this collective behavior. This stabilization mechanism is a unique fermionic feature. It is fundamentally different from the recent observation of spin dynamics in a thermal Bose gas [207], which was stabilized by the tight confinement of the harmonic trap.

## 6.3 Suppression of collective dynamics at intermediate interactions

Similar to the temperature, the interaction strength also plays a fundamental role for a many-body system, providing a link from the weakly-interacting to the strongly-correlated regime. The observation of collective spin dynamics in chapter 5 – well captured in a mean-field approach – naturally raises the question, when this approximation breaks down. In this context, it is particularly interesting how an increased interaction strength affects the role of forward and lateral collisions (see section 6.1).

One way to increase the interaction strength of a quantum gas system are Feshbach resonances [119], which are widely available in  $^{40}\text{K}$  (see appendix B). However, they are located at larger magnetic fields ( $B > 15\text{ G}$ ), where spin-changing collisions are energetically suppressed. For bulk systems, the density additionally provides a tuning knob for the interaction strength. This is typically limited to small variations due to feasible particle numbers, temperatures and trapping frequencies. In the available regime, spin oscillations have shown no significantly different behavior (see section 5.4.2).

In this section, a completely different situation will be investigated, which is more sensitive to the density. I will report on the first observation of fermionic spin instabilities, which constitute another fundamental realization of collective spin dynamics. This will reveal an intriguing collisionally-induced spin stabilization mechanism at intermediate interaction strengths. A stability diagram will be mapped out, which can be qualitatively reproduced, combining a mean-field approach with the collision term.

### 6.3.1 Observation of fermionic spin instabilities

Dynamical spin instabilities have been widely explored with spinor Bose-Einstein condensates [70, 81, 82, 222], showing an intriguing analogy to the non-rigid pendulum in the quantum limit [82, 238]. These collective excitations exhibit an exponentially growing spin redistribution, mediated by spin-changing collisions. In contrast to spin dynamics with initially prepared coherences (see chapter 5), small fluctuations are sufficient to seed instability-driven dynamics. Experiments with ultracold bosons have demonstrated that spin instabilities can be even induced by quantum fluctuations [81].

Here, I present experiments, which demonstrate spin-instability dynamics for the first time in a fermionic quantum gas. The fermionic spin instabilities directly emerge in an interacting Fermi sea without initially prepared coherences. Note that in our system the initial state exhibits small coherences due to experimental imperfections such as a misalignment of the coils, which appear on a classical level.

It turns out that the emergence of spin instabilities is favored in magnetically excited spin configurations. For example, the spin mixture  $m = \{\pm 1/2\}$ , which has the lowest magnetic energy of the  $M = 0$  spin system, remains stable also at very low magnetic fields. In contrast, a Fermi sea, prepared in the magnetically excited spin mixture  $m = \{\pm 3/2\}$ , shows a completely different dynamical behavior (for preparation see section 3.2.3). It exhibits giant and long-lived collective dynamics, which are depicted in Fig. 6.9 A. This instability dynamics start with an increasing population of the spin configuration  $\pm 1/2$ , which has the lower magnetic energy. It is followed by oscillatory dynamics with a frequency of approximately 3 Hz and an amplitude of about 60%. An even more counterintuitive effect occurs, when the magnetically excited spin mixture  $m = \{\pm 9/2\}$  is prepared. A collective spin cascade emerges, which is depicted in

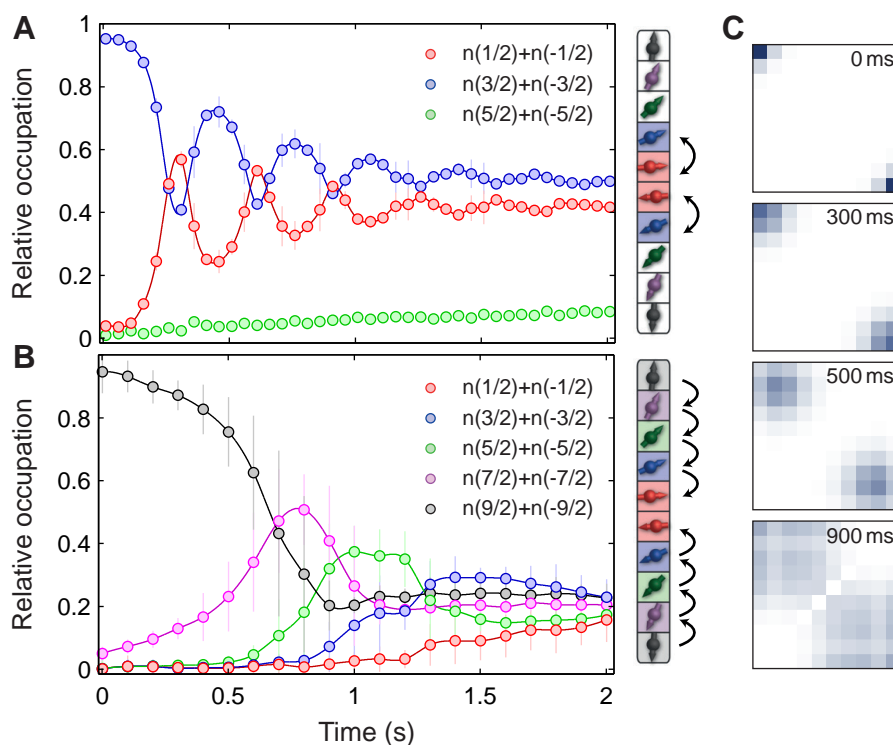


**Figure 6.9: Observation of spin instabilities in a fermionic quantum gas.** The relative population of the spin states  $n(m)$  is depicted as a function of time. (A) A spin instability starting from the spin mixture  $m = \{\pm 3/2\}$  is shown. The experimental parameters are  $B = 0.1$  G,  $n_p = 5.9 \times 10^{12}$  cm $^{-3}$ , and  $T = 0.14$  T $_F$ . Experimental data have also been published in [1]. (B) A spin cascade starting from  $m = \{\pm 9/2\}$  is depicted. The experimental parameters are  $B = 34$  mG,  $n_p = 3.1 \times 10^{12}$  cm $^{-3}$ , and  $T = 0.45$  T $_F$ . (C) Depicted are calculated density matrices for the parameters in B using a single-mode approximation (equation 5.9) with an initial spin rotation  $\theta = 0.1$ .

Fig. 6.9 B. The spin of the particles is consecutively redistributed from the initial spin configuration to those with lower magnetic energies ( $\pm 9/2 \rightarrow \pm 7/2 \rightarrow \pm 5/2 \rightarrow \pm 3/2 \rightarrow \pm 1/2$ ).

In general, the spin instabilities are well reproduced in each experimental run, even though they are induced by coherence fluctuations. Moreover, note the very long-lived collective behavior for up to 2 s, which even exceeds the lifetime of the spin oscillations studied in chapter 5. However, the dynamics also imply that magnetically excited spin mixtures are difficult to handle at low magnetic field. It serves as an explanation for the unexpected spin dynamics observed in optical lattices involving higher bands, where the spin mixture  $m = \{\pm 3/2\}$  was employed (see section 4.4).

Using the collisionless Boltzmann equation (see equation 5.9), the spin-instability dynamics can be well reproduced, similar to the giant spin oscillations (for details see appendix C). This underlines, that also these dynamics are driven by mean-field interactions as in the bosonic case [67, 68]. A general problem for the calculations are the unknown initial coherence fluctuations. They are approximated by applying a small spin rotation ( $\theta \leq 0.1$ ), which initializes the instability dynamics. An example for such a calculation is depicted in Fig. 6.9 C, where four density matrices from the time evolution

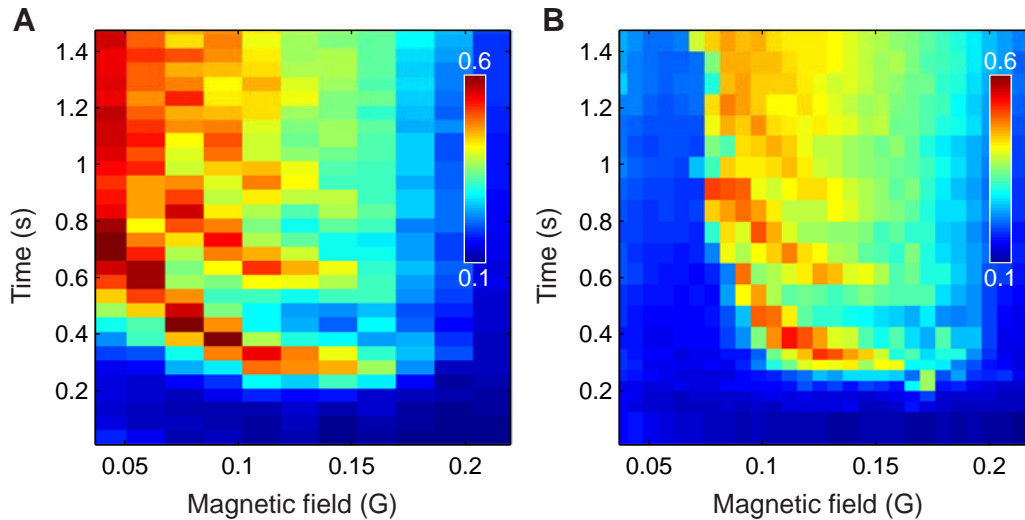


**Figure 6.10: Spin instabilities for two different densities.** The relative population  $n(\pm 1/2)$  is shown for different magnetic fields as a function of time. Two densities are compared for otherwise identical parameters,  $n_p = 5.9 \times 10^{12} \text{ cm}^{-3}$  (**A**) and  $n_p = 7.2 \times 10^{12} \text{ cm}^{-3}$  (**B**). As initial state, the spin mixture  $m = \{\pm 3/2\}$  is prepared at a temperature of  $T \approx 0.2 T_F$ . The data reveal a different dynamical behavior at low magnetic field ( $B < 80 \text{ mG}$ ). Experimental data have also been published in [1].

of the spin mixture  $m = \{\pm 9/2\}$  are shown. These calculations also demonstrate that the occupation of new spin components is associated with the formation of pronounced coherences in the system.

### 6.3.2 Suppression of instability dynamics at higher densities

The observed spin instabilities are ideally suited to investigate the influence of higher densities on the different collision processes introduced in section 6.1. These excitations are driven by coherence fluctuations. Hence, a small parameter change can induce a completely different macroscopic behavior of the many-body system, which is demonstrated in the following.

The experimental data depicted in Fig. 6.10 show spin-instability dynamics for different magnetic fields, comparing two slightly different densities. In both cases, the spin mixture  $m = \{\pm 3/2\}$  is prepared and exhibits collective behavior apparent in long-lived spin dynamics. The observed frequency increases for higher magnetic fields alongside a smaller amplitude, reflecting the influence of the Zeeman energy. However, increasing the density only by less than 25% ( $n_p = 5.9 \times 10^{12} \text{ cm}^{-3} \rightarrow n_p = 7.2 \times 10^{12} \text{ cm}^{-3}$ ), a completely different dynamical behavior is found at low magnetic fields ( $B < 80 \text{ mG}$ ). In this regime, the collective spin dynamics are fully suppressed for the higher density, leading to abrupt spin stabilization.

This observation motivates to investigate the occurrence of spin instabilities. For this purpose, the magnetically excited spin mixture  $m = \{\pm 3/2\}$  is prepared and the spin occupations are recorded after a time evolution of  $t = 2 \text{ s}$ . If a spin instability has emerged, the oscillatory dynamics are damped out after this time (see Fig. 6.9 A). A quasi-equilibrium state is reached, consisting of a mixture of the spin configurations

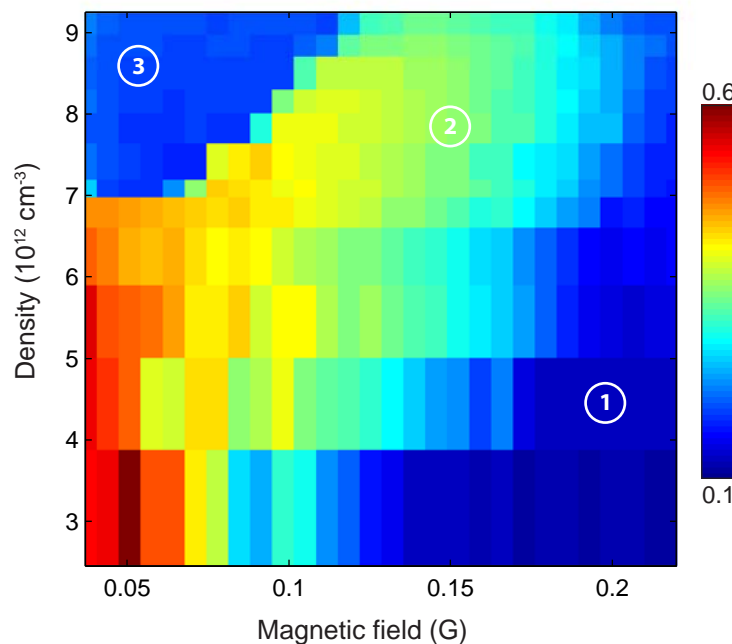


**Figure 6.11: Stability diagram of the magnetically excited spin mixture  $m = \{\pm 3/2\}$ .** The occupations  $n(\pm 1/2)$  are depicted versus magnetic field and density after a time evolution of  $t = 2$  s. A finite occupation indicates that a spin instability has emerged. Three regions can be identified: Zeeman-protected regime ①, spin-instability regime ②, and stable high-density regime ③. As initial state, the spin mixture  $m = \{\pm 3/2\}$  is prepared with a temperature  $T = 0.19 \pm 0.05 T_F$ . Experimental data have also been published in [1].

$\pm 1/2$  and  $\pm 3/2$ . Without the emergence of a spin instability, the Fermi sea remains in the initial spin states  $\pm 3/2$ . This gives a direct measure whether a spin instability has occurred.

The resulting stability diagram has been mapped out, depicted in Fig. 6.11. Plotted are the occupations of the spin states  $\pm 1/2$  as a function of magnetic field and density. Three different regimes can be identified:

#### **Zeeman-protected regime**

At large magnetic fields and low densities, no spin instabilities are observed (region ① in Fig. 6.11). The spin mixture  $m = \{\pm 3/2\}$  is stabilized by an external magnetic field, which induces a large detuning between the initial and final spin configuration. Spin-changing collisions are off-resonant.

#### **Spin-instability regime**

At lower magnetic fields or higher densities, spin-changing collisions are possible leading to the emergence of spin instabilities (region ② in Fig. 6.11). This is reflected in the continuous change of the spin occupations.

#### **Stabilized high-density regime**

Unexpectedly, the initial spin mixture  $m = \{\pm 3/2\}$  remains stable at high densities and low magnetic fields (region ③ in Fig. 6.11). This occurs despite the fact that spin-changing collisions are energetically possible in this regime. Note the abrupt change in the spin occupations at approximately  $n_p = 7.0 \times 10^{12} \text{ cm}^{-3}$ .

The Zeeman-protected (region ①) and the spin-instability regime (region ②) can be captured in a mean-field approach. In this parameter regime, the spin instabilities are driven by the interplay between mean-field interactions and Zeeman energy. However, the pure mean-field approach cannot explain the stable high-density regime (region ③).

For a deeper understanding of this feature, a numerical simulation of the stability diagram has been performed, combining the mean-field approach with a relaxation approximation. The damping is introduced as a global term, yielding a Boltzmann equation of the following form:

$$\partial_t \rho(t) = \underbrace{\frac{1}{i\hbar} \left[ \bar{V} \sum_{kl} (U_{klij} - U_{kjil}) \rho_{kl}(t), \rho(t) \right]}_{\text{collisionless Boltzmann equation}} + \underbrace{\frac{1}{i\hbar N} [qS_z^2, \rho(t)] - \Gamma \cdot \rho(t)|_{i \neq j}}_{\text{damping}}. \quad (6.6)$$

The last term corresponds to a relaxation approximation of the collision term, which reduces the coherences exponentially, reflecting lateral collisions. For the simulations, the experimental parameters from Fig. 6.11 were used. The initial coherence fluctuations were approximated with a small spin rotation ( $\theta = 0.1$ ) of the spin mixture  $m = \{\pm 3/2\}$ . For each density and magnetic field, the time evolution was calculated until coherent mean-field dynamics were damped out.

In a first simulation, the damping rate  $\Gamma$  was calculated with a linearized version of the collision term without free parameters (for details see [1]). These calculations yield a density-dependent damping rate  $\Gamma$ . The resulting stability diagram is depicted in Fig. 6.12 A. A comparison of this numerical result with the experimental data in Fig. 6.11 shows a good agreement. In particular, the calculations reproduce all experimentally observed regimes: the Zeeman-protected (region ①), the spin-instability regime (region ②), and also the high-density regime (region ③). Note that a global factor of 2.25 was inserted for the damping rate. This leads to a better quantitative agreement between the experimental data and the simulations without qualitatively changing the obtained results.

In a second simulation, the stability diagram was calculated with the same parameters but with a density-independent damping rate of  $\Gamma = 2$  Hz. The corresponding result is depicted in Fig. 6.12 B and shows an important difference: it reproduces the Zeeman-protected (region ①) and the spin-instability regime (region ②), while the spin stabilization is clearly absent (region ③).

This study allows for the conclusion that the spin-stabilization mechanism can be attributed to the density dependence of the damping rate. This implies that higher densities associated with an increased interaction strength lead to enhanced relaxation, which induces the stabilization. In terms of the microscopic processes, this reflects the enhanced role of lateral collisions (represented by the damping rate  $\Gamma$ ) compared to the mean-field interactions (represented by the interaction integral  $\bar{V}$ ). Figure 6.12 C depicts the corresponding ratio  $\Gamma/\bar{V}$ , which increases with density. Above a specific ratio, spin instabilities are suppressed.

One can understand the role of dissipation in the following way: Spin instabilities driven by forward scattering generate coherences (see section 6.3.1), while damping processes driven by lateral collisions reduce coherences (see section 6.1.2). In terms of the single-particle density matrix, lateral collisions project the state onto the diagonal elements of the initial state. This is similar to the measurement projection associated

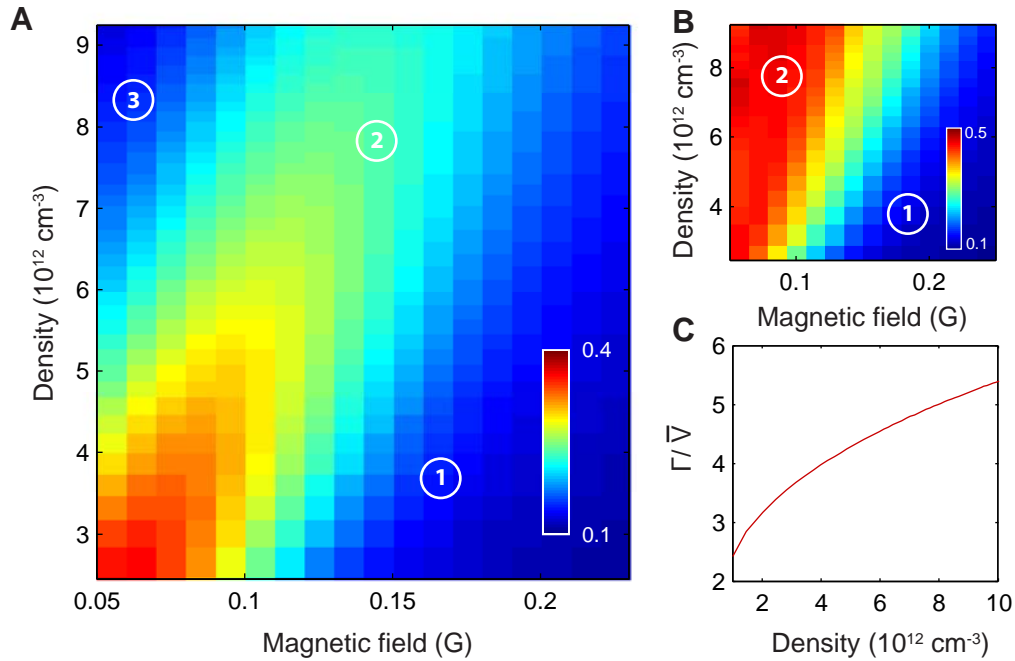


**Figure 6.12: Numerical simulation of the stability diagram.** (A) The calculated spin occupation  $n(\pm 1/2)$  is plotted versus magnetic field and density after a time evolution of  $t = 3.5 \text{ s}$ , where mean-field dynamics are damped out. For the simulation, the experimental parameters from Fig. 6.11 are used. The seed in the coherences is modeled with a spin rotation  $\theta = 0.1$  of the spin mixture  $m = \{\pm 3/2\}$ . The density-dependent damping rate is calculated using a linearized approach of the collision term [1] and globally scaled with a factor of 2.25, kindly provided by U. Ebling [203]. (B) Simulated stability diagram for a density-independent damping rate of  $\Gamma = 2 \text{ Hz}$ . (C) Ratio of the damping rate in A and the interaction integral as a function of density.

with the quantum-Zeno effect [239, 240]. In further analogy to this phenomenon, any coherent evolution of the system is suppressed.

Note that only a qualitative agreement is found, which is expected due to several strong simplifications: First of all, a global damping rate  $\Gamma$  for all coherences was assumed, which is in fact different for each collision channel. Moreover, the linearization ansatz for the damping rate is only valid for small changes of the initial state [203]. In addition, it turns out that the damping depends on the instantaneous spin configuration [1] and is time-dependent. These additional features have not been included in the simulations. This leads to the smooth crossover between the spin-instability (region ②) and the stabilized regime (region ③) in contrast to the experiments.

In conclusion, the presented experiments demonstrate that higher densities can induce a completely different macroscopic behavior of the high-spin Fermi sea. Collective behavior is entirely suppressed, when lateral collisions dominate. This implies that magnetically excited spin configurations can be stabilized by the intrinsic collisional properties of the many-body system. Still, some observations remains puzzling, such as the abruptness of the transition or the role of the harmonic trap. The results have triggered further ongoing theoretical studies [211], which might provide the answer and lead to a better quantitative agreement.

## 6.4 Spin-relaxation dynamics in high-spin fermions

So far the presented experiments were focused on the interplay between forward and lateral collisions. The latter induce a suppression of collective dynamics at higher temperatures and densities. As worked out in section 6.1, lateral collisions are dominated by spin-conserving processes due to the quadratic dependence on the scattering length. They are similar to conventional particle-hole excitations in spin 1/2 fermions and induce a spatial relaxation of the many-body system.

Beyond this, high-spin systems also allow for spin-changing lateral collisions, introduced as the process (iii) in section 6.1. These collisions have been theoretically studied for bosonic systems [202] and lead to relaxation involving spin and spatial degrees of freedom. This has important consequences for an interacting binary Fermi sea: despite its equilibrium spatial distribution, the spin configuration corresponds to an excited state. Therefore, it is exposed to spin-changing lateral collisions, which induce spin-relaxation dynamics among all available spin states. Even though this process is suppressed compared to spin-conserving lateral collisions, it can be clearly distinguished in the dynamics of the spin occupations.

In this section, I will investigate spin-changing lateral collisions in a high-spin Fermi sea. The presented experiments demonstrate for the first time spin-relaxation dynamics in a fermionic quantum gas. As a key result, the observed dynamics drive the system towards a spin equilibration and are well captured within a single-mode approximation of the collision term. A study of the spin-relaxation properties will be presented.

### 6.4.1 A single-mode approximation for the collision term

The high-spin Boltzmann equation 6.3 including the collision term can be numerically solved in one dimension [203]. For higher-dimensional systems as in the experiments simplifications are inevitable, for example a linearization approach or a relaxation approximation of the Boltzmann equation [202, 232].

Here, I present a single-mode approximation for the collision term [1, 65, 79, 205]. In connection with the described experiments, it was derived by U. Ebling and coworkers and implemented during this research work. The single-mode approximation requires significantly less numerical effort and can also be easily applied for higher-dimensional systems. The justification for the single-mode approximation follows the same route as in the mean-field case (see section 5.3): If the trap dynamics are faster than the collision process, the spatial dependencies are averaged out and an effective long-range potential is induced. Since spin-changing lateral collisions appear at a very small rate (see Fig. 6.1 B), this assumption is well justified.

To implement a single-mode approximation for the collision term, the procedure is also similar to the mean-field case. The Wigner function is assumed to separate into a product of a spatial and a spin part, where the spatial part is approximated with the Thomas-Fermi distribution (see appendix A). This results in a Boltzmann equation with the collisionless part and an additional single-mode collision term [2]:

$$\partial_t \rho(t) = \underbrace{\frac{1}{i\hbar} \left[ \bar{V} \sum_{kl} (U_{klij} - U_{kjil}) \rho_{kl}(t) + qS_z^2, \rho(t) \right]}_{\text{collisionless part}} + \underbrace{\bar{C} \sum_{abcd} T^{abcd} \rho_{ac} \rho_{bd}}_{\text{collision term}}. \quad (6.7)$$

$\bar{C}$  is the collisional integral, given by the following expression:

$$\bar{C} = \frac{1}{N} \int d\mathbf{r} \int d\mathbf{p} \int d\mathbf{q} |\mathbf{q}| f_0(\mathbf{r}, \mathbf{p}) f_0(\mathbf{r}, \mathbf{p} - \mathbf{q}). \quad (6.8)$$

This term reflects the rate of lateral collisions and corresponds to a convolution of the initial and final spatial distribution weighted with the momentum transfer  $\mathbf{q}$ . Note that the magnetic field is neglected. This leads to deviations only at large magnetic fields as discussed in section 6.4.3.  $T_{mn}^{abcd}$  is a tensor, given by [2]

$$T_{mn}^{abcd} = \frac{m}{4\pi\hbar^4} \left( \tilde{U}_{mabd}\delta_{nc} + \tilde{U}_{ncbd}\delta_{ma} - \sum_l U_{malb}U_{ncll} \right), \quad (6.9)$$

which includes the higher-order coupling constant  $\tilde{U}_{abcd}$ , given by

$$\tilde{U}_{abcd} = \left( \frac{4\pi\hbar^2}{m} \right)^2 \sum_{F,M} a_F^2 \langle ab|FM\rangle \langle FM|cd\rangle. \quad (6.10)$$

The collision term includes only quadratic terms of the density matrix like the collisionless Boltzmann equation. Hence, the numerical treatment can be performed in the same way. Note, that it is a non-trivial question whether lateral collisions can be conceptually described in a single-mode approximation. These collisions change the momentum configuration, while in the single-mode approximation all spatial degrees of freedom are integrated out. It turns out that spin-changing lateral collisions are well described within this approach, while it fails in capturing spin-conserving lateral collisions (see appendix C).

## 6.4.2 Observation of spin-relaxation dynamics

Lateral spin-changing collisions lead to spin-relaxation dynamics of the fermionic many-body system, which were first observed in this work. To limit spin dynamics only to these collisions, the spin mixture  $m = \{\pm 1/2\}$  is initially prepared. Due to the absence of coherences, collective mean-field dynamics are suppressed and the density matrix remains diagonal during the time evolution.

In a first experiment, a 1d system is realized. This geometry allows to compare the experiment with calculations of the Boltzmann equation 6.3 with spatial resolution. Experimentally, the spin mixture is loaded into a deep two-dimensional optical lattice confining the atoms into tubes. At a lattice depth of  $25 E_{\text{rec}}$ , the tunneling time between the tubes is approximately 200 ms and remains well below the experimental time scale. Spin-relaxation dynamics recorded in this configuration is depicted in Fig. 6.13 A. The system gradually occupies all ten available spin states and evolves towards equal spin populations [2]. The spin dynamics occur on a time scale of several milliseconds and yields an excellent agreement with the numerical solution of the Boltzmann equation 6.3 without free parameters (for details see [206]).

In the 3d bulk system, the spin mixture is prepared in the optical dipole trap and the subsequent spin dynamics are monitored. The time evolution of the spin states is depicted in Fig. 6.13 B. This experiment reveals the same qualitative behavior of the bulk system compared to the 1d system. However, the corresponding time scale has

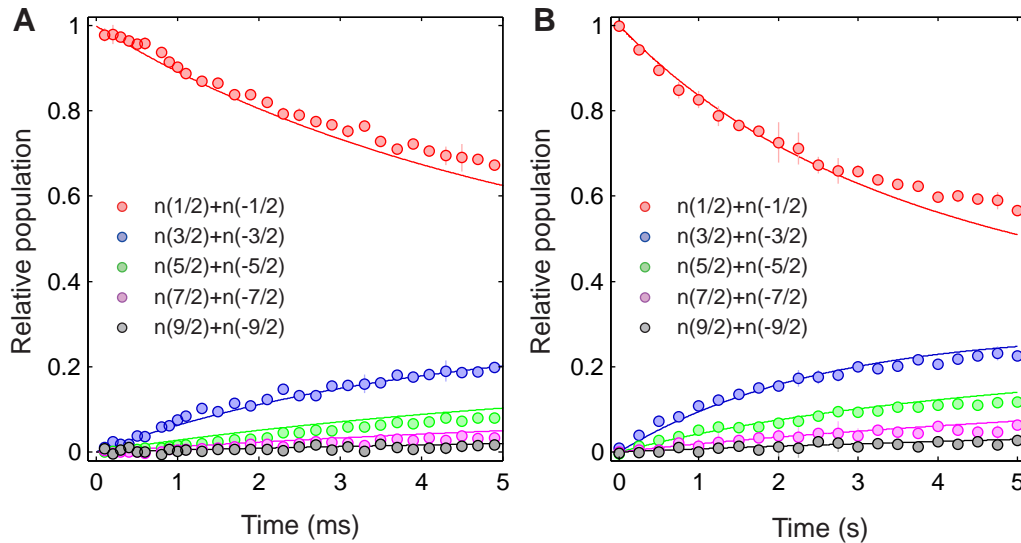


**Figure 6.13: Spin-relaxation dynamics in different geometries.** (A) Spin-relaxation dynamics in a 1d geometry with  $\omega_{x,y,z} = 2\pi \times (84, 47000, 47000)$  Hz are depicted, realized in a deep 2d lattice. The experimental parameters are  $N = 100$  per tube,  $T = 0.2 T_F$  and  $B = 0.12$  G. Solid lines are 1d simulations of the Boltzmann equation 6.3, which are kindly provided by U. Ebling [203]. (B) Spin-relaxation measurements in a 3d bulk system at trapping frequencies  $\omega_{x,y,z} = 2\pi \times (33, 33, 137)$  Hz. The experimental parameters are  $N = 1.3 \times 10^5$ ,  $T = 0.15 T_F$ , and  $B = 0.34$  G. Solid lines are calculations using the single-mode approximation (equation 6.7). Experimental data have also been published in [2].

increased by three orders of magnitude from milliseconds to seconds. This reflects the strongly reduced density compared to the tube geometry.

In this system, simulations of the Boltzmann equation 6.3 are not possible and the data are compared to calculations using the single-mode approximation (equation 6.7). As a key result, the data of the spin-relaxation dynamics are in very good agreement with corresponding calculations without free parameters.

### 6.4.3 Studying the spin-relaxation properties

The experiments presented in the last section constitute the first observation of spin-relaxation dynamics in a fermionic quantum gas. This motivates to study the properties of this unique high-spin process, featuring a relaxation among spin and spatial degrees of freedom. Here, studies of the magnetic field and the density dependence as well as thermalization properties are presented.

#### Density dependence

In general, the density determines the collision rate of a many-body system. To investigate this for spin-changing lateral collisions, spin-relaxation dynamics were monitored for five different densities, featuring a spin redistribution from the initial spin mixture  $m = \{\pm 1/2\}$  into further spin configurations. The density is increased by changing the particle number while keeping the temperature constant. By fitting an exponential decay, the relaxation rate is determined from the data. The result of this analysis is

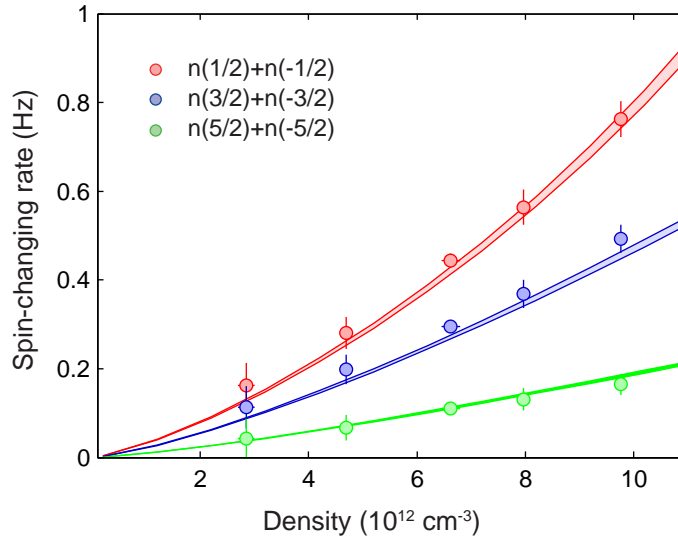


**Figure 6.14: Density dependence of spin-relaxation dynamics.** The absolute spin-changing rates for the spin configurations  $\pm 1/2$ ,  $\pm 3/2$  and  $\pm 5/2$ , obtained by fitting exponential decays to the dynamics as in Fig. 6.13 B, are depicted. While the temperature is constant at  $T = 0.26 T_F$ , the particle number is increased. The magnetic field is  $B = 0.11 \text{ G}$ . Solid lines are calculations obtained from a single-mode approximation (equation 6.7). Shaded area accounts for uncertainties in temperature and particle number. Experimental data have also been published in [2].

depicted in Fig. 6.14, revealing in general a small relaxation rate ( $\Gamma_{\text{lat}}^{\text{sc}} < 1 \text{ Hz}$ ). It increases for higher densities, which demonstrates that an enhanced redistribution among the available spin states can be realized by tuning the density.

The experimental data are compared to single-mode approximation calculations (equation 6.7) without free parameters. As a result, the dynamics precisely follow the calculated rate, given by the collisional integral  $\bar{C}$  (equation 6.8). The calculations also reveal a small nonlinear increase, which is different from the mean-field interaction integral, having a linear dependence (see Fig. 5.11). This highlights, that the collisional integral  $\bar{C}$  increases faster with density than the mean-field integral  $\bar{V}$ , reflecting the enhanced role of lateral collisions at intermediate interactions.

### Magnetic field dependence

To study the influence of the Zeeman energy, the spin mixture  $m = \{\pm 1/2\}$  is monitored after a time evolution of  $t = 2 \text{ s}$  for different magnetic fields. The result is depicted in Fig. 6.15 A, from which several observations can be drawn:

First, spin-changing collisions are only strongly suppressed at large magnetic fields ( $B > 4.5 \text{ G}$ ). The mechanism behind this is entirely different from the collective spin dynamics (see section 5.4), which is driven by the interplay between Zeeman and interaction energy. For lateral spin-changing collisions, where the momentum is changed, the Zeeman energy must be compared to the Fermi energy. This energy is typically much larger ( $\approx \text{kHz}$ ) than the spin-changing mean-field interaction ( $\approx \text{Hz}$ ) and hence larger magnetic fields are required to suppress spin dynamics. Therefore, one can conclude that particles are redistributed involving all occupied spatial states of the Fermi sea

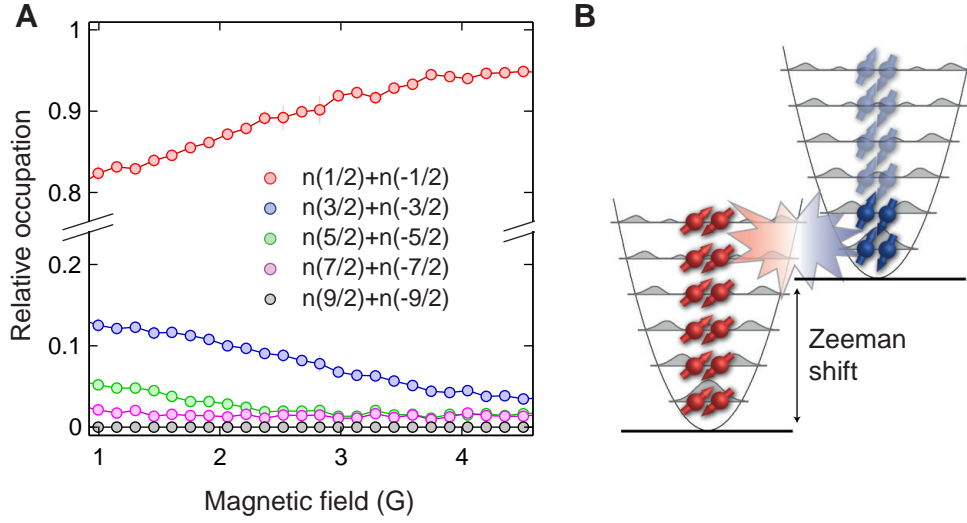


**Figure 6.15: Dependence of spin-relaxation dynamics on the magnetic field.** (A) Spin populations  $n(m)$  are depicted after a time evolution of  $t = 2$  s versus the magnetic field. The experimental parameters are  $N = 2.7 \times 10^5$  and  $T = 0.2 T_F$ . (B) A sketch of the magnetic field influence for spin-changing lateral collisions is shown. The spatial distribution of the spin states  $\pm 1/2$  is detuned with respect to  $\pm 3/2$ . Experimental data have also been published in [2].

(see Fig. 6.15 B).

As a second observation, spin-relaxation dynamics are suppressed at different magnetic fields depending on the spin configurations. This is consistent with the Zeeman energy difference between the initial spin mixture  $m = \{\pm 1/2\}$  and the corresponding spin configuration. Moreover, it implies that higher collision quanta are directly involved in spin-relaxation dynamics.

This proof-of-principle experiment could have several prosperous applications. It constitutes a measure for the collisional integral  $\bar{C}$  as a function of the momentum transfer. This could serve as a novel tool to determine the temperature of the system, which is directly connected to the data. It also provides new possibilities for many-body relaxation [215]: The spin-changing lateral collision rate can be fully suppressed at larger magnetic fields, while spin-conserving lateral collisions are not significantly influenced. This demonstrates that the ratio between both processes  $\Gamma_{\text{lat}}^{\text{sc}}/\Gamma_{\text{lat}}^{\text{nsc}}$  can be widely tuned up to a complete suppression. One can therefore regard the  $m = \{\pm 1/2\}$  system as a two-component Fermi sea with tunable losses into further spin states. This allows to continuously tune the character of this spin system from an open to a closed system.

### Thermalization properties

As discussed in section 6.1, spin-conserving collisions are strongly enhanced compared to spin-changing lateral collisions. Hence, one can assume that also in the presence of spin-changing lateral collisions the initial spin system is close to a thermal distribution, mediated by spin-conserving lateral collisions [230, 231] (see Fig. 6.16 A). This motivates to study the global temperature of the system under the influence of spin-relaxation dynamics, which is presented in the following.

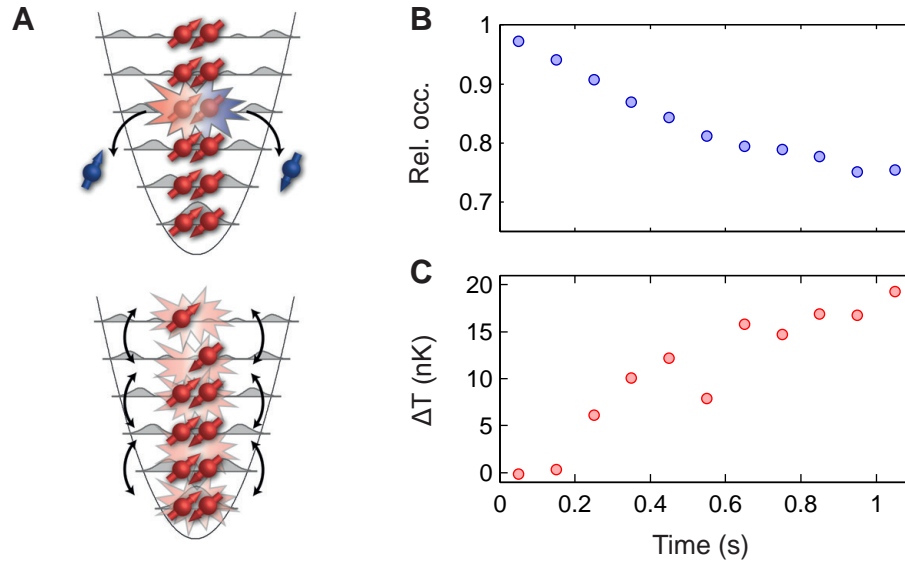


**Figure 6.16: Temperature increase due to spin-relaxation dynamics.** (A) A sketch of the thermalization process is depicted. After a spin-changing lateral collision (upper part), spin-conserving lateral collisions lead to a proper thermalization (lower part). (B) The spin occupations  $n(\pm 1/2)$  are depicted as a function of time. This effective particle loss leads to an increase of the absolute temperature, shown in (C). The magnetic field is  $B = 0.12$  G, the particle number  $N = 3.9 \times 10^5$ , and the initial temperature  $T = 0.24 T_F$  corresponding to 65 nK. The reference measurement for the temperature increase without spin-changing collisions is performed at  $B = 7.6$  G (see text). Experimental data have also been published in [2].

To investigate the thermalization process experimentally, two experiments have been performed, where the temperature has been monitored during the time evolution: First, a system at high magnetic field was studied, where spin-changing collisions are strongly suppressed ( $B = 7.6$  G). During the time evolution of 1 s, the temperature increases from 65 nK to 80 nK due to photon scattering [133]. This provides a suitable reference for a second experiment at low magnetic field ( $B = 0.12$  G), where significant spin-relaxation dynamics occur. The corresponding spin redistribution is depicted in Fig. 6.16 B. To determine the temperature of the multi-component system, all spin components  $m \neq 1/2$  are transferred into the  $f = 7/2$  manifold, which is transparent for the detection light. This allows to reliably determine the temperature, which is compared to the first experiment (see Fig. 6.16 C).

As an important result, the absolute temperature increases in the presence of spin-changing collisions [241]. The system is initially prepared in a very cold two-component Fermi sea, where only a few spatial states are unoccupied. Losses through spin-changing lateral collisions perforate the Fermi sea, which thermalizes by spin-conserving lateral collisions, associated with an absolute temperature increase.

## 6.5 Conclusion and outlook

In this chapter, I have presented a detailed study of relaxation effects in a high-spin Fermi sea. As a central result, the experiments demonstrate that collective spin dynamics crucially depend on global parameters such as temperature and density. This can be attributed to the interplay between several microscopic collision processes. These occur on very different time scales and are dominated by the fermionic quantum statistics. At ultralow temperatures, Pauli blocking stabilizes collective dynamics due to the suppression of lateral collisions. Higher interaction strengths lead to an intriguing spin-stabilization mechanism induced by lateral collisions, thus fully suppressing any collective dynamics. In this context, the first demonstration of mean-field driven spin instabilities in a fermionic quantum gas could be achieved. Finally spin-relaxation dynamics have been studied for the first time, driven by spin-changing lateral collisions, which lead to a relaxation among spin and spatial degrees of freedom.

The presented results have triggered further theoretical studies, which are ongoing and which might provide deeper insight into the role of different collision processes with a more analytical approach [211]. Future experiments could study the interplay between forward and lateral collisions in lower dimensional systems [59, 61]. In such experiments, the influence of lateral collisions should be enhanced and experimental data could be directly compared to numerical simulations with spatial resolution [203]. Prosperous applications arise from the observed spin-changing lateral collisions, which constitute a new relaxation effect. Due to the intrinsic momentum resolution of this process, this could serve as a new method to determine the temperature of a many-body system, which could also be extended to lattice systems [242, 243]. In addition, by tuning the magnetic field a precise control of the lateral collisions allows to tune the character of a spin system continuously from an open to a closed system, providing a novel tool for many-body relaxation [215].

As a final comment, the experiments presented in the last three chapters have studied fermionic spin dynamics driven by high-spin interactions in different regimes – from the local two-particle spin dynamics to many-body spin dynamics. Nevertheless, fundamental questions have still remained unanswered: What is the connection between giant spin oscillations in bulk systems and two-particle spin dynamics in optical lattices? Is there a continuous crossover? Will one find new phenomena between these regimes? These questions could be directly addressed in future experiments, for example at the *Bose-Fermi Mixture* setup by studying fermionic spin dynamics at the intermediate lattice depths with prepared coherences.

# Appendix A

## Non-interacting fermions

This appendix contains additional information on non-interacting fermions. It provides definitions and formulas employed in the main text to describe non-interacting fermions either harmonically-trapped or confined in optical lattices.

### Fundamental constants

Common name	Abbreviation	Value
Speed of light	$c$	$2.99792458 \times 10^8 \text{ m} \cdot \text{s}^{-1}$
Vacuum permittivity	$\epsilon_0$	$8.8541878 \times 10^{-12} \text{ F} \cdot \text{m}^{-1}$
Elementary charge	$e$	$1.6021773 \times 10^{-19} \text{ C}$
Planck constant	$h$	$6.6260755 \times 10^{-34} \text{ J} \cdot \text{s}$
Planck constant (reduced)	$\hbar$	$1.0545887 \times 10^{-34} \text{ J} \cdot \text{s}$
Electron mass	$m_e$	$9.1093897 \times 10^{-31} \text{ kg}$
Boltzmann constant	$k_B$	$1.380658 \times 10^{-23} \text{ J} \cdot \text{K}^{-1}$
Atomic mass unit	$u$	$1.6605387 \times 10^{-27} \text{ kg}$
Gravity of Earth (Hamburg)	$g$	$9.813749 \text{ m} \cdot \text{s}^{-2}$
Bohr radius	$a_B$	$5.2917721 \times 10^{-11} \text{ m}$
Bohr magneton	$\mu_B$	$9.27400915 \times 10^{-24} \text{ J} \cdot \text{T}^{-1}$

**Table A.1: Fundamental constants in the International System of Units.** These constants [244] are used in this thesis. Atomic properties of  $^{40}\text{K}$  can be found in [245] and in the references therein. Scattering lengths of  $^{40}\text{K}$  are provided in Table 2.2.

### Fermions confined in a harmonic trap

In the experiments presented in this thesis, the atoms are confined in an optical dipole trap. After the evaporation, the trap is compressed, which justifies assuming a harmonic potential of the Gaussian-shaped trap. There are several excellent descriptions available for these systems [148, 246]. Here, the formulas important for the calculations in the main text are provided.

The single-particle Hamiltonian for the harmonic trap is given by

$$\mathcal{H}(\mathbf{r}, \mathbf{p}) = \frac{1}{2m} (p_x^2 + p_y^2 + p_z^2) + \frac{m\omega^2}{2} (x^2 + y^2 + \lambda z^2) \quad (\text{A.1})$$

For an ideal Fermi gas, the distribution follows the Fermi-Dirac statistics

$$f_{\text{FD}}(E, T) = \frac{1}{\zeta \exp\left(\frac{E}{k_{\text{B}}T}\right) + 1}, \quad (\text{A.2})$$

where  $\zeta = \exp(\mu/k_{\text{B}}T)$  is the fugacity, which is related to the chemical potential  $\mu$ . At zero temperature, the chemical potential coincides with the Fermi energy  $E_{\text{F}}$ , which corresponds to the highest occupied energy level in the harmonic trap. The Fermi energy can be calculated with

$$E_{\text{F}} = \hbar\omega(6\lambda N)^{1/3}, \quad (\text{A.3})$$

where  $N$  is the particle number. It is related to the Fermi temperature by  $T_{\text{F}} = E_{\text{F}}/k_{\text{B}}$ .

To calculate the density distribution in a harmonic trap, a semiclassical approximation can be employed. This assumes that the thermal energy is larger than the spacing of the trap levels and constitutes a reasonable approximation for the shallow trap geometry. In a phase-space representation, the Thomas-Fermi distribution of the trapped Fermi gas is given by [148, 247]

$$f_{\text{TF}}(\mathbf{r}, \mathbf{p}) = \frac{1}{(2\pi\hbar)^3} \frac{1}{\exp\left(\frac{\mathcal{H}(\mathbf{r}, \mathbf{p}) - \mu}{k_{\text{B}}T}\right) + 1}. \quad (\text{A.4})$$

The spatial density distribution is derived from the integration over the momentum degree of freedom, yielding

$$n(\mathbf{r}) = \frac{1}{(2\pi\hbar)^3} \int d\mathbf{p} f_{\text{TF}}(\mathbf{r}, \mathbf{p}). \quad (\text{A.5})$$

To calculate this, it is suitable to rewrite the spatial density in terms of polylogarithmic functions  $\text{Li}_n\{x\} = \sum_{k=1}^{\infty} x^k/k^n$  and to introduce the rescaled coordinate  $r = x^2 + y^2 + \lambda z^2$ . This results in the following equation:

$$n(r) = -\frac{(k_{\text{B}}mT)^{3/2}}{(2\pi)^{3/2}\hbar^3} \text{Li}_{3/2}\left\{-\zeta \exp\left(\frac{m\omega^2}{2k_{\text{B}}T}r\right)\right\}. \quad (\text{A.6})$$

The fugacity in this expression can be determined by the relation

$$\text{Li}_3(-\zeta) = \frac{T_{\text{F}}^3}{6T^3}. \quad (\text{A.7})$$

This allows for a straight-forward calculation of the density distribution. The peak density is defined as  $n_{\text{p}} = n(\mathbf{r} = 0)$  and the average density as  $\bar{n} = \int dr n(r)/N$ .

Note that for an interacting two-component spin mixture, it is in general a very complex problem to calculate the density distribution. However, since the experiments are performed in the weakly interacting regime, the interaction influence on the spatial shape is negligible. In a balanced spin mixture, the density is calculated using the particle number of one spin component. The temperature and the trap frequencies are calibrated in separate experiments. To account for the two-component spin mixture, the resulting density is multiplied by a factor of two.

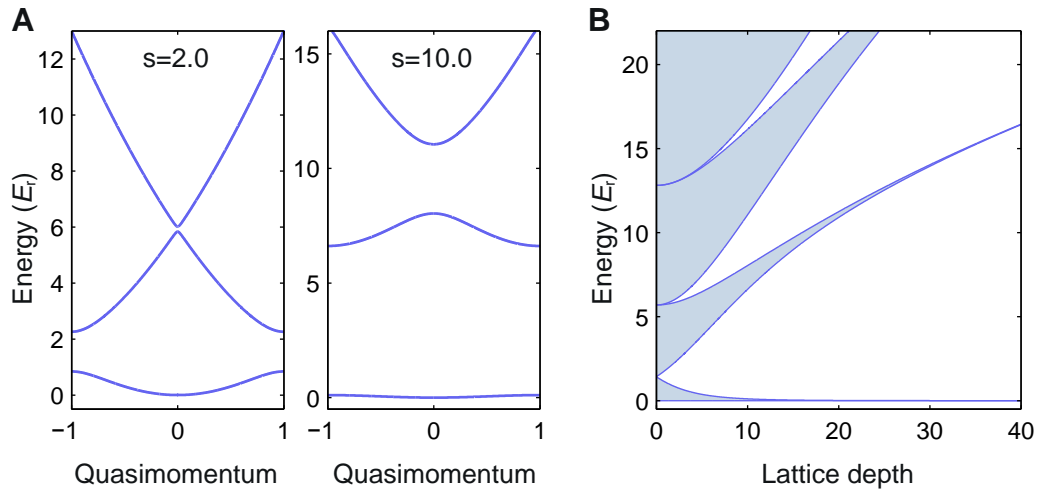


**Figure A.1: Band structure of a 1d optical lattice.** (A) Depicted is the band structure for the lattice depths  $s = 2.0$  and  $s = 10.0$ . For this representation in the so-called reduced zone scheme [174], the band structure is plotted within the first Brillouin zone as a function of the quasimomentum  $q$ . The employed units are  $k_{\text{BZ}} = k_{\text{lat}}$ . (B) The width of the energy bands is plotted as a function of the lattice depth.

## Fermions in periodic potentials

In the *Bose-Fermi Mixture* setup, a 3d cubic optical lattice is implemented, which can be superimposed on the atoms in the dipole trap [124, 125, 134]. The corresponding lattice potential leads to the formation of a band structure  $E_q^n$ , containing energy bands  $n$  for each quasimomentum  $q$  separated by band gaps. The corresponding lattice potential is separable in all spatial dimensions and the total energy spectrum is given by the sum of the individual spatial directions, each described by the Hamiltonian [247]

$$\mathcal{H}_{\text{lat}} = \frac{p^2}{2m} + s \cdot E_r \cdot \sin^2(k_{\text{lat}} z). \quad (\text{A.8})$$

Here,  $s$  is the dimensionless parameter for the lattice depth  $V_L = s E_r$ , where  $E_r = \hbar^2 k_{\text{lat}}^2 / 2m$  is the atomic recoil energy with  $k_{\text{lat}} = 2\pi / \lambda_{\text{lat}}$ . The eigenstates of this Hamiltonian are Bloch states, which have the same periodicity as the potential according to the Bloch theorem [174]. In a Fourier expansion they are given by

$$|\psi(q, n)\rangle = e^{-iqk_{\text{lat}}z} \sum_{l=-\infty}^{\infty} c_{q,l}^n e^{-i2lk_{\text{lat}}z}. \quad (\text{A.9})$$

The eigenenergies  $E_q^n$  of the Hamiltonian A.8 form a band structure, containing energy bands  $n$  for each quasimomentum  $q$  separated by band gaps. Note that the resulting spectrum  $E_q^n$  is uniquely defined by the lattice depth  $s$ , which is exemplarily depicted in Fig. A.1 A. For increasing lattice depth, the band width decreases while the band gap increases (see Fig. A.1 B).

Due to the Pauli exclusion principle, each single-particle state of the system can be occupied only once. The highest energy of the occupied single-particle states at zero temperature corresponds to the Fermi energy  $E_F$ . In quantum gas experiments,

typically only the lowest band is occupied, allowing for two ground states of the system: If the Fermi energy lies within the band gap, all available states in the lowest band are populated and a band insulator is formed, which is insulating and incompressible. If the Fermi energy lies within the lowest band, free states are available corresponding to a metallic state.

## Appendix B

# Feshbach resonances in $^{40}\text{K}$

In this work, the physics of interacting spin mixtures has been studied. Alongside the detailed investigation of spin dynamics in a fermionic quantum gas, several Feshbach resonances in  $^{40}\text{K}$  have also been investigated. This was necessary, since these resonances constitute a severe problem for the preparation of spin mixtures (see 3.2.3). Moreover, they are of general interest, providing an intriguing tool to tune interactions and losses in a wide parameter range.

Indeed, there is a zoo of Feshbach resonances present in  $^{40}\text{K}$ , which exceeds the typically used resonances (see Table B.1) by far. In the course of this research work, 20 new Feshbach resonances have been observed and identified (see Table B.2). This has been worked out in the diploma theses of N. Fläschner [108] and M. Langbecker [109], which I co-supervised. Here, I have summarized the results and compare them to calculations provided by T. Hanna and coworkers [117]. Parallel to the experiments performed during this work, in addition 26 Feshbach resonances have been found in the group of J. Walvaren in Amsterdam. The results are presented in the thesis of A. Ludewig [248]. A joint publication including in addition experimental data from the groups of I. Bloch in Munich and T. Esslinger in Zurich and several theory coworkers is in preparation.

At a Feshbach resonance, an unbound state of the two scattering particles is coupled to a virtual bound molecular state, which changes the interaction strength and losses dependent on the magnetic field [117, 119]. The scattering length has therefore a complex form:  $\tilde{a} = a - bi$ , where  $a$  describes the conventional elastic scattering and  $b$  corresponds to inelastic two-body collisions. The magnetic field dependence of  $a$  is given by:

$$a(B) = a_{\text{BG}} \left( 1 - \frac{\Delta B(B - B_0)}{(B - B_0)^2 + (\gamma_B/2)^2} \right). \quad (\text{B.1})$$

Here,  $B_0$  is the resonance position and  $\Delta B$  the width of the Feshbach resonance.  $\gamma_B$  is the decay rate of the closed channel and  $a_{\text{BG}}$  the background scattering length. The magnetic field dependence of  $b$  is given by

$$b(B) = 2a_{\text{res}} \frac{(\gamma_B/2)^2}{(B - B_0)^2 + (\gamma_B/2)^2}, \quad (\text{B.2})$$

where  $\gamma_B = \hbar\gamma/\mu_{\text{res}}$  with the differential magnetic moment  $\mu_{\text{res}}$  and the resonance length  $a_{\text{res}} = a_{\text{BG}}\Delta B/\gamma_B$ .

$m = \{m_1, m_2\}$	$M$	Partial wave	$B_{\text{exp}}(\text{G})$	$\Delta B_{\text{exp}}(\text{G})$	Refs.
$\{-9/2, -7/2\}$	-8	s	$202.10 \pm 0.07$	$7.0 \pm 0.2$	[48, 243, 249]
$\{-9/2, -5/2\}$	-7	s	$224.21 \pm 0.05$	$9.7 \pm 0.6$	[141, 250]

**Table B.1: Typically used Feshbach resonances in  $^{40}\text{K}$ .** So far, experiments have investigated mainly the following spin mixtures:  $\{-9/2, -7/2\}$  and  $\{-9/2, -5/2\}$ . The Feshbach resonances typically used in these mixtures are shown. Given are the total magnetization  $M = m_1 + m_2$ , the partial wave, the resonance position  $B_{\text{exp}}(\text{G})$  and the width  $\Delta B_{\text{exp}}(\text{G})$ .

To determine Feshbach resonances experimentally, a spin mixture of  $m = \{+9/2, +7/2\}$  with about  $5 \times 10^4$  atoms per spin state is prepared in an optical dipole trap. The trapping frequencies are  $\omega = 2\pi \times 50 \text{ Hz}$  and the temperature is approximately  $T = 0.3 \text{ T}_F$ . For the investigation of different collision channels, the spin mixtures are prepared at a magnetic field of  $B = 45 \text{ G}$  with rf-sweeps. After this preparation, the magnetic field is ramped to its final value and a waiting time of 100 ms is applied. Subsequently, the magnetic field is switched off and the atoms are counted after a time-of-flight applying a Stern-Gerlach gradient field. The position  $B_{\text{exp}}(\text{G})$  and the width  $\Delta B_{\text{exp}}(\text{G})$  of the Feshbach resonances are determined with atomic losses (see also [108]). Note that the atom loss gives a reasonable estimate for the Feshbach resonance position accompanied by small deviations [53]. The width of the losses is mainly connected to inelastic two-body collisions and three-body losses and does not serve to precisely determine the width of the resonance. However, it serves as a measure for magnetic field ranges with enhanced losses and is crucial for the preparation of spin mixtures. The experimental data are compared to calculations using multi-channel quantum defect theory [119], kindly provided by T. Hanna and coworkers [117]. These calculations include the scattering length as a function of the magnetic field, sampled with a resolution of 0.5 G. To extract the resonance position  $B_{\text{th}}(\text{G})$  and the resonance width  $\Delta B_{\text{th}}(\text{G})$  from the calculations, equation B.1 was fitted to the theoretical data. The comparison of experiment and theory, depicted in Table B.2, shows a good agreement for the resonance position. This is expected, since the molecular potentials are very well known for  $^{40}\text{K}$ .

As can be drawn from Table B.2, one Feshbach resonance of the spin mixture  $m = \{+1/2, -1/2\}$  has particular properties, which have been studied in detail (see [109]). This spin configuration corresponds to the magnetic ground state of the two-particles states of the  $M = 0$  spin system. Thus it is stable against spin-changing collisions at large magnetic fields, which widely avoids losses. Calculations reveal a Feshbach resonance at a magnetic field of 389.6 G with a width of approximately 26.4 G, allowing to tune the scattering length range between  $-3000 a_B$  and  $+3000 a_B$ . This is about three times as wide as the conventional Feshbach resonances, which has motivated a detailed analysis. For a precise determination, a new method based on spin waves has been worked out, which is in detail described in the diploma thesis of M. Langbecker [109]. The idea behind this is similar to the gradient compensation presented in section 3.3.2. It relies on the fact that the phase of the dipole oscillations induced by spin waves is inverted when the sign of the interaction changes from positive to negative. This occurs at the resonance position as well as at its zero crossing. It turns out that this method allows for a precise determination. The experimental values of the position are  $B_{\text{exp}}(\text{G}) = 389.5(0.1)$  and of the width  $\Delta B_{\text{exp}}(\text{G}) = 25.9(0.8)$ , which is in very good agreement with the data.

$m = \{m_1, m_2\}$	$M$	Partial wave	$B_{\text{exp}}(\text{G})$	$\Delta B_{\text{exp}}(\text{G})$	$B_{\text{th}}(\text{G})$	$\Delta B_{\text{th}}[\text{G}]$
$\{+1/2, -1/2\}$	0	s	15.3 (3.8)	3.8	17.3	0.1
	0	s	30.5 (3.8)	3.8	30.9	0.2
	0	s	53.4 (3.8)	3.8	53.4	0.4
	0	s	87.5 (3.8)	3.8	87.1	0.4
	0	s	245.6 (0.8)	2.5	246.6	2.0
	0	s	389.5 (0.1)	25.9 (0.8)	389.6	26.4
$\{+3/2, -3/2\}$	0	s	95.1 (3.8)	3.8	93.8	1.8
	0	s	181.9 (3.8)	3.8	181.5	2.2
$\{+5/2, -5/2\}$	0	s	61.0 (3.8)	15.0	61.5	4.2
$\{+7/2, -7/2\}$	0	s	35.0 (1.0)	9.3	35.0	3.4
	0	s	148.0 (3.8)	3.8	145.8	0.2
$\{+9/2, -9/2\}$	0	s	18.0 (0.4)	6.7	18.8	1.8
$\{+9/2, -7/2\}$	+1	s	13.4 (1.9)	3.0	14.5	0.4
	+1	s	29.0 (1.9)	8.0	30.2	2.9
	+1	p	138.4 (1.0)	40.8	138	
$\{+9/2, -5/2\}$	+2	s	26.7 (1.9)	8.0	27.1	1.4
	+2	s	63.8 (0.3)	29.8	63.3	6.0
$\{+9/2, -3/2\}$	+3	s	53.4 (3.8)	11.0	52.4	3.1
	+3	s	141.1 (0.8)	45.5	140.5	14.0
$\{+9/2, -1/2\}$	+4	s	114.0 (7.6)	>50	113.5	7.8

**Table B.2: New Feshbach resonances in  $^{40}\text{K}$ .** 20 new Feshbach resonances have been identified, which are listed in the table. Given are the corresponding spin mixture, the total magnetization  $M = m_1 + m_2$ , the partial wave, the resonance position  $B_{\text{exp}}(\text{G})$  and the width  $\Delta B_{\text{exp}}(\text{G})$ . Furthermore, data for the calculated resonance position  $B_{\text{th}}(\text{G})$  and width  $\Delta B_{\text{th}}(\text{G})$  are shown, provided by T. Hanna and coworkers [117].

The experimental study demonstrates, that 20 new Feshbach resonances have been observed in  $^{40}\text{K}$ , where 19 have an s-wave character and one is a p-wave resonance. Furthermore, another 11 loss features are listed in Table B.3, which might also be associated with Feshbach resonances, where no data is available. In general, most Feshbach resonances observed in our experiment are accompanied by strong losses in a broad magnetic field range. These fields have to be circumvented in particular during the evaporation, which limits the available parameter regimes significantly. Alternatively, the spin mixtures can be finally prepared after the evaporation of stable spin mixtures. However, in general the lifetime is strongly reduced for most spin mixtures.

As a consequence, this also provides a new tuning knob: Losses can be tuned at Feshbach resonances, while the interactions remain widely constant. This allows for various future applications, for example the study of a quantum-Zeno insulator in optical lattices, which has been worked out in the course of this research work. The result is discussed in the thesis of J. Heinze [107]. In addition, the broad Feshbach resonance in the spin mixture  $m = \{+1/2, -1/2\}$  is prosperous for future applications. Located at an accessible magnetic field of  $B = 389.6 \text{ G}$ , its broad width of approximately 26.4 G is approximately three times larger compared to conventionally used Feshbach resonances. Due to the suppression of losses, this resonance also constitutes an ideal candidate for two-component studies, since it requires less control over the magnetic field. In addi-

$m = \{m_1, m_2\}$	$M$	$B_{\text{exp}}(\text{G})$	$\Delta B_{\text{exp}}(\text{G})$
$\{+5/2, -9/2\}$	-2	22.9	10.0
$\{+1/2, -1/2\}$	0	40.3	< 1
	0	46.7	< 1
$\{+5/2, -5/2\}$	0	30.5	7.0
$\{+7/2, -7/2\}$	0	64.5	9.6
$\{+9/2, -9/2\}$	0	36.3	14.0
	0	92.6	36.7
$\{+9/2, -7/2\}$	+1	66.3	25.6
$\{+7/2, -5/2\}$	+1	61.0	20.0
$\{+5/2, -3/2\}$	+1	121.6	> 40
$\{+9/2, -5/2\}$	+2	163.4	6.7

**Table B.3: Further magnetic field values in  $^{40}\text{K}$  with enhanced losses.** Listed are magnetic fields, at which strong losses occur. Given is the corresponding spin mixture, the total magnetization  $M = m_1 + m_2$ , the loss position  $B_{\text{exp}}(\text{G})$  and the loss width  $\Delta B_{\text{exp}}(\text{G})$ . These magnetic fields are probably associated with a Feshbach resonance. Either there are no data available or the corresponding loss features arise from higher partial wave Feshbach resonances.

tion, the absolute value of the magnetization of the involved spin states makes this spin mixture less sensitive for magnetic field gradients, which is very important for current studies of spin-orbital coupling with fermionic atoms [251]. Moreover, combining different Feshbach resonances constitutes an ideal starting point for high-spin mixtures with controllable interactions. From the current available data, three-component mixtures with two attractive and one repulsive scattering length are available, allowing to study unconventional high-spin BCS pairing [88, 90, 208]. So far, there is no combination known, where three-component mixtures with exclusively attractive interactions can be realized in  $^{40}\text{K}$ . This is possible with  $^6\text{Li}$ , where experiments in this direction are currently performed.

# Appendix C

## Details for fermionic spin dynamics

At this point, details for the main subject of this thesis – spin dynamics in a fermionic quantum gas - will be provided. This includes further information on the data analysis and the interaction matrices for all available spin configurations. Moreover, additional details for the spin rotation of incoherent states and the numerical treatment of the Boltzmann equation in single-mode approximation are given.

### Interactions of the spin systems in $^{40}\text{K}$

In section 4.2, two-particle spin dynamics have been investigated for two spin systems: a pseudo-spin  $3/2$  system including the two-particles states  $|7/2, 3/2\rangle$  and  $|9/2, 1/2\rangle$  (see section 4.2.2) and the spin  $9/2$  system including the two-particle states  $|\pm 1/2\rangle$ ,  $|\pm 3/2\rangle$ ,  $|\pm 5/2\rangle$ ,  $|\pm 7/2\rangle$ , and  $|\pm 9/2\rangle$  (see section 4.2.4). These spin systems were chosen to cover two cases: the most fundamental and the most complex spin system available in  $^{40}\text{K}$ . To complement this, an overview of the interaction matrices is given for all available spin systems in the lowest hyperfine manifold of  $^{40}\text{K}$ , which could be studied in future experiments.

In principle, there are 13 different spin systems available, where spin dynamics occur ( $M = -6, \dots, 6$ ). The interaction matrices are independent of the sign of the total magnetization due to the rotational symmetry of the system. They are listed in Table C.1, according to the basis provided in Table 2.1.

$M = m_1 + m_2$	Interaction matrix ( $a_B$ )
$\pm 8, \pm 7$	(168.53)
$\pm 6$	$\begin{pmatrix} 167.77 & 1.16 \\ 1.16 & 166.76 \end{pmatrix}$
$\pm 5$	$\begin{pmatrix} 167.01 & 1.24 \\ 1.24 & 167.52 \end{pmatrix}$
$\pm 4$	$\begin{pmatrix} 165.87 & 1.9 & -0.78 \\ 1.9 & 165.87 & 2.95 \\ -0.78 & 2.95 & 163.9 \end{pmatrix}$
$\pm 3$	$\begin{pmatrix} 164.35 & 2.49 & -0.78 \\ 2.49 & 164.98 & 2.53 \\ -0.78 & 2.53 & 166.31 \end{pmatrix}$
$\pm 2$	$\begin{pmatrix} 161.64 & 4.14 & -2.22 & 1.64 \\ 4.14 & 162.09 & 5.4 & -3.69 \\ -2.22 & 5.4 & 161.53 & 7.43 \\ 1.64 & -3.69 & 7.43 & 158.21 \end{pmatrix}$
$\pm 1$	$\begin{pmatrix} 156.95 & 6.26 & -3.04 & 1.31 \\ 6.26 & 159.61 & 5.94 & -2.4 \\ -3.04 & 5.94 & 161.9 & 4.32 \\ 1.31 & -2.4 & 4.32 & 165.02 \end{pmatrix}$
0	$\begin{pmatrix} 145.77 & 11.18 & -6.48 & 4.50 & -3.69 \\ 11.18 & 154.12 & 10.19 & -6.99 & 5.83 \\ -6.48 & 10.19 & 156.23 & 10.86 & -8.78 \\ 4.50 & -6.99 & 10.86 & 155.66 & 13.40 \\ -3.69 & 5.83 & -8.78 & 13.40 & 151.62 \end{pmatrix}$

**Table C.1: Interaction matrices of spin systems in the lowest hyperfine manifold of  $^{40}\text{K}$ .** Matrices of different subspaces with the involved two-particle states  $|m_1, m_2\rangle$  are listed according to their total magnetization  $M = m_1 + m_2 = -8, \dots, +8$  with the same basis as in Table 2.1. The described experiments are performed in the  $M = 5$  and  $M = 0$  spin system, involving two and five two-particle states, respectively (see section 2.2.2).

## Fitting of the spin-dynamics data

From the spin-dynamics experiments, the data are obtained in a Stern-Gerlach experiment. In each experimental run, the occupation of each spin component is measured simultaneously. Therefore, the experiments require a special treatment in the data analysis.

Up to ten different spin components can be involved in the dynamics, which oscillate with up to ten frequencies. For a better reliability of the data analysis, a high-dimensional fit algorithm was employed to extract each frequency from all data sets in conformity (see also [1, 5]).

Therefore, to each oscillating spin state, the following fit function is applied:

$$n^{(m)}(t) = \underbrace{O^{(m)}}_{\text{offset}} + \underbrace{A^{(m)} \exp(-D^{(m)}t)}_{\text{slow in-/decrease}} + \underbrace{\sum_j C_j^{(m)} \exp(-\Gamma_j t) \cos(\omega_j t + \phi_j)}_{\text{damped spin oscillations}}. \quad (\text{C.1})$$

Here,  $O^{(m)}$  is a general offset and the slow overall increase or decrease of the population of the individual spin states is expressed in the second term, employing an exponential function with amplitude  $A^{(m)}$  and time constant  $D^{(m)}$ . The spin oscillations are described by the sum in the third term, where  $C_j^{(m)}$  is the amplitude,  $\omega_j$  the frequency,  $\phi_j$  the initial phase and  $\Gamma_j$  the damping constant. The sum is taken over the number of all contributing frequencies  $j$ .

For the two-particle dynamics, the two-level and the five-level system have been investigated (see section 4.2). Regarding the two-level system (see section 4.2.2), four single-particle spin states are involved in the spin oscillations ( $|1/2\rangle$ ,  $|3/2\rangle$ ,  $|7/2\rangle$ ,  $|9/2\rangle$ ). Further spin states, which are slowly populated due to tunneling processes, only show a slow overall increase of their spin populations. These are fitted with  $n^{(m)}(t) = \tilde{A}^{(m)} (1 - \exp(-\tilde{\Gamma}^{(m)}t))$ , where  $\tilde{A}^{(m)}$  is the amplitude and  $\tilde{\Gamma}^{(m)}$  the time constant. For the investigated five-level system (see section 4.2.4), all spin states participate in the time evolution ( $|-9/2\rangle, \dots, |9/2\rangle$ ). Due to the switching time of the magnetic field ( $t_{\text{switch}} \approx 500 \mu\text{s}$ ), individual phases  $\phi_j \neq 0$  for each spin components are considered.

For the collective spin dynamics in bulk systems, the spin-oscillation data were also fitted with formula C.1. However, similar to the two-level system, only two spin configurations are involved. This restricts the fitting to one frequency and the corresponding four oscillating spin components. Moreover, when no significant overall increase or decrease was visible in the data, the second part of equation C.1 was omitted.

## Spin rotations of arbitrary spin mixtures

In section 5.1.2, the role of coherences for collective spin dynamics has been worked out and a preparation scheme has been demonstrated. Here, some technical details for the calculations will be provided and the spin rotations of further spin mixtures ( $m = \{\pm 3/2\}$  and  $m = \{\pm 9/2\}$ ) will be presented.

At low magnetic field, all ten spin states of the  $f=9/2$  manifold are simultaneously coupled. Therefore, the procedure corresponds to a rotationally symmetric transformation in spin space, since different spin states remain indistinguishable. This rotation is generated by the angular momentum operators  $S_{\pm}$  depending on the total spin  $f$  [252]. Since the rf-pulses couple the spin states with  $\Delta m = \pm 1$ , the corresponding generators of rotation are given by

$$\begin{aligned} S_x &= \frac{1}{2} (S_+ + S_-) , \\ S_y &= \frac{1}{2i} (S_+ - S_-) . \end{aligned} \quad (\text{C.2})$$

Without loss of generality, the phase between the operators  $S_+$  and  $S_-$  can be set to zero.

The rotation of the spin state  $|m\rangle$  of one single atom is described by

$$|m(\theta)\rangle = \exp\left(-\frac{iS_{x,y}\theta}{2}\right) |m\rangle , \quad (\text{C.3})$$

where  $\theta$  is the spin rotation angle. Note that a factor of  $1/2$  was inserted, such that a full rotation is obtained at  $\theta = 2\pi$ .

This concept can be generalized to a density matrix  $\rho$ , which is not a pure state as above but an incoherent state. The rotation of the initial density matrix  $\rho_0$  is given accordingly by

$$\rho(\theta) = \exp\left(-\frac{iS_{x,y}\theta}{2}\right) \cdot \rho \cdot \exp\left(+\frac{iS_{x,y}\theta}{2}\right) . \quad (\text{C.4})$$

This can be applied to all spin mixtures. Throughout this work, the absolute values of the density matrix are always plotted; however, the off-diagonal elements can be complex. Note that the spin rotation is a linear operation, which changes each diagonal entry of the density matrix independently. The patterns shown in Fig. 5.4 are interference effects, which lead to checkerboard-like structures. When a ten-component Fermi sea occupying all diagonal elements of the density matrix is rotated, it remains fully unaffected by the rf-manipulation.

In the following, measurements of spin rotations of two further spin mixtures are provided. The result is similar to the rotation of the spin mixture  $m = \{\pm 1/2\}$ , demonstrated in section 5.1.2. The spin mixture  $m = \{\pm 3/2\}$  has been used in section 5.4.5. It allowed for the first observation of collective spin dynamics dominated by collisions with  $\Delta m = 2$ . For this purpose, a rf-pulse was applied to this mixture, yielding significant occupations and coherences between the spin configurations  $\pm 1/2$  and  $\pm 5/2$ . The experimental result of this rf-manipulation is depicted in Fig. C.1 A. The spin mixture  $m = \{\pm 9/2\}$  was employed to demonstrate spin dynamics in further spin mixtures. It was rotated in spin space resulting in occupations and coherences between the spin configurations  $\pm 9/2$  and  $\pm 7/2$ . The experimental result of this preparation is depicted in Fig. C.1 B. Note that also for these spin mixtures a very agreement is found with the Rabi-frequency as only free parameters.

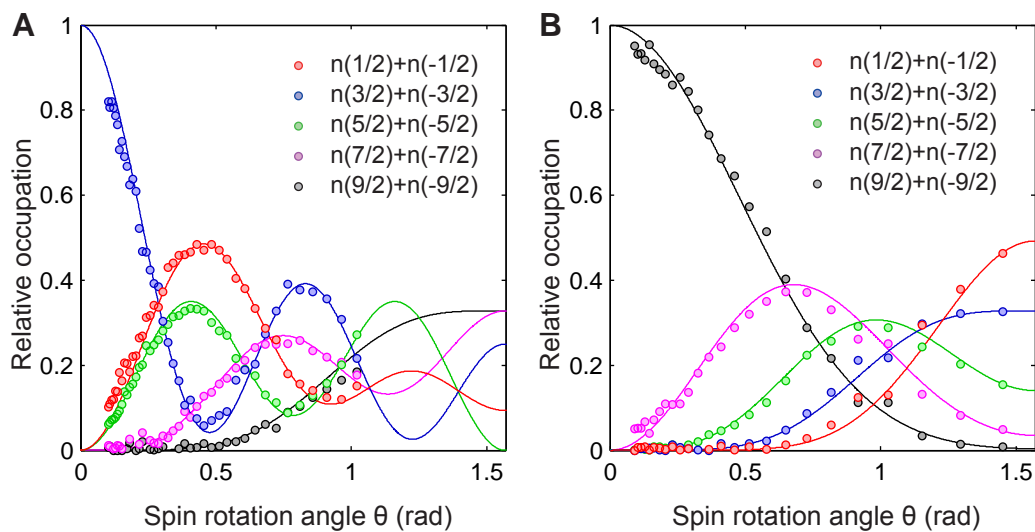


**Figure C.1: Preparation of single-particle coherences for different spin mixtures.** Measured spin occupations starting from the spin mixture  $m = \{\pm 3/2\}$  (**A**) and  $m = \{\pm 3/2\}$  (**B**) are depicted as a function of the rotation angle  $\theta$ . The rf-pulse is applied at a frequency of 53.7 kHz (22 kHz) and at a magnetic field of  $B = 0.17$  G ( $B = 0.07$  G) for **A** (**B**). Solid lines are calculations using equation 5.7, with the Rabi-frequency as the only free parameter.

For completeness, the employed generators of rotation  $S_x$  and  $S_y$  and the projection operator  $S_z$  are provided for the ten-dimensional spin space of the  $f = 9/2$  manifold, yielding three  $10 \times 10$  matrices:

$$\begin{aligned}
S_x &= \begin{pmatrix} 0 & \frac{3}{2} & 0 & 0 & 0 & 0 & 0 & 0 & 0 & 0 \\ \frac{3}{2} & 0 & 2 & 0 & 0 & 0 & 0 & 0 & 0 & 0 \\ 0 & 2 & 0 & \frac{\sqrt{21}}{2} & 0 & 0 & 0 & 0 & 0 & 0 \\ 0 & 0 & \frac{\sqrt{21}}{2} & 0 & \sqrt{6} & 0 & 0 & 0 & 0 & 0 \\ 0 & 0 & 0 & \sqrt{6} & 0 & \frac{5}{2} & 0 & 0 & 0 & 0 \\ 0 & 0 & 0 & 0 & \frac{5}{2} & 0 & \sqrt{6} & 0 & 0 & 0 \\ 0 & 0 & 0 & 0 & 0 & \sqrt{6} & 0 & \frac{\sqrt{21}}{2} & 0 & 0 \\ 0 & 0 & 0 & 0 & 0 & 0 & \frac{\sqrt{21}}{2} & 0 & 2 & 0 \\ 0 & 0 & 0 & 0 & 0 & 0 & 0 & 2 & 0 & \frac{3}{2} \\ 0 & 0 & 0 & 0 & 0 & 0 & 0 & 0 & \frac{3}{2} & 0 \end{pmatrix} \\
S_y &= \begin{pmatrix} 0 & -\frac{3}{2}i & 0 & 0 & 0 & 0 & 0 & 0 & 0 & 0 \\ \frac{3}{2}i & 0 & -2i & 0 & 0 & 0 & 0 & 0 & 0 & 0 \\ 0 & 2i & 0 & -\frac{\sqrt{21}}{2}i & 0 & 0 & 0 & 0 & 0 & 0 \\ 0 & 0 & \frac{\sqrt{21}}{2}i & 0 & -\sqrt{6}i & 0 & 0 & 0 & 0 & 0 \\ 0 & 0 & 0 & \sqrt{6}i & 0 & -\frac{5}{2}i & 0 & 0 & 0 & 0 \\ 0 & 0 & 0 & 0 & \frac{5}{2}i & 0 & -\sqrt{6}i & 0 & 0 & 0 \\ 0 & 0 & 0 & 0 & 0 & \sqrt{6}i & 0 & -\frac{\sqrt{21}}{2}i & 0 & 0 \\ 0 & 0 & 0 & 0 & 0 & 0 & \frac{\sqrt{21}}{2}i & 0 & -2i & 0 \\ 0 & 0 & 0 & 0 & 0 & 0 & 0 & 2i & 0 & -\frac{3}{2}i \\ 0 & 0 & 0 & 0 & 0 & 0 & 0 & 0 & \frac{3}{2}i & 0 \end{pmatrix} \quad (C.5) \\
S_z &= \begin{pmatrix} \frac{9}{2} & 0 & 0 & 0 & 0 & 0 & 0 & 0 & 0 & 0 \\ 0 & \frac{7}{2} & 0 & 0 & 0 & 0 & 0 & 0 & 0 & 0 \\ 0 & 0 & \frac{5}{2} & 0 & 0 & 0 & 0 & 0 & 0 & 0 \\ 0 & 0 & 0 & \frac{3}{2} & 0 & 0 & 0 & 0 & 0 & 0 \\ 0 & 0 & 0 & 0 & \frac{1}{2} & 0 & 0 & 0 & 0 & 0 \\ 0 & 0 & 0 & 0 & 0 & -\frac{1}{2} & 0 & 0 & 0 & 0 \\ 0 & 0 & 0 & 0 & 0 & 0 & -\frac{3}{2} & 0 & 0 & 0 \\ 0 & 0 & 0 & 0 & 0 & 0 & 0 & -\frac{5}{2} & 0 & 0 \\ 0 & 0 & 0 & 0 & 0 & 0 & 0 & 0 & -\frac{7}{2} & 0 \\ 0 & 0 & 0 & 0 & 0 & 0 & 0 & 0 & 0 & -\frac{9}{2} \end{pmatrix}
\end{aligned}$$

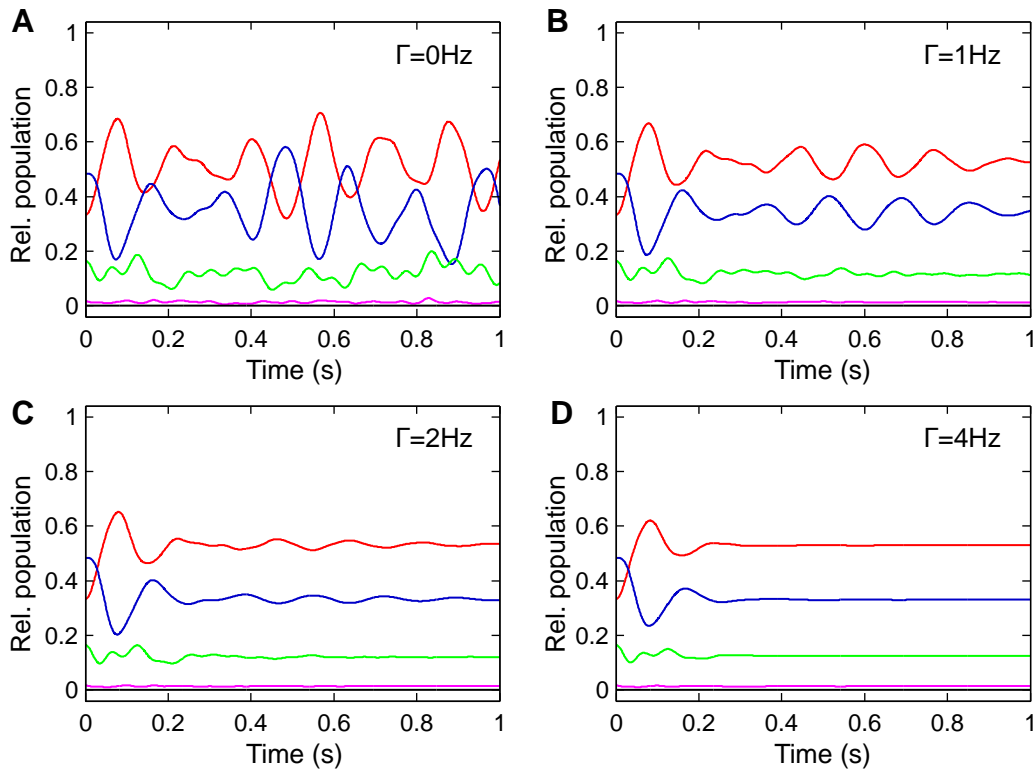


**Figure C.2: Single-mode calculations with inserted phenomenological damping.** Calculated spin occupations are depicted as a function of different damping rates  $\Gamma$  as indicated in the figure. The same parameters have been used as for the proof-of-principle experiment shown in section 5.5. In general, for the calculations a damping rate of  $\Gamma = 1 - 2$  Hz is assumed, which matches the experimental findings. The mean-field oscillation properties such as the frequency and amplitude are not significantly affected.

## Details for the single-mode approximation

In chapter 5 and 6, a single-mode approximation has been worked out – first for the pure mean-field approach and second for the collision term. In this section, details for the implementation will be provided. Furthermore, it will be demonstrated that not only spin dynamics initialized by prepared coherences but also spin instabilities are captured in this approach.

For the simulations, the particle number, the temperature, and the trapping frequencies are inserted. These are determined in separate experiments prior to the spin-dynamics experiments. The corresponding statistical errors are accounted for in the simulations, but those are typically small. In this context, systematic errors are hard to estimate: The particle number has systematic uncertainties due to different absorption cross sections (for details on this issue see [106, 137]). In addition, the accuracy of the temperature determination is mainly limited by the finite time-of-flight. Moreover, the trapping frequencies are calibrated with dipole oscillations, which also leads to small deviations for multi-mode fermions [203].

With these input parameters, the simulations are in principle performed without

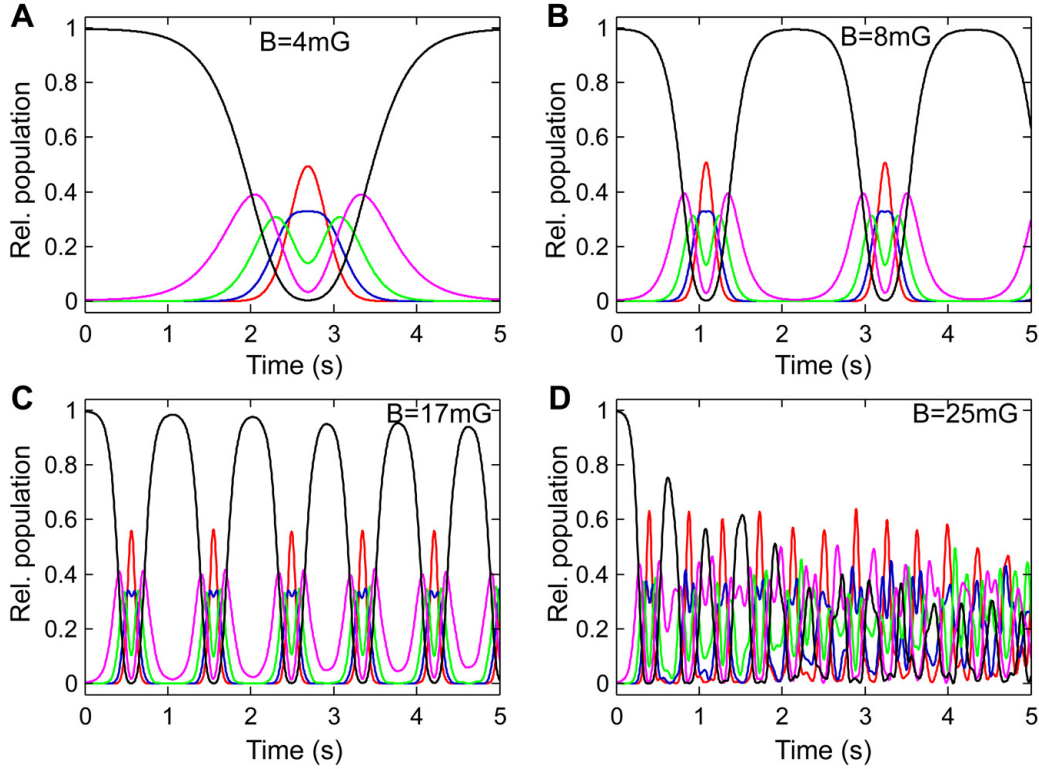


**Figure C.3: Simulations of fermionic spin instabilities for different magnetic fields.** Calculated spin occupations are depicted as a function of different magnetic fields as indicated in the figure. The initial state is the spin mixture  $m = \{\pm 9/2\}$  with a small spin rotation of  $\theta = 0.05$ . The temperature is  $T = 0.1T_F$ , and the peak density is  $n_p = 1 \times 10^{13} \text{ cm}^{-3}$ .

free parameters. An additional assumption is the phenomenological damping rate  $\Gamma$  in the Boltzmann equation:

$$\partial_t \rho(t) = \underbrace{\frac{1}{i\hbar} \left[ \bar{V} \sum_{kl} (U_{klij} - U_{kjil}) \rho_{kl}(t), \rho(t) \right]}_{\text{collisionless Boltzmann equation}} + \underbrace{\frac{1}{i\hbar N} [qS_z^2, \rho(t)] - \Gamma \cdot \rho(t)}_{\text{damping}} \Big|_{i \neq j}. \quad (\text{C.6})$$

As worked out in chapter 6, the damping term globally reduces the coherences of the system and damps the collective spin dynamics. This effect is demonstrated in Fig. C.2, where collective spin dynamics for the parameter of the proof-of-principle experiment (see Fig. 5.5) are simulated for different  $\Gamma$ . As expected, the mean-field dynamics are damped out. For the simulations, the damping rate  $\Gamma$  is chosen between 1–2 Hz, which is in good agreement with the experiments. Additionally, this leads to the Fourier broadening visible in the frequency analysis of the spin oscillations.

In the following, I demonstrate that also spin instabilities can be reproduced in a single-mode approximation. In section 6.3.1, density matrices of such a simulation have been shown, revealing the spin occupations alongside the formation of coherences. The unknown initial coherence fluctuations constitute a general problem. They are modeled with a small spin rotation  $\theta \leq 0.1$ . In Fig. C.3, a simulation for the initial spin mixture

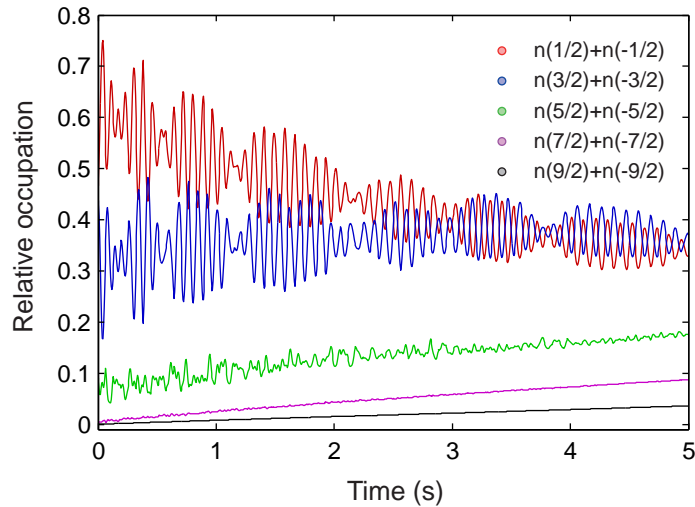


**Figure C.4: Long-term spin dynamics calculation in a single-mode approximation.** Plotted is a numerical simulation of the dynamics using the 3d Boltzmann equation including the collision term in single-mode approximation (equation 6.7). The same parameters as in the experiment in Fig. 6.1 have been used. The simulations reproduce the spin oscillations (mean-field dynamics) and also the subsequent relaxation of the system towards an equilibrium spin distribution (spin-changing lateral collisions).

$m = \{\pm 9/2\}$  with a spin rotation of  $\theta = 0.05$  is depicted. The time evolution reveals giant collective dynamics even though the initial coherences are very small. In contrast to the spin-cascade experiment presented in section 6.3.1, coherent dynamics lead to oscillations between all spin configurations. Probably the presence of a magnetic field gradient damps this oscillatory behavior in the experiment. In general, this demonstrates that spin instabilities can be reproduced within the single-mode approximation approach. The dynamics are depicted for different magnetic fields as indicated in the figure, revealing a fully different spin dynamics. In particular for higher magnetic fields, a dephasing of the spin configurations is found, consistent with the experiments.

Moreover, the collision term was implemented in the single-mode approximation as worked out in section 6.4.1. It has been demonstrated in section 6.4.2 that this approach reproduces the slow spin redistribution induced by spin-changing lateral collisions. Further simulations have been performed to investigate the influence of the single-mode collision term on the collective spin dynamics. For this purpose, the dynamics of the long-term experiment as shown in Fig. 6.1 was simulated without free parameters. The result is depicted in Fig. C.4, where three observations can be found: First, the mean-field driven spin oscillations are very well reproduced. This underlines again that the single-mode approximation accounts for spin-changing forward collisions, which is expected from the detailed study described in section 5.4. Note that the beat note visible in the simulation is also a mean-field effect and arises from the interplay between several involved scattering lengths. Moreover, the spin redistribution is reproduced, highlighting that spin-changing lateral collisions can also be described in a single-mode approximation as discussed in section 6.4. However, the damping of the spin oscillations is significantly underestimated. This can be attributed to the integration over the spatial degrees of freedom, which are obviously important for the correct descrip-

tion. Therefore, spin-conserving incoherent collisions are not described in the employed single-mode approximation. In contrast to the single-mode approximation approach, simulations of the Boltzmann equation with collision term and spatial resolution in 1d reproduce the observed damping much better [2].

# List of Figures

1.1	The key results of this thesis. . . . .	3
2.1	Zeeman splitting of the ground-state hyperfine manifolds of $^{40}\text{K}$ . . . . .	8
2.2	Sketch of a high-spin scattering process. . . . .	11
2.3	Zeeman energy of the five spin configurations of the $M = 0$ spin system. . . . .	15
3.1	The experimental procedure to study fermionic spin dynamics. . . . .	19
3.2	Density distribution of an ultracold Fermi sea in the magnetic trap. . . . .	20
3.3	Optimization of the MOT loading procedure. . . . .	21
3.4	Optimization of the evaporation in the magnetic trap. . . . .	22
3.5	Rabi-oscillations between two spin states within the $f = 9/2$ manifold of $^{40}\text{K}$ . . . . .	23
3.6	Radio-frequency sweeps between the spin states of the $f = 9/2$ hyperfine manifold of $^{40}\text{K}$ . . . . .	24
3.7	Effect of Feshbach resonances on the evaporation efficiency. . . . .	26
3.8	Controlling temperature and particle number of a Fermi sea. . . . .	27
3.9	Detection of high-spin fermions. . . . .	29
3.10	Compensation of the magnetic offset field in the transverse direction. . . . .	31
3.11	Compensation of the magnetic offset field in the axial direction. . . . .	32
3.12	Compensation of the magnetic gradient field. . . . .	34
3.13	Local microwave transfer in an elongated Fermi gas. . . . .	35
3.14	Calibration of the magnetic field gradient. . . . .	36
4.1	Sketch of the multi-band spectroscopy technique. . . . .	41
4.2	Momentum-resolved band structure of fermions in optical lattices. . . . .	42
4.3	Dispersion relation for the third band. . . . .	43
4.4	Spatial distribution of the atoms in deep optical lattices. . . . .	47
4.5	Sketch of the pseudo-spin $3/2$ system. . . . .	48
4.6	Observation of spin-changing collisions in a pseudo-spin $3/2$ system. . . . .	49
4.7	Sketch of the black-out-pulse technique. . . . .	50
4.8	Observation of high-contrast spin oscillations. . . . .	51
4.9	Crossover from the depolarized to the polarized regime. . . . .	53
4.10	A fermionic spin resonance. . . . .	54
4.11	The multi-flavor spin $9/2$ system. . . . .	56
4.12	Coherent multi-flavor spin dynamics in the spin $9/2$ system. . . . .	57
4.13	High-spin interactions at the crossover to the depolarized multi-flavor regime. . . . .	58
4.14	Crossover to the depolarized multi-flavor regime. . . . .	59

4.15	Spectra for different spin-exchange processes. . . . .	61
4.16	Sketch of tunneling at defects. . . . .	63
4.17	Sketch of tunneling in the core. . . . .	65
4.18	Impact of small tunneling on the two-particle spin dynamics. . . . .	66
4.19	Transition from the two-body to the many-body regime. . . . .	67
4.20	Spin-oscillation properties from the two-body to the many-body regime. . . . .	68
4.21	Numerical simulation of spin oscillations in a four-well system. . . . .	69
4.22	Principle of multi-band spin dynamics. . . . .	71
4.23	Observation of spin-population transfer into higher bands due to spin-changing collisions. . . . .	73
5.1	Can a Fermi sea perform collective dynamics of its spin degree of freedom? . . . . .	76
5.2	Single-particle density matrix for the lowest hyperfine manifold of $^{40}\text{K}$ . . . . .	77
5.3	Density matrix for different incoherent states. . . . .	79
5.4	Preparation of single-particle coherences in a Fermi sea. . . . .	80
5.5	Giant and long-lived spin oscillations in an ultracold Fermi sea. . . . .	82
5.6	Structure formation in a Fermi sea due to spin-changing collisions. . . . .	83
5.7	Observed spatial distribution of a Fermi sea exposed to spin-changing collisions. . . . .	85
5.8	Combination of spin waves and spin-changing collisions. . . . .	86
5.9	Validity of the single-mode approximation. . . . .	88
5.10	Spin-oscillation properties for different magnetic fields. . . . .	90
5.11	The interaction integral $\bar{V}$ . . . . .	91
5.12	Spin-oscillation properties for different densities. . . . .	92
5.13	Spin-oscillation properties for different spin rotations. . . . .	93
5.14	Spin oscillations in different spin mixtures. . . . .	94
5.15	Direct observation of spin oscillations with $\Delta m = 2$ . . . . .	96
6.1	Long-term spin dynamics. . . . .	100
6.2	Collision processes in a high-spin Fermi sea. . . . .	101
6.3	Impact of lateral collisions on the density matrix. . . . .	103
6.4	Sketch of lateral collisions at finite temperature. . . . .	105
6.5	Realizing the same mean-field interaction at higher temperatures. . . . .	106
6.6	Spin dynamics in a Fermi sea for increasing temperature. . . . .	107
6.7	Mean-field oscillation properties for increasing temperature. . . . .	108
6.8	Damping of the spin oscillations for increasing temperature. . . . .	109
6.9	Observation of spin instabilities in a fermionic quantum gas. . . . .	111
6.10	Spin instabilities for two different densities. . . . .	112
6.11	Stability diagram of the magnetically excited spin mixture $m = \{\pm 3/2\}$ . . . . .	113
6.12	Numerical simulation of the stability diagram. . . . .	115
6.13	Spin-relaxation dynamics in different geometries. . . . .	118
6.14	Density dependence of spin-relaxation dynamics. . . . .	119
6.15	Dependence of spin-relaxation dynamics on the magnetic field. . . . .	120
6.16	Temperature increase due to spin-relaxation dynamics. . . . .	121
A.1	Band structure of a 1d optical lattice. . . . .	125

C.1	Preparation of single-particle coherences for different spin mixtures. . .	135
C.2	Single-mode calculations with inserted phenomenological damping. . .	137
C.3	Simulations of fermionic spin instabilities for different magnetic fields. .	138
C.4	Long-term spin dynamics calculation in a single-mode approximation. .	139



# List of Tables

2.1	Spin configurations in the lowest hyperfine manifold of $^{40}\text{K}$ . . . . .	13
2.2	Total scattering lengths for the lowest manifold of $^{40}\text{K}$ . . . . .	14
A.1	Fundamental constants in the International System of Units. . . . .	123
B.1	Typically used Feshbach resonances in $^{40}\text{K}$ . . . . .	128
B.2	New Feshbach resonances in $^{40}\text{K}$ . . . . .	129
B.3	Further magnetic field values in $^{40}\text{K}$ with enhanced losses. . . . .	130
C.1	Interaction matrices of spin systems in the lowest hyperfine manifold of $^{40}\text{K}$ . . . . .	132



# Bibliography

- [1] J. S. Krauser, U. Ebling, N. Fläschner, J. Heinze, K. Sengstock, M. Lewenstein, A. Eckardt and C. Becker: “[Giant Spin Oscillations in an Ultracold Fermi Sea](#)”, *Science* **343** (6167), 157–160 (2014).
- [2] U. Ebling, J. S. Krauser, N. Fläschner, K. Sengstock, C. Becker, M. Lewenstein and A. Eckardt: “Relaxation dynamics of a closed high-spin Fermi system far from equilibrium”, arXiv:1312.6704 (2013).
- [3] J. Heinze, J. S. Krauser, N. Fläschner, K. Sengstock, C. Becker, U. Ebling, A. Eckardt and M. Lewenstein: “[Engineering Spin Waves in a High-Spin Ultracold Fermi Gas](#)”, *Phys. Rev. Lett.* **110**, 250402 (2013).
- [4] J. Heinze, J. S. Krauser, N. Fläschner, B. Hundt, S. Götze, A. P. Itin, L. Mathey, K. Sengstock and C. Becker: “[Intrinsic Photoconductivity of Ultracold Fermions in Optical Lattices](#)”, *Phys. Rev. Lett.* **110**, 085302 (2013).
- [5] J. S. Krauser, J. Heinze, N. Fläschner, S. Götze, O. Jürgensen, D.-S. Lühmann, C. Becker and K. Sengstock: “[Coherent multi-flavour spin dynamics in a fermionic quantum gas](#)”, *Nat. Phys.* **8**, 813–818 (2012).
- [6] J. Heinze, S. Götze, J. S. Krauser, B. Hundt, N. Fläschner, D.-S. Lühmann, C. Becker and K. Sengstock: “[Multiband Spectroscopy of Ultracold Fermions: Observation of Reduced Tunneling in Attractive Bose-Fermi Mixtures](#)”, *Phys. Rev. Lett.* **107**, 135303 (2011).
- [7] U. Bissbort, S. Götze, Y. Li, J. Heinze, J. S. Krauser, M. Weinberg, C. Becker, K. Sengstock and W. Hofstetter: “[Detecting the Amplitude Mode of Strongly Interacting Lattice Bosons by Bragg Scattering](#)”, *Phys. Rev. Lett.* **106**, 205303 (2011).
- [8] W. Gerlach and O. Stern: “Das magnetische Moment des Silberatoms”, *Zeitschrift für Physik* **9**, 349–352 (1922).
- [9] W. Pauli: “Zur Quantenmechanik des magnetischen Elektrons”, *Zeitschrift für Physik* **43**, 601–623 (1927).
- [10] P. A. M. Dirac: “[The Quantum Theory of the Electron](#)”, *Proceedings of the Royal Society of London. Series A* **117** (778), 610–624 (1928).
- [11] M. H. Anderson, J. R. Ensher, M. R. Matthews, C. E. Wieman and E. A. Cornell: “[Observation of Bose-Einstein Condensation in a Dilute Atomic Vapor](#)”, *Science* **269** (5221), 198–201 (1995).

- [12] C. C. Bradley, C. A. Sackett, J. J. Tollett and R. G. Hulet: “Evidence of Bose-Einstein Condensation in an Atomic Gas with Attractive Interactions”, Phys. Rev. Lett. **75**, 1687–1690 (1995).
- [13] K. B. Davis, M. O. Mewes, M. R. Andrews, N. J. van Druten, D. S. Durfee, D. M. Kurn and W. Ketterle: “Bose-Einstein Condensation in a Gas of Sodium Atoms”, Phys. Rev. Lett. **75**, 3969–3973 (1995).
- [14] B. DeMarco and D. S. Jin: “Onset of Fermi Degeneracy in a Trapped Atomic Gas”, Science **285** (5434), 1703–1706 (1999).
- [15] A. G. Truscott, K. E. Strecker, W. I. McAlexander, G. B. Partridge and R. G. Hulet: “Observation of Fermi Pressure in a Gas of Trapped Atoms”, Science **291** (5513), 2570–2572 (2001).
- [16] F. Schreck, L. Khaykovich, K. L. Corwin, G. Ferrari, T. Bourdel, J. Cubizolles and C. Salomon: “Quasipure Bose-Einstein Condensate Immersed in a Fermi Sea”, Phys. Rev. Lett. **87**, 080403 (2001).
- [17] D. G. Fried, T. C. Killian, L. Willmann, D. Landhuis, S. C. Moss, D. Kleppner and T. J. Greytak: “Bose-Einstein Condensation of Atomic Hydrogen”, Phys. Rev. Lett. **81**, 3811–3814 (1998).
- [18] A. Robert, O. Sirjean, A. Browaeys, J. Poupard, S. Nowak, D. Boiron, C. I. Westbrook and A. Aspect: “A Bose-Einstein Condensate of Metastable Atoms”, Science **292** (5516), 461–464 (2001).
- [19] G. Modugno, G. Ferrari, G. Roati, R. J. Brecha, A. Simoni and M. Inguscio: “Bose-Einstein Condensation of Potassium Atoms by Sympathetic Cooling”, Science **294** (5545), 1320–1322 (2001).
- [20] T. Weber, J. Herbig, M. Mark, H.-C. Nägerl and R. Grimm: “Bose-Einstein Condensation of Cesium”, Science **299** (5604), 232–235 (2003).
- [21] Y. Takasu, K. Maki, K. Komori, T. Takano, K. Honda, M. Kumakura, T. Yabuzaki and Y. Takahashi: “Spin-Singlet Bose-Einstein Condensation of Two-Electron Atoms”, Phys. Rev. Lett. **91**, 040404 (2003).
- [22] A. Griesmaier, J. Werner, S. Hensler, J. Stuhler and T. Pfau: “Bose-Einstein Condensation of Chromium”, Phys. Rev. Lett. **94**, 160401 (2005).
- [23] S. Kraft, F. Vogt, O. Appel, F. Riehle and U. Sterr: “Bose-Einstein Condensation of Alkaline Earth Atoms:  $^{40}\text{Ca}$ ”, Phys. Rev. Lett. **103**, 130401 (2009).
- [24] M. Lu, N. Q. Burdick, S. H. Youn and B. L. Lev: “Strongly Dipolar Bose-Einstein Condensate of Dysprosium”, Phys. Rev. Lett. **107**, 190401 (2011).
- [25] K. Aikawa, A. Frisch, M. Mark, S. Baier, A. Rietzler, R. Grimm and F. Ferlaino: “Bose-Einstein Condensation of Erbium”, Phys. Rev. Lett. **108**, 210401 (2012).
- [26] J. M. McNamara, T. Jeltsov, A. S. Tychkov, W. Hogervorst and W. Vassen: “Degenerate Bose-Fermi Mixture of Metastable Atoms”, Phys. Rev. Lett. **97**, 080404 (2006).

- [27] T. Fukuhara, Y. Takasu, M. Kumakura and Y. Takahashi: “Degenerate Fermi Gases of Ytterbium”, *Phys. Rev. Lett.* **98**, 030401 (2007).
- [28] B. J. DeSalvo, M. Yan, P. G. Mickelson, Y. N. Martinez de Escobar and T. C. Killian: “Degenerate Fermi Gas of  $^{87}\text{Sr}$ ”, *Phys. Rev. Lett.* **105**, 030402 (2010).
- [29] M. Lu, N. Q. Burdick and B. L. Lev: “Quantum Degenerate Dipolar Fermi Gas”, *Phys. Rev. Lett.* **108**, 215301 (2012).
- [30] K. Aikawa, A. Frisch, M. Mark, S. Baier, R. Grimm and F. Ferlaino: “Reaching Fermi Degeneracy via Universal Dipolar Scattering”, *Phys. Rev. Lett.* **112**, 010404 (2014).
- [31] I. Bloch, J. Dalibard and W. Zwerger: “Many-body physics with ultracold gases”, *Rev. Mod. Phys.* **80**, 885–964 (2008).
- [32] M. Lewenstein, A. Sanpera, V. Ahufinger, B. Damski, A. Sen(De) and U. Sen: “Ultracold atomic gases in optical lattices: mimicking condensed matter physics and beyond”, *Advances in Physics* **56** (2), 243–379 (2007).
- [33] D. Jaksch, C. Bruder, J. I. Cirac, C. W. Gardiner and P. Zoller: “Cold Bosonic Atoms in Optical Lattices”, *Phys. Rev. Lett.* **81**, 3108–3111 (1998).
- [34] M. Greiner, O. Mandel, T. Esslinger, T. W. Hänsch and I. Bloch: “Quantum phase transition from a superfluid to a Mott insulator in a gas of ultracold atoms”, *Nature* **415**, 39–44 (2002).
- [35] S. Ospelkaus, C. Ospelkaus, O. Wille, M. Succo, P. Ernst, K. Sengstock and K. Bongs: “Localization of Bosonic Atoms by Fermionic Impurities in a Three-Dimensional Optical Lattice”, *Phys. Rev. Lett.* **96**, 180403 (2006).
- [36] K. Günter, T. Stöferle, H. Moritz, M. Köhl and T. Esslinger: “Bose-Fermi Mixtures in a Three-Dimensional Optical Lattice”, *Phys. Rev. Lett.* **96**, 180402 (2006).
- [37] C. Becker, P. Soltan-Panahi, J. Kronjäger, S. Dörscher, K. Bongs and K. Sengstock: “Ultracold quantum gases in triangular optical lattices”, *New J. Phys.* **12** (6), 065025 (2010).
- [38] R. Jördens, N. Strohmaier, K. Günter, H. Moritz and T. Esslinger: “A Mott insulator of fermionic atoms in an optical lattice”, *Nature* **455**, 204–207 (2008).
- [39] U. Schneider, L. Hackermüller, S. Will, T. Best, I. Bloch, T. A. Costi, R. W. Helmes, D. Rasch and A. Rosch: “Metallic and Insulating Phases of Repulsively Interacting Fermions in a 3D Optical Lattice”, *Science* **322** (5907), 1520–1525 (2008).
- [40] S. Sugawa, K. Inaba, S. Taie, R. Yamazaki, M. Yamashita and Y. Takahashi: “Interaction and filling-induced quantum phases of dual Mott insulators of bosons and fermions”, *Nat. Phys.* **7**, 642–648 (2011).

- [41] P. Soltan-Panahi, J. Struck, P. Hauke, A. Bick, W. Plenkers, G. Meineke, C. Becker, P. Windpassinger, M. Lewenstein and K. Sengstock: “Multi-component quantum gases in spin-dependent hexagonal lattices”, *Nat. Phys.* **7**, 434–440 (2011).
- [42] T. Kinoshita, T. Wenger and D. S. Weiss: “Observation of a One-Dimensional Tonks-Girardeau Gas”, *Science* **305** (5687), 1125–1128 (2004).
- [43] N. Syassen, D. M. Bauer, M. Lettner, T. Volz, D. Dietze, J. J. García-Ripoll, J. I. Cirac, G. Rempe and S. Dürr: “Strong Dissipation Inhibits Losses and Induces Correlations in Cold Molecular Gases”, *Science* **320** (5881), 1329–1331 (2008).
- [44] K. Baumann, C. Guerlin, F. Brennecke and T. Esslinger: “Dicke quantum phase transition with a superfluid gas in an optical cavity”, *Nature* **464**, 1301–1306 (2010).
- [45] J. Simon, W. S. Bakr, R. Ma, M. E. Tai, P. M. Preiss and M. Greiner: “Quantum simulation of antiferromagnetic spin chains in an optical lattice”, *Nature* **472** (7343), 307–312 (2011).
- [46] J. Struck, C. Ölschläger, R. Le Targat, P. Soltan-Panahi, A. Eckardt, M. Lewenstein, P. Windpassinger and K. Sengstock: “Quantum Simulation of Frustrated Classical Magnetism in Triangular Optical Lattices”, *Science* **333** (6045), 996–999 (2011).
- [47] D. Greif, T. Uehlinger, G. Jotzu, L. Tarruell and T. Esslinger: “Short-Range Quantum Magnetism of Ultracold Fermions in an Optical Lattice”, *Science* **340** (6138), 1307–1310 (2013).
- [48] C. A. Regal, M. Greiner and D. S. Jin: “Observation of Resonance Condensation of Fermionic Atom Pairs”, *Phys. Rev. Lett.* **92**, 040403 (2004).
- [49] C. Chin, M. Bartenstein, A. Altmeyer, S. Riedl, S. Jochim, J. H. Denschlag and R. Grimm: “Observation of the Pairing Gap in a Strongly Interacting Fermi Gas”, *Science* **305** (5687), 1128–1130 (2004).
- [50] G. B. Partridge, K. E. Strecker, R. I. Kamar, M. W. Jack and R. G. Hulet: “Molecular Probe of Pairing in the BEC-BCS Crossover”, *Phys. Rev. Lett.* **95**, 020404 (2005).
- [51] M. W. Zwierlein, J. R. Abo-Shaeer, A. Schirotzek, C. H. Schunck and W. Ketterle: “Vortices and superfluidity in a strongly interacting Fermi gas”, *Nature* **435**, 1047–1051 (2005).
- [52] G.-B. Jo, Y.-R. Lee, J.-H. Choi, C. A. Christensen, T. H. Kim, J. H. Thywissen, D. E. Pritchard and W. Ketterle: “Itinerant Ferromagnetism in a Fermi Gas of Ultracold Atoms”, *Science* **325** (5947), 1521–1524 (2009).
- [53] S. Zhang and T.-L. Ho: “Atom loss maximum in ultra-cold Fermi gases”, *New J. Phys.* **13** (5), 055003 (2011).

- [54] D. Pekker, M. Babadi, R. Sensarma, N. Zinner, L. Pollet, M. W. Zwierlein and E. Demler: “[Competition between Pairing and Ferromagnetic Instabilities in Ultracold Fermi Gases near Feshbach Resonances](#)”, Phys. Rev. Lett. **106**, 050402 (2011).
- [55] G. J. Conduit and E. Altman: “[Effect of three-body loss on itinerant ferromagnetism in an atomic Fermi gas](#)”, Phys. Rev. A **83**, 043618 (2011).
- [56] N. Navon, S. Nascimbene, F. Chevy and C. Salomon: “[The Equation of State of a Low-Temperature Fermi Gas with Tunable Interactions](#)”, Science **328** (5979), 729–732 (2010).
- [57] A. Sommer, M. Ku, G. Roati and M. W. Zwierlein: “[Universal spin transport in a strongly interacting Fermi gas](#)”, Nature **472**, 201–204 (2011).
- [58] X. Du, L. Luo, B. Clancy and J. E. Thomas: “[Observation of Anomalous Spin Segregation in a Trapped Fermi Gas](#)”, Phys. Rev. Lett. **101**, 150401 (2008).
- [59] M. Feld, B. Frohlich, E. Vogt, M. Koschorreck and M. Kohl: “[Observation of a pairing pseudogap in a two-dimensional Fermi gas](#)”, Nature **480** (7375), 75–78 (2011).
- [60] T. Yefsah, A. T. Sommer, M. J. H. Ku, L. W. Cheuk, W. Ji, W. S. Bakr and M. W. Zwierlein: “[Heavy solitons in a fermionic superfluid](#)”, Nature **499** (7459), 426–430 (2013).
- [61] M. Koschorreck, D. Pertot, E. Vogt and M. Kohl: “[Universal spin dynamics in two-dimensional Fermi gases](#)”, Nat. Phys. **9** (7), 405–409 (2013).
- [62] L. A. Sidorenkov, M. K. Tey, R. Grimm, Y.-H. Hou, L. Pitaevskii and S. Stringari: “[Second sound and the superfluid fraction in a Fermi gas with resonant interactions](#)”, Nature **498** (7452), 78–81 (2013).
- [63] T.-L. Ho: “[Spinor Bose Condensates in Optical Traps](#)”, Phys. Rev. Lett. **81**, 742–745 (1998).
- [64] C. K. Law, H. Pu and N. P. Bigelow: “[Quantum Spins Mixing in Spinor Bose-Einstein Condensates](#)”, Phys. Rev. Lett. **81**, 5257–5261 (1998).
- [65] T. Ohmi and K. Machida: “[Bose-Einstein Condensation with Internal Degrees of Freedom in Alkali Atom Gases](#)”, J. Phys. Soc. Jpn. **67**, 1822–1825 (1998).
- [66] D. M. Stamper-Kurn, M. R. Andrews, A. P. Chikkatur, S. Inouye, H.-J. Miesner, J. Stenger and W. Ketterle: “[Optical Confinement of a Bose-Einstein Condensate](#)”, Phys. Rev. Lett. **80**, 2027–2030 (1998).
- [67] Y. Kawaguchi and M. Ueda: “[Spinor Bose-Einstein condensates](#)”, Physics Reports **520** (5), 253 – 381 (2012).
- [68] D. M. Stamper-Kurn and M. Ueda: “[Spinor Bose gases: Symmetries, magnetism, and quantum dynamics](#)”, Rev. Mod. Phys. **85**, 1191–1244 (2013).

- [69] J. Stenger, S. Inouye, D. M. Stamper-Kurn, H.-J. Miesner, A. P. Chikkatur and W. Ketterle: “[Spin domains in ground-state Bose-Einstein condensates](#)”, *Nature* **396**, 345–348 (1998).
- [70] L. E. Sadler, J. M. Higbie, S. R. Leslie, M. Vengalattore and D. M. Stamper-Kurn: “[Spontaneous symmetry breaking in a quenched ferromagnetic spinor Bose-Einstein condensate](#)”, *Nature* **443**, 312–315 (2006).
- [71] J. Kronjäger, C. Becker, P. Soltan-Panahi, K. Bongs and K. Sengstock: “[Spontaneous Pattern Formation in an Antiferromagnetic Quantum Gas](#)”, *Phys. Rev. Lett.* **105**, 090402 (2010).
- [72] B. Lücke, M. Scherer, J. Kruse, L. Pezzé, F. Deuretzbacher, P. Hyllus, O. Topic, J. Peise, W. Ertmer, J. Arlt, L. Santos, A. Smerzi and C. Klempt: “[Twin Matter Waves for Interferometry Beyond the Classical Limit](#)”, *Science* **334** (6057), 773–776 (2011).
- [73] C. Gross, E. Strobel, H. Nicklas, T. Zibold, N. Bar-Gill, G. Kurizki and M. K. Oberthaler: “[Atomic homodyne detection of continuous-variable entangled twin-atom states](#)”, *Nature* **480**, 219–223 (2011).
- [74] A. Widera, F. Gerbier, S. Fölling, T. Gericke, O. Mandel and I. Bloch: “[Coherent Collisional Spin Dynamics in Optical Lattices](#)”, *Phys. Rev. Lett.* **95**, 190405 (2005).
- [75] A. Widera, F. Gerbier, S. Fölling, T. Gericke, O. Mandel and I. Bloch: “[Precision measurement of spin-dependent interaction strengths for spin-1 and spin-2 <sup>87</sup>Rb atoms](#)”, *New J. Phys.* **8** (8), 152 (2006).
- [76] H. Schmaljohann, M. Erhard, J. Kronjäger, M. Kottke, S. van Staa, L. Cacciapuoti, J. J. Arlt, K. Bongs and K. Sengstock: “[Dynamics of  \$F = 2\$  Spinor Bose-Einstein Condensates](#)”, *Phys. Rev. Lett.* **92**, 040402 (2004).
- [77] M.-S. Chang, Q. Qin, W. Zhang, L. You and M. S. Chapman: “[Coherent spinor dynamics in a spin-1 Bose condensate](#)”, *Nat. Phys.* **1**, 111–116 (2005).
- [78] J. Kronjäger, C. Becker, M. Brinkmann, R. Walser, P. Navez, K. Bongs and K. Sengstock: “[Evolution of a spinor condensate: Coherent dynamics, dephasing, and revivals](#)”, *Phys. Rev. A* **72**, 063619 (2005).
- [79] J. Kronjäger, C. Becker, P. Navez, K. Bongs and K. Sengstock: “[Magnetically Tuned Spin Dynamics Resonance](#)”, *Phys. Rev. Lett.* **97**, 110404 (2006).
- [80] A. T. Black, E. Gomez, L. D. Turner, S. Jung and P. D. Lett: “[Spinor Dynamics in an Antiferromagnetic Spin-1 Condensate](#)”, *Phys. Rev. Lett.* **99**, 070403 (2007).
- [81] C. Klempt, O. Topic, G. Gebreyesus, M. Scherer, T. Henninger, P. Hyllus, W. Ertmer, L. Santos and J. J. Arlt: “[Parametric Amplification of Vacuum Fluctuations in a Spinor Condensate](#)”, *Phys. Rev. Lett.* **104**, 195303 (2010).
- [82] C. Gerving, T. Hoang, B. Land, M. Anquez, C. Hamley and M. Chapman: “[Non-equilibrium dynamics of an unstable quantum pendulum explored in a spin-1 Bose-Einstein condensate](#)”, *Nat Commun* **3**, 1169– (2012).

- [83] A. de Paz, A. Chotia, E. Maréchal, P. Pedri, L. Vernac, O. Gorceix and B. Laburthe-Tolra: “Resonant demagnetization of a dipolar Bose-Einstein condensate in a three-dimensional optical lattice”, *Phys. Rev. A* **87**, 051609 (2013).
- [84] A. de Paz, A. Sharma, A. Chotia, E. Maréchal, J. H. Huckans, P. Pedri, L. Santos, O. Gorceix, L. Vernac and B. Laburthe-Tolra: “Nonequilibrium Quantum Magnetism in a Dipolar Lattice Gas”, *Phys. Rev. Lett.* **111**, 185305 (2013).
- [85] X.-W. Guan, M. T. Batchelor and C. Lee: “Fermi gases in one dimension: From Bethe ansatz to experiments”, *Rev. Mod. Phys.* **85**, 1633–1691 (2013).
- [86] T. B. Ottenstein, T. Lompe, M. Kohnen, A. N. Wenz and S. Jochim: “Collisional Stability of a Three-Component Degenerate Fermi Gas”, *Phys. Rev. Lett.* **101**, 203202 (2008).
- [87] T. Lompe, T. B. Ottenstein, F. Serwane, A. N. Wenz, G. Zürn and S. Jochim: “Radio-Frequency Association of Efimov Trimers”, *Science* **330** (6006), 940–944 (2010).
- [88] T.-L. Ho and S. Yip: “Pairing of Fermions with Arbitrary Spin”, *Phys. Rev. Lett.* **82**, 247–250 (1999).
- [89] L. He, M. Jin and P. Zhuang: “Superfluidity in a three-flavor Fermi gas with SU(3) symmetry”, *Phys. Rev. A* **74**, 033604 (2006).
- [90] A. Rapp, G. Zaránd, C. Honerkamp and W. Hofstetter: “Color Superfluidity and “Baryon” Formation in Ultracold Fermions”, *Phys. Rev. Lett.* **98**, 160405 (2007).
- [91] R. W. Cherng, G. Refael and E. Demler: “Superfluidity and Magnetism in Multicomponent Ultracold Fermions”, *Phys. Rev. Lett.* **99**, 130406 (2007).
- [92] P. Azaria, S. Capponi and P. Lecheminant: “Three-component Fermi gas in a one-dimensional optical lattice”, *Phys. Rev. A* **80**, 041604 (2009).
- [93] J.-P. Martikainen, J. J. Kinnunen, P. Törmä and C. J. Pethick: “Induced Interactions and the Superfluid Transition Temperature in a Three-Component Fermi Gas”, *Phys. Rev. Lett.* **103**, 260403 (2009).
- [94] T. Ozawa and G. Baym: “Population imbalance and pairing in the BCS-BEC crossover of three-component ultracold fermions”, *Phys. Rev. A* **82**, 063615 (2010).
- [95] K. Inaba and S.-I. Suga: “Superfluid State of Repulsively Interacting Three-Component Fermionic Atoms in Optical Lattices”, *Phys. Rev. Lett.* **108**, 255301 (2012).
- [96] K. Inaba and S.-I. Suga: “Superfluid, Staggered State, And Mott Insulator Of Repulsively Interacting Three-component Fermionic Atoms In Optical Lattices”, *Mod. Phys. Lett. B* **27** (12), 1330008 (2013).
- [97] W. Hofstetter: “Ultracold atoms in optical lattices: tunable quantum many-body systems”, *Philosophical Magazine* **86** (13-14), 1891–1906 (2006).

- [98] C. Honerkamp and W. Hofstetter: “**Ultracold Fermions and the  $SU(N)$  Hubbard Model**”, *Phys. Rev. Lett.* **92**, 170403 (2004).
- [99] M. Hermele, V. Gurarie and A. M. Rey: “**Mott Insulators of Ultracold Fermionic Alkaline Earth Atoms: Underconstrained Magnetism and Chiral Spin Liquid**”, *Phys. Rev. Lett.* **103**, 135301 (2009).
- [100] M. A. Cazalilla, A. F. Ho and M. Ueda: “**Ultracold gases of ytterbium: ferromagnetism and Mott states in an  $SU(6)$  Fermi system**”, *New J. Phys.* **11** (10), 103033 (2009).
- [101] A. V. Gorshkov, M. Hermele, V. Gurarie, C. Xu, P. S. Julienne, J. Ye, P. Zoller, E. Demler, M. D. Lukin and A. M. Rey: “**Two-orbital  $SU(N)$  magnetism with ultracold alkaline-earth atoms**”, *Nat. Phys.* **6**, 289–295 (2010).
- [102] S. Taie, Y. Takasu, S. Sugawa, R. Yamazaki, T. Tsujimoto, R. Murakami and Y. Takahashi: “**Realization of a  $SU(2) \times SU(6)$  System of Fermions in a Cold Atomic Gas**”, *Phys. Rev. Lett.* **105**, 190401 (2010).
- [103] S. Taie, R. Yamazaki, S. Sugawa and Y. Takahashi: “**An  $SU(6)$  Mott insulator of an atomic Fermi gas realized by large-spin Pomeranchuk cooling**”, *Nat. Phys.* **8** (11), 825–830 (2012).
- [104] N. Bornemann, P. Hyllus and L. Santos: “**Resonant Spin-Changing Collisions in Spinor Fermi Gases**”, *Phys. Rev. Lett.* **100**, 205302 (2008).
- [105] Y. Dong and H. Pu: “**Spin mixing in spinor Fermi gases**”, *Phys. Rev. A* **87**, 043610 (2013).
- [106] S. Götze: Ph.D. thesis, Universität Hamburg, to be published.
- [107] J. Heinze: “From Higher Bands to Higher Spins: Ultracold Fermions in Novel Regimes”, Ph.D. thesis, Universität Hamburg (2013).
- [108] N. Fläschner: “Higher Lattice Orbital Dynamics and Feshbach Resonances in Ultracold  $^{40}\text{K}$ ”, Master’s thesis, Universität Hamburg (2011).
- [109] M. Langbecker: “Tunable Interactions and Lattice Geometries in Fermionic Quantum Gases”, Master’s thesis, Universität Hamburg (2013).
- [110] T. Lahaye, C. Menotti, L. Santos, M. Lewenstein and T. Pfau: “**The physics of dipolar bosonic quantum gases**”, *Reports on Progress in Physics* **72** (12), 126401–(2009).
- [111] P. Zeeman: “Ueber einen Einfluss der Magnetisirung auf die Natur des von einer Substanz emittirten Lichtes”, in “Verhandlungen der Physikalischen Gesellschaft zu Berlin”, page 127 (1882).
- [112] G. Breit and I. I. Rabi: “**Measurement of Nuclear Spin**”, *Phys. Rev.* **38**, 2082–2083 (1931).
- [113] M. Vengalattore, S. R. Leslie, J. Guzman and D. M. Stamper-Kurn: “**Spontaneously Modulated Spin Textures in a Dipolar Spinor Bose-Einstein Condensate**”, *Phys. Rev. Lett.* **100**, 170403 (2008).

- [114] F. Deuretzbacher, G. Gebreyesus, O. Topic, M. Scherer, B. Lücke, W. Ertmer, J. Arlt, C. Klempt and L. Santos: “**Parametric amplification of matter waves in dipolar spinor Bose-Einstein condensates**”, Phys. Rev. A **82**, 053608 (2010).
- [115] K. Huang and C. N. Yang: “**Quantum-Mechanical Many-Body Problem with Hard-Sphere Interaction**”, Phys. Rev. **105**, 767–775 (1957).
- [116] M. M. Boyd, T. Zelevinsky, A. D. Ludlow, S. Blatt, T. Zanon-Willette, S. M. Foreman and J. Ye: “**Nuclear spin effects in optical lattice clocks**”, Phys. Rev. A **76**, 022510 (2007).
- [117] T. Hanna: Private communication.
- [118] S. Falke, H. Knöckel, J. Friebe, M. Riedmann, E. Tiemann and C. Lisdat: “**Potassium ground-state scattering parameters and Born-Oppenheimer potentials from molecular spectroscopy**”, Phys. Rev. A **78**, 012503 (2008).
- [119] C. Chin, R. Grimm, P. Julienne and E. Tiesinga: “**Feshbach resonances in ultracold gases**”, Rev. Mod. Phys. **82**, 1225–1286 (2010).
- [120] F. Werner, O. Parcollet, A. Georges and S. R. Hassan: “**Interaction-Induced Adiabatic Cooling and Antiferromagnetism of Cold Fermions in Optical Lattices**”, Phys. Rev. Lett. **95**, 056401 (2005).
- [121] B. Pasquiou, G. Bismut, Q. Beaufils, A. Crubellier, E. Maréchal, P. Pedri, L. Vernac, O. Gorceix and B. Laburthe-Tolra: “**Control of dipolar relaxation in external fields**”, Phys. Rev. A **81**, 042716 (2010).
- [122] L. I. Schiff and H. Snyder: “**Theory of the Quadratic Zeeman Effect**”, Phys. Rev. **55**, 59–63 (1939).
- [123] S. Stellmer, R. Grimm and F. Schreck: “**Detection and manipulation of nuclear spin states in fermionic strontium**”, Phys. Rev. A **84**, 043611 (2011).
- [124] S. Ospelkaus-Schwarzer: “Quantum Degenerate Fermi-Bose Mixtures of  $^{40}\text{K}$  and  $^{87}\text{Rb}$  in 3D Optical Lattices”, Ph.D. thesis, Universität Hamburg (2004).
- [125] C. Ospelkaus: “Fermi-Bose mixtures - From mean-field interactions to ultracold chemistry”, Ph.D. thesis, Universität Hamburg (2006).
- [126] N. Masuhara, J. M. Doyle, J. C. Sandberg, D. Kleppner, T. J. Greytak, H. F. Hess and G. P. Kochanski: “**Evaporative Cooling of Spin-Polarized Atomic Hydrogen**”, Phys. Rev. Lett. **61**, 935–938 (1988).
- [127] B. DeMarco, J. L. Bohn, J. P. Burke, M. Holland and D. S. Jin: “**Measurement of  $p$ -Wave Threshold Law Using Evaporatively Cooled Fermionic Atoms**”, Phys. Rev. Lett. **82**, 4208–4211 (1999).
- [128] C. J. Myatt, E. A. Burt, R. W. Ghrist, E. A. Cornell and C. E. Wieman: “**Production of Two Overlapping Bose-Einstein Condensates by Sympathetic Cooling**”, Phys. Rev. Lett. **78**, 586–589 (1997).

- [129] F. Schreck, G. Ferrari, K. L. Corwin, J. Cubizolles, L. Khaykovich, M.-O. Mewes and C. Salomon: “[Sympathetic cooling of bosonic and fermionic lithium gases towards quantum degeneracy](#)”, *Phys. Rev. A* **64**, 011402 (2001).
- [130] G. Roati, F. Riboli, G. Modugno and M. Inguscio: “[Fermi-Bose Quantum Degenerate  \$^{40}\text{K}\$ - \$^{87}\text{Rb}\$  Mixture with Attractive Interaction](#)”, *Phys. Rev. Lett.* **89**, 150403 (2002).
- [131] B. DeMarco, S. B. Papp and D. S. Jin: “[Pauli Blocking of Collisions in a Quantum Degenerate Atomic Fermi Gas](#)”, *Phys. Rev. Lett.* **86**, 5409–5412 (2001).
- [132] R. Grimm, M. Weidemüller and Y. B. Ovchinnikov: “[Optical Dipole Traps for Neutral Atoms](#)”, in B. Bederson and H. Walther (editors), “Advances In Atomic, Molecular, and Optical Physics”, volume 42 of *Advances In Atomic, Molecular, and Optical Physics*, pages 95–170, Academic Press (2000).
- [133] W. Ketterle, D. Durfee and D. Stamper-Kurn: “Making, probing and understanding Bose-Einstein condensates”, in M. Inguscio, S. Stringari and C. Wieman (editors), “Bose-Einstein condensation in atomic gases, Proceedings of the International School of Physics ”Enrico Fermi”, Course CXL”, IOS Press, Amsterdam (1999).
- [134] M. Weinberg: “Observation of the Amplitude Mode in Strongly Correlated Bose-Einstein Condensates”, Master’s thesis, Universität Hamburg (2010).
- [135] B. Hundt: “Momentum-Resolved Optical Lattice Modulation Spectroscopy on Bose-Fermi Mixtures”, Master’s thesis, Universität Hamburg (2011).
- [136] W. Ketterle, K. B. Davis, M. A. Joffe, A. Martin and D. E. Pritchard: “[High densities of cold atoms in a \*dark\* spontaneous-force optical trap](#)”, *Phys. Rev. Lett.* **70**, 2253–2256 (1993).
- [137] M. Erhard: “”Experimente mit mehrkomponentigen Bose-Einstein-Kondensaten””, Ph.D. thesis, Universität Hamburg (2004).
- [138] J. Kronjäger: “Coherent Dynamics of Spinor Bose-Einstein Condensates”, Ph.D. thesis, Universität Hamburg (2007).
- [139] C. Zener: “[Non-Adiabatic Crossing of Energy Levels](#)”, *Proceedings of the Royal Society of London. Series A* **137** (833), 696–702 (1932).
- [140] C. A. Regal, C. Ticknor, J. L. Bohn and D. S. Jin: “[Tuning p-Wave Interactions in an Ultracold Fermi Gas of Atoms](#)”, *Phys. Rev. Lett.* **90**, 053201 (2003).
- [141] C. A. Regal and D. S. Jin: “[Measurement of Positive and Negative Scattering Lengths in a Fermi Gas of Atoms](#)”, *Phys. Rev. Lett.* **90**, 230404 (2003).
- [142] C. Ticknor, C. A. Regal, D. S. Jin and J. L. Bohn: “[Multiplet structure of Feshbach resonances in nonzero partial waves](#)”, *Phys. Rev. A* **69**, 042712 (2004).
- [143] M. J. Holland, B. DeMarco and D. S. Jin: “[Evaporative cooling of a two-component degenerate Fermi gas](#)”, *Phys. Rev. A* **61**, 053610 (2000).

- [144] D. Guéry-Odelin, J. Söding, P. Desbiolles and J. Dalibard: “**Is Bose-Einstein condensation of atomic cesium possible?**”, EPL (Europhysics Letters) **44** (1), 25 (1998).
- [145] G. Roati, M. Zaccanti, C. D’Errico, J. Catani, M. Modugno, A. Simoni, M. Inguscio and G. Modugno: “ **$^{39}\text{K}$  Bose-Einstein Condensate with Tunable Interactions**”, Phys. Rev. Lett. **99**, 010403 (2007).
- [146] A. Görlitz, T. L. Gustavson, A. E. Leanhardt, R. Löw, A. P. Chikkatur, S. Gupta, S. Inouye, D. E. Pritchard and W. Ketterle: “**Sodium Bose-Einstein Condensates in the F=2 State in a Large-Volume Optical Trap**”, Phys. Rev. Lett. **90**, 090401 (2003).
- [147] J. P. Burke, J. L. Bohn, B. D. Esry and C. H. Greene: “**Impact of the  $^{87}\text{Rb}$  singlet scattering length on suppressing inelastic collisions**”, Phys. Rev. A **55**, R2511–R2514 (1997).
- [148] B. DeMarco: “Quantum Behavior of an Atomic Fermi Gas”, Ph.D. thesis, University of Colorado (1996).
- [149] C. Becker: “Multi component Bose-Einstein condensates: From mean field physics to strong correlations”, Ph.D. thesis, Universität Hamburg (2008).
- [150] J. M. McGuirk, H. J. Lewandowski, D. M. Harber, T. Nikuni, J. E. Williams and E. A. Cornell: “**Spatial Resolution of Spin Waves in an Ultracold Gas**”, Phys. Rev. Lett. **89**, 090402 (2002).
- [151] T. Nikuni, J. E. Williams and C. W. Clark: “**Linear spin waves in a trapped Bose gas**”, Phys. Rev. A **66**, 043411 (2002).
- [152] J. N. Fuchs, D. M. Gangardt and F. Laloë: “**Large amplitude spin waves in ultracold gases**”, Eur. Phys. J. D **25**, 57–75 (2003).
- [153] K. D. Nelson, X. Li and D. S. Weiss: “**Imaging single atoms in a three-dimensional array**”, Nat Phys **3** (8), 556–560 (2007).
- [154] T. Gericke, P. Wurtz, D. Reitz, T. Langen and H. Ott: “**High-resolution scanning electron microscopy of an ultracold quantum gas**”, Nat Phys **4** (12), 949–953 (2008).
- [155] W. S. Bakr, J. I. Gillen, A. Peng, S. Fölling and M. Greiner: “**A quantum gas microscope for detecting single atoms in a Hubbard-regime optical lattice**”, Nature **462**, 74–77 (2009).
- [156] J. F. Sherson, C. Weitenberg, M. Endres, M. Cheneau, I. Bloch and S. Kuhr: “**Single-atom-resolved fluorescence imaging of an atomic Mott insulator**”, Nature **467**, 68–72 (2010).
- [157] P. Windpassinger and K. Sengstock: “**Engineering novel optical lattices**”, Reports on Progress in Physics **76** (8), 086401– (2013).
- [158] C. Wu, J.-p. Hu and S.-c. Zhang: “**Exact SO(5) Symmetry in the Spin-3/2 Fermionic System**”, Phys. Rev. Lett. **91**, 186402 (2003).

- [159] M. Colomé-Tatché, C. Klempt, L. Santos and T. Vekua: “[Adiabatic spin cooling using high-spin Fermi gases](#)”, *New J. Phys.* **13** (11), 113021 (2011).
- [160] Z. Cai, H.-H. Hung, L. Wang, D. Zheng and C. Wu: “[Pomeranchuk Cooling of  \$SU\(2N\)\$  Ultracold Fermions in Optical Lattices](#)”, *Phys. Rev. Lett.* **110**, 220401 (2013).
- [161] H.-H. Tu, G.-M. Zhang and L. Yu: “[Spin-quadrupole ordering of spin- \$\frac{3}{2}\$  ultracold fermionic atoms in optical lattices in the one-band Hubbard model](#)”, *Phys. Rev. B* **74**, 174404 (2006).
- [162] K. Rodríguez, A. Argüelles, M. Colomé-Tatché, T. Vekua and L. Santos: “[Mott-Insulator Phases of Spin-3/2 Fermions in the Presence of Quadratic Zeeman Coupling](#)”, *Phys. Rev. Lett.* **105**, 050402 (2010).
- [163] J. Jaramillo, S. Greschner and T. Vekua: “[Band-to-Mott-insulator transformations in four-component alkali-metal fermions at half-filling](#)”, *Phys. Rev. A* **88**, 043616 (2013).
- [164] A. Rapp and A. Rosch: “[Ground-state phase diagram of the repulsive  \$SU\(3\)\$  Hubbard model in the Gutzwiller approximation](#)”, *Phys. Rev. A* **83**, 053605 (2011).
- [165] P. Corboz, A. M. Läuchli, K. Penc, M. Troyer and F. Mila: “[Simultaneous Dimerization and  \$SU\(4\)\$  Symmetry Breaking of 4-Color Fermions on the Square Lattice](#)”, *Phys. Rev. Lett.* **107**, 215301 (2011).
- [166] Z. Cai, H.-H. Hung, L. Wang and C. Wu: “[Quantum magnetic properties of the  \$SU\(2N\)\$  Hubbard model in the square lattice: A quantum Monte Carlo study](#)”, *Phys. Rev. B* **88**, 125108 (2013).
- [167] D. Clément, N. Fabbri, L. Fallani, C. Fort and M. Inguscio: “[Multi-band spectroscopy of inhomogeneous Mott-insulator states of ultracold bosons](#)”, *New J. Phys.* **11** (10), 103030 (2009).
- [168] P. T. Ernst, S. Götze, J. S. Krauser, K. Pyka, D.-S. Lühmann, D. Pfannkuche and K. Sengstock: “[Probing superfluids in optical lattices by momentum-resolved Bragg spectroscopy](#)”, *Nat. Phys.* **6**, 56–61 (2010).
- [169] N. Fabbri, S. D. Huber, D. Clément, L. Fallani, C. Fort, M. Inguscio and E. Altman: “[Quasiparticle Dynamics in a Bose Insulator Probed by Interband Bragg Spectroscopy](#)”, *Phys. Rev. Lett.* **109**, 055301 (2012).
- [170] S. Friebel, C. D’Andrea, J. Walz, M. Weitz and T. W. Hänsch: “ [\$CO\_2\$ -laser optical lattice with cold rubidium atoms](#)”, *Phys. Rev. A* **57**, R20–R23 (1998).
- [171] G. Roati, W. Jastrzebski, A. Simoni, G. Modugno and M. Inguscio: “[Optical trapping of cold fermionic potassium for collisional studies](#)”, *Phys. Rev. A* **63**, 052709 (2001).
- [172] R. Jáuregui, N. Poli, G. Roati and G. Modugno: “[Anharmonic parametric excitation in optical lattices](#)”, *Phys. Rev. A* **64**, 033403 (2001).

- [173] M. Greiner, I. Bloch, O. Mandel, T. W. Hänsch and T. Esslinger: “Exploring Phase Coherence in a 2D Lattice of Bose-Einstein Condensates”, *Phys. Rev. Lett.* **87**, 160405 (2001).
- [174] N. Ashcroft and D. Mermin: *Solid state physics*, Thomson Learning, Toronto (1976).
- [175] J. Hubbard: “Electron Correlations in Narrow Energy Bands”, Proceedings of the Royal Society of London. Series A. Mathematical and Physical Sciences **276** (1365), 238–257 (1963).
- [176] D. Jaksch and P. Zoller: “The cold atom Hubbard toolbox”, *Annals of Physics* **315** (1), 52 – 79 (2005).
- [177] G. H. Wannier: “The Structure of Electronic Excitation Levels in Insulating Crystals”, *Phys. Rev.* **52**, 191–197 (1937).
- [178] R. B. Diener and T.-L. Ho: “Fermions in Optical Lattices Swept across Feshbach Resonances”, *Phys. Rev. Lett.* **96**, 010402 (2006).
- [179] D.-S. Lühmann, K. Bongs, K. Sengstock and D. Pfannkuche: “Self-Trapping of Bosons and Fermions in Optical Lattices”, *Phys. Rev. Lett.* **101**, 050402 (2008).
- [180] H. P. Büchler: “Microscopic Derivation of Hubbard Parameters for Cold Atomic Gases”, *Phys. Rev. Lett.* **104**, 090402 (2010).
- [181] A. Georges, G. Kotliar, W. Krauth and M. J. Rozenberg: “Dynamical mean-field theory of strongly correlated fermion systems and the limit of infinite dimensions”, *Rev. Mod. Phys.* **68**, 13–125 (1996).
- [182] A. Sotnikov: Private communication.
- [183] F. Gerbier, A. Widera, S. Fölling, O. Mandel and I. Bloch: “Resonant control of spin dynamics in ultracold quantum gases by microwave dressing”, *Phys. Rev. A* **73**, 041602 (2006).
- [184] U. Schollwöck: “The density-matrix renormalization group in the age of matrix product states”, *Annals of Physics* **326** (1), 96–192 (2011).
- [185] A. Auerbach: *Interacting Electrons and Quantum Magnetism*, Springer (1998).
- [186] O. Jürgensen: Private communication.
- [187] O. Jürgensen: Ph.D. thesis, Universität Hamburg, to be published.
- [188] O. Jürgensen, J. Heinze and D.-S. Lühmann: “Large-amplitude superexchange of high-spin fermions in optical lattices”, *New Journal of Physics* **15** (11), 113017– (2013).
- [189] N. Fabbri, D. Clément, L. Fallani, C. Fort, M. Modugno, K. M. R. van der Stam and M. Inguscio: “Excitations of Bose-Einstein condensates in a one-dimensional periodic potential”, *Phys. Rev. A* **79**, 043623 (2009).

- [190] T. Müller, S. Fölling, A. Widera and I. Bloch: “[State Preparation and Dynamics of Ultracold Atoms in Higher Lattice Orbitals](#)”, Phys. Rev. Lett. **99**, 200405 (2007).
- [191] L. Tarruell, D. Greif, T. Uehlinger, G. Jotzu and T. Esslinger: “[Creating, moving and merging Dirac points with a Fermi gas in a tunable honeycomb lattice](#)”, Nature **483**, 302–305 (2012).
- [192] J. F. Sherson, S. J. Park, P. L. Pedersen, N. Winter, M. Gajdacz, S. Mai and J. Arlt: “[The pump-probe coupling of matter wave packets to remote lattice states](#)”, New J. Phys. **14** (8), 083013 (2012).
- [193] G. Wirth, M. Ölschläger and A. Hemmerich: “[Evidence for orbital superfluidity in the P-band of a bipartite optical square lattice](#)”, Nat. Phys. **7**, 147–153 (2011).
- [194] C. Wu, D. Bergman, L. Balents and S. Das Sarma: “[Flat Bands and Wigner Crystallization in the Honeycomb Optical Lattice](#)”, Phys. Rev. Lett. **99**, 070401 (2007).
- [195] K. Sun, W. V. Liu, A. Hemmerich and S. Das Sarma: “[Topological semimetal in a fermionic optical lattice](#)”, Nat. Phys. **8** (1), 67–70 (2012).
- [196] A. Kantian, A. J. Daley, P. Törmä and P. Zoller: “[Atomic lattice excitons: from condensates to crystals](#)”, New J. Phys. **9** (11), 407 (2007).
- [197] X. Du, Y. Zhang, J. Petricka and J. E. Thomas: “[Controlling Spin Current in a Trapped Fermi Gas](#)”, Phys. Rev. Lett. **103**, 010401 (2009).
- [198] F. Piéchon, J. N. Fuchs and F. Laloë: “[Cumulative Identical Spin Rotation Effects in Collisionless Trapped Atomic Gases](#)”, Phys. Rev. Lett. **102**, 215301 (2009).
- [199] S. S. Natu and E. J. Mueller: “[Anomalous spin segregation in a weakly interacting two-component Fermi gas](#)”, Phys. Rev. A **79**, 051601 (2009).
- [200] U. Ebling, A. Eckardt and M. Lewenstein: “[Spin segregation via dynamically induced long-range interactions in a system of ultracold fermions](#)”, Phys. Rev. A **84**, 063607 (2011).
- [201] Y. Endo and T. Nikuni: “[Spin-Dynamics of a Trapped Spin-1 Bose Gas above the Bose-Einstein Transition Temperature](#)”, J. Low Temp. Phys. **152** (1-2), 21–46 (2008).
- [202] S. S. Natu and E. J. Mueller: “[Spin waves in a spin-1 normal Bose gas](#)”, Phys. Rev. A **81**, 053617 (2010).
- [203] U. Ebling: Private communication.
- [204] E. Wigner: “[On the Quantum Correction For Thermodynamic Equilibrium](#)”, Phys. Rev. **40**, 749–759 (1932).
- [205] S. Yi, O. E. Müstecaplıoğlu, C. P. Sun and L. You: “[Single-mode approximation in a spinor-1 atomic condensate](#)”, Phys. Rev. A **66**, 011601 (2002).

- [206] U. Ebling: Ph.D. thesis, ICFO, The Institute of Photonic Sciences.
- [207] H. K. Pechkis, J. P. Wrubel, A. Schwettmann, P. F. Griffin, R. Barnett, E. Tiesinga and P. D. Lett: “[Spinor Dynamics in an Antiferromagnetic Spin-1 Thermal Bose Gas](#)”, Phys. Rev. Lett. **111**, 025301 (2013).
- [208] P. Lecheminant, E. Boulat and P. Azaria: “[Confinement and Superfluidity in One-Dimensional Degenerate Fermionic Cold Atoms](#)”, Phys. Rev. Lett. **95**, 240402 (2005).
- [209] N. Tsuji, T. Oka, P. Werner and H. Aoki: “[Dynamical Band Flipping in Fermionic Lattice Systems: An ac-Field-Driven Change of the Interaction from Repulsive to Attractive](#)”, Phys. Rev. Lett. **106**, 236401 (2011).
- [210] S. Braun, J. P. Ronzheimer, M. Schreiber, S. S. Hodgman, T. Rom, I. Bloch and U. Schneider: “[Negative Absolute Temperature for Motional Degrees of Freedom](#)”, Science **339** (6115), 52–55 (2013).
- [211] R. Schmidt: Private communication.
- [212] M. Srednicki: “[Chaos and quantum thermalization](#)”, Phys. Rev. E **50**, 888–901 (1994).
- [213] M. Rigol, V. Dunjko and M. Olshanii: “[Thermalization and its mechanism for generic isolated quantum systems](#)”, Nature **452** (7189), 854–858 (2008).
- [214] J. Dziarmaga: “[Dynamics of a quantum phase transition and relaxation to a steady state](#)”, Advances in Physics **59** (6), 1063–1189 (2010).
- [215] A. Polkovnikov, K. Sengupta, A. Silva and M. Vengalattore: “[Colloquium: Nonequilibrium dynamics of closed interacting quantum systems](#)”, Rev. Mod. Phys. **83** (3), 863–883 (2011).
- [216] J. Berges, S. Borsányi and C. Wetterich: “[Prethermalization](#)”, Phys. Rev. Lett. **93**, 142002 (2004).
- [217] M. Gring, M. Kuhnert, T. Langen, T. Kitagawa, B. Rauer, M. Schreitl, I. Mazets, D. A. Smith, E. Demler and J. Schmiedmayer: “[Relaxation and Prethermalization in an Isolated Quantum System](#)”, Science **337** (6100), 1318–1322 (2012).
- [218] T. Langen, R. Geiger, M. Kuhnert, B. Rauer and J. Schmiedmayer: “[Local emergence of thermal correlations in an isolated quantum many-body system](#)”, Nat Phys **9** (10), 640–643 (2013).
- [219] T. Kinoshita, T. Wenger and D. S. Weiss: “[A quantum Newton’s cradle](#)”, Nature **440** (7086), 900–903 (2006).
- [220] S. Hofferberth, I. Lesanovsky, B. Fischer, T. Schumm and J. Schmiedmayer: “[Non-equilibrium coherence dynamics in one-dimensional Bose gases](#)”, Nature **449** (7160), 324–327 (2007).
- [221] M. Cheneau, P. Barmettler, D. Poletti, M. Endres, P. Schausz, T. Fukuhara, C. Gross, I. Bloch, C. Kollath and S. Kuhr: “[Light-cone-like spreading of correlations in a quantum many-body system](#)”, Nature **481** (7382), 484–487 (2012).

- [222] M. Erhard, H. Schmaljohann, J. Kronjäger, K. Bongs and K. Sengstock: “[Bose-Einstein condensation at constant temperature](#)”, Phys. Rev. A **70**, 031602 (2004).
- [223] C. Lhuillier and L. Laloë: “[Transport properties in a spin polarized gas, I](#)”, J. Phys. France **43**, 197 – 224 (1982).
- [224] C. Lhuillier and L. Laloë: “[Transport properties in a spin polarized gas, II](#)”, J. Phys. France **43** (2), 225–241 (1982).
- [225] L. Corruccini, D. Osheroff, D. Lee and R. Richardson: “[Spin-wave phenomena in liquid  \$^3\text{He}\$  systems](#)”, Journal of Low Temperature Physics **8** (3-4), 229–254– (1972).
- [226] B. R. Johnson, J. S. Denker, N. Bigelow, L. P. Lévy, J. H. Freed and D. M. Lee: “[Observation of Nuclear Spin Waves in Spin-Polarized Atomic Hydrogen Gas](#)”, Phys. Rev. Lett. **52**, 1508–1511 (1984).
- [227] E. P. Bashkin: “[Spin waves in polarized paramagnetic gases](#)”, JETP Lett. **33**, 8–11 (1981).
- [228] L. P. Lévy and A. E. Ruckenstein: “[Collective Spin Oscillations in Spin-Polarized Gases: Spin-Polarized Hydrogen](#)”, Phys. Rev. Lett. **52**, 1512–1515 (1984).
- [229] J. R. Owers-Bradley: “[Spin-polarized  \$^3\text{He}\$ - \$^4\text{He}\$  liquids](#)”, Reports on Progress in Physics **60** (11), 1173– (1997).
- [230] M. R. Gallis and G. N. Fleming: “[Environmental and spontaneous localization](#)”, Phys. Rev. A **42** (1), 38–48 (1990).
- [231] K. Hornberger and J. E. Sipe: “[Collisional decoherence reexamined](#)”, Phys. Rev. A **68** (1), 012105– (2003).
- [232] P. Massignan, G. M. Bruun and H. Smith: “[Viscous relaxation and collective oscillations in a trapped Fermi gas near the unitarity limit](#)”, Phys. Rev. A **71**, 033607 (2005).
- [233] C. Kittel: *Introduction to Solid State Physics*, Wiley, New York, 8th edition (2004).
- [234] M. J. Martin, M. Bishof, M. D. Swallows, X. Zhang, C. Benko, J. von Stecher, A. V. Gorshkov, A. M. Rey and J. Ye: “[A Quantum Many-Body Spin System in an Optical Lattice Clock](#)”, Science **341** (6146), 632–636 (2013).
- [235] C. Lhuillier and F. Laloë: “[Spin Oscillations in Polarized Gases](#)”, Phys. Rev. Lett. **54**, 1207–1207 (1985).
- [236] L. Mathey, E. Tiesinga, P. S. Julienne and C. W. Clark: “[Collisional cooling of ultracold-atom ensembles using Feshbach resonances](#)”, Phys. Rev. A **80**, 030702 (2009).
- [237] B. Vacchini and K. Hornberger: “[Quantum linear Boltzmann equation](#)”, Physics Reports **478** (46), 71–120 (2009).

- [238] M. Leibscher and B. Schmidt: “Quantum dynamics of a plane pendulum”, Phys. Rev. A **80**, 012510 (2009).
- [239] B. Misra and E. C. G. Sudarshan: “The Zeno’s paradox in quantum theory”, J. Math. Phys. **18** (4), 756–763 (1977).
- [240] W. M. Itano, D. J. Heinzen, J. J. Bollinger and D. J. Wineland: “Quantum Zeno effect”, Phys. Rev. A **41**, 2295–2300 (1990).
- [241] E. Timmermans: “Degenerate Fermion Gas Heating by Hole Creation”, Phys. Rev. Lett. **87** (24), 240403– (2001).
- [242] D. Greif, L. Tarruell, T. Uehlinger, R. Jördens and T. Esslinger: “Probing Nearest-Neighbor Correlations of Ultracold Fermions in an Optical Lattice”, Phys. Rev. Lett. **106**, 145302 (2011).
- [243] R. Jördens, L. Tarruell, D. Greif, T. Uehlinger, N. Strohmaier, H. Moritz, T. Esslinger, L. De Leo, C. Kollath, A. Georges, V. Scarola, L. Pollet, E. Burovski, E. Kozik and M. Troyer: “Quantitative Determination of Temperature in the Approach to Magnetic Order of Ultracold Fermions in an Optical Lattice”, Phys. Rev. Lett. **104**, 180401 (2010).
- [244] P. J. Mohr, B. N. Taylor and D. B. Newell: “CODATA recommended values of the fundamental physical constants: 2010”, Rev. Mod. Phys. **84**, 1527–1605 (2012).
- [245] T. Tiece: “Properties of Potassium”, (2010).
- [246] D. A. Butts and D. S. Rokhsar: “Trapped Fermi gases”, Phys. Rev. A **55**, 4346–4350 (1997).
- [247] L. Pitaevskii and S. Stringari: *Bose-Einstein Condensation*, Oxford University Press (2002).
- [248] A. Ludewig: “Feshbach resonances in  $^{40}\text{K}$ ”, Ph.D. thesis, University of Amsterdam (2012).
- [249] U. Schneider, L. Hackermüller, J. P. Ronzheimer, S. Will, S. Braun, T. Best, I. Bloch, E. Demler, S. Mandt, D. Rasch and A. Rosch: “Fermionic transport and out-of-equilibrium dynamics in a homogeneous Hubbard model with ultracold atoms”, Nat. Phys. **8**, 213–218 (2012).
- [250] N. Strohmaier, D. Greif, R. Jördens, L. Tarruell, H. Moritz, T. Esslinger, R. Sensarma, D. Pekker, E. Altman and E. Demler: “Observation of Elastic Doublon Decay in the Fermi-Hubbard Model”, Phys. Rev. Lett. **104**, 080401 (2010).
- [251] P. Wang, Z.-Q. Yu, Z. Fu, J. Miao, L. Huang, S. Chai, H. Zhai and J. Zhang: “Spin-Orbit Coupled Degenerate Fermi Gases”, Phys. Rev. Lett. **109**, 095301 (2012).
- [252] J. J. Sakurai: *Modern Quantum Mechanics*, Addison-Wesley Publishing Company, Inc., revised edition (1994).



# Danksagung

Während der vergangenen Jahre haben mich viele hilfsbereite Personen bei meiner Promotion unterstützt und damit zum Erfolg dieser Arbeit beigetragen. Es ist mir ein besonderes Anliegen, diesen meine tiefe Dankbarkeit auszudrücken! Darüber hinaus möchte ich einige Personen namentlich hervorheben:

An erster Stelle gebührt mein herzlicher Dank meinem Doktorvater Prof. Dr. Klaus Sengstock. Nicht nur von seiner fachlichen Expertise, sondern auch von seiner ausgeprägten wissenschaftlichen Intuition und seinem kritischen Hinterfragen von Ergebnissen habe ich entscheidend profitiert. Damit ist diese Forschungsarbeit unter den hervorragenden Rahmenbedingungen am Institut für Laserphysik erst möglich geworden.

Des Weiteren gilt mein Dank den Professoren, die meine Arbeit mitbetreut haben. Ich danke Prof. Dr. Ludwig Mathey für die Übernahme des Zweitgutachtens der Dissertation, Prof. Dr. Henning Moritz für die Übernahme des Zweitgutachtens der Disputation und Prof. Dr. Günter Sigl für die Übernahme des Prüfungsvorsitzes.

Einen besonderen Dank möchte ich meinen direkten Mitarbeitern aussprechen, mit denen ich am Projekt „Bose-Fermi Mischungen“ zusammenarbeiten durfte. Ich danke Christoph Becker für die hervorragende Leitung des Projekts, seine Motivation und seine persönliche Unterstützung. Darüber hinaus danke ich meinen Mitdoktoranden Sören Götzke, Jannes Heinze und Nick Fläschner, mit denen ich über Jahre hinweg eng zusammengearbeitet habe. Deren ausdauerndes Engagement und deren Hilfsbereitschaft haben nicht nur zu vielen spannenden Ergebnissen geführt, sondern uns auch eine wunderbare gemeinsame Zeit beschert. Vielen Dank für die großartige Unterstützung! Zudem danke ich meinen Mitstreitern Christof Weitenberg, Benno Rem, Juliette Simonet, Dominik Vogel, Malte Weinberg, Bastian Hundt und Maria Langbecker.

Ich hatte das große Glück, für das tiefere Verständnis der erzielten Ergebnisse mit verschiedenen Theoriegruppen zusammenarbeiten zu können, die damit das Projekt entscheidend mit nach vorne gebracht haben. Dazu gehören Dirk-Sören Lühmann sowie Ludwig Mathey und Alexander Itin in Hamburg. Zudem danke ich unseren Frankfurter Kollegen Walter Hofstetter, Yongqiang Li, Ulf Bissbort und Andrii Sotnikov. Des Weiteren bin ich unseren Mitstreitern in Barcelona, Maciej Lewenstein, André Eckhart und Ulrich Ebling, für die äußerst erfolgreiche Zusammenarbeit sehr dankbar.

Abschließend möchte ich mich mit einem besonderen Dank an meine Familie und meine Freunde wenden. Ihr habt immer an mich geglaubt und mir in der gesamten Promotion unermüdlich zur Seite gestanden!